NUCLEAR ROCKET TECHNOLOGY CONFERENCE (U)

LEWIS RESEARCH CENTER
CLEVELAND, OHIO
APRIL 19-20, 1966

NATIONAL AERONAUTICS AND SPACE ADMINISTRATION

NUCLEAR ROCKET TECHNOLOGY CONFERENCE (U)

LEWIS RESEARCH CENTER
CLEVELAND, OHIO
APRIL 19-20, 1966

Scientific and Technical Information Division 1966
NATIONAL AERONAUTICS AND SPACE ADMINISTRATION
Washington, D.C.

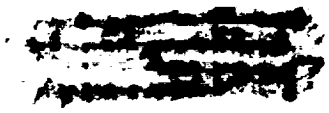

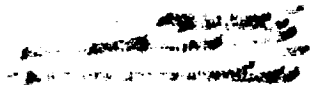

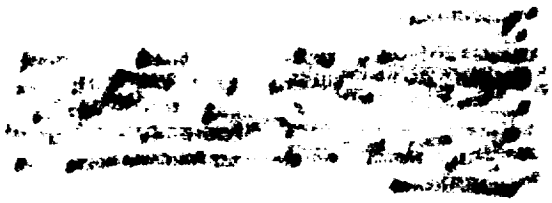

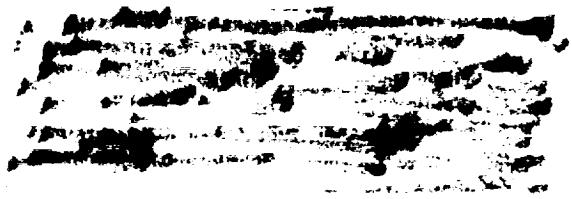

FOREWORD

The Lewis Research Center has a strong interest in nuclear rocket propulsion and provides active support of the graphite reactor program in such nonnuclear areas as cryogenics, two-phase flow, propellant heating, fluid systems, heat transfer, nozzle cooling, nozzle design, pumps, turbines, and startup and control problems. A parallel effort has also been expended to evaluate the engineering feasibility of a nuclear rocket reactor using tungsten-matrix fuel elements and water as the moderator. Both of these efforts have resulted in significant contributions to nuclear-rocket technology.

Many successful static firings of nuclear rockets have been made with graphite-core reactors. Sufficient information has also been accumulated to permit a reasonable judgment as to the feasibility of the tungsten water-moderated reactor concept. We therefore consider that this technology conference on the nuclear rocket work that has been sponsored by the Lewis Research Center is timely. The conference has been prepared by NASA personnel, but the information presented includes substantial contributions from both NASA and AEC contractors. The conference excludes from consideration the many possible mission requirements for nuclear rockets. Also excluded is the direct comparison of nuclear rocket types with each other or with other modes of propulsion.

The graphite reactor support work presented on the first day of the conference was partly inspired through a close cooperative effort between the Cleveland extension of the Space Nuclear Propulsion Office (headed by Robert W. Schroeder) and the Lewis Research Center. Much of this effort was supervised by Mr. John C. Sanders, chairman for the first day of the conference, and by Mr. Hugh M. Henneberry.

The tungsten water-moderated reactor concept was initiated at Lewis by Mr. Frank E. Rom and his coworkers. The supervision of the recent engineering studies has been shared by Mr. Samuel J. Kaufman, chairman for the second day of the conference, and Mr. Roy V. Humble. Dr. John C. Evvard served as general chairman for the conference.

Abe Silverstein
Director

CONTENTS

GRAPHITE NUCLEAR ROCKET

INTRODUCTION

The U. S. nuclear rocket program is directed by Mr. Harry B. Finger through his joint AEC-NASA Space Nuclear Propulsion Office. He utilizes three field offices also called SNPO in his activities.

SNPO, Albuquerque, maintains liaison with the effort performed at the Los Alamos laboratory. The principal function of the Nevada SNPO is to manage the Nuclear Rocket Development Station commonly referred to as NRDS. SNPO, Cleveland, headed by Mr. Robert W. Schroeder, is responsible for the NERVA development including the engine and its applications. The prime contractor for NERVA is the Aerojet-General Corporation, and Westinghouse Astronuclear Laboratory (WANL) serves as the principal subcontractor. There are also many smaller contracts supporting the program.

The SNPO-Cleveland responsibility includes coordination of the NERVA research and development effort of all the pertinent contractors and government laboratories. In particular, the Lewis Research Center contributes to the program by (a) initiating long-term nuclear rocket programs that go beyond the immediate requirements of NERVA, and (b) furnishing extensive support to NERVA in nonnuclear areas such as cryogenics, two-phase flow, propellant heating, fluid systems, heat transfer, nozzle cooling, nozzle design, pumps, turbines, and startup and control problems. This information is presented in papers II to IV as follows:

PROPELLANT FLOW SYSTEM COMPONENTS - Neutron and gamma radiation intensities from the reactor cause propellant heating and associated cavitation of liquid hydrogen in the pump. The compromises between tank pressure and pump design to alleviate this difficulty have been studied. Pump performance problems during the "boot-strap" startup are also included.

HEAT TRANSFER AND FLUID MECHANICS - The steady-state cooling of the nuclear rocket exhaust nozzle for full-power operation is discussed. Separate effects on both the gas and coolant sides of the wall appreciably reduce the severity of the heating load. Even though severe thermal stress concentrations are estimated, it appears that a well-designed regeneratively cooled system will enable the use of conventional stainless steel materials. The presentation is concluded with a discussion of the gaseous and two-phase heat transfer and pressure drops encountered during the transient startup period.

STARTUP DYNAMICS AND CONTROL - The highlights of experimental and analytical nuclear rocket system dynamics, primarily those associated with an unfueled reactor flow system startup, are presented. Effects of boiling hydrogen two-phase flow and pump stall on the "boot-strap" operation are discussed. Status of the application of fluidic devices to control systems is reported.

Mr. Milton Klein, Deputy Manager of the AEC-NASA Space Nuclear Propulsion Office, Washington, D. C., in the first paper, reviews in detail the overall nuclear rocket program and presents the history, recent successes, programs, and goals of the graphite-core nuclear rocket.

I. STATUS OF GRAPHITE-NUCLEAR-ROCKET PROGRAM

Milton Klein

AEC-NASA Space Nuclear Propulsion Office

INTRODUCTION

The nuclear-rocket program is providing propulsion system technology, which will add significantly to this country's ability to perform the space missions of the future and enable us to accomplish the desired missions without being limited by propulsion considerations. This program covers a broad range of technologies, including nuclear reactors, rocket-engine components, and engine systems, and involves NASA centers, AEC laboratories, universities, and industrial contractors. The work described in this report is that portion of the nuclear-rocket program performed by the NASA Lewis Research Center and its contractors. That work not only has contributed directly to the goals of the nuclear-rocket program but also constitutes an important contribution to the total fund of technology in advanced materials, in heat transfer, in fluid systems, and in controls.

To provide information on the complete nuclear-rocket program, it was suggested that a paper summarizing the activities not included in the following Lewis reports be prepared. Accordingly, this paper has been written to provide, first, a perspective of the overall nuclear-rocket program and, second, a detailed review of the activities concerned with graphite solid-core reactors and engines.

NUCLEAR-ROCKET PROGRAM DESCRIPTION

The several parts of the nuclear-rocket program are as follows:

(1) Graphite solid-core reactors and engines
  (a) Kiwi/NERVA - Los Alamos/Aerojet-Westinghouse
  (b) NERVA engine technology - Aerojet and Westinghouse
  (c) Supporting research and technology - Lewis
  (d) Phoebus - Los Alamos
  (e) Proposed NERVA engine development - Aerojet and Westinghouse

(2) Other concepts
  (a) Tungsten solid-core reactors - Argonne and Lewis
  (b) Cavity reactor

(3) Advanced nonreactor component and engine systems technology - Lewis
(4) Stage technology
(5) Application studies

The primary effort in the program has been and continues to be that related to the graphite solid-core reactors and engines utilizing such reactors. This work includes the Kiwi and NERVA reactor activities of Los Alamos and Aerojet-Westinghouse, respectively, NERVA engine technology, Phoebus reactor work at Los Alamos, supporting research and technology at Lewis, and, proposed for initiation next year, NERVA engine development.

The other solid-core reactor effort has been related to tungsten reactors, conducted at Lewis and at the Argonne National Laboratory. This work has had the objective of examining the feasibility and performance potential of tungsten reactors for nuclear rockets. Since performance can be no better than the capability of the fuel elements, the work has been largely fuel-element and materials oriented. The Lewis work is focused on a water-moderated-reactor system and that at Argonne on a fast-reactor system. This work has shown that such reactors are feasible and that they appear to have a performance potential in terms of specific impulse comparable with that of graphite reactors. On the basis of the work done so far, tungsten reactors appear to offer the possibility of longer-duration operation. However, the primary missions toward which the nuclear-rocket program is now aimed do not require operating durations longer than those attainable with graphite. The present plans for tungsten systems, therefore, are to conclude the work now underway and not to proceed toward establishing a complete technology base. Because of budgetary constraints, the work is being terminated somewhat earlier than would be desirable for technology purposes. The Lewis work on tungsten systems is described in papers V to VIII.

A temperature limit is imposed in solid-core systems by the structural strength of the fuel-bearing material. Cavity reactors have been proposed to exceed that limit. Their theoretical potential performance ranges from the order of 1200 seconds specific impulse for dust bed concepts to perhaps 2500 to 3000 seconds for gaseous-core concepts, with liquid-core systems having a potential of the order of 1500 to 1600 seconds. These values compare with the upper limit of approximately 1000 seconds for solid-core systems.

The problems of attaining the theoretical specific impulse of these cavity-reactor concepts are severe. At this stage it is not known that such systems are feasible or what their realistic performance potential might be. The theoretical performance, however, is sufficiently great that some work is warranted. The cavity-reactor effort which we sponsor examines primarily the fundamental problems of fluid mechanics and heat transfer associated with such systems. Some of that work is being done at Lewis, but there was not time on the Lewis agenda to provide adequate coverage of the subject.

As a companion to the reactor work aimed at the long-term goal of ever higher performance, there is work, primarily at Lewis, to advance the technology of nonreactor

components that will be needed if such performance is to be achieved. Lewis is depended on heavily to pave the way for these advanced systems.

At present, relatively little effort is being devoted to the area of stage technology. However, with the success of the engine work, greater emphasis on stage technology is called for. Particularly important is an examination of the effects of radiation heating on the propellant; basic work on that subject is being done at Lewis. Long-term cryogenic storage is another of the important problem areas.

The final category of work listed is that of application studies. In the nuclear-rocket program, a limited number of such studies is performed in order to provide information on performance trade-offs and to guide our efforts generally. Particularly significant during the past few years has been the work done to define the effect of engine thrust on performance for the various missions toward which our program is directed.

Out of these studies arose a very interesting prospect - the possibility that an engine designed for a thrust level of 200 000 to 250 000 pounds, used singly or in clusters, could perform all the principal missions for which nuclear rockets appear advantageous. This engine size is not necessarily optimum in every case, but, in those cases in which it is not optimum, the performance penalty is relatively small. The development of such an engine would therefore not only be "cost-effective," but would also provide a means for gaining a maximum amount of experience on a single engine design. This concept of a versatile engine has been extended to the concept of a propulsion module composed of that engine and the associated propellant tankage, as shown in figure I-1. The propellant tank is sized at 33 feet in diameter to make it compatible with the Saturn V as a third stage. The propellant loading can be changed by shortening the tank or by adding additional propellant tankage. This propulsion module concept, which was proposed by Marshall Space Flight Center, is of significance in our present technology effort as well as in our future planning.

GRAPHITE SOLID-CORE REACTORS AND ENGINES

Now let us return to the program on graphite solid-core reactors and engines. Figure I-2 shows a drawing of the NERVA nuclear-rocket engine. The principal components of the engine are the reactor, with its core and reflector regions; the turbopump; the jet nozzle, with a bleed port to carry hot hydrogen to the turbine; and the control system.

At the present time we are in a technology program. In general, our objective is to establish the technology for graphite nuclear-rocket engines so that it will be possible to proceed with confidence into the development of any required engines.

As an end technology objective in itself and to unify the many aspects of the nuclear-rocket program, engine system investigations are being conducted with the following specific objectives:

(1) Determination of allowable ranges of startup parameters

(2) Exploration of engine performance characteristics, limits, and interactions

(3) Evaluation of control concepts

The NERVA technology investigations utilize a 50 000-pound-thrust engine system (1000 MW) rated at a specific impulse of approximately 760 seconds.

In order to carry out this engine-system activity, it is obviously necessary to have suitable components. The principal and crucial component is, of course, the reactor. But, in addition to the reactor work, it has been necessary to provide the nonreactor components required to conduct the engine-system investigations. The principal activities in this regard are the development of a suitable nozzle with the hot bleed port referred to earlier, a suitable liquid-hydrogen turbopump, and a suitable control system. At the same time as these components are being developed for the system investigations, it is also necessary to keep in mind the need for establishing the technology of such components as required for future engine development.

For all these components, the basic work has been done at Lewis. Hydrogen heat-transfer research has been important in the nozzle efforts. Lewis is engaged in examining the radiation effects on materials and components. Radiation is, of course, the special environment associated with nuclear rockets; apart from those effects, the technology of the nonreactor components is directly related to that of chemical-rocket systems. All these technology efforts form the basis for the development of the 200 000- to 250 000-pound-thrust NERVA engine that has been defined for future mission use.

Graphite-Reactor Technology

Only a short time ago, 23 months to be exact, a nuclear-rocket reactor had not achieved a measurable time of operation at design power and temperature. Late in 1962 in the first test of the chosen graphite-reactor design, the Kiwi B-4A, major structural damage of the reactor occurred. To be sure, there had been significant accomplishments and progress by that time at Los Alamos. A graphite-uranium fuel element had been designed that withstood the thermal stresses and, to a limited extent, withstood corrosion by the hydrogen propellant. Design methods had been developed. Startup of the reactor with liquid hydrogen fed to the system had been demonstrated. (The matter of startup on liquid hydrogen had been a worry because of the potential two-phase-flow instabilities. However, by careful preliminary analysis and experiment, this particular problem had been well worked out, so that the problem did not materialize.) In addition, a reactor-control system had been developed that was capable of controlling this high-power density machine in a responsive and stable fashion and doing so automatically.

But a suitable structural design had yet to be demonstrated. Until that particular problem was solved, complete reactor operation obviously could not be demonstrated nor was it possible to examine fully the fuel-element or the control-system behavior or the other aspects of reactor operation.

For the year and a half after the 1962 test, further reactor testing was deferred in favor of an increased examination of individual components, subsystem testing, and cold-flow testing. By May 1964 there was readiness for another test. That May 1964 Kiwi test, less than 2 years ago, achieved nearly full-power operation for about 1 minute. The contrast between that test and the more recent tests is indeed remarkable. In the May 1964 test, operation was cut short after about 1 minute because of a hydrogen fire caused by a leak in the nozzle. Nevertheless, that 1 minute of operation was extremely gratifying because the reactor operation during that period was excellent and the condition of the reactor after the test was excellent. While the test was of relatively short duration, it had proved the suitability of the structural design that had evolved. As a result, at this conference, continuing concrete accomplishment can be discussed.

Since the ill-fated Kiwi-B4A test in November 1962, six reactors have been tested at power, as shown in figure I-3. In all these cases, the reactor operation was good. The reactor has proved to be a reliable and predictable component. It has proved to have a wide range of stable operation. These reactors have accumulated a total operating time of approximately 4 hours of which approximately 1 hour and 10 minutes have been at full power and full temperature, which, at altitude conditions, is equivalent to a thrust level of approximately 55 000 pounds at a specific impulse of approximately 760 seconds for an assumed area ratio nozzle of 40 or nearly 800 seconds for an assumed area ratio nozzle of 100. The longest operation of a single reactor was that on the breadboard engine, the NRX/EST, the testing of which was completed last month. On this system, 110 minutes of power operation were accumulated of which approximately 28 minutes were at the full-power condition.

With the solution of the structural design problems demonstrated through all these tests, the major technical effort is now concentrated on the objective of achieving long-duration reactor operation. Our goal is to provide a capability of about 60 minutes of full-power operation on a single reactor. This time compares with a mission operating duration requirement for a single engine of 15 to 20 minutes in some cases and 30 to 40 minutes in others. The 60-minute goal was chosen to provide margin as well as to provide more economy in development, that is, to permit more tests on a single reactor.

The duration capability of the reactor is limited by the corrosion of graphite by the hydrogen propellant. This corrosion takes place in several areas of the reactor. Figure I-4 is a cross-sectional sketch of a fuel-element cluster. Each cluster contains six fuel elements surrounding an unfueled central graphite element. Through this central element passes a metal support rod that is attached to a graphite support block at the hot

end of the cluster. The load of the fuel elements and the pressure load are carried to this graphite support block at the hot end and in turn to the metal support rod that is attached at the cold end to a metal support plate. There are approximately 250 clusters in a core, all hung from the cold end, as shown in figure I-5. Each fuel element is made of graphite containing uranium and is hexagonal in shape. Its dimensions are 3/4 inch across flats and approximately 52 inches long.

The graphite is subject to attack by hydrogen wherever it exists at high temperature. The principal areas of attack are the fuel element and the periphery of the reactor core, where hydrogen is used to establish a proper pressure relation for structural purposes and to provide cooling to certain parts. This corrosion attack is minimized by coating certain surfaces with a corrosion-resistant material, and design features are employed to minimize flows of hydrogen to other graphite surfaces.

Since the fuel element is the keystone of the system, it is the principal area of corrosion concern. As illustrated in figure I-6, it is subject to varying kinds of attack - in the coolant passages, on the external surfaces at the hot end, and potentially, on the external surfaces between elements because of bypass leakage. The coolant passages and the exterior surfaces at the hot end are coated with niobium carbide, as are the cluster support blocks. It has not thus far been necessary to coat the exterior surfaces of the element above the hot end, since flows in that region may be sufficiently low to avoid serious attack there.

Through extensive laboratory work, great progress has been made in minimizing fuel-element corrosion. Figure I-7 shows the improvement in fuel-element performance over the past several years. The vertical bars represent demonstrated fuel-element lifetime for the years 1964 and 1965 and projected for 1966. For each year, two measures of performance are shown. To the left are data from reactor tests; to the right are data from electrically heated furnace tests. Furnace testing is employed as a reasonable corrosion simulation of reactor performance. Test data from electrically heated experiments are used for purposes of fuel-element development as well as for quality control. As might be expected, performance in electrically heated tests is always ahead of the performance in the reactor because of the lag in time between development of an improved element and the test of that element in a reactor.

In 1964, a reactor duration of about $10\frac{1}{2}$ minutes was achieved at slightly under 4400° R fuel temperature, which gives a chamber temperature of about 4100° R. Performance has been increased to the point that there has already been achieved, in a 1966 reactor test, a duration of about 30 minutes at this temperature, and our goal for the next year or so is to operate a single reactor for about 60 minutes. Furnace tests in 1964 showed performance of about 25 minutes at a slightly higher temperature. We have now, in a few specimens, achieved in furnace tests close to 2 hours at 4400° R.

Recently, a new coating technique was developed that gives promise of extending the corrosion resistance of the element substantially. With this technique, a fuel-element specimen was tested for nearly 2 hours at a fuel-element exit temperature of 4800° R. This temperature would provide a specific inpulse of more than 850 seconds for an assumed area ratio nozzle of 100. Therefore, it appears clearly possible to have a fuel element that substantially exceeds the goal of 60 minutes of operation at a chamber temperature of 4100° R and even 60 minutes at substantially higher temperatures.

While work is proceeding toward improvement of the corrosion resistance of the reactor, efforts are also underway toward a higher power reactor. This work is being done by Los Alamos in what is called the Phoebus program. Table I-1 compares certain features of the Kiwi and NRX (the NERVA technology reactors) that have been tested to date and the 5000-megawatt reactor called Phoebus 2. The Phoebus 1 testing program is a stepping stone toward the Phoebus 2 that uses hardware the same size as the Kiwi and NRX reactors tested to date. The Kiwi and NRX reactors have a diameter of 35 inches. The Phoebus 2 reactor will have a diameter of approximately 55 inches. The design power of the Kiwi and NRX is 1120 megawatts and of the Phoebus 2, approximately 5000 megawatts. The hydrogen flow rate will go from 70 to 285 pounds per second, and an increase in the exit gas temperature from 4100° R to between 4500° and 5000° R is desired. The Phoebus 2 reactor is similar to the reactors tested to date except that they contain more fuel elements. The fuel elements are of nearly identical design, but in order to provide more power, a larger number of elements are required, leading to the increase in reactor diameter.

To test the Phoebus reactor, it is necessary to have in the test facility a suitable liquid-hydrogen feed system. To provide such a pumping system is a development program in itself. This work has been going on at Rocketdyne and employs a parallel pumping system, illustrated in figure I-8, which is an outgrowth of the pump that was developed for reactor testing in the Kiwi program. It is a four-stage axial-flow pump driven by a five-stage turbine. Two such pumps will be operated in parallel for testing the large reactor. Development testing of this type of system in the parallel pumping mode has been performed, showing stable operation. Primary effort at this time is the development testing of the improved pump in a single pump mode.

Engine System Technology

With the success of the reactor program, increased attention has been devoted to obtaining an understanding of the complete nuclear-rocket-engine system. In figure I-9 are shown the major elements of the program. Underlying this work is an intensive program of system analysis, both steady state and dynamic. But even sophisticated analysis must

be supplemented by experiments to verify the analysis and fill voids in our understanding. The experimental work includes an examination of the behavior of the individual components: reactor, turbopump, nozzle, and control system. It employs cold-flow systems, which involve the operation together of all the components as a system except that a non-power reactor is used. These cold-flow systems have been useful in examining the first few seconds of engine operation. The work at Lewis has been particularly important in providing a thorough understanding of the engine system through the cold-flow engine experiments conducted at the Plum Brook Station. The Lewis work was supplemented by cold-flow testing at Aerojet, all of which was preliminary to power testing of the engine system. The first power test of the engine system employed a breadboard engine called EST for Engine System Test. The testing of EST just completed marks the high point of our work to date. The next phase of engine-system-technology investigations employs a system in a down-firing position in a test stand that provides altitude simulation. It will also be more nearly configured to a flight system than the breadboard engine.

Now let us return to the recent test program on the breadboard engine, the so-called EST program. Those who have seen photographs of that breadboard engine at the test cell may wonder what the difference is between it and the previous reactor tests. The next two figures indicate the difference. Figure I-10 is a drawing showing the means for supplying hydrogen in a reactor test. As shown in the schematic drawing, in such a test, the reactor, placed on its test car and plugged into the test-cell wall, is fed hydrogen from the Dewar by use of a turbopump located in the facility. The turbine is driven by a facility supply of high-pressure gaseous hydrogen. The hydrogen flows through the tubes forming the nozzle wall, through the reflector, and then into the reactor core and out the jet nozzle. In the breadboard engine, as shown in figure I-11, the facility turbopump driven by a separate supply of gaseous hydrogen is bypassed, as indicated by the dashed lines. Instead, an engine-type turbopump is located on the test car and the turbine of that turbopump is driven by hydrogen bled from the nozzle chamber that is diluted with cold hydrogen gas to a temperature of approximately 1200° R. The breadboard engine therefore involves all the principal components of a flight engine, the same flows and therefore essentially the same system interactions as a flight engine.

Figure I-12 shows the breadboard engine plugged in at the test cell at the Nuclear Rocket Development Station in Nevada. The reactor is located on the shed that houses various reactor-control components. To the left of this shed is another shielded enclosure in which are located the turbopump, the turbine-power-control valve, and related components. Those components are not present in a reactor test. The enclosure for those components was shielded so that it was unnecessary to qualify them completely for radiation resistance. Figure I-13 is a view of the interior of the enclosure showing the turbopump and the turbine-power-control valve. The angle of this photograph makes the space look relatively crowded. Actually, there was plenty of room to work around the components.

The objectives of the breadboard engine test program were

(1) To demonstrate the hot-bleed-cycle nuclear-rocket engine

(2) To demonstrate bootstrap startups to power region

(3) To provide data on

(a) Steady-state and transient operation of the system

(b) Component interactions

(c) Alternate control modes

Several new components were being tested in the system for the first time. The nozzle shown in figure I-14 was the same as that used in previous NRX reactor tests except for the addition of a hot bleed port. This bleed port is a crucial element of the system, since it must duct hydrogen at temperatures in excess of 4000° R from the chamber. The nozzle is made of stainless-steel U-channels brazed into slots in a forged stainless-steel pressure shell.

The turbopump in the engine system, shown in figure I-15, consists of a centrifugal pump driven by a two-stage turbine. It delivers hydrogen at a flow rate in excess of 70 pounds per second and has hydrogen cooled and lubricated bearings.

An integrated engine-control system, shown schematically in figure I-16, was used for the first time. As previously indicated, an important objective of the breadboard-engine test was the exploration of various control modes. Engine control is achieved through the regulation of two components. One is the reactor control drum, 12 of which are located in the reflector region around the reactor core. Those drums control neutron power that, in turn, affects temperature and pressure. The other control component is the valve that controls the flow of drive gas to the turbine and, thereby, affects the hydrogen pumping rate.

Several control loops are available to regulate the control drum and valve positions. Neutron power can be sensed and used to control the reactor control drums. Chamber temperature can be sensed and used to control the reactor control drums. Chamber pressure can be sensed and used to control the turbine-power-control valve to control hydrogen flow. Closed-loop or open-loop control can also be used, as well as various combinations of these loops. Experimental investigations of these control variations were conducted in the breadboard-engine-test program.

After cold-flow tests on the breadboard engine to check out the system as well as establish certain base point comparisons with previous cold-flow testing, a series of power tests was conducted, as given in table I-2. In all, there were 10 startups of the system. During these startups, pressure in the propellant Dewar and temperature of the reflector were varied. In the several tests, a variety of control modes was tried, and numerous experiments were conducted to determine the system response to pressure, temperature, and power transients. In all, 110 minutes of power operation were accumulated, including about 28 minutes at full power.

One aspect of the testing program was aimed at exploring the bootstrap start characteristics of the system. In a bootstrap start, the engine uses the energy available from the pressure in the propellant tank and reactor heat to start. There is no external source of starting energy. Bootstrap starts have been conducted in cold-flow tests at Lewis and at Aerojet in Sacramento, but those tests were limited in that they obviously could not carry the system into the power region. They showed that such starts were feasible but more data were needed for the extension from the first few seconds into power operation.

In figure I-17, cold-flow data, which are represented by dashed lines labeled CFDTS are compared with the breadboard engine data, which are represented by the solid lines. A satisfactory start would require the pump speed to increase to 2000 to 3000 rpm in a few seconds. There are comparisons for propellant tank pressures at 70, at 45 and 50, and at 35 pounds per square inch absolute. For 70 and 45 pounds per square inch absolute, the bootstrap start is satisfactory in bringing the turbopump to speed. For a propellant tank pressure of 35 pounds per square inch absolute, the startup is marginal at best. All these tests were at an atmospheric exhaust pressure of 12.7 pounds per square inch absolute. The breadboard-engine-test data are in good agreement with the cold-flow data. There are some differences, but they do not seem to be of major significance at this point.

Another aspect of the breadboard EST program was to explore operation of the engine system over the entire operating range. Figure I-18 is an engine map plotting nozzle chamber temperature, which is related to specific impulse, against the nozzle chamber pressure. The normal operating line is shown. The region of principal interest is bounded within the lines shown. The structural limit is related to the temperature capability of the fuel-cluster metal support rod. That limit and the fuel-material temperature limit are related to natural characteristics. The other bounds shown are chosen, in some respects arbitrarily, to limit the range of interest. If it were necessary to operate to the lower right, it would be possible to define a system to do so. Our objective then was to examine operation within the bounds shown.

Figure I-19 shows in a simplified, idealized way where the breadboard engine was operated. Region 1 is around the design point; a number of experiments were conducted there. Region 2 is an intermediate temperature and power region, and a number of transient response and control system experiments were performed in that region. Region 3 is the bootstrap start region and, as mentioned earlier, a number of experiments were conducted there. In addition, the limits of the system in terms of temperature and pressure were explored. The engine was mapped across from the operating point by throttling down on flow and power until a predetermined point approaching the structural temperature limit was reached. As expected, it was possible to throttle the engine at full specific impulse over a range of chamber pressures from about 200 pounds per square inch absolute to the full operating pressure of about 550 pounds per square inch absolute.

Similarly, the engine was mapped across the 3400° R line and the 2500° R line. Figure I-19 also shows operations with fixed turbine-power-control-valve settings for ramping power down from one level to another.

As previously indicated, in the course of the test series a number of controls experiments were performed. For example, the system was operated with the neutron power loop eliminated. It was operated on pressure control alone. It was operated open loop with fixed or programed turbine-power-control-valve positions and reactor-control-drum positions. A startup experiment was performed with the control drums fixed, power rising with the increasing bootstrap-start flow of hydrogen. The response of the control system to various temperature, pressure, and flow transients was examined. Throughout the test, the system was generally stable.

The bootstrap start phase of operation took about 10 to 15 seconds, and then temperature was raised at the rate of more than 100° R per second. Thus, about 50 seconds were involved in going from startup to design point, although in these tests there were calibration holds on the way to full power that lengthened the time.

In summary, the breadboard-engine-system test program showed that

(1) The hot-bleed-cycle system operation is stable and flexible over a wide range.

(2) The system can be throttled at full specific impulse.

(3) Several start techniques are feasible.

(4) Alternate control modes are available.

(5) Multiple starts and many tests are possible from one hardware assembly.

A preliminary assessment of the behavior of the major engine components is shown in table I-3. This assessment is preliminary because post-test examination has only just begun on the system. The behavior of the nozzle and the bleed port was quite satisfactory. They have been inspected with remote television and appear to be in good shape. Figure I-20 shows the bleed port looking into the turbine-inlet line, taken between tests. The turbopump and the turbine-power-control valve both operated satisfactorily. There was difficulty with only one significant component - the turbine-power-control-valve actuator. It exhibited excessive wear after the first day of power testing and was replaced. The replacement also exhibited wear and that one was replaced. An improved model was then installed and worked well through the remainder of the series. The reactor performance was clearly satisfactory. The reactor is now being inspected in the disassembly process. Significant corrosion was expected to be in evidence in the fuel elements and is being observed. The reactor control drums and their actuators operated satisfactorily.

With the completion of the breadboard-engine program, attention is being turned to the next phase of the engine-system program, the building of a ground-experimental engine, called XE, to be tested in a down-firing position into an altitude exhaust system. An exploded view of the ground-experimental engine is shown in figure I-21. Shown are the reactor, the nozzle, the turbopump assembly and lines in the upper thrust structure,

and the test stand adapter, which is fixed to the test stand. The engine is divided into two modular parts. It is so designed that the upper thrust structure can be replaced remotely in case it becomes necessary to do so during the test program. This experimental engine will be tested in Engine Test Stand No. 1, nearing completion at the Nuclear Rocket Development Station. A recent photograph is shown in figure I-22. A crucial part of this facility is the exhaust duct that fits into the chamber below the test pad level. That exhaust duct is essentially a large, cooled nozzle. The elbow of the duct is shown in figure I-23 to give an idea of its size. Attached to each end of the elbow are straight sections approximately 40 to 50 feet long.

The objectives in the ground-experimental (XE) program are to provide data on

(1) Systems interaction and control at altitude conditions
(2) Systems interaction and control with a system configured closely to flight system
(3) System limits
(4) Cooldown and restart characteristics
(5) Malfunction studies
(6) Facility operations throughout the full operating range
(7) Remote maintenance

A very important aspect of the experimental engine program is to gain experience in the operation of the complex engine - test-stand system.

Finally, experience is to be gained with remote maintenance techniques. It is important to have the capability of replacing a component during a test series in case it should fail. The replacement module approach in the XE system is a step toward this capability. In the XE program, this approach will be studied.

For most such operations and for routine disassembly, a shielded maintenance-assembly-disassembly building is used. Such a facility for engines is nearing completion at the Nuclear Rocket Development Station. A photograph of the interior of the main shielded bay is shown in figure I-24. Large remotely operated manipulators are employed in the operations.

NERVA Engine Development

With the testing of the XE engine, completion of the basic technology phase of the graphite-reactor-engine program will be approached. The tests to be performed in the near future are indicated at the bottom of figure I-25. Additional NERVA technology reactor experiments are planned this year: the NRX-A5 and the NRX-A6. In addition, the Phoebus reactor program is underway with an intermediate-power test scheduled in the summer of 1966 leading to high-power reactor testing beginning late in 1967 preceded by a cold-flow test in the spring of 1967. The XE ground-experimental engine program will

begin in 1967 and continue into 1968.

The success of the program has led to the establishment of plans to proceed with the development of the specific NERVA engine required for future missions. Indeed, that development work is planned for initiation in late 1966. The size of the NERVA engine is shown in figure I-26 in comparison with the technology engine system. It uses directly the technology that has been established through the program now underway. It is simply a larger version. As mentioned earlier, the reactor is of essentially the same design except that more fuel elements are used. The fuel-element outside dimensions are the same. The diameter of the coolant channels is increased from 100 to 110 mils. Otherwise, the element is identical. Extrusions of the modified elements have already been made. The nozzle comparison is shown in figure I-27. The nozzle that has been used until now is compared with the Phoebus 2 nozzle that will serve as the basis for the NERVA engine. The same basic design approach is used. However, the material is changed. As higher performance is achieved, the nozzle will be fabricated of Hastelloy X instead of the stainless steel used in the present nozzle.

A pacing factor in the development of the large NERVA engine is the construction of test stands required for the higher thrust engine. Figure I-28 is an artist's sketch of such a test complex. Design of the facility will be initiated in the near future. The test-stand complex, called Engine/Stage Test Stands 2 & 3, is being designed to test engines and, at some future date, a complete propulsion module. Two positions are contemplated operating off a central control and logistic center. A close-up view of one of these test positions is shown in concept in figure I-29. It employs a similar approach to that employed in Engine Test Stand No. 1.

CONCLUDING REMARKS

This completes a quick summary of the graphite reactor and engine program. The work done to date gives a high confidence in our ability to proceed with assurance to the development of the large NERVA engine. That engine will provide a major advance in this country's propulsion capability. Nuclear rockets can be made available to provide a flexibility of choice among future mission options as we proceed in the space program beyond Apollo.

TABLE I-1. - COMPARISON OF NOMINAL DESIGN VALUES

OF KIWI, PHOEBUS 1, AND PHOEBUS 2

Reactor	Diameter, in.	Design power, MW	Reactor flow rate, lb/sec	Exit gas temperature, ^{o}R
Kiwi/NRX	35	1120	70	4100
Phoebus 1	35	1100 to 1500	70 to 94	4100 to 4500
Phoebus 2	55	5000	285	4500 to 5000

TABLE I-2. - ENGINE-SYSTEM POWER TESTS

Date	Start	Power (maximum), MW	Temperature (maximum), ^{o}R	Duration, min	Partial list of experiments
2/3/66	1	440	2550	11	Normal bootstrap temperature response
	2	250	2050	13	Chilled reflector start; turbine-power-control-valve response; temperature limiter
2/11/66	3	230	2000	9	Fixed drum start; control drum response
	4	160	1450	--	Low-pressure start (abort)
	5	350	2590	22	Normal start; pressure response; temperature and power limiter; cross loop limiter; 2500^{o} R mapping; no-flux-loop control
3/3/66	6	1090	4100	6	Normal start; design power and temperature
	7	1040	3690	15	Normal start; 3400^{o} R mapping; on-off controller
3/16/66	8	170	1500	--	Control positioning error led to automatic flow shutdown
	9	1090	4090	18	Low pressure start; design point system response; 4000^{o} R mapping
3/25/66	10	1130	4175	16	Duration capability; design point system response
			Total	110 (28 min nominal full power)	

TABLE I-3. - PRELIMINARY ASSESSMENT OF BEHAVIOR OF MAJOR ENGINE COMPONENTS FOR ENGINE-SYSTEM TEST

Subsystem or component	Behavior	Remarks
Nozzle/bleed port	Satisfactory	Inspected with television
Feed system:		
Turbopump	Satisfactory	
Turbine-power-control valve	Satisfactory	
Turbine-power-control-valve actuator	Excessive wear	Replaced with improved model
Reactor	Satisfactory	Post mortem required
Reactor-control-drum actuator	Satisfactory	Sluggish operation of one actuator due to hydraulic line freeze; insulation installed

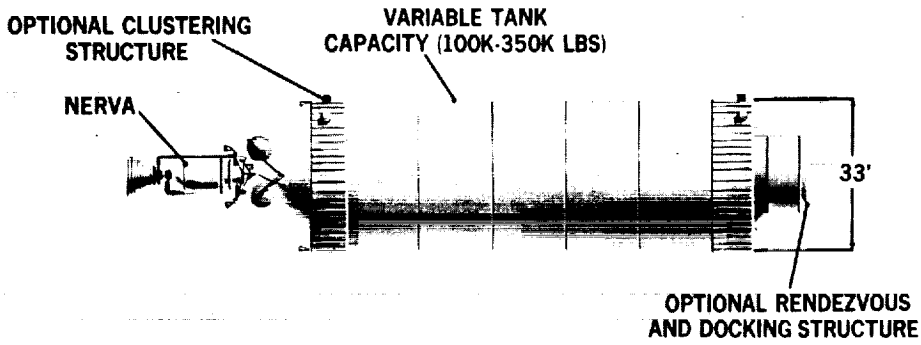

Figure I-1. - Propulsion module concept.

This figure UNCLASSIFIED

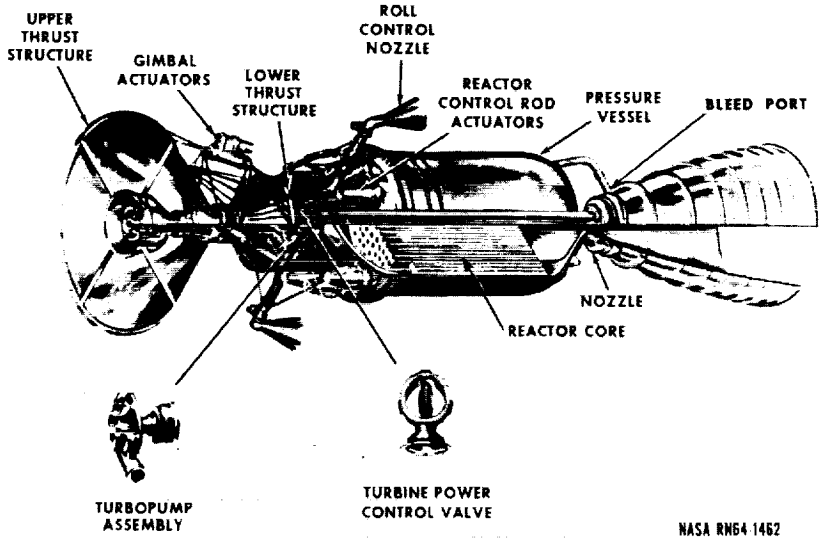

Figure I-2. - NERVA engine.

This figure CONFIDENTIAL

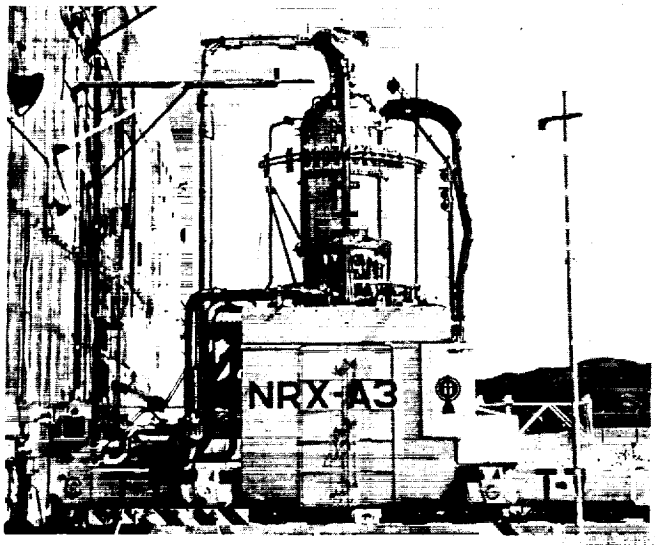

KIWI-B4D POWER	MAY 13, 1964
KIWI-B4E POWER	AUGUST 28, 1964
KIWI-B4E RESTART	SEPTEMBER 10, 1964
NRX-A2 POWER	SEPTEMBER 24, 1964
NRX-A2 RESTART	OCTOBER 15, 1964
KIWI TNT	JANUARY 12, 1965
NRX-A3 POWER	APRIL 23, 1965
NRX-A3 RESTART (1ST)	MAY 20, 1965
NRX-A3 RESTART (2ND)	MAY 28, 1965
PHOEBUS-1A POWER	JUNE 25, 1965
NRX/EST	DEC. 1965-EARLY 1966

Figure I-3. - Graphite-reactor and engine-system-test activities.

This figure UNCLASSIFIED

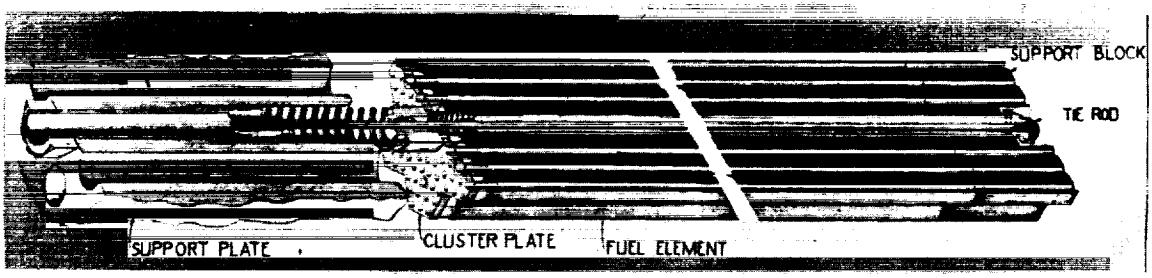

Figure I-4. - Fuel-element cluster.

This figure CONFIDENTIAL

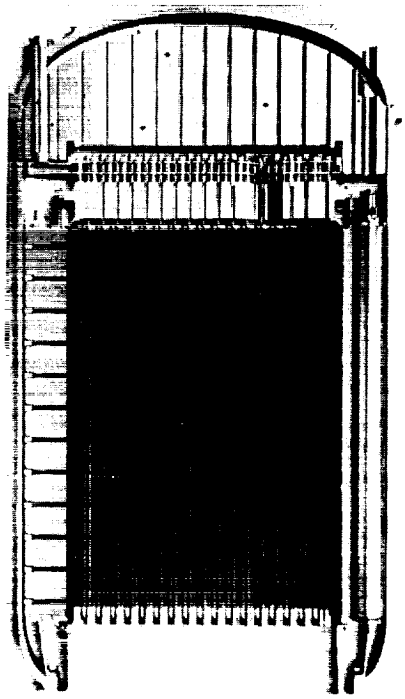

Figure I-5. - NERVA reactor model.

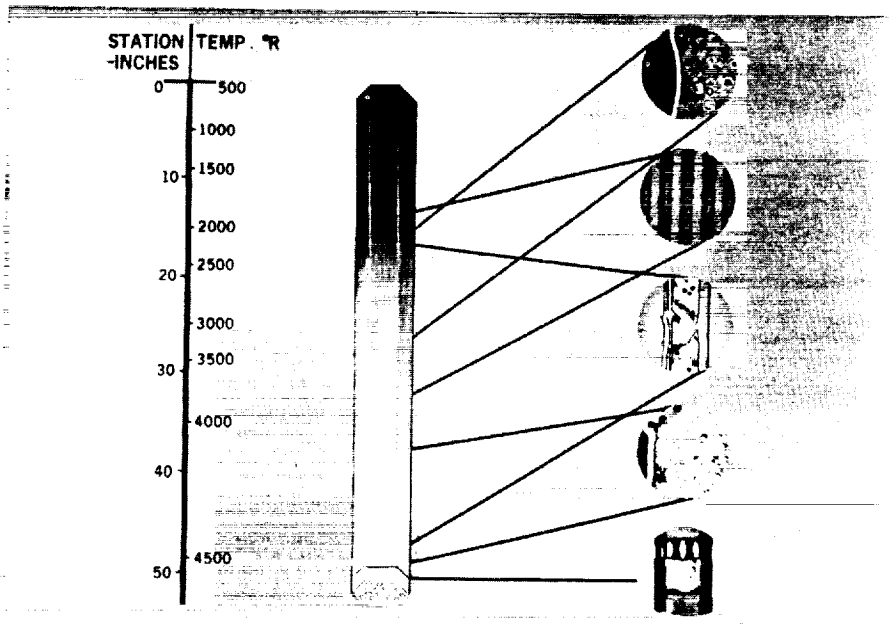

Figure I-6. - Corrosion findings.

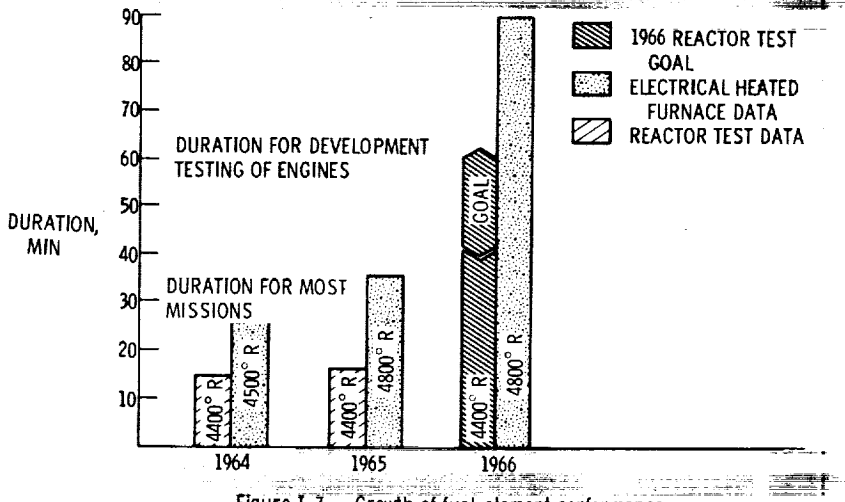

Figure I-7. - Growth of fuel-element performance.

This figure UNCLASSIFIED

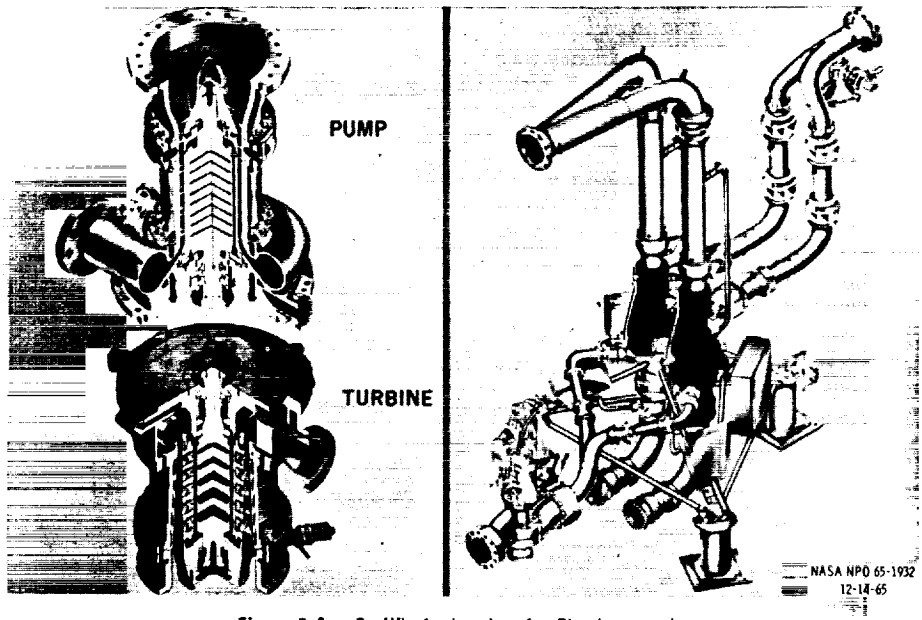

Figure I-8. - Facility feed system for Phoebus reactor.

This figure CONFIDENTIAL

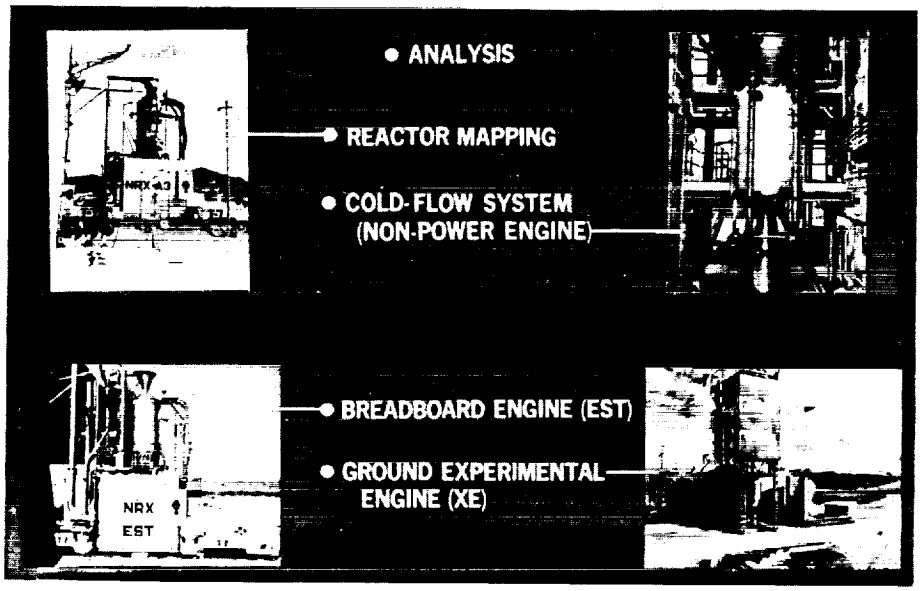

Figure I-9. - Elements of engine-system-technology investigation.

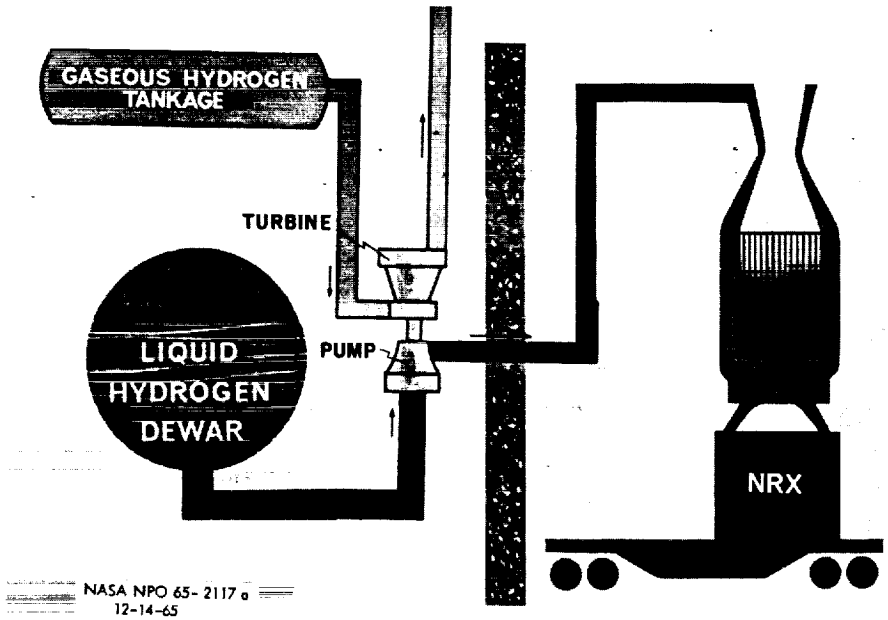

Figure I-10. - Reactor test.

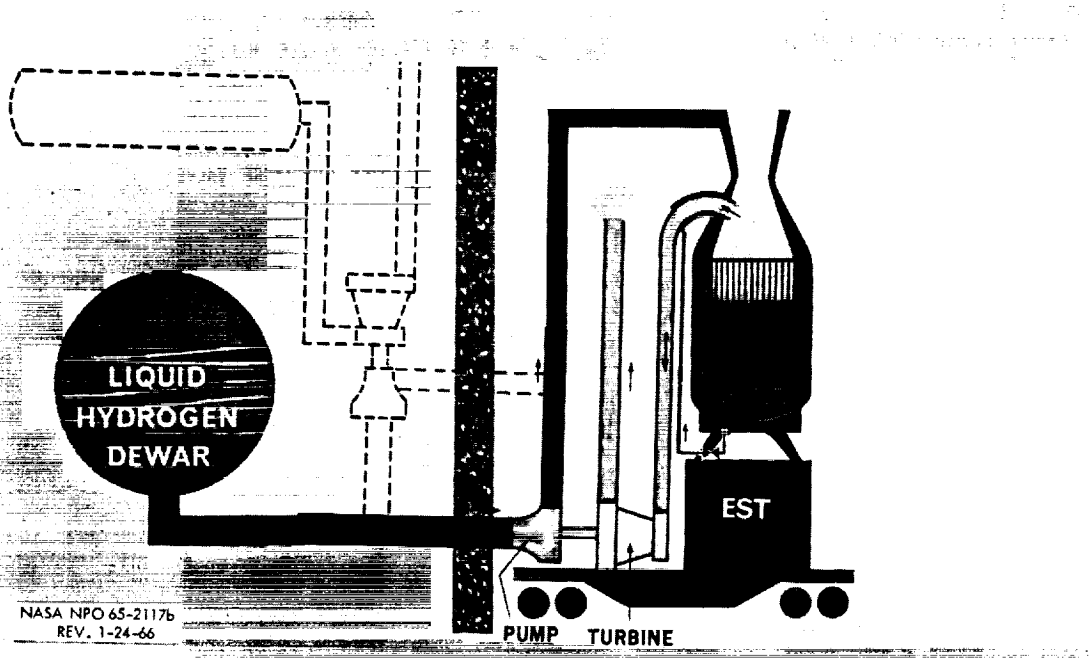

Figure I-11. - Breadboard-engine-system test.

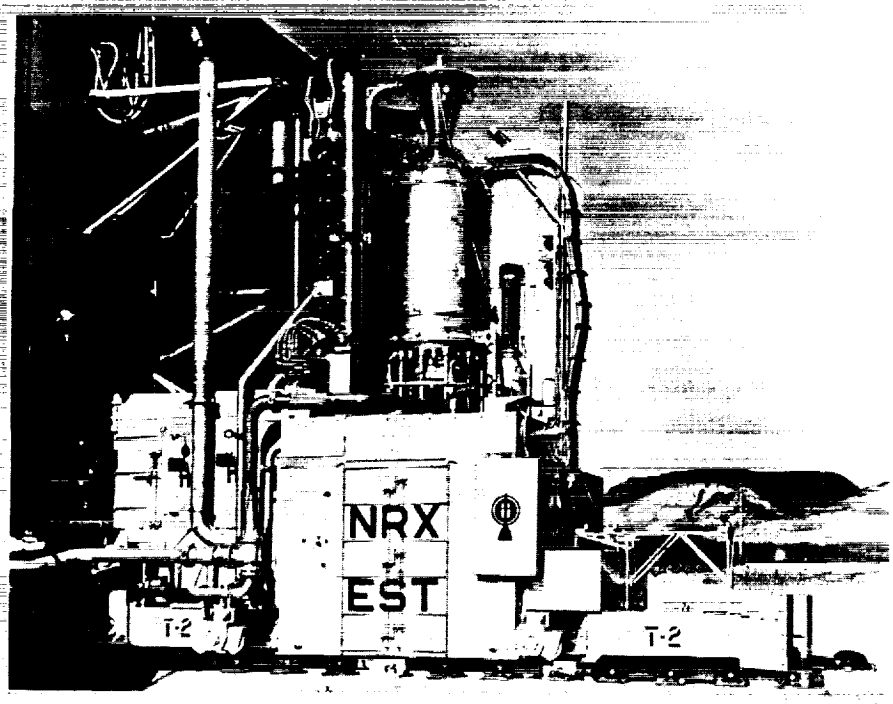

Figure I-12. - Engine system test (EST).

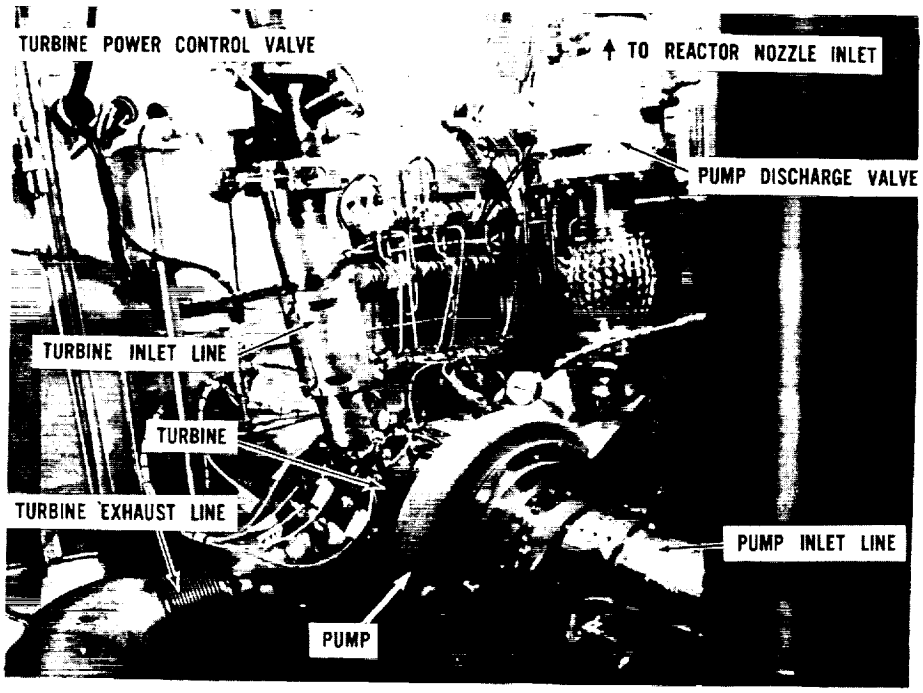

Figure I-13. - Engine components within NRX/EST enclosure.

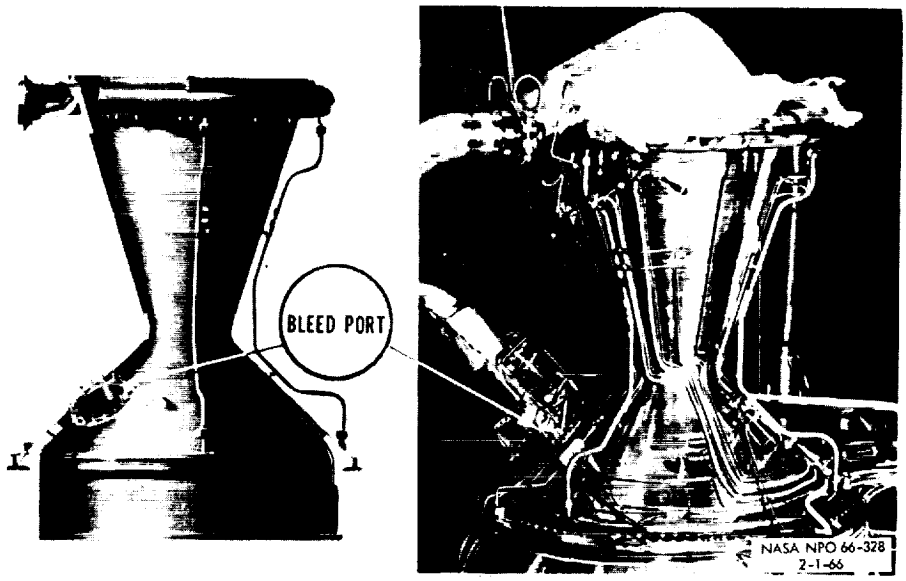

Figure I-14. - Hot-bleed-port nozzle used in engine-system tests.

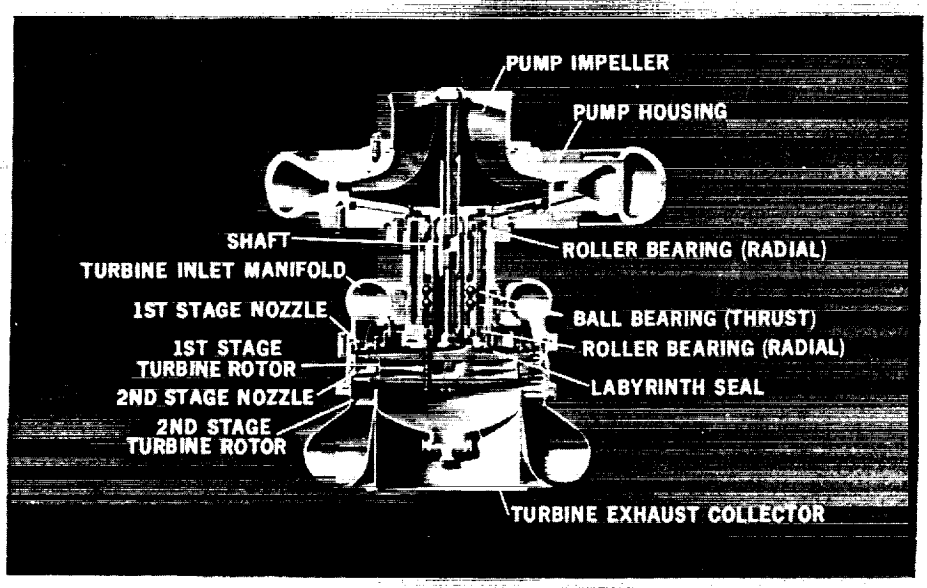

Figure I-15. - Engine system turbopump assembly.

This figure CONFIDENTIAL

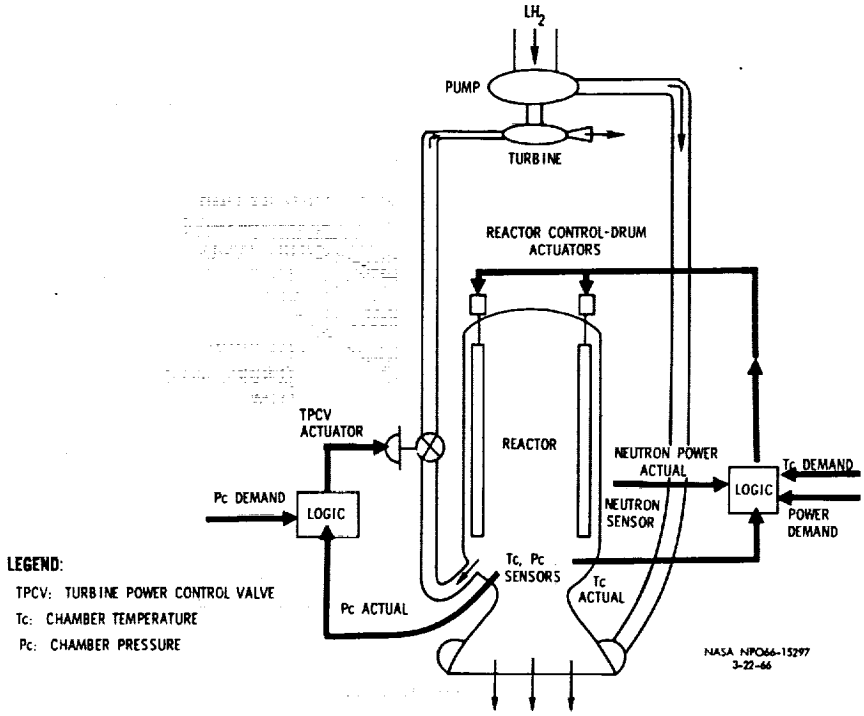

Figure I-16. - Nuclear-rocket-engine control schematic.

This figure UNCLASSIFIED

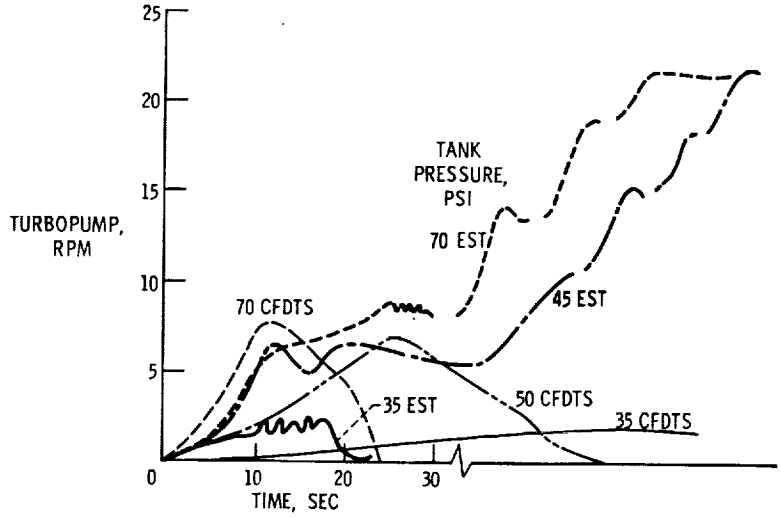

Figure I-17. - Engine-system-test start characteristic (atmospheric exhaust pressure, 12.7 psia).

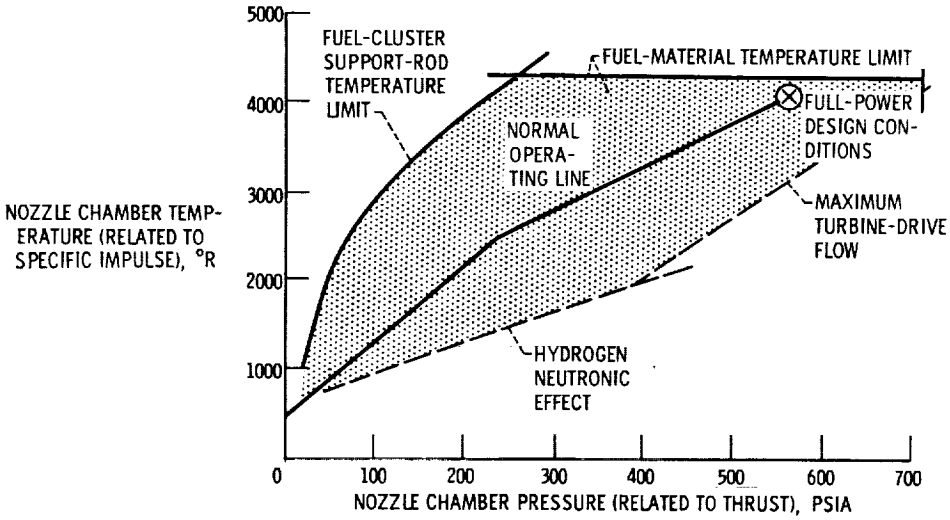

Figure I-18. - Engine-system operating map.

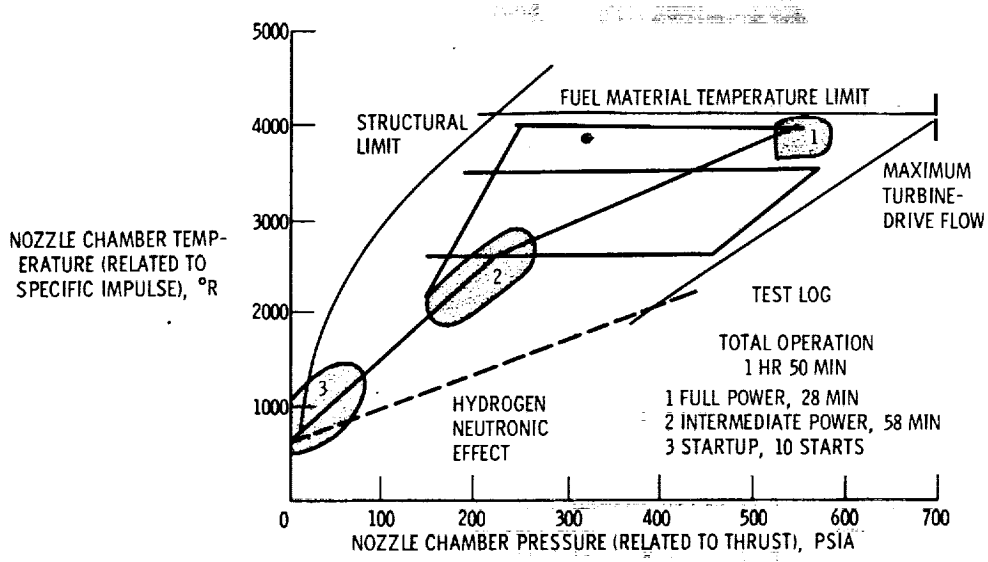

Figure I-19. - Engine-system-test exploration of operating map.

This figure UNCLASSIFIED

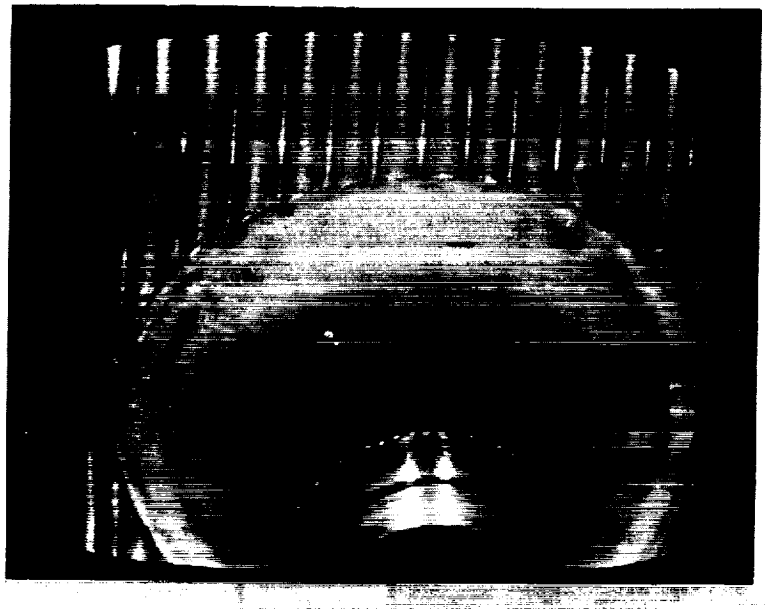

Figure I-20. - Nozzle hot bleed port installed on breadboard engine (remote television photograph).

This figure CONFIDENTIAL

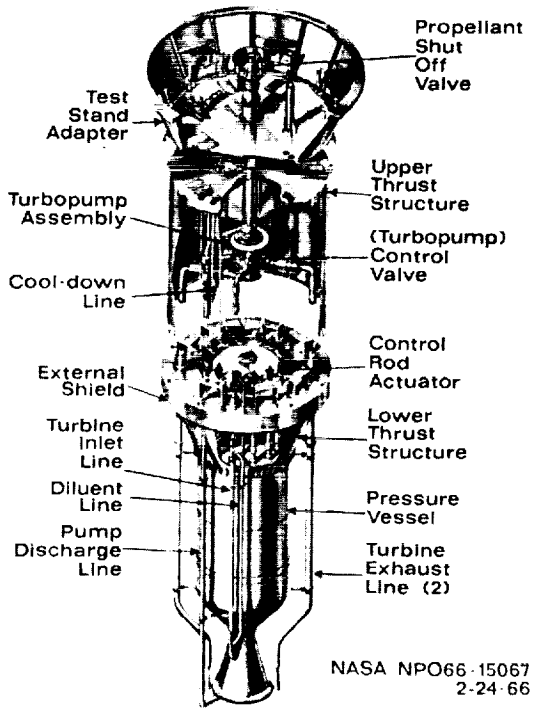

Figure I-21. - Ground-experimental engine (XE).

Figure I-22. - Engine Test Stand No. 1.

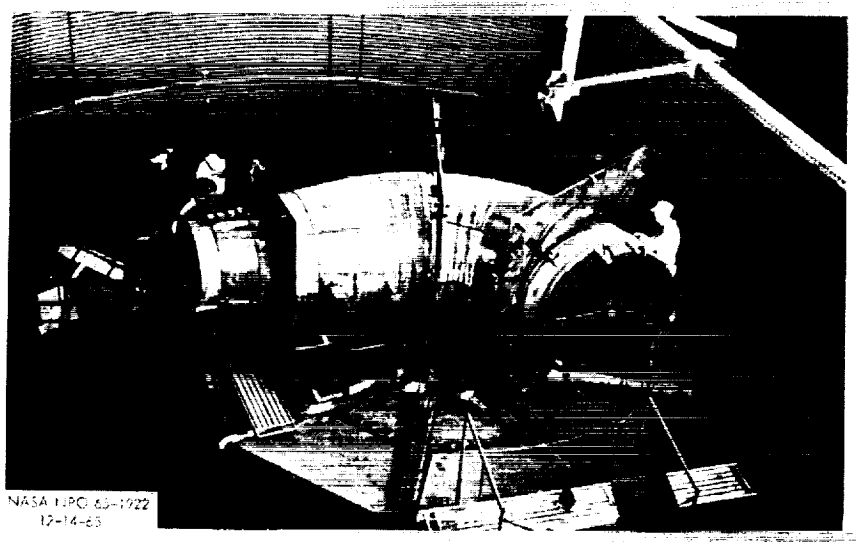

Figure I-23. - Exhaust-duct-elbow fabrication (ETS-1).

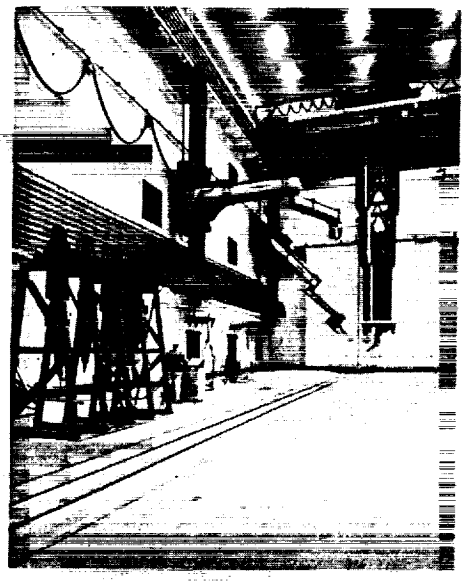

Figure I-24. - Engine maintenance - assembly - disassembly handling equipment.

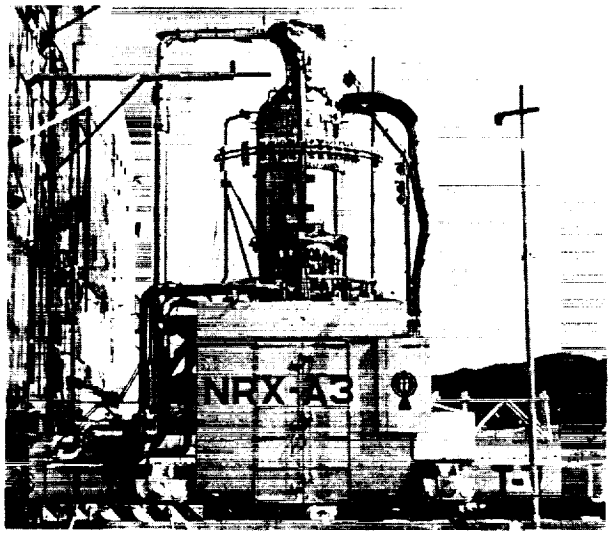

KIWI-B4D POWER	MAY 13, 1964
KIWI-B4E POWER	AUGUST 28, 1964
KIWI-B4E RESTART	SEPTEMBER 10, 1964
NRX-A2 POWER	SEPTEMBER 24, 1964
NRX-A2 RESTART	OCTOBER 15, 1964
KIWI TNT	JANUARY 12, 1965
NRX-A3 POWER	APRIL 23, 1965
NRX-A3 RESTART (1ST)	MAY 20, 1965
NRX-A3 RESTART (2ND)	MAY 28, 1965
PHOEBUS-1A POWER	JUNE 25, 1965
NRX/EST	DEC. 1965-EARLY 1966
NRX-A5 POWER	SUMMER 1966
PHOEBUS-1B POWER	SUMMER 1966
NRX-A6 POWER	WINTER 1966-67
PHOEBUS-2CF	SPRING 1967
PHOEBUS-1C POWER	SUMMER 1967
XE-1 POWER	SPRING 1967

Figure I-25. - Graphite-reactor and engine-system-test activitites.

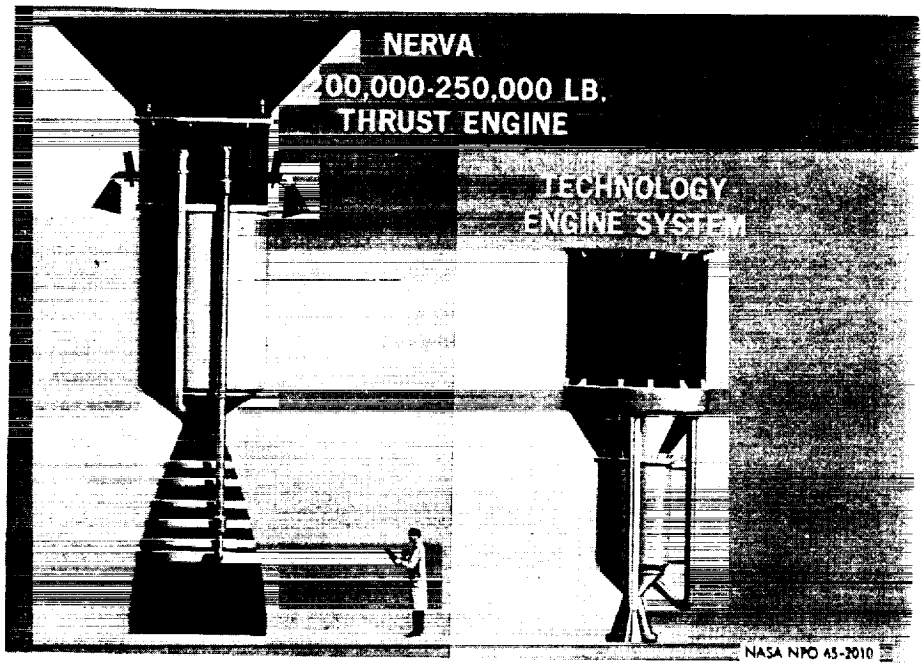

Figure I-26. - Engine configurations.

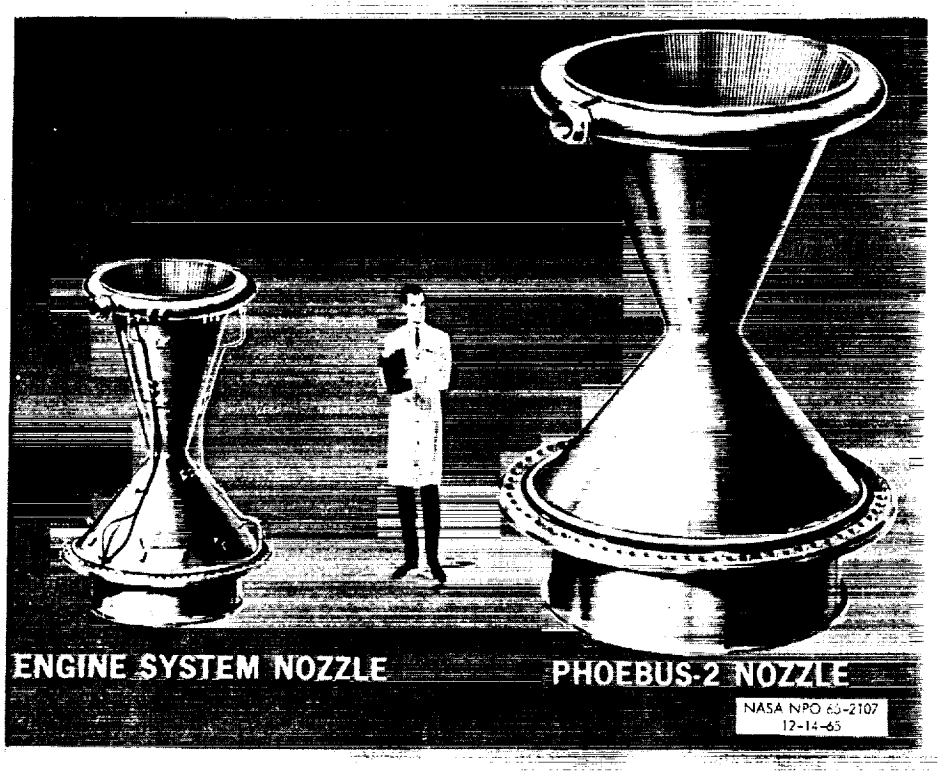

Figure I-27. - Nozzle comparison.

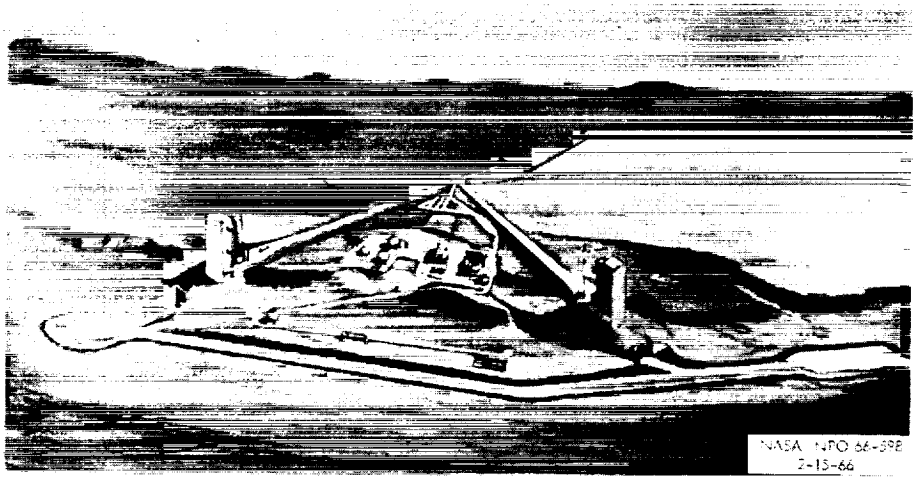

Figure I-28. - Engine/Stage Test Stand 2 & 3 complex site plane.

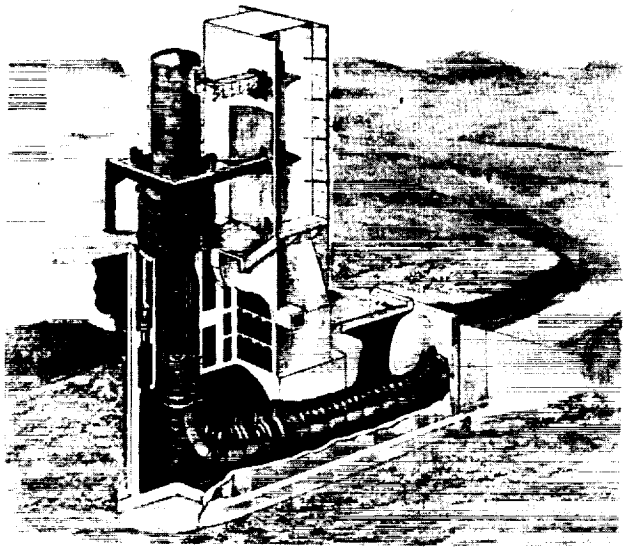

Figure I-29. - Engine/Stage Test Stand 2 & 3 concept.

X66-51408

II. PROPELLANT FLOW SYSTEM COMPONENTS*

Melvin J. Hartmann, Donald J. Connolley, Sidney C. Huntley,
Richard A. Rudey, and Irving M. Karp

INTRODUCTION

Nuclear radiation heating of the propellant and feed system components presents some problems unique to the nuclear rocket. The results of recent studies will provide information useful to the optimization, design, and operation of the nuclear-rocket feed system.

The schematic drawing of a nuclear rocket, shown in figure II-1, can be utilized to indicate the feed system components. The large volume of liquid hydrogen is stored in the tank at relatively low pressure. The pump provides the propellant flow at the high pressures necessary for the operation of the system. The hydrogen flows to those portions of the system that require cooling, such as the nozzle and the reflector, and then flows into the dome and through the reactor. Hydrogen that has been heated in the reactor is then expanded through the nozzle to obtain thrust. Hot hydrogen is bled off from the nozzle and mixed with lower temperature hydrogen to provide gases for the turbine. The turbine supplies the power necessary to drive the pump. The turbine discharge may be used for auxiliary systems aboard the vehicle.

During operation of this propellant feed system, the reactor is operating at full power, and all the system components are subjected to nuclear radiation. The hydrogen, the tank, and the other components of the feed system are all heated by this radiation. Because of the radiation heating, the propellant flowing from the tank is continuously increasing in temperature. As the propellant temperature approaches the boiling point, vapor may form in the pump and inlet line. Because of this vapor, the pump fails to deliver the necessary pressure to operate the system. This pump problem is illustrated in figure II-2, which shows a pump rotor operating in water. The pump rotor is viewed from the inlet side using high-speed photography. In figure II-2(a), the pump is shown operating with the inlet pressure well above fluid vapor pressure, as would be the case when the propellant is highly subcooled. As the fluid temperature increases and approaches saturation, large vaporous regions occur in the low pressure portions of the

*This paper is unclassified

pump blading, as shown in figure II-2(b). These vaporous regions are referred to as cavitation. This large amount of cavitation disturbs the flow in the blade passages, and the pump performance is severely degraded. Under these conditions, the pump could not provide the flow and pressure necessary to operate the system. Thus, a pump performance limit occurs when the propellant temperature increases to some point as fluid vapor pressure approaches the tank pressure.

Four areas of major importance to the nuclear-rocket feed system will be presented in this paper. The general levels of radiation and the amount of shielding are the factors that determine the extent of heat deposited in the propellant feed system. Some of the considerations that are involved in shielding requirements for a nuclear vehicle will be considered first. Secondly, in the area of propellant heating, the temperature history of the propellant flowing from tanks subjected to relatively high levels of heat input will be discussed, and a method of predicting this temperature history will be presented. Attention will then be focused on the factors that control the cavitation limit of the pump. The fourth area, which represents an additional feed system problem associated with the pump although not closely tied to radiation heating, is that of off-design performance of the pump during system startup. Prediction of the performance of the feed system components and the interrelation of the components will be emphasized throughout the discussion.

SHIELDING CONSIDERATIONS

A configuration to illustrate the considerations involved in the determination of the shielding requirement for nuclear vehicles is shown in figure II-3. The engine and propellant tank are shown in their usual orientation, and a crew compartment may be located in the stage. The case of a cluster of engines is represented by the phantom engine and propellant tank.

The following discussion considers the radiation and required attenuation around the reactors during operation and shutdown. In order to achieve the required attenuation, the reactor shield weights are indicated, but they cannot be considered as final weight values. The actual shield weight requires a more detailed evaluation than can be included in this paper. Many items on a nuclear vehicle, other than the propellant feed system, require protection against radiation. Instrumentation and electronic equipment can be damaged or fail to operate properly in high radiation fields. Engine components can be damaged or overheated by excessive radiation. In particular, the manned crew is extremely vulnerable to biological damage and may set severe radiation constraints.

Each radiation-sensitive item will require that its radiation environment over the entire history of its use on the vehicle be evaluated and any necessary reduction in radia-

tion determined. The total shield that may be distributed throughout the vehicle must achieve this required radiation environment with minimum shield weight. The entire vehicle may consist of more engines and more stages than shown in figure II-3. Although some items can best be shielded individually, it may be more efficient to place most of the shielding around the reactors.

The reactor assembly itself contains reflector and supporting structure around the reactor core, which provide some of the required shielding. Additional shadow shielding (fig. II-3) is necessary to protect equipment in the region directly above the reactor, to prevent excessive radiation into the propellant feed system, and to protect the crew during engine operation. Additional side shielding, which extends part of the way or the full length of the reactor, may be necessary to protect items around the reactor that are not shielded by the shadow shield. It may be necessary to reduce the radiation streaming around the shadow shield that can scatter into the crew compartment and, in a configuration with clustered engines or tanks, it may be necessary to reduce the radiation into adjacent tanks and components.

Operating Radiation Levels

Radiation levels around the reactor during operation are extremely high. As an example, the radiation environment around an unshielded NERVA engine operating at 5000 megawatts is shown in figure II-4. The gamma dose rates are shown by the solid lines and neutron dose rates by the dashed lines. Neutron and gamma dose levels greater than 10^8 rads per hour exist in the close vicinity of the reactor. These dose levels are sufficiently high to produce radiation problems in some of the equipment in this region. If the crew members are located in the same vehicle stage as the reactor, they will be subjected to excessive radiation.

The amount of shielding required to obtain a desired reduction in dose is shown in figure II-5. The attenuation factor for both neutrons and gammas, which is defined as the ratio of unshielded dose rate to shielded dose rate, is plotted against various thicknesses of borated zirconium hydride, which is representative of a shield material that attenuates both neutrons and gammas reasonably well.

An attenuation factor of about 10 in both neutrons and gammas may be required for much of the equipment in the vicinity of the reactor. Depending on where the equipment is located with respect to the reactor, this attenuation may be obtained by a shadow shield alone, by a side shield, or by a combination of both. If a crew compartment is located in the same vehicle stage, the dose rate to the crew will depend on the configuration of the stage, the mode of operation of the vehicle, and the design of the crew compartment. Shadow shielding to attenuate direct radiation up to a factor of 10^3 and side shielding to

attenuate scattered radiation up to a factor of 10 may be required to protect the crew. In figure II-5, about 75 grams per square centimeter of shielding are required to obtain an attenuation of 10 in gammas, and about 215 grams per square centimeter of shield are required to obtain an attenuation of 10^3.

Some estimates of the weight associated with these shield thicknesses, when the shield was wrapped around a NERVA-size reactor, are presented in figure II-6. The shield thickness of 75 grams per square centimeter represents about 5000 pounds of shadow shield, and 215 grams per square centimeter of shielding represent about 14 000 pounds of shadow shield. A thickness of about 75 grams per square centimeter also represents about 23 000 pounds of full side shield. These weights might be substantially reduced by tailoring the shields, so that they produce the desired radiation attenuation with minimum shield material.

Radiation Levels After Shutdown

Situations may arise where a crew member has to approach the shutdown engine. Engine malfunctions, for example, may necessitate minor repairs. Rendezvous maneuvers or docking at an orbiting space station may also necessitate close approaches to a shutdown reactor. The shielding requirements for these situations will depend on the operating history of the reactor, the shutdown time, and the distance from the reactor. Gamma dose-rate contours around an unshielded NERVA engine that has operated at 5000 megawatts for 30 minutes and has been shut down for 1 day are presented in figure II-7. Shielding will be required all around the reactor before it can be approached. Because the nozzle opening cannot be shielded, there will be a large excluded region on this end of the engine due to the radiation streaming through the nozzle.

The shield thickness required to obtain a desired dose rate at a point 10 feet from the reactor (in the approachable region) for various shutdown times is shown in figure II-8. If a total dose of 25 rads incurred during an approach of 30 minutes could be tolerated, then the dose rate at that point must be reduced to 50 rads per hour. About 60 grams per square centimeter of shielding are required to approach the reactor after a 20-day shutdown period, while 135 grams per square centimeter of shielding would be required after a 1-day shutdown period. In figure II-6, the 60 grams per square centimeter of shielding represent about 18 000 pounds of side shielding and about 4000 pounds of shadow shielding. The 135-gram-per-square-centimeter shield represents about 48 000 pounds of side shielding and 9000 pounds of shadow shield. These weights could vary over a wide range depending on the values assigned to the tolerable dose limit, the time spent in the radiation field, as well as the distance of approach, engine operating history, shutdown time, and engine size. These weights serve mainly to indicate that substantial shielding would

be required for a man to make a close approach to an engine within a few days after shutdown.

The shutdown discussion has pertained to radiation from the fission products contained in the reactor. After shutdown, however, radioactivity induced in the engine (particularly in the nozzle), as well as the radiation that streams out of the nozzle opening and scatters off the nozzle walls, can contribute appreciably to the dose field all around the reactor. The background dose rate at any point will depend very largely on the nozzle design (size, amount, and type of materials used).

PROPELLANT HEATING

During operation, the nuclear-rocket propellant is heated as a result of radiation being absorbed in the tank walls and in the propellant itself. The effect of this heating is to increase the temperature of the propellant as it flows from the tank. Figure II-9 is a schematic representation of the effect of this heating on the propellant. Presented in the figure are tank and fluid vapor pressure as a function of time before and throughout engine operation. The exit propellant temperature history is also shown. For the operating sequence presented, it is assumed that the tank is at some arbitrary pressure prior to engine startup and that the fluid is saturated. Then, just prior to engine starting, the tank is pressurized to a higher pressure, which is maintained throughout the operation. As the operation continues, both the fluid exit temperature and the vapor pressure increase and ultimately approach the saturation temperature and tank pressure, respectively.

A detailed knowledge of the exit temperature and, thus, vapor pressure history is required because it influences the selection of pumps, insulation, shielding, venting devices, and tank structure. A knowledge of the flow model induced by the nuclear heating is required before the exit temperature history can be obtained.

To gain insight into this flow model, a small-scale flow visualization experiment was conducted with a two-dimensional glass tank, which is shown schematically in figure II-10. Nuclear radiation heating was simulated by infrared radiation. The side infrared lamps deposit energy in blackened side walls. The bottom infrared lamps deposit energy in the fluid through a transparent glass tank bottom, which simulates nuclear radiation heating of the propellant. The working fluid in this test was a mixture of trichloroethane and alcohol. This fluid was chosen because it permitted a radiation absorption profile in the liquid that is similar to that expected in a nuclear-rocket propellant. The flow patterns induced in the liquid by the heating were studied by means of a schlieren system.

Figure II-11 represents a sequence from a schlieren motion picture that was taken during a typical test run. Four frames are shown, which cover the time period for the flow to develop fully. In the first three frames, a boundary layer is seen to form at the

tank walls. Warm fluid from this boundary is carried to the free surface. The bulk fluid appears to be in a state of highly turbulent mixing. The final frame shows the flow fully developed. Two distinct regions exist in the fluid; the bulk fluid is completely mixed (i. e., no temperature gradients), and a stratified layer exists at the surface.

Information gained from these small-scale tests enabled the formulation of an analytical flow model in which the nuclear internal and wall heating yield highly turbulent mixing of the bulk fluid and stratification, respectively. The model was then verified by tests conducted with liquid hydrogen. The material presented herein includes the formulation of this model and results from tests conducted in liquid hydrogen with nuclear radiation as the energy source. Also included are liquid-hydrogen tests wherein nuclear radiation was simulated by electrical heating techniques.

Analytical Flow Model

A schematic diagram of the flow model is presented in figure II-12. A propellant tank is shown in which internal heating of the liquid and wall heating occur. Boundary layer flow along the tank walls, which results from the wall heating, is shown as it feeds into the liquid near the free surface. The liquid has been separated into two regions, a completely mixed bulk region and a stratified layer near the surface. The corresponding temperature profile along the tank centerline is also shown. The temperature rise that results from the heat input, sometime after the start of flow, is shown. The height of the liquid-free surface x_s and the bottom of the stratified layer x_o are designated. Initially, before the tank was pressurized, the liquid was saturated. Thus, the entire height of the tank was at a constant temperature. The temperature rise shown along the abscissa was measured from this point so the initial temperature profile occurs at zero temperature rise. Pressurizing the tank to its operating level causes the temperature at the liquid surface to increase to a saturation temperature ΔT_s corresponding to the operating pressure level.

The region of constant temperature rise was assumed to result from the internal heating contribution. Coupling of the internal and wall heating contributions was assumed to result in a temperature gradient in the stratified layer. The temperature rise in the stratified layer was assumed to vary according to the relation

$$\Delta T^* \propto \left(\frac{x - x_o}{x_s - x_o} \right)^n$$

where ΔT^* varies from bulk temperature rise at the bottom of the stratified layer

$x = x_o$ to saturation temperature rise at the surface $x = x_s$. The bulk temperature rise and the exponent n were obtained from a knowledge of the individual heating contributions. The growth of the stratified layer $x_s - x_o$ was obtained by a consideration of the energy that entered the stratified layer because of the free convective boundary layer flow.

The energy balance of the system was considered in terms of the rate of energy leaving the system, the rate of energy entering the system, and the rate of accumulation of system energy. The interrelation of these terms may be shown by the expression

$$\dot{w}C_p\,\Delta T(o,t) = \dot{Q}(x_s) - \frac{d}{dt}\int_{V_s} C_p\,\Delta T(x,t)\rho\,dV \qquad (1)$$

where

$\dot{w}$	flow rate of liquid leaving exit, lb/sec
C_p	specific heat of liquid at constant pressure, Btu/(lb)(^oF)
$\Delta T(o,t)$	temperature rise at tank exit at given time t, ^oR
$\dot{Q}(x_s)$	total heating rate entering the liquid, function of height of liquid x_s at any time, Btu/sec
ρ	liquid density, lb/ft^3
V	volume, ft^3
V_s	volume of liquid in tank, function of height of liquid, ft^3
$\Delta T(x,t)$	temperature rise at x at given time t, ^oR

The heating rate $\dot{Q}(x_s)$ includes both the heat entering the liquid through the walls and the heat being deposited internally in the liquid.

Equation (1) was made nondimensional by using reference values of flow rate $\dot{w}$ and saturation temperature rise ΔT_s. The total heating rate into the full tank $\dot{Q}_L$ was also used to make the heating rate nondimensional. This operation led to the expression

$$\frac{\Delta T}{\Delta T_s}(o,\tau) = \left(\frac{\dot{Q}_L}{\dot{w}C_p\,\Delta T_s}\right)\left[\frac{\dot{Q}(x_s)}{\dot{Q}_L}\right] - \frac{d}{d\tau}\int_{V_s/V_L} \frac{\Delta T}{\Delta T_s}\left(\frac{x}{L},\tau\right) d\left(\frac{V}{V_L}\right) \qquad (2)$$

where $\tau = t/t_{run}$ is total run time in seconds, V_L is the initial liquid volume in cubic feet, and L is the initial liquid height in feet.

The reference values of $\dot{Q}_L$, $\dot{w}$, and ΔT_s are combined into a heating parameter

that consists of initial operating conditions only. The nondimensional energy equation thus shows that the exit temperature variation with time will be a function of the heating parameter $\dot{Q}_L/(\dot{w}C_p \Delta T_s)$ operating on the normalized heating rate distribution $\dot{Q}(x_s)/\dot{Q}_L$ and a term containing the nondimensional temperature profile, which may be thought of as the liquid flow model. Equation (2) also shows the relation between the various parameters, a knowledge of which is required to predict the exit temperature history.

Nuclear Radiation Experiments

The model used in the energy equation was developed from noncryogenic tests. To substantiate this flow model in liquid hydrogen, an experiment was conducted under contract with the General Dynamics Corporation. An insulated test tank of about 125-gallon capacity was placed above the Aerospace Systems Test Reactor (fig. II-13). To avoid excessive radiation exposure in the surrounding area, the experiment was shielded by submersion in water. This necessitated a liner tank, shown in the figure, which served solely as a water barrier. Provision was made for pressurization and flow, as indicated. The flow model, in essence the temperature as a function of position, was explored by platinum resistance thermometers within the tank.

Some tests were conducted with the reactor against the liner tank and others with 4 inches of water between the two, as shown in figure II-13. These two configurations enabled testing with different heating distributions in the hydrogen. The internal heating profiles for the two test configurations are shown in figure II-14. Presented are the heating rates on the tank centerline as a function of liquid height for the two tank positions. The ordinate has been arbitrarily normalized to 1 megawatt of reactor power, since the heating is proportional to reactor power that was varied through the program. The curves display the typical exponential radiation attenuation. The effect of the 4 inches of water is readily seen; a large fraction of the neutron component has been eliminated, which reduces the magnitude of the heating and gives a much flatter profile for the second configuration.

The total heating of the liquid integrated over the liquid volume is presented in figure II-15. (This is the integral shown in eq. (1).) The total heating rate up to a point in the tank plotted against liquid height for the two configurations is shown. This total heating rate is composed of three components; two nuclear in origin, an internal heating of the liquid and a nuclear wall-heating component, and a third component, the ambient wall heating, that results from conduction through the insulation. Although the centerline profiles (fig. II-14) for the two configurations differ considerably and the integral curves differ in magnitude, the integral curves have nearly the same shape. This results primarily from tank geometry; that is, the region of the tank in which there is a large differ-

ence in the profiles is that region with little liquid which, when integrated, contributes only slightly to the total heating.

A series of tests was conducted wherein the effects of varying total heating, configurations, flow rate, and tank pressure were studied. A representative set of data is presented in figure II-16. The temperature rise is plotted against time from start of flow as seen by four sensors on the centerline of the tank; one at the bottom in the exit port, three others at 15, 21, and 27 inches up from the bottom. It is seen that, for all sensors, the temperature rises are gradual until the liquid surface approaches the sensor. A sharp increase in temperature rise then occurs, which indicates the passing of a warm stratified layer. When the surface reaches the sensor, saturation temperature is indicated. At some particular time, when the level is at 27 inches for example, it is seen that the sensors several inches below the surface are all recording about the same temperature rise, approximately 1° R. This indicates that the bulk fluid is completely mixed. Thus, it is seen that the hydrogen is divided into the two regions observed in the infrared experiments, completely mixed bulk fluid and a stratified layer. A comparison of the experimental data and the predicted temperature histories indicates that the analysis presented earlier yields a reasonable prediction of the temperature history.

Data from six tests are presented in figure II-17 as generalized temperature histories. Exit temperature rise normalized to saturation temperature rise is plotted as a function of flow time normalized to the total run time. It is seen that the data fall into two sets that are characterized by heating parameters of about 0.38 and 0.12. The operational variables of flow rate, pressure, and total heating were varied within each set to yield the appropriate heating parameters. The data within each set generalize to a single temperature history.

The fact that the data presented on figure II-17 with similar heating parameters and similar heating rate distributions yielded the same generalized exit temperature histories indicates that the assumptions used to obtain the flow model were adequate over the range of variables explored.

Electrical Heating Experiments

Some liquid hydrogen experiments, conducted in a test facility at Lewis Research Center, explored the effect of heating rate distribution in the flow model. These experiments supplemented the nuclear heating experiments inasmuch as the different reactor tank positioning did not result in an appreciable change in the normalized heating rate distribution. The normalized heating rate distribution had been indicated as one of the parameters that affected exit temperature history in the generalized energy equation (eq. (2)). The first objective of these experiments was to simulate electrically nuclear

heating and, for the second objective, the electrical heaters were used to extend the testing to a wide range of heating rate distribution.

The test equipment consisted of a tank that had the same size (125 gal) and geometry as the nuclear experiment and was heated with radiant heating along the tank bottom and the tank walls (fig. II-18). The tank and radiant heaters were contained in a vacuum shell (not shown) to reduce the heat leak into the system. The radiant heaters, separately controlled, were then adjusted to simulate both the ambient heat leak and the nuclear heat deposited in the walls. The nuclear heat deposited in the liquid was simulated by a network of wires placed inside the tank. Practical considerations led to the design presented in figure II-19. The immersion heater consisted of 25 elements, spaced 1-inch vertically and controlled separately to match the internal nuclear heating gradient. Each element was constructed from a continuous length of 0.020-inch resistive heating wire that ran chordwise back and forth across the tank at 1/4-inch horizontal spacings. The elements were placed at 90^{o} with respect to adjacent elements to minimize the coupling of induced flow patterns.

To establish the validity of using the immersion heater to simulate the internal nuclear heat deposited in the liquid, a test was conducted, which was compared with a nuclear test. A comparison of the heating rates established is presented in figure II-20. The electric heating rate distribution, shown by the solid curve, indicates about the same trend as the nuclear heating rate distribution (dashed curve). Test results in which this distribution was used and the operational variables were set to give a heating parameter similar to that of the nuclear test are presented in figure II-21. The generalized exit temperature histories are about the same although the electric simulation test was slightly higher during the early portion of the run and lower near the end. This variation between the two temperature histories indicates that less energy was being stored in the stratified layer for simulation tests. These test results indicate that the line-source-type heating from the wire grid work resulted in flow spikes of hot fluid, which tended to reduce the thickness of the stratified layer. Although it was thought this would be the most logical approach, the immersion heater did not simulate the smooth deposition of nuclear heating.

The infrared tests with the noncryogenic liquid indicated that a high degree of turbulent mixing occurred in the tank bottom (fig. II-11). This turbulent mixing was somewhat like hot-plate heating. The radiant heater arrangement used in the present experiment was capable of providing additional power to the tank bottom heater, thereby giving a turbulent addition of heat without the flow spikes of hot liquid from the wire line sources. An example of the radiant heating rate distribution selected to simulate a nuclear heating rate distribution without using the immersion heater is presented in figure II-22. The normalized heating rate distribution with electric radiant heating is compared with a heating rate distribution from the nuclear tests. The operational variables were set to obtain similar heating parameters, and test results using these heating rate distributions

are presented in figure II-23. A comparison of the electric radiant heating test and the nuclear heating test shows that the generalized exit temperature histories are almost identical. A reasonable simulation of the effect of nuclear heating was obtained, then, using just the radiant heaters.

The radiant heaters were then used to extend the test program to other heating rate distributions. The range of heating rate distributions tested are presented in figure II-24. The heating rate distribution of a typical nuclear test is shown for comparison. In different tests, the heat flux was progressively varied from essentially all wall heating to essentially all bottom heating. These cases are depicted in figure II-24 as high wall and high bottom, respectively. Throughout this entire range of heating rate distributions, no gross change in flow patterns was observed.

The exit temperature history for the high-bottom heating rate distribution was predicted by the analytical flow model. The operational variables established for a test run were applied to the analysis. The predicted exit temperature history and the tested data are presented in figure II-25. A comparison of the test data and the predicted generalized exit temperature history shows that the effect of the high-bottom heating rate was predictable.

The electrical heating studies have shown that the test results with nuclear heating could be simulated in the particular tank used. This simulation was accomplished with only the bottom and wall radiant heaters. With no gross change in liquid flow behavior over a wide variation in heating rate distribution, no anomalies are expected to occur in the flow model. It is expected, therefore, that exit temperature history will be predictable over the range of operating conditions to be encountered with nuclear-rocket-type heating.

HYDROGEN PUMP PERFORMANCE

The preceding sections have shown that the temperature history of the propellant flowing from the tank will vary over a wide range of temperatures from subcooled to saturation. As the temperature approaches saturation, the problem of encountering pump cavitation arise. This imposes a temperature limit on the operation of the system, as illustrated in figure II-26. The temperature rise histories that would result from a high and a low heating rate are characterized in the figure. In terms of system operation, the temperature limit T_{LIMIT} must be known in order to establish the temperature history needed to obtain the required run time. Some of the factors that influence this temperature limit in the pumping process will be discussed in this section.

High-pressure pump stages, such as the centrifugal pump discussed earlier, are particularly susceptible to the detrimental effects of cavitation. Because of this effect

of cavitation on performance, an inducer stage is used upstream of the high-pressure stage when it is necessary to pump propellants at very low pressure levels above vapor pressure. An inducer employs a particular type of blading, which can achieve the necessary pressure rise even when substantial cavitation vapor occurs.

An experimental inducer and a centrifugal-flow hydrogen pump combination are shown in figure II-27. Although the inducer is shown as a separate stage, it can also be made an integral part of the high-pressure centrifugal stage. During operation, the hydrogen flow enters the pump at near tank outlet conditions and is gradually pressurized as it flows through the inducer. It then flows through the centrifugal stage, where it is raised to a high pressure and delivered to the engine. Inducers are also used in combination with axial flow pumps, as shown in figure II-28. Operation of this unit would be the same as for the centrifugal pump, except that the high pressure is generated in four axial-flow stages. In both of these pumps, the primary function of the inducer is to increase the fluid pressure to a sufficient value so that vapor will be avoided in the following high-pressure stages. To do this, the inducers are designed with very long helical-type blading, as shown in figures II-27 and II-28. This type of blading repressurizes very slowly any vapor that is ingested or formed on the blades such that the vapor is collapsed prior to the discharge.

An inducer operating at high speed in water is shown in figure II-29, which is a series of photographs that shows the various phases of operation as related to the margin of inlet pressure above vapor pressure. Figure II-29(a) shows operation with an inlet pressure much higher than vapor pressure, which could be comparable to operating with a subcooled liquid. No vapor is visible on the blade surfaces. Figure II-29(b) shows the effect of a reduction of inlet pressure above vapor pressure, which can be compared to approaching saturation. Moderate quantities of vapor or cavitation are formed in the low-pressure region of the blade tip and on the surface near leading edge. The vapor formed is collapsed prior to the discharge, and inducer head rise has not been affected. Reducing the inlet pressure above vapor pressure results in more vapor or cavitation on the blading, as shown in figure II-29(c). This vapor is also collapsed prior to the discharge, which indicates that the head rise has not been affected. Continually decreasing the inlet pressure above the vapor pressure results in the condition shown in figure II-29(d), where extensive cavitation is seen throughout the inducer blading. At this condition, inducer head rise has been seriously degraded.

The cavitating performance of an inducer can be characterized as shown in figure II-30, where the head rise divided by the noncavitating head rise is shown as a function of the inlet pressure above vapor pressure (NPSH) in feet of liquid. Operation at high values of NPSH is comparable to that seen in figure II-29(a), where no vapor is being formed. As NPSH is reduced, vapor is formed in increasing quantities until a degradation in performance is obtained (fig. II-29(d)). A minimum allowable NPSH can be estab-

lished and a useful operating range defined by setting a limit to the allowable degradation of performance. The 0.9 value of normalized head rise, as shown in figure II-30, is generally acceptable from the standpoint of not affecting the performance of a following high-pressure stage. This NPSH limit is generally obtained experimentally by reducing the inlet pressure while maintaining the vapor pressure constant. However, it can also be related to the propellant heating situation by considering the increasing vapor pressure that results from increasing temperature. For this type of operation, inlet pressure or tank pressure would be held constant, and the performance would be encountered as the vapor pressure increased.

Cavitation Performance

During the pumping of liquid hydrogen, it has been observed that performance obtained at lower values of NPSH is more suitable than that obtained in other fluids. To understand this, it should be recalled that an inducer operates successfully with extensive cavitation or vaporous regions within the blade passage. This phase-change process, which limits the inducer performance, is affected by the properties of the fluid that is being pumped. The phase-change process on an inducer blade is depicted in figure II-31. The flow over a long inducer blade is shown where the blade is rotated in the downward direction, and the incoming flow is shown by the arrow. The under side of the blade is the high-pressure surface, and the upper side is the low-pressure surface. A vapor cavity is shown on the low-pressure surface of the inducer blade. The vapor that is formed in the low-pressure region cools a thin film of the liquid below the temperature of the bulk or incoming liquid. This cooling of a liquid film results in a reduction in local vapor pressure, as shown in the vapor pressure diagram of figure II-31. The bulk, or incoming fluid, and the cooled film are indicated in the vapor pressure diagram. The temperature drop and local vapor pressure drop (VP drop) are related through the characteristics of the fluid by the slope of the vapor pressure curve. A simple heat balance that equates the heat for vaporization to the heat withdrawn from the thin liquid film can be written as

$$\rho_V V_v^* L = \rho_L C_L A^* (\Delta T) h \tag{3}$$

where the heat for vaporization is determined by the product of the vapor density ρ_V, the volume of the vapor formed V_v^*, and the latent heat of vaporization L. The heat withdrawn from the liquid film is the product of the liquid density ρ_L, the specific heat of the liquid C_L, the area of the cavity surface A^*, the temperature drop in the liquid film ΔT, and the effective thickness of the cooled film h. By replacing the temperature drop

ΔT with the vapor pressure drop ΔVP and the slope of the fluid vapor pressure-temperature relation dp/dT, the following expression for the local change in vapor pressure can be obtained:

$$\Delta VP = K^* \left(\frac{\rho_V}{\rho_L} \frac{L}{C_L} \frac{dp}{dT} \right) \left(\frac{1}{\alpha} \right)^m u^n \tag{4}$$

where the hydraulic constant K^* contains the terms required for geometric similarity (including V_v^* and A^*). The effective thickness of the cooled film has been replaced by the diffusivity α and the reference fluid velocity u both raised to an exponent dependent on the heat- and mass-transfer process involved. The hydraulic constant and the exponents can be determined from experimental data.

Equation (4) has been checked for various fluids in a cavitating venturi, which has this same type of vapor cavity and in which the pressure drop within the cavity could be measured and compared with the calculated value. For the fluids run in the venturi, which were water, nitrogen, glycol, and Freon, the measured and predicted values were identical over a range of temperatures and velocities. Thus, this simple heat balance equation was sufficient to characterize the cavitating venturi. The Bureau of Standards is presently testing this same venturi in hydrogen. At this time, their data are not available, but the predicted pressure drop for hydrogen at various temperatures has been calculated and is presented in figure II-32. For liquid hydrogen at 37° R, which is the boiling point at a pressure of 1 atmosphere, the fluid properties are such that a vapor pressure drop of about 130 feet is predicted. Liquid-hydrogen fluid properties produced a very large change in vapor pressure drop as a result of a small change in temperature. An increase in the hydrogen temperature from 37° to 42° R increased the predicted vapor pressure drop from about 130 to 300 feet. Conversely, the predicted vapor pressure drop decreases as the hydrogen temperature decreases below 37° R. Predicted vapor pressure drop for water is noted to be relatively small for the case of room-temperature water (75° F). It is necessary to raise the water temperature to 450° F in order to obtain an estimated vapor pressure drop of 130 feet of liquid.

The reduction in local vapor pressure in the region of the cavity allows a reduction in inlet pressure to the inducer. This increase in local vapor pressure drop with hydrogen temperature potentially allows the margin of inlet pressure above fluid vapor pressure to be lowered with the same performance. Thus, the performance curve of figure II-30 may shift to lower margins of inlet pressure about vapor pressure.

Experiments specifically designed to investigate these hydrogen temperature effects on the performance of a pump inducer have been conducted at Lewis. For these experiments, an inducer was installed in the bottom of a liquid hydrogen tank, as shown in

figure II-33. Both the inducer and its housing were completely immersed in the liquid. Flow entered the inducer through a converging inlet duct, was pressurized by the inducer, and returned to the tank. Pressure and temperature data were both measured at the inlet and pressure was measured at the exit of the inducer to determine the performance. Flow rate was measured in the discharge line. A wide range of propellant temperatures was set in the tank by the use of auxiliary systems available to the facility.

The effect of liquid-hydrogen temperature on the performance of the inducer is shown in figure II-34. The head rise divided by the noncavitating head rise is plotted as a function of varying inlet pressure above vapor pressure or NPSH for constant values of inlet temperature. To isolate the temperature effects, all the data were obtained at a constant flow rate and rotational speed. At a constant inlet temperature, for example 32° R, the experimental performance (indicated by the dashed line) was obtained by decreasing the inlet pressure until a degradation in performance was obtained. Increasing the temperature produced an improvement in inducer operating range by moving both the initial drop-off and the complete breakdown in head rise to lower values of NPSH. At a liquid-hydrogen temperature of 42° R, the inducer was still capable of producing 95 percent of its normal head rise at 0 NPSH. This indicates that a saturated liquid is entering the inducer.

The solid curves shown in figure II-34 are the predicted effects of temperature on inducer performance. To obtain these curves, experimental data at 32° and 37° R were used to evaluate the hydraulic constant K^* of the cavity. With this constant evaluated, the vapor pressure-drop equation was used to calculate the 34° and 42° R curves. The calculated curves show the same performance trend with the temperature that was obtained experimentally. Thus, the trend of temperature effects on performance can be reasonably predicted by the heat balance model.

By rearranging and replotting this data, the change in performance with temperature can be related to system operation as shown in figure II-35. The head rise divided by noncavitating head rise is plotted as a function of varying temperature for constant values of inlet or tank pressure. The arrows indicate the saturation temperatures corresponding to the pressures shown. The temperature limit at which cavitation would become a problem in an engine feed system can be estimated. For example, at a tank pressure of 15 pounds per square inch, an increase in the propellant temperature would produce a degradation in performance at a temperature less than the corresponding saturation temperature. This temperature at which the assumed 0.9 limit in performance is obtained thus defines the limit of system operation as a function of tank outflow temperature. At a tank pressure of 30 pounds per square inch, an increase in the propellant temperature would produce a small degradation in performance. At this pressure, the performance of the example inducer remained above the 0.9 limit throughout the temperature range, even at the corresponding saturation temperature. This combination of conditions would allow the pump to operate over the entire range of tank outflow temperature that results from

nuclear heating. Thus, the temperature limit imposed by cavitation is highly dependent on the selected operating conditions of the system. By using the 0.9 performance drop as a limit, the example inducer would be capable of pumping all the propellant in the tank at tank pressures above 25 pounds per square inch. At lower values of tank pressure and corresponding saturation temperatures, the amount of propellant left in the tank would be dependent on the tank outflow temperature history as affected by nuclear heating.

Effect of Vapor Ingestion

To examine the effect of vapor ingestion on the performance of an inducer, electric heating elements were installed in the outer wall and the center body of the inducer inlet, as shown in figure II-36. This inducer test section was investigated in the same test facility that was shown in figure II-33. Temperatures and pressures were measured above the heater element and at the face of the inducer. The measurements were taken in such a manner that the volume of vapor could be estimated.

The resulting inducer performance data obtained with liquid hydrogen at about 37° R and with 14-kilowatt heater power input to the hydrogen flowing into the inducer are shown in figure II-37. This corresponds to a heat input of about 1 Btu per pound of hydrogen flow for this particular test. The inducer head rise over noncavitating head rise has been plotted for a range of inlet pressures above fluid vapor pressure. The estimated volume flow as a percent of total volume flow entering the inducer is shown and can be seen to increase as the NPSH is decreased. As an example, it is estimated that a volume of vapor equivalent to 15 percent of the inducer flow is ingested by the inducer when the inducer head rise is degraded to 0.9. These data were obtained at a nominal hydrogen temperature of 37° R in the tank. Since most of the heat addition resulted in nucleate boiling, the temperature rise of the liquid while passing through the heated section was very small.

The effect on the inducer performance of varying the level of heat addition to the propellant in the inlet pipe is shown in figure II-38. The inducer head rise over noncavitating head rise is shown for a range of NPSH. Increasing heat input to the liquid necessitated increasing the NPSH to avoid an extensive drop in inducer head rise. The data in this figure were obtained for a constant value of liquid flow and rotational speed. However, as previously shown in this paper, the volume flow increased as a result of the increase in vapor formed as the inlet pressure above vapor was decreased. The vapor volume could also be expected to vary with the level of heater power applied. The effect of the ingested vapor volume at the 0.9 noncavitating head rise point can be observed in figure II-39(a). The required NPSH for the 0.9 noncavitating head point is shown as it varies with inducer liquid flow. The flow coefficient can be considered proportional to volume flow rate. For no heat, the required NPSH increases with flow. A similar trend is

shown for all levels of heater power. If the flow is adjusted to an increased flow for the estimated vapor volume, the curve shown in figure II-39(b) results. It was assumed that the zero heat data was the base, as shown by the open symbols, and the heat input generated additional vapor volume. The solid points are the same data as shown in figure II-39(a) except that they are adjusted to higher volume flows, which accounts for the estimated vapor ingested for that particular data point. For example, the point at a flow coefficient of 0.063 and 14-kilowatt heater power, at which 15-percent vapor volume was observed, was adjusted to a flow coefficient of 0.073. The single curve indicates that the NPSH increase required to collapse the vapor entering the inducer inlet is only that required to account for increased inlet volume flow. However, an adjusted flow coefficient of 0.079 represents the maximum volume flow that can be achieved even with a large increase in NPSH. The data of figure II-39(a) represent the performance based on the liquid volume flow, whereas the curve in figure II-39(b) is the performance based on the total, which is the vapor and liquid volume flow. The total volume flow curve can be determined by the data obtained with no heat addition. Thus, in those cases where it is necessary to provide for some vapor ingestion, the inducer size or design point may be selected so that a relatively small increase in NPSH is required.

PUMP PERFORMANCE DURING STARTUP

The startup of a nuclear engine is somewhat unique from other rocket systems, in that it may take up to 30 seconds to achieve full power. During this relatively long time, accurate control over the system must be maintained throughout all the phases of the startup transient. To achieve this control, a detailed knowledge of component operating characteristics, including the pump, is required for all of the off-design conditions encountered during the startup transient.

The performance of the pump during startup is illustrated in figure II-40, where the low-speed portion of the pump performance is plotted in terms of pressure rise, flow rate, and rotational speed. An example transient, indicated by the dashed line, was obtained during cold-flow system startup tests with an axial flow pump. The known region of pump performance is indicated by the constant speed lines between stall and some limiting value of flow rate. The startup was initiated by allowing flow to pass through the pump under the action of tank pressure, which produced pump windmilling and resulted in the negative pressure rise portion of the transient to point A. At this point, power was supplied to the turbine, and the pump was accelerated into the known region of performance, as indicated by the remainder of the dashed line. Pump performance above 25 percent of design speed is relatively well understood; hence, the following analysis will consider the performance in the low-speed and windmilling regions of the transient.

Complete details of the windmilling analysis are given in the reference list. The following is a brief description of this analysis. The windmilling region can be analyzed by using the flow model shown in figure II-41. The sketch shows several blades of an axial stage, where the flow and rotor speed are described by the velocity-vectors V and U. The performance of the stage can be described by a one-dimensional, incompressible energy equation, which is

$$\frac{\Delta p}{\rho} = \frac{\Delta V^2}{2g} + \frac{U\,\Delta V_u}{g} + \frac{C_f V^2 + (U - CV)^2}{2g} \tag{5}$$

This equation describes the change in static pressure across the stage $\Delta p/\rho$ in terms of the change in kinetic engines $\Delta V^2/2g$, the work done $U\,\Delta V_u/g$, the viscous flow loss $C_f V^2/2g$, and the entrance flow loss $(U - CV)^2/2g$, when C_f and C are the friction and entrance loss coefficients, respectively. By substituting physical quantities for a particular stage design, the change in pressure can be described in terms of flow rate $\dot{w}$ and rotational speed N such that

$$\Delta p = K_1 \dot{w}^2 + K_2 N \dot{w} + K_3 N^2 \tag{6}$$

Generalizing equation (6) with flow rate yields an equation in terms of the speed parameter $(N/\dot{w})$, which is

$$\frac{\Delta p}{\dot{w}^2} = K_1 + K_2\left(\frac{N}{\dot{w}}\right) + K_3\left(\frac{N}{\dot{w}}\right)^2 \tag{7}$$

Equation (7) is capable of solution down to zero speed and throughout the windmilling region.

The analysis was applied to the axial flow hydrogen pump (fig. II-42), which was used for the system startup tests. The pump contains a mixed flow inducer stage and six identical high-pressure axial flow stages. Mean diameter design considerations of each stage were used to evaluate the terms in equation (5), and a generalized equation (eq. (7)) was obtained.

The resultant windmilling performance calculated for this pump is compared with experimental data in figure II-43. Both the calculated performance and the data indicated by the symbols are plotted in terms of the generalized pressure drop, that is, the negative pressure rise over flow rate squared as a function of the generalized rotor speed expressed as rotor speed over flow rate. To estimate the effects of the large inlet flow deflections on the stage discharge angles, two boundary conditions were evaluated; one was

based on design fluid angles, and the other assumed that the flow followed the blade angle. Good agreement between data and the design fluid angle curve is indicated at zero speed and throughout the windmilling region. The performance was calculated to the steady-state windmilling point indicated as the zero torque or zero work point. Operation between this point and zero speed represents the accelerating region of windmilling. Operation beyond this point (higher values of $N/\dot{w}$) represents the powered region of pump performance.

With the analytical model for the windmilling region, a complete generalized pump curve can be developed, as shown in figure II-44. Both the normal or known region and the windmilling region of performance are plotted in this figure in terms of the generalized pressure rise and rotor speed. The normal or known operating region can be described analytically by a blade-element technique or by available pump data. Available pump data were used in the example shown in figure II-44. The segment of the curve between the two regions can be obtained by interpolation, as shown by the dashed line. The resultant generalized curve represents pump performance from zero speed to the limit of the normal operating region.

With appropriate values of flow rate and rotor speed, the curve can be expanded into a low-speed pump map, as shown in figure II-45. Pump pressure rise is shown as a function of flow rate for several constant speeds from 0 to 6000 rpm (approximately 25 percent of design speed). The solid curves represent the predicted performance, and the symbols represent data obtained from the system startup tests. Good agreement between the predicted and experimental data is indicated for all the operating regions illustrated in figure II-44. The example startup transient (fig. II-40) is shown on the constructed map, as indicated by the dashed line. The path followed by the pump falls within the analyzed regions of performance.

The results of the analysis described indicates that axial-flow pump performance can be reasonably predicted during engine system startup. The development of the windmilling model and the interpolation technique shown in figure II-44 provide a method of describing pump performance in the extreme off-design operation encountered during startup.

SUMMARY

Recent studies that affect the optimization between shielding, tank heating rates, and pressure levels and the cavitation-limiting condition in the pump of a nuclear-rocket feed system have been discussed. Efforts have been concentrated on improving the ability to predict or characterize the effect of radiation heating on the limiting factors of the various feed system components. Results of these studies are as follows:

1. There are a large number of factors that must be considered in the determination of the nuclear shielding requirements of a vehicle. In some stages, the crew may set such stringent requirements that propellant system heating will not result in a difficult problem. In other stages, substantial radiation heating may occur. It is desirable to develop a single-propellant feed system that is as tolerant of radiation heating as possible to cover this wide range of operating conditions.

2. Flow from hydrogen tanks subjected to high levels of radiation heating indicates a continuously increasing temperature with the final temperature at saturation for the given tank pressure. It is necessary to predict this temperature history rather precisely, since it determines the NPSH available to the pump. Prediction methods were presented for the determination of propellant temperature history. Nuclear radiation and electrical heating tests were conducted to verify the assumptions.

3. Pump inducers have demonstrated the capability to operate in liquid hydrogen at lower margins of NPSH than a similar inducer in other fluids. It has been shown that this required margin of NPSH decreases as the hydrogen temperature is increased. A method of determining inducer performance trends with hydrogen temperature was presented.

4. Vapor formed in the inlet pipe as a result of radiation heating must be ingested by the pump inducer. The increase in inlet pressure above vapor pressure to allow for vapor ingestion can be estimated by methods presented. Methods for adjusting the inducer design to account for vapor ingestion were discussed.

5. During system startup, the pump may be caused to windmill, and it is operated over a wide range of pressures and flow rates. Methods of estimating the windmilling and off-design performance have been presented. The calculation of off-design performance would be appreciable to multistage axial flow pumps, since they may be required for future nuclear rocket engines. The predicted performances are particularly useful for the determination of the system startup transient.

BIBLIOGRAPHY

Pumps and Inducers

Crouse, James E.; Montgomery, John C.; and Soltis, Richard F.: Investigation of the Performance of an Axial-Flow-Pump Stage Designed by the Blade-Element Theory - Design and Overall Performance. NASA TN D-591, 1961.

Rostafinski, Wojciech; Rudey, Richard A.; Lacy, Donald D.; Lillis, Patrick R.: Performance Characteristics of an Axial-Flow Liquid-Hydrogen Pump During Startup. NASA TM X-1213, 1966.

Ruggeri, Robert S.; and Gelder, Thomas F.: Cavitation and Effective Liquid Tension of Nitrogen in a Tunnel Venturi. NASA TN D-2088, 1964.

Sandercock, Donald M.; Soltis, Richard F.; and Anderson, Douglas A.: Cavitation and Noncavitation Performance of an 80.6° Flat-Plate Helical Inducer at Three Rotational Speeds. NASA TN D-1439, 1962.

Soltis, Richard F.: Some Visual Observations of Cavitation in Rotating Machinery. NASA TN D-2681, 1965. (Technical Film Supplement C-239 available on request.)

Stahl, H. A.; and Stepanoff, A. J.: Thermodynamic Aspects of Cavitation in Centrifugal Pumps. ASME Trans., vol. 78, Nov. 1956, pp. 1691-1693.

Wilcox, W. W.; Meng, P. R.; and Davis, R. L.: Performance of an Inducer-Impeller Combination at or Near Boiling Conditions for Liquid Hydrogen. Vol. 8 of Advances in Cryogenic Engineering, K. D. Timmerhaus, ed., Plenum Press, 1963, pp. 446-455.

Tank Heating

Anderson, Bernhard H.; and Kolar, Michael J.: Experimental Investigation of the Behavior of a Confined Fluid Subjected to Nonuniform Source and Wall Heating. NASA TN D-2079, 1963.

Anderson, B. H.; Huntley, S. C.; and Connolley, D. J.: Propellant Heating Studies With Wall and Nuclear Heating. Paper 64-WA/AV-8, ASME, Nov. 29-Dec. 4, 1964.

Anderson, Bernhard H.; and Danilowicz, Ronald L.: Analytical and Experimental Study of Nuclear Heating of Liquid Hydrogen. NASA TN D-2934, 1965.

Huntley, Sidney C.; Gauntner, James W.; and Anderson, Bernhard H.: Wall and Bottom Heating of Liquid Hydrogen in a Propellant Tank. NASA TN D-3256, 1966.

Huntley, Sidney C.; and Gauntner, James W.: Simulated Nuclear Heating of Liquid Hydrogen in a Propellant Tank. NASA TN D-3328, 1966.

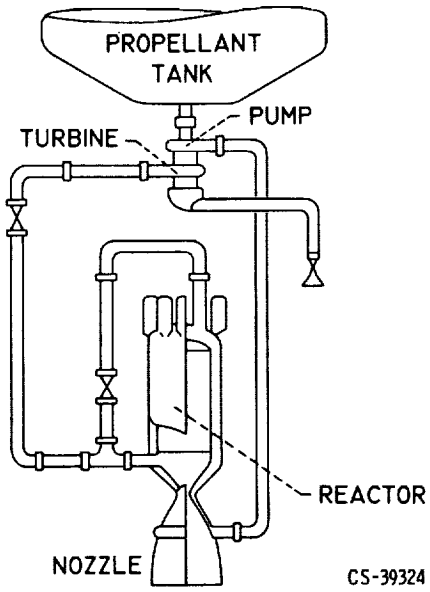

Figure II-1. - Nuclear rocket.

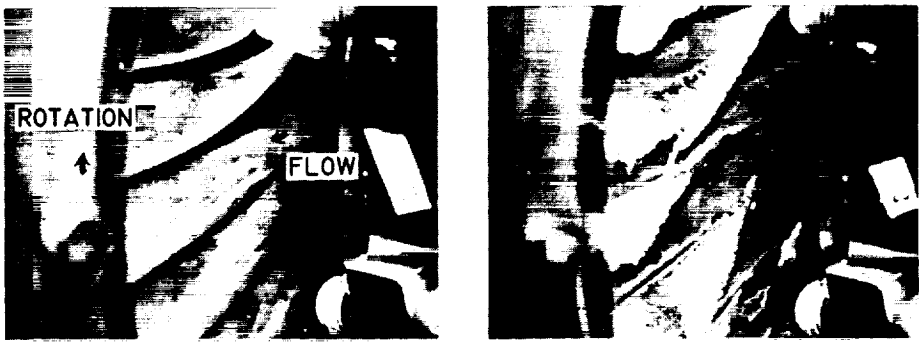

(a) Noncavitating. (b) Cavitating.

Figure II-2. - Cavitating centrifugal impeller.

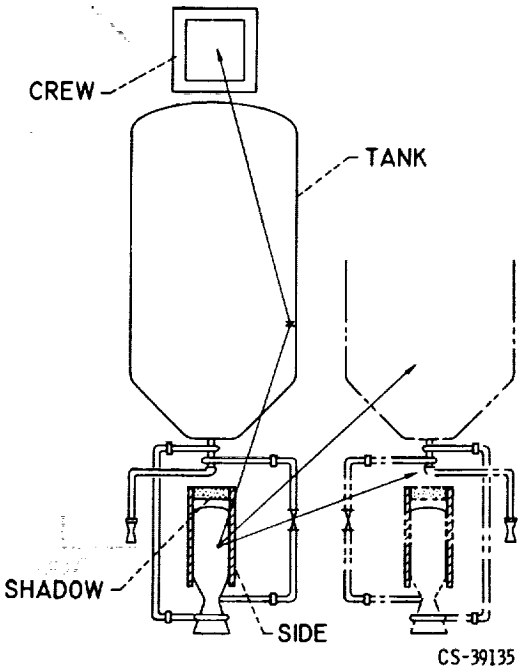

Figure II-3. - Nuclear vehicle shielding.

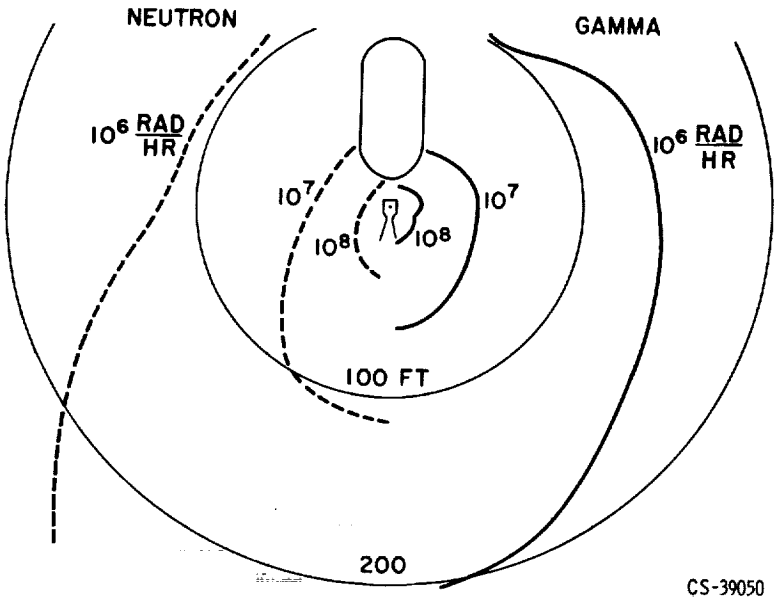

Figure II-4. - Radiation field around 5000 megawatt operating reactor.

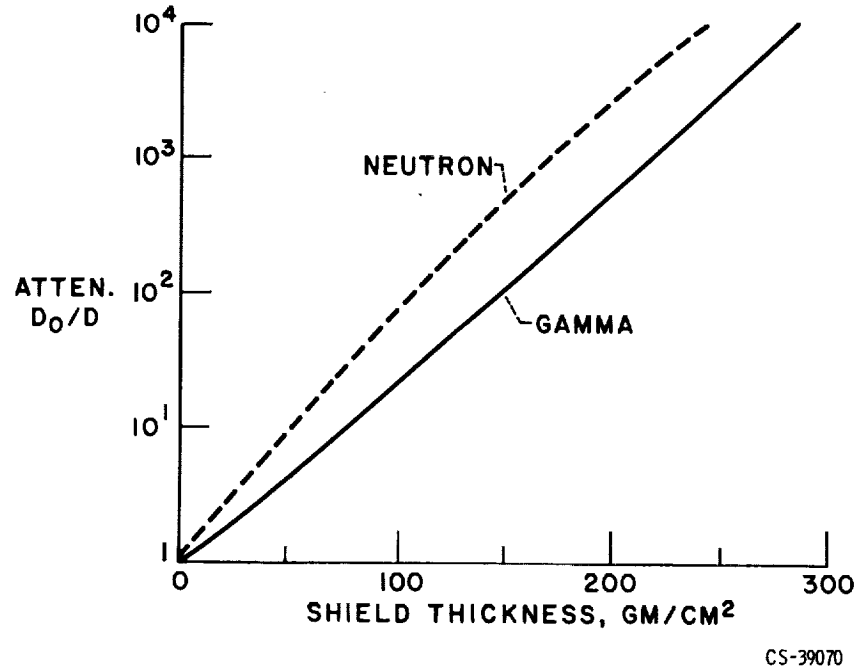

Figure II-5. - Dose attenuation with shielding.

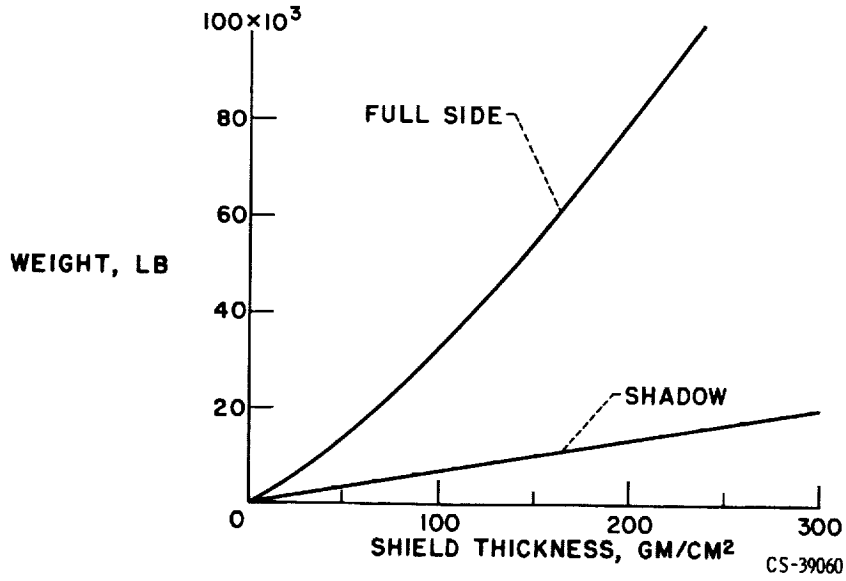

Figure II-6. - Shield weight for NERVA-size reactor.

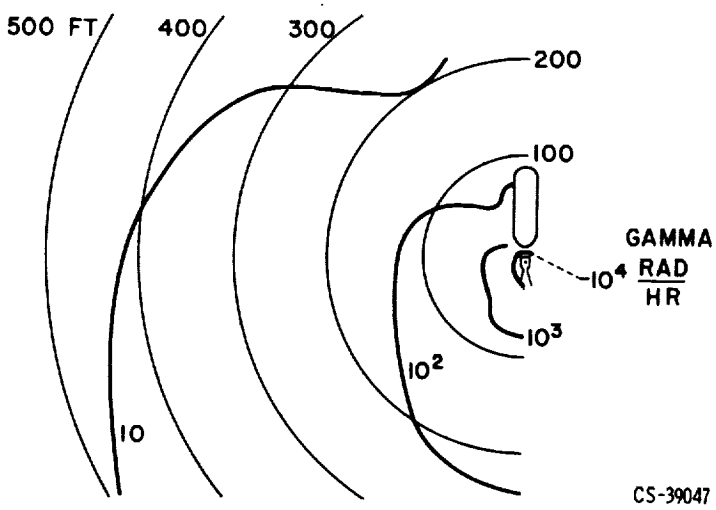

Figure II-7. - Radiation field around shutdown reactor 1 day after operation.

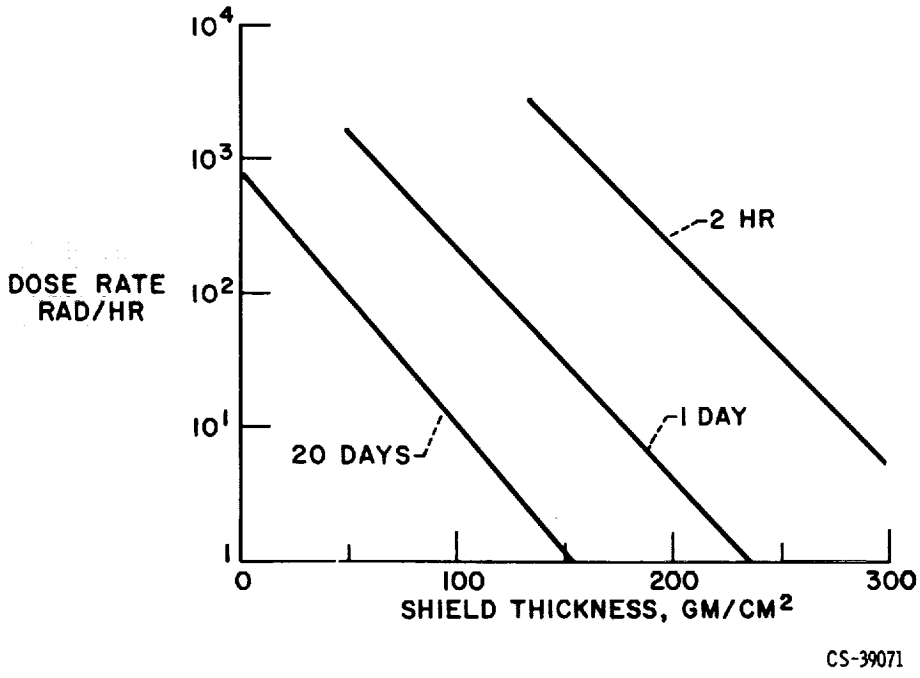

Figure II-8. - Shutdown dose rates 10 feet from reactor.

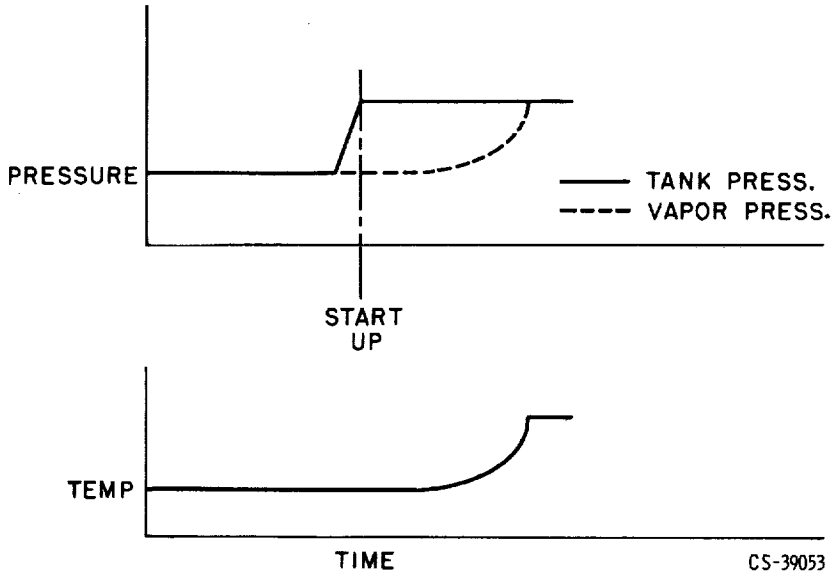

Figure II-9. - Propellant outflow history.

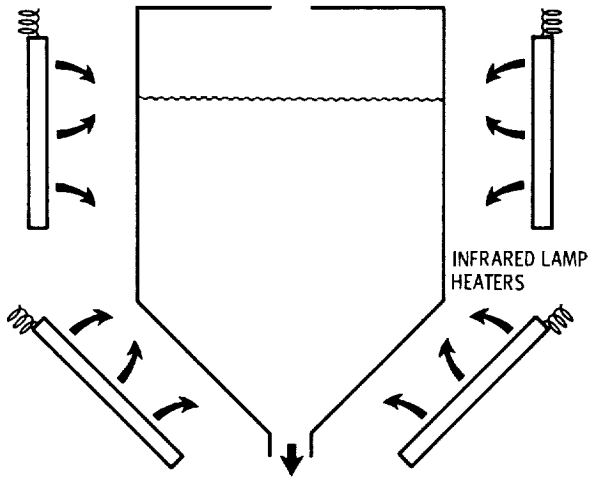

Figure II-10. - Schematic diagram of flow visualization experiment.

Figure II-11. - Schlieren pictures.

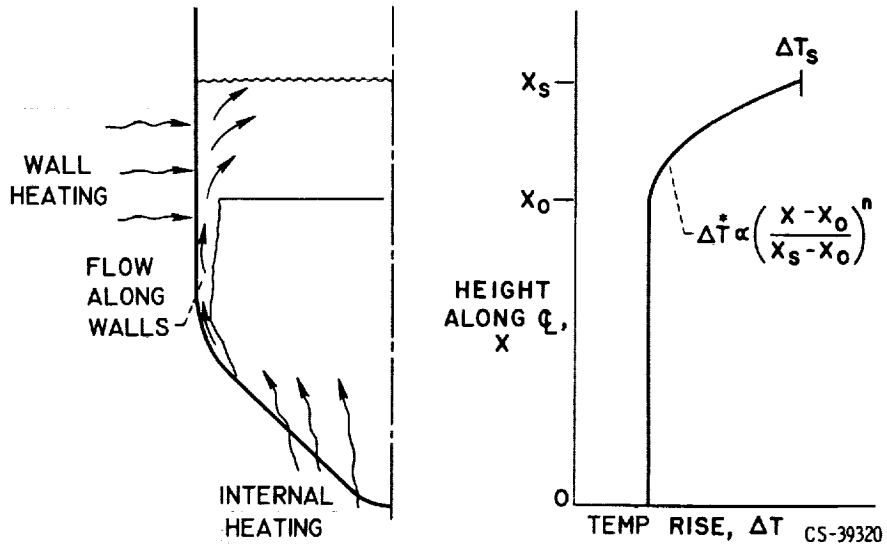

Figure II-12. - Schematic diagram of flow model.

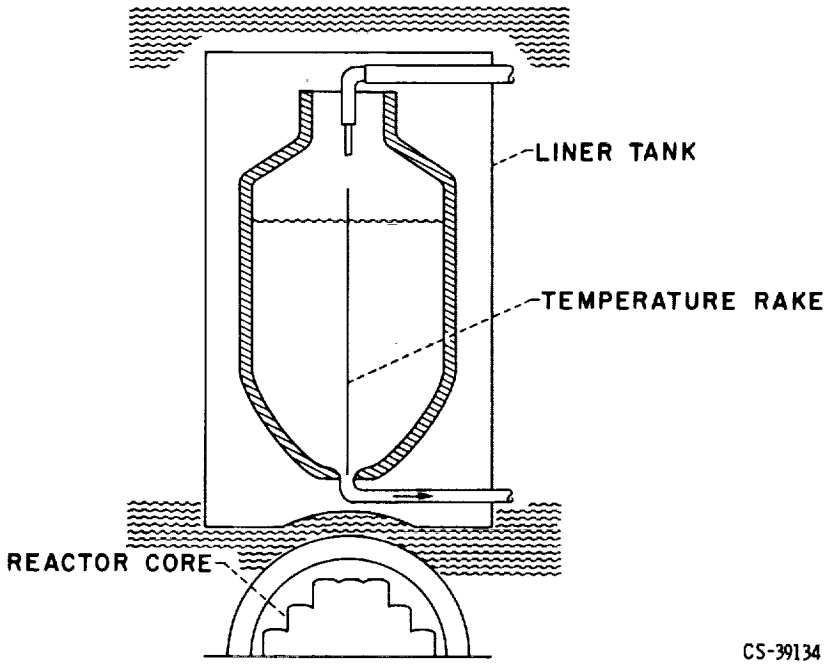

Figure II-13. - Nuclear-tank heating facility.

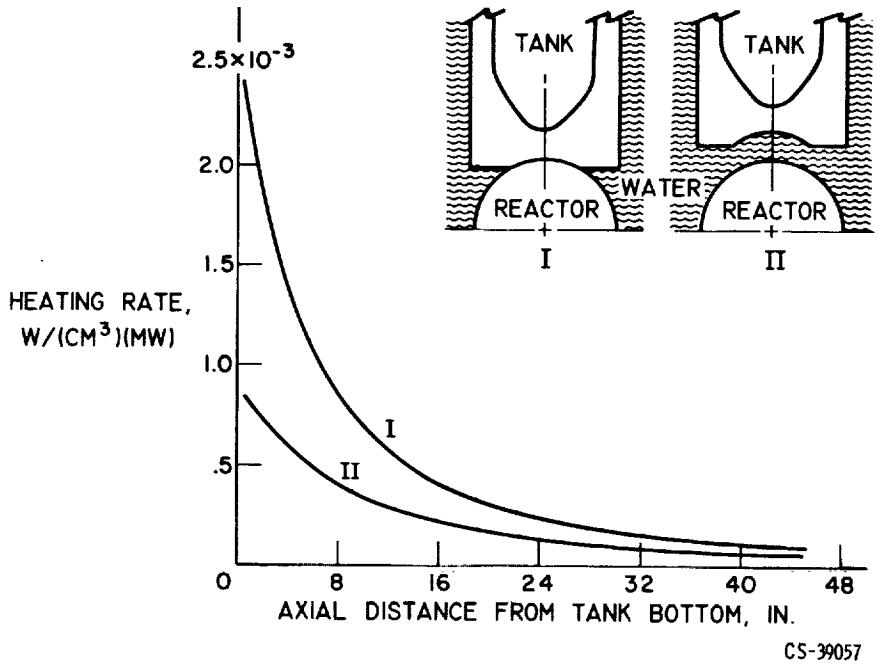

Figure II-14. - Tank centerline heating rates.

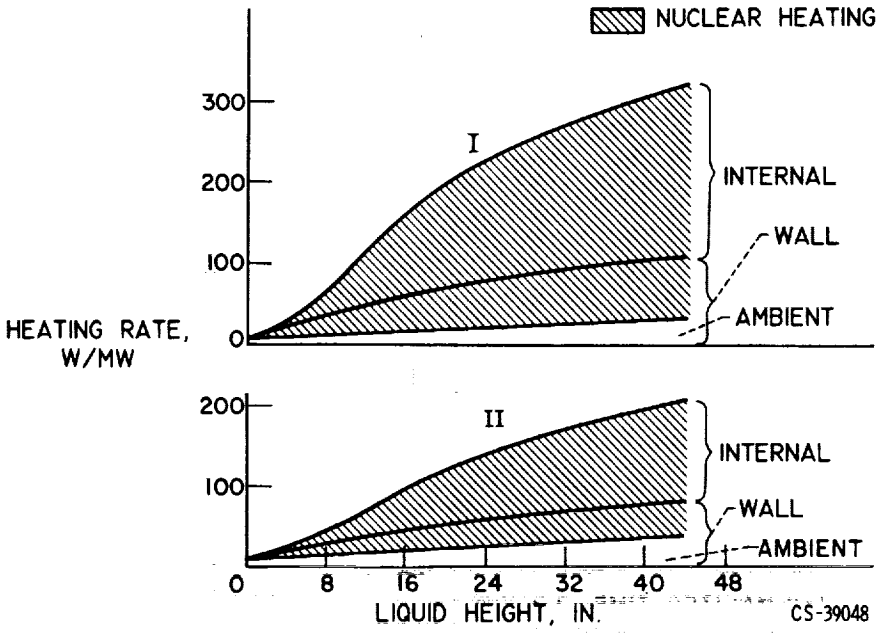

Figure TT-15. - Total heating rates.

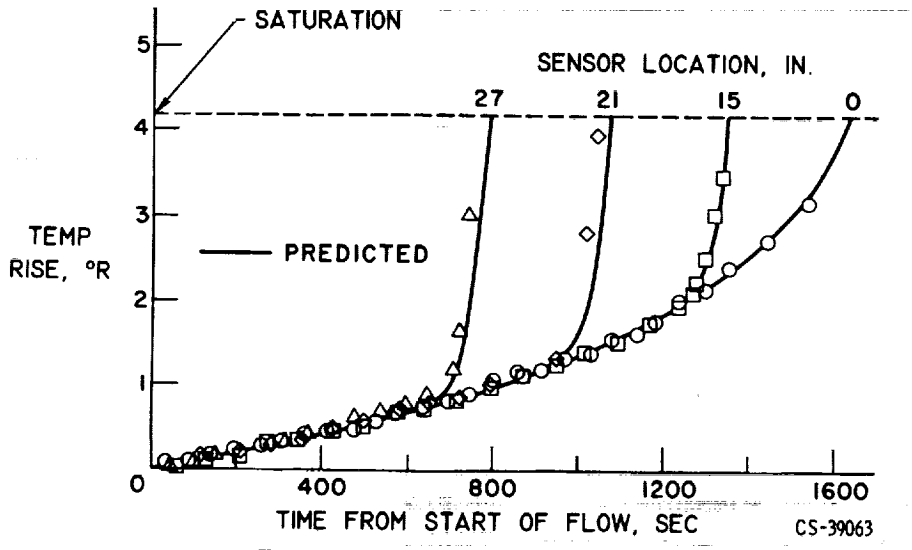

Figure TT-16. - Temperature histories for nuclear test.

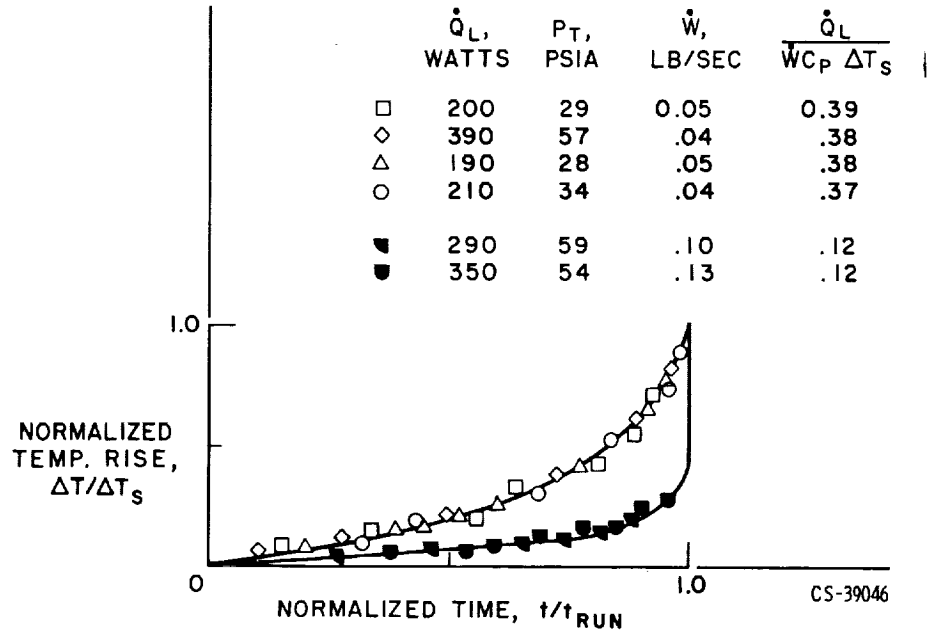

Figure II-17. - Generalized nuclear results.

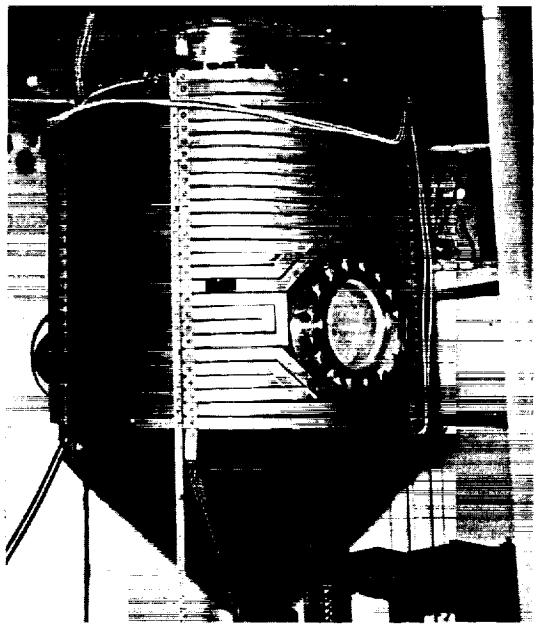

Figure II-18. - Tank with radiant heaters.

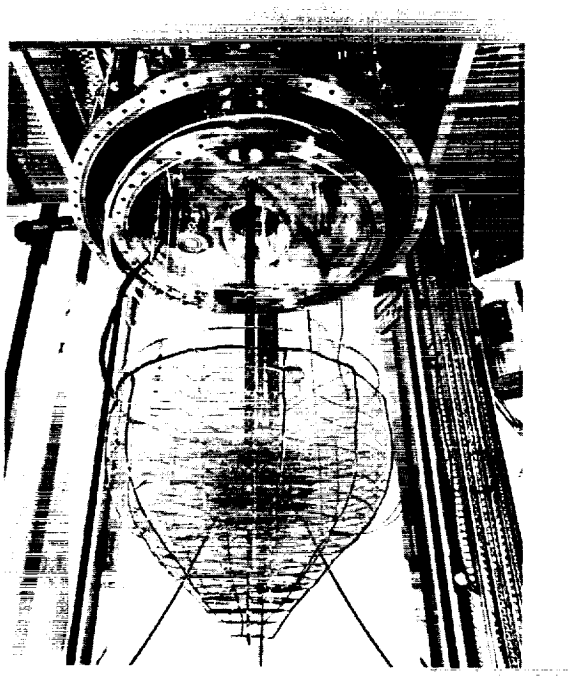

CS-39045

Figure II-19. - Immersion heater.

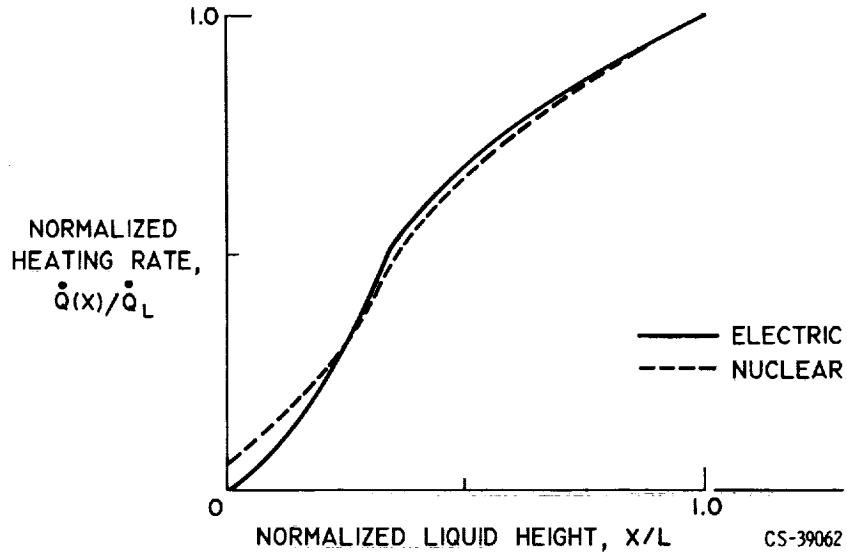

Figure II-20. - Heating rate distribution with immersion heating.

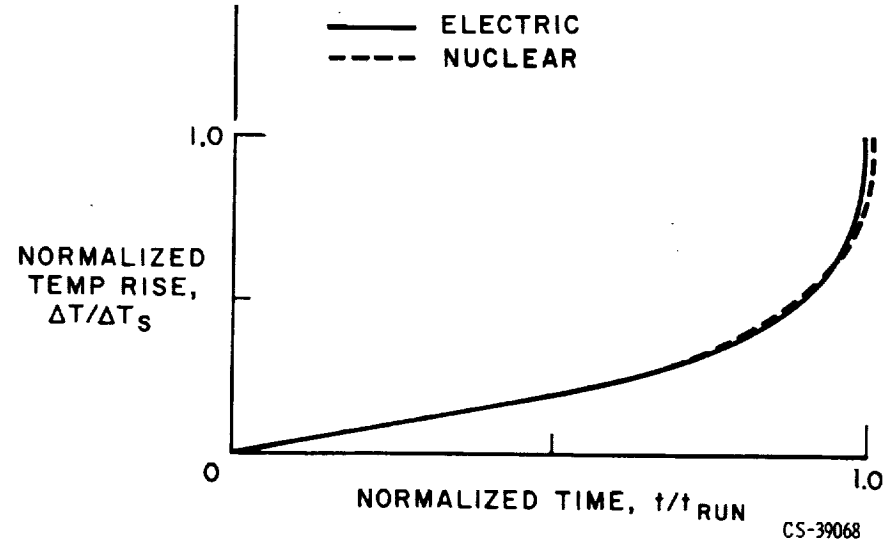

Figure II-21. - Generalized temperature history with immersion heating.

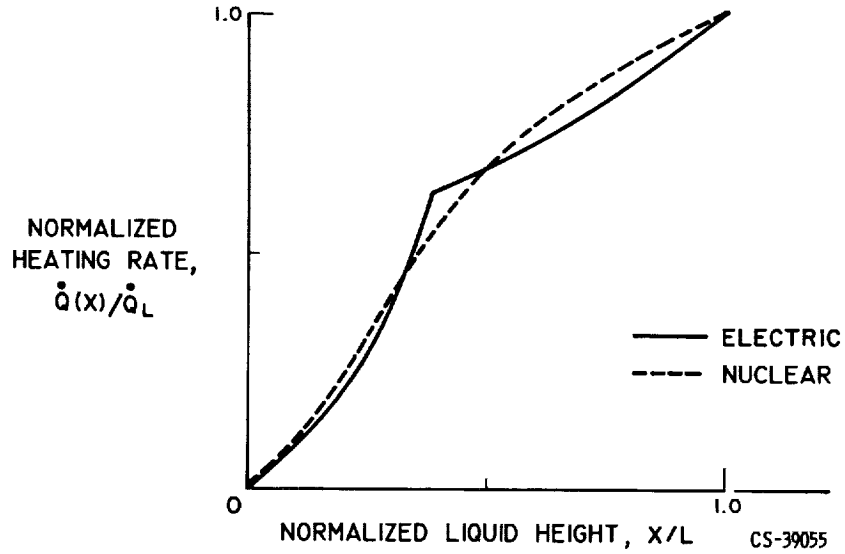

Figure II-22. - Heating rate distribution with radiant heating.

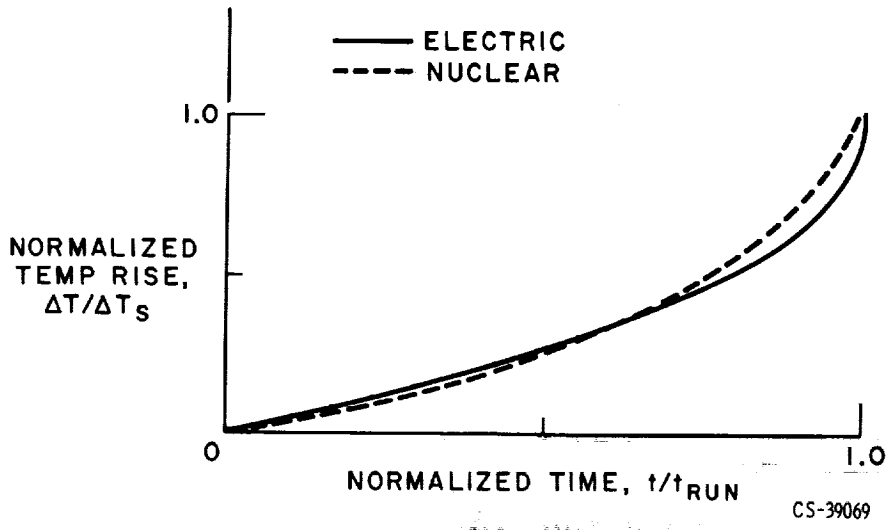

Figure II-23. - Generalized temperature history with radiant heating.

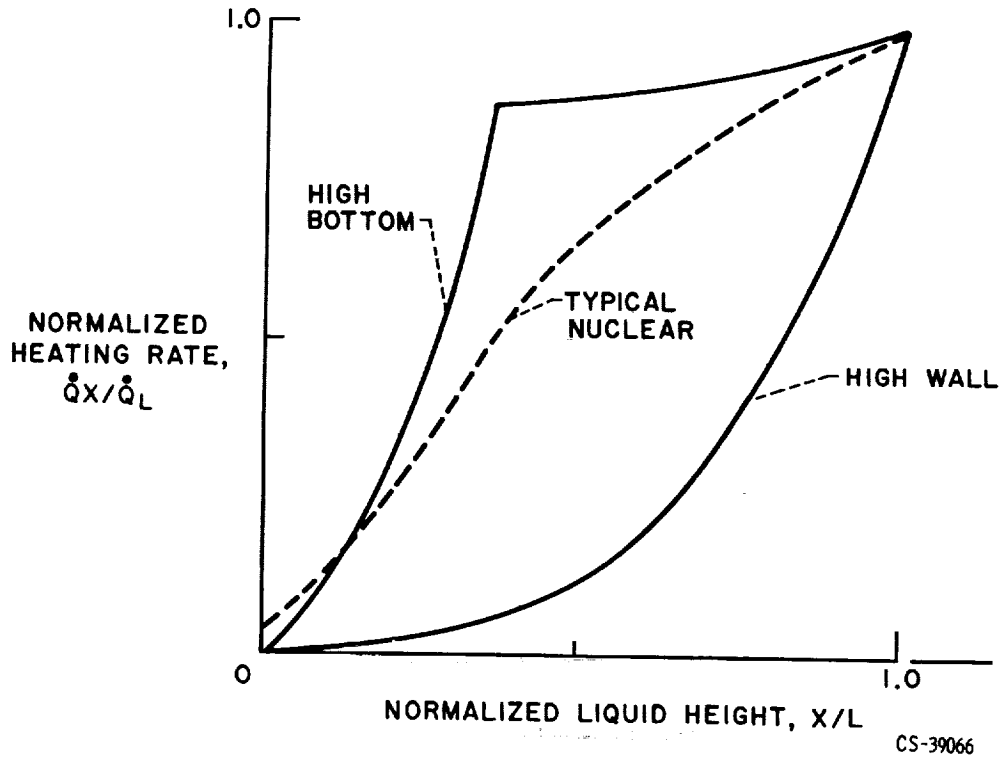

Figure II-24. - Range of radiant heater tests.

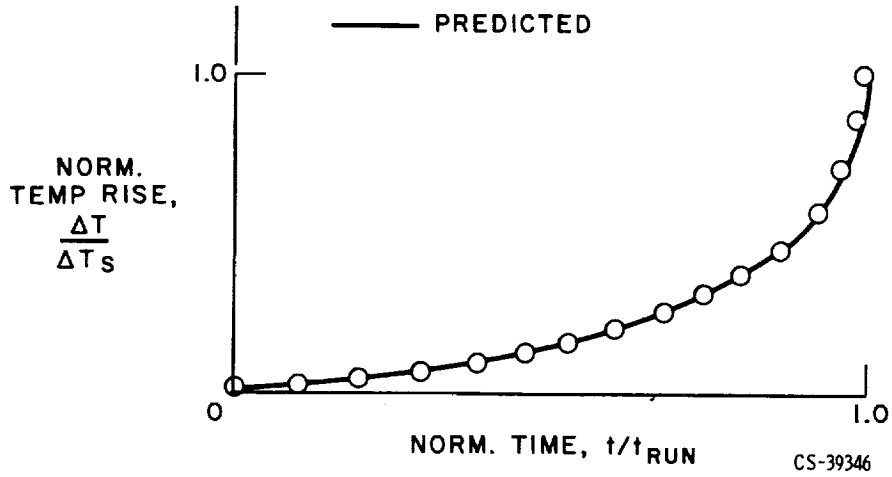

Figure II-25. - Temperature history for high-bottom heating.

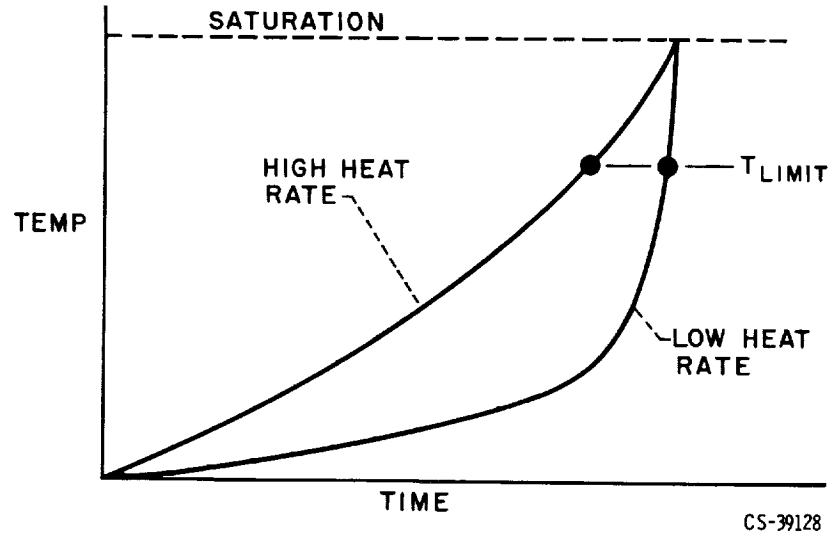

Figure II-26. - Temperature outflow history.

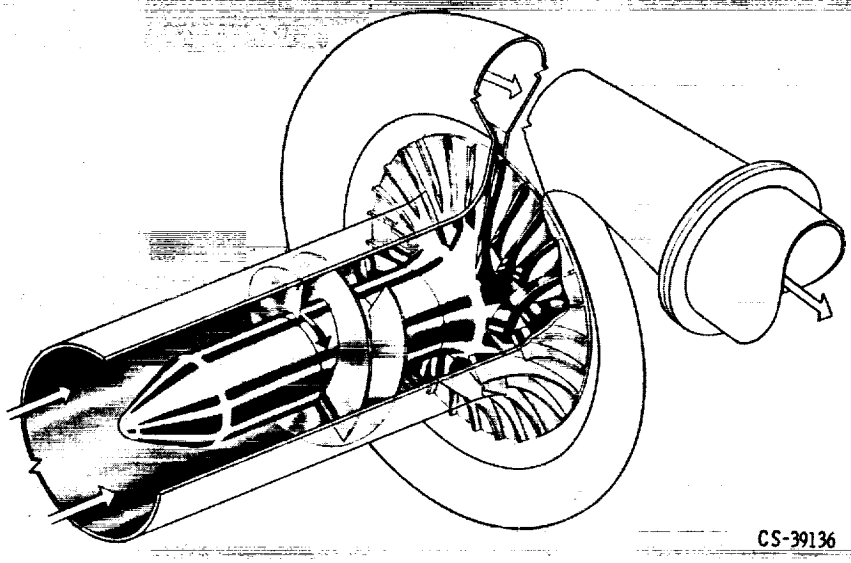

CS-39136

Figure II-27. - Centrifugal pump with inducer.

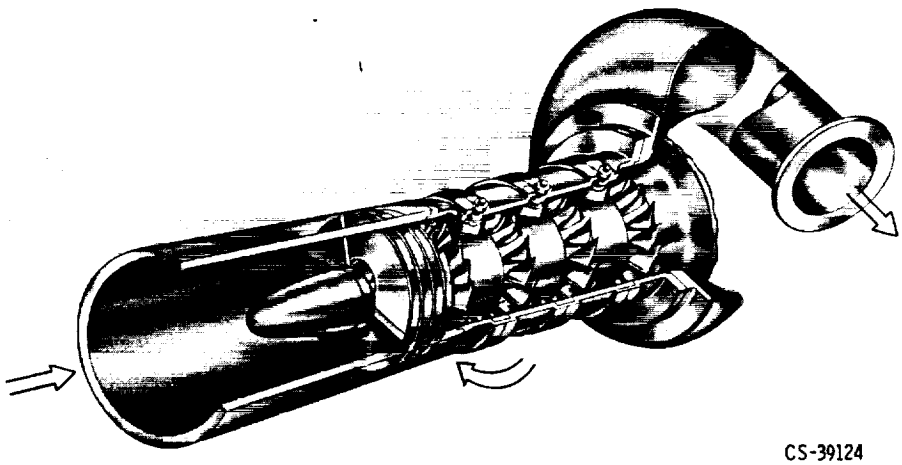

CS-39124

Figure II-28. - Axial pump with inducer.

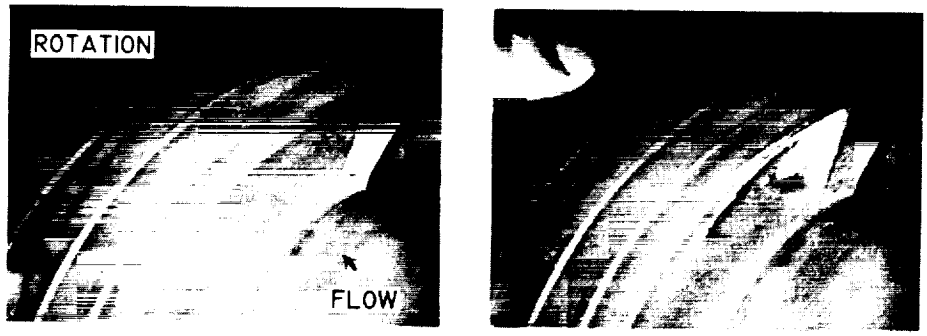

(a) No cavitation.

(b) Moderate cavitation.

(c) Extensive cavitation.

(d) Cavitation breakdown.

Figure II-29. - Cavitating inducer.

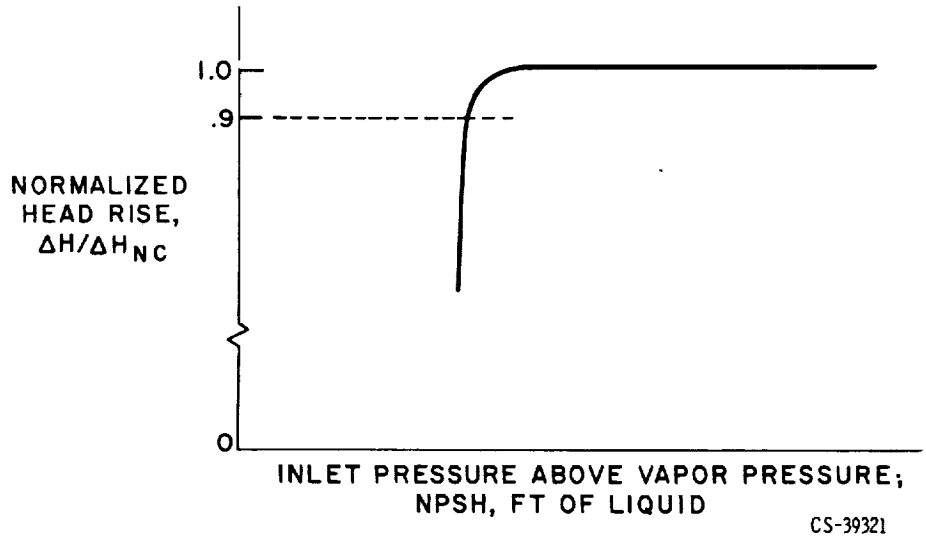

Figure II-30. - Inducer cavitation performance.

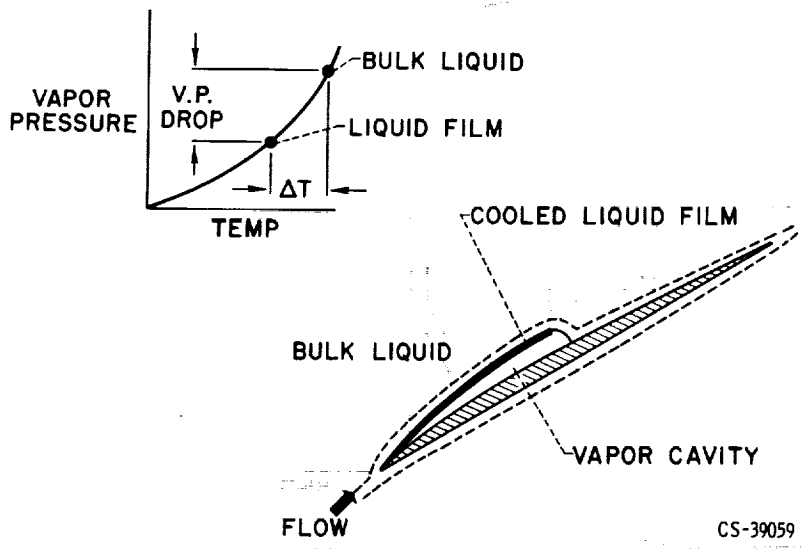

Figure II-31. - Cavitation cooling.

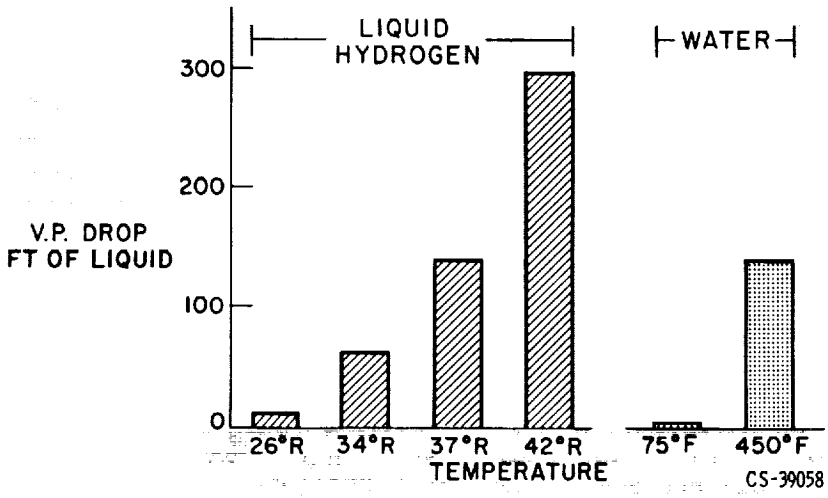

Figure II-32. - Predicted vapor pressure drop.

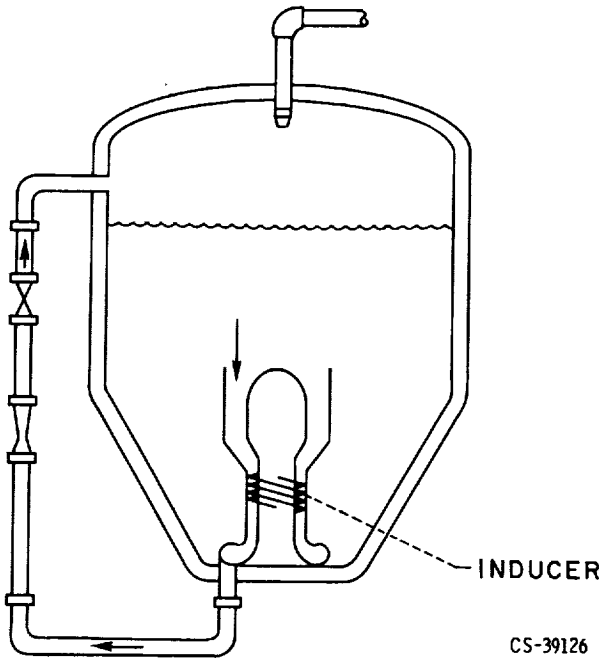

Figure II-33. - Pump cavitation facility.

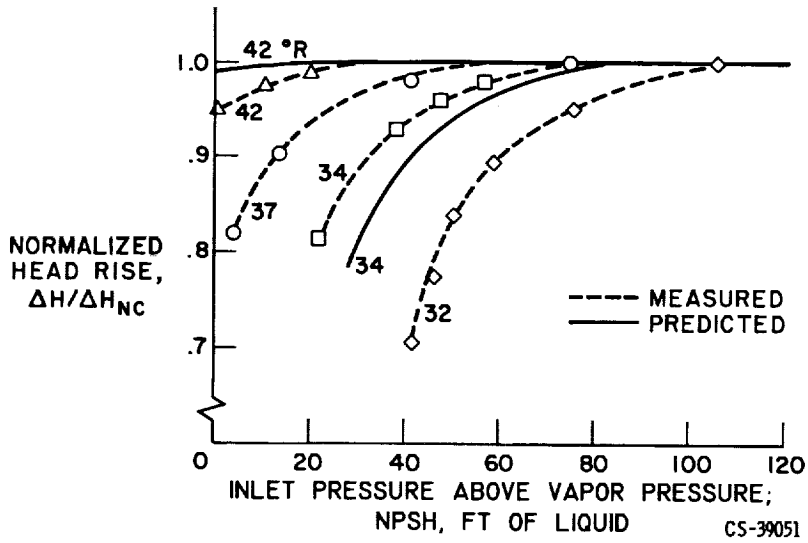

Figure II-34. - Temperature effect on inducer cavitation performance.

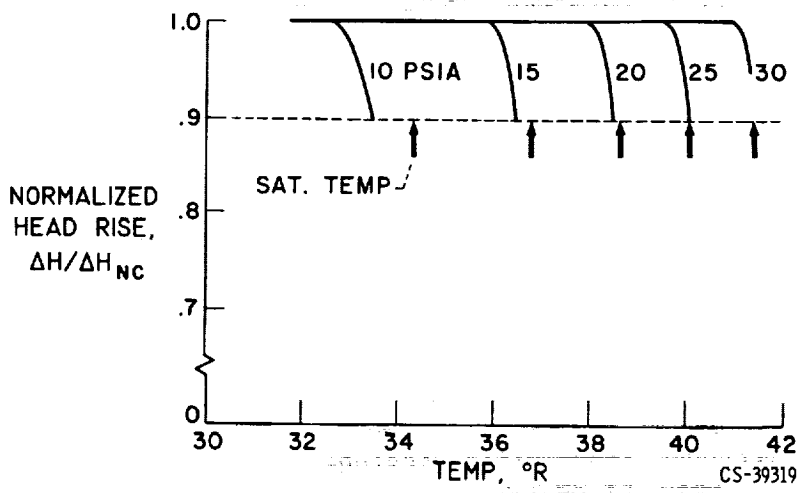

Figure II-35. - Tank pressure effects on inducer cavitation performance.

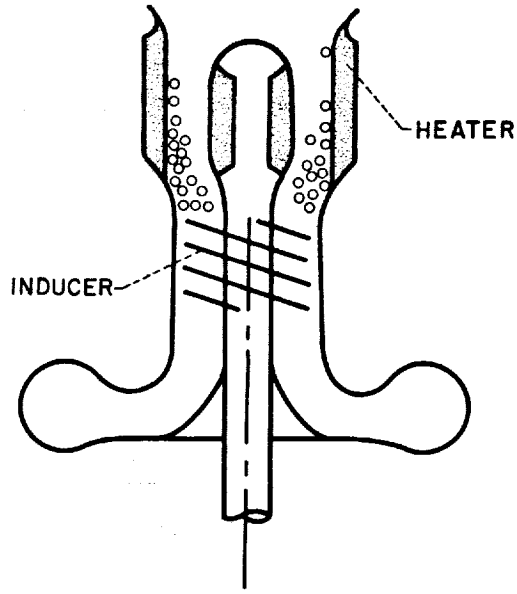

CS-39166

Figure II-36. - Vapor formation with heated inlet pipe.

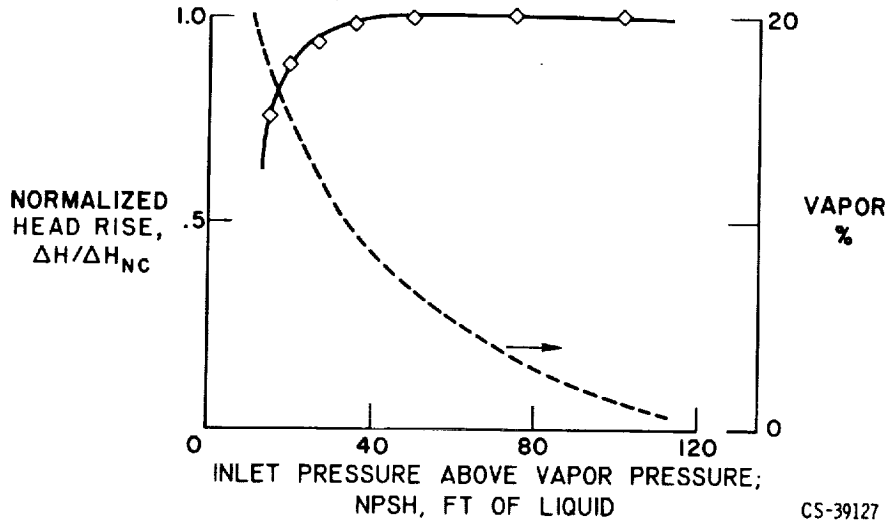

Figure II-37. - Effect of vapor formation resulting from heated inlet pipe on inducer performance.

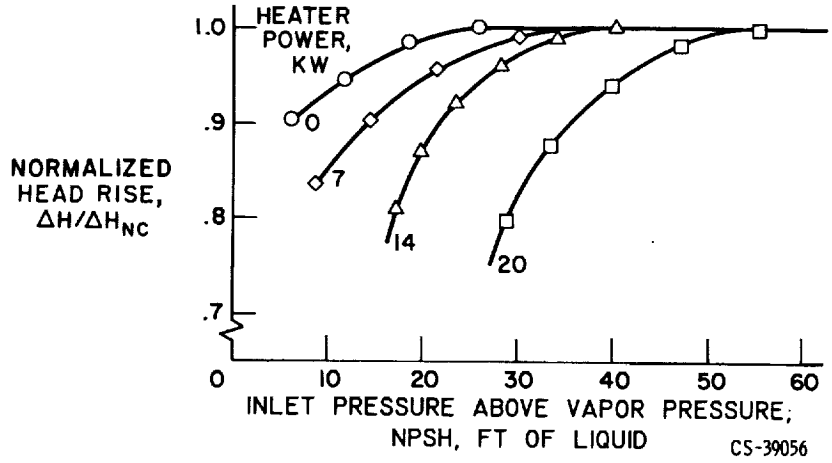

Figure II-38. - Heated inlet pipe effects on inducer cavitation performance.

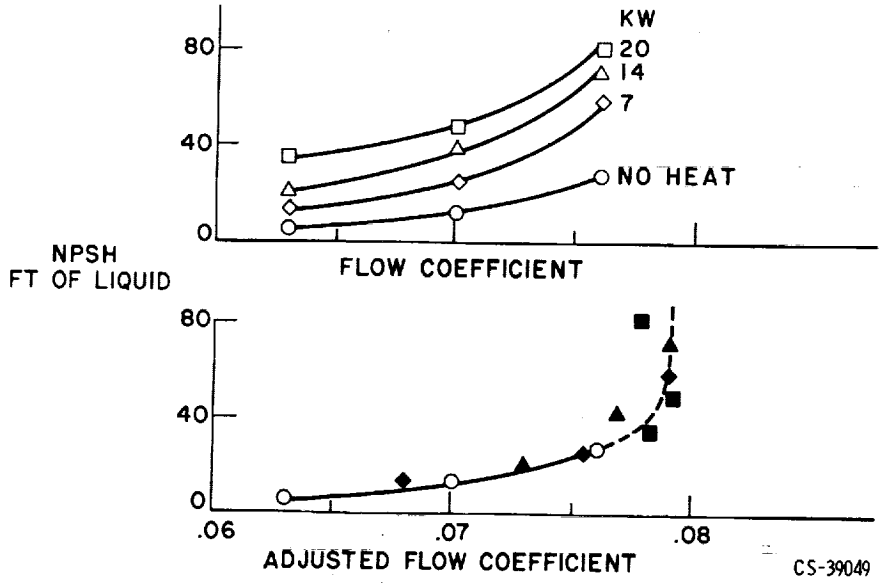

Figure II-39. - Inducer performance with vapor ingestion for 0.9 normalized head rise.

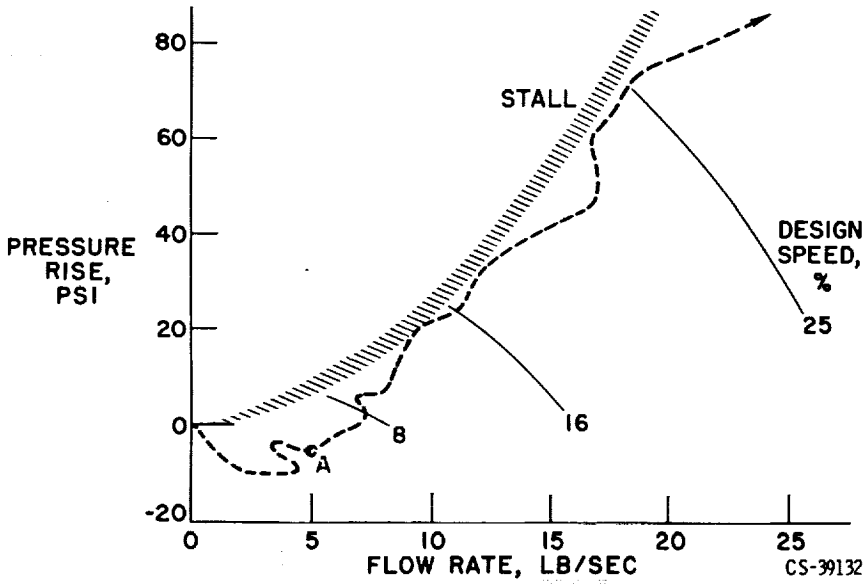

Figure II-40. - Pump startup transient.

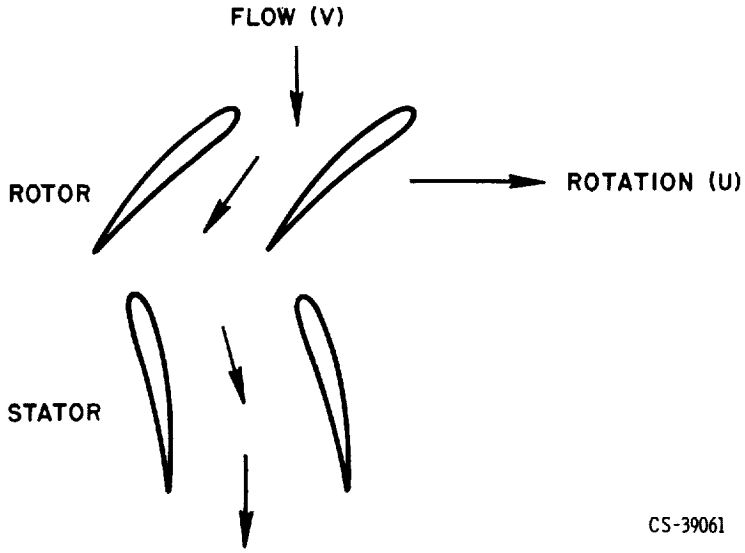

Figure II-41. - Axial-stage flow model.

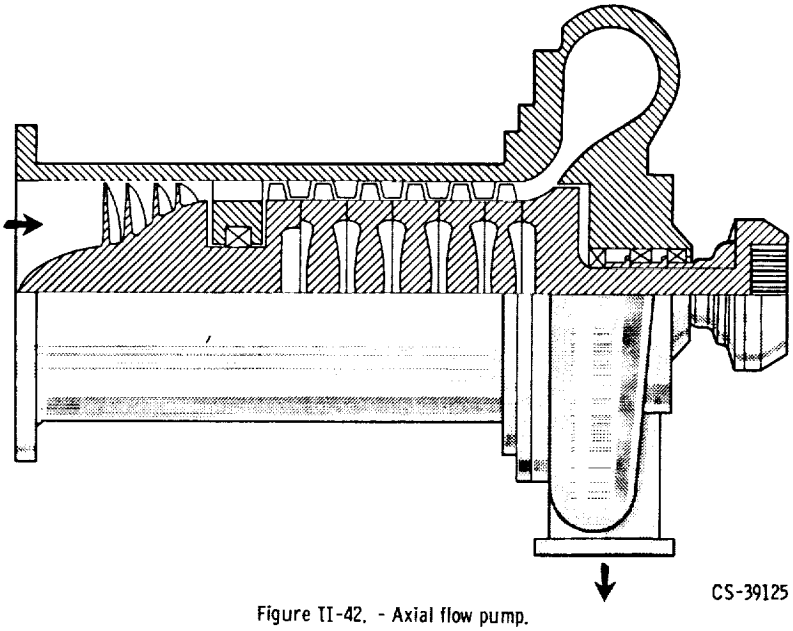

Figure II-42. - Axial flow pump.

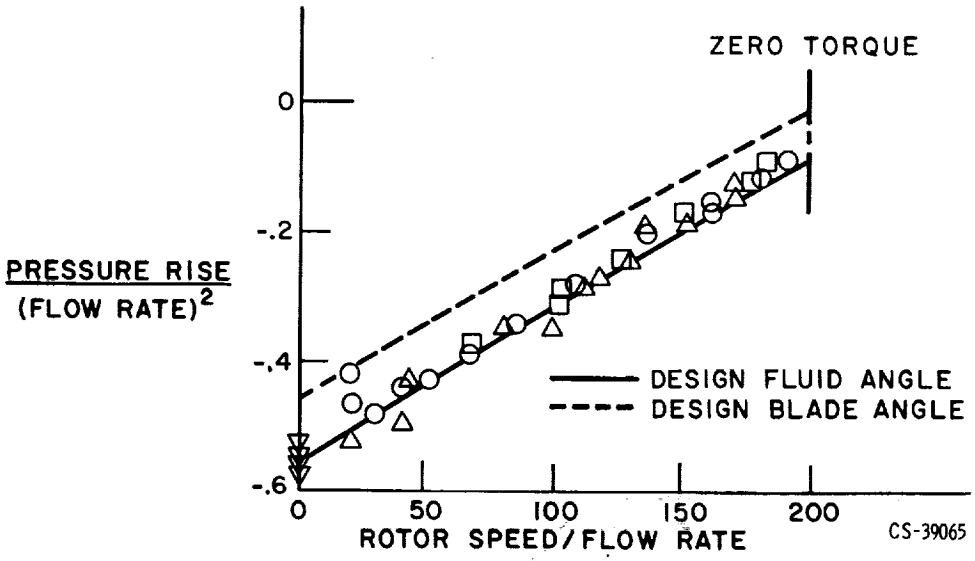

Figure II-43. - Pump windmilling performance.

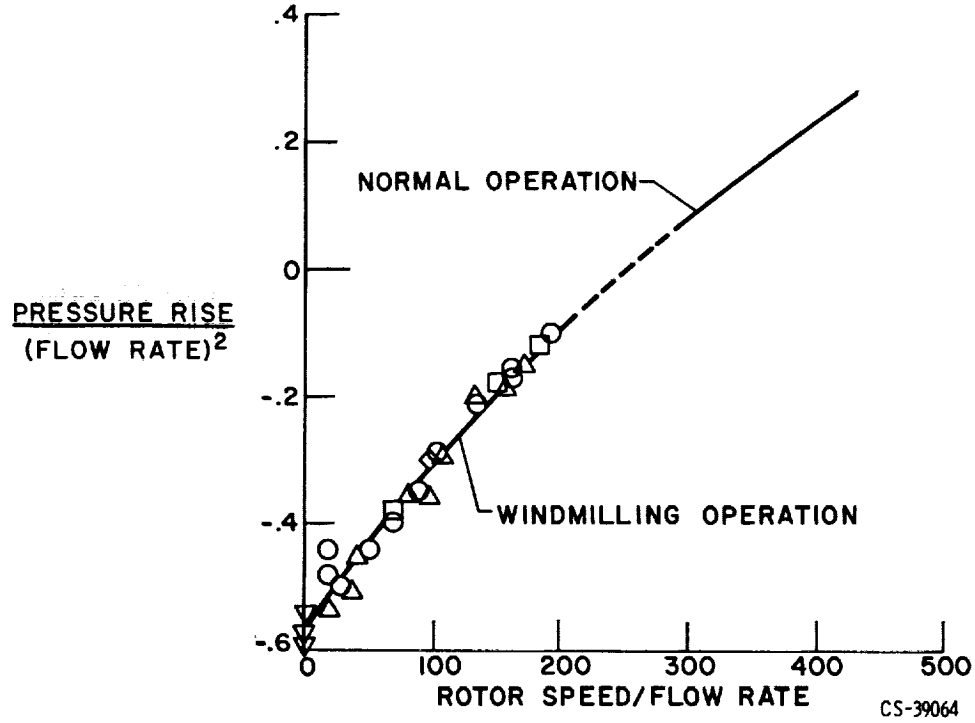

Figure II-44. - Generalized pump performance.

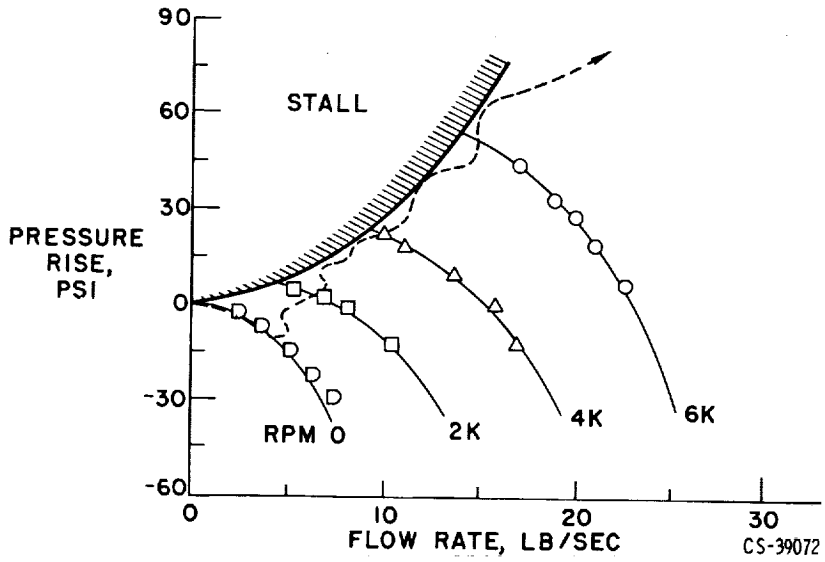

Figure II-45. - Pump performance map.

X66-51409

III. HEAT TRANSFER AND FLUID MECHANICS*

Robert W. Graham, Rudolph A. Duscha, William L. Jones, and George E. Turney

Lewis Research Center

INTRODUCTION

Some of the heat-transfer and fluid mechanical phenomena associated with the operational problems of the nuclear rocket are elaborated upon herein. Not only is the progress that has been made in the past 4 years described, but the areas are indicated where general understanding is inadequate. The discussion is organized in two major parts: (1) the difficult heat-transfer problems associated with the steady-state operation of the nuclear rocket (Some of this discussion is pertinent to the chemical rocket as well.); (2) the heat transfer and related pressure drop involved in the transient startup of the nuclear rocket. Paper IV (STARTUP DYNAMICS AND CONTROLS) pursues this startup problem in its stability and controls aspects. Heat transfer and stability are inherently related.

When the flow of hydrogen is traced through the passages of the nuclear engine (fig. III-1), a number of convective heat-transfer problems are apparent. Within the nozzle cooling passages, the cooling capability of the cryogenic hydrogen must be considered. It must cope with the heating load imposed by the high-temperature hydrogen flowing through the nozzle on the other side of the wall.

After leaving the nozzle cooling passages, the hydrogen flows through the reflector, providing a cooling function there. By the time it reaches the reactor core, the hydrogen has reached a temperature of 300° R. Within the core it is boosted to a temperature of 4500° R or higher and then it imposes the high-temperature conditions upon the nozzle. Some challenging heat-transfer problems exist in the core. However, this discussion is focused on the nozzle gas side and coolant side heat transfer. The ability to cool the nozzle is perhaps the most critical heat-transfer problem in the steady-state operation of the nuclear rocket. As a design procedure, the heat-transfer prediction techniques must lead to an estimation of the wall temperature in the nozzle.

If the gas-side wall temperatures for a NERVA nozzle were to be calculated using the limited heat-transfer information available several years ago, such as the Bartz

*This paper is unclassified.

Simplified equation on the gas side and a straight pipe flow equation on the coolant side, the result would be discouraging. Shown in figure III-2 is the gas-side wall temperature in ^{o}R as a function of nozzle length. The predicted temperature at the throat is in excess of 2600^{o} R. This prediction of such high temperatures, caused people elsewhere and at Lewis to reexamine nozzle heat transfer both on the hot gas side and on the coolant side. How the results of such heat-transfer experiments have led toward lower predicted values of nozzle wall temperatures is described herein.

STEADY-STATE OPERATION

Gas Side Heat-Transfer Coefficients

Several heat-transfer experiments have been performed both at Lewis and elsewhere which have indicated that the heat-transfer rates at the throat of rocket nozzles are considerably less than those predicted by any of the commonly used convective heat-transfer correlations for turbulent flow. The results from two typical experiments are shown in figure III-3.

The local heat-transfer coefficient divided by the calculated maximum value at the throat of the rocket nozzle is plotted against nozzle area ratio. The vertical line represents the nozzle throat with the converging portion of the nozzle to the left and the diverging portion to the right. The curve labeled Bartz represents the heat-transfer coefficient distribution obtained using a Bartz Simplified calculation.

The two other curves are from experimental data obtained from two different nozzle heat-transfer experiments. The nozzles of both experiments had the same contraction and expansion angles but had different area ratios and were of different scale. One experiment used heated air and the other a liquid hydrogen-oxygen rocket. The data from these two experiments, although for entirely different temperatures, pressures, and heat fluxes, show close agreement. The important result from both these experiments is that the heat-transfer coefficient in the vicinity of the throat of the nozzle is only about 60 percent of the calculated value.

Acceleration effects on heat transfer. - The sizeable reduction of 60 percent in throat heat transfer will cause a big reduction in the estimated wall temperature there. This reduction must be associated with what is happening to the flow within the throat, and large flow accelerations are known to occur in the vicinity of the throat.

A heat-transfer experiment in a low-speed, two-dimensional air tunnel conducted by Moretti and Kays at Stanford showed that acceleration would reduce heat transfer appreciably. Moretti and Kays air tunnel is shown schematically at the top of figure III-4. One wall of the two-dimensional tunnel could be varied to provide the flow acceleration.

Heat-transfer measurements were made on the cooled opposite wall. In this figure, free-stream velocity and Stanton number are plotted against distance along the tunnel. (The Stanton number is a function of the heat-transfer coefficient.) Flow velocities for a typical run were about 60 feet per second before the flow acceleration and about 180 feet per second following the acceleration. The measured Stanton number drops during the flow acceleration to a value about 50 percent of the calculated value. Following the flow acceleration, it recovers to the calculated value.

The obvious question at this point is why does acceleration reduce heat transfer. Moretti and Kays suggest that acceleration reduces turbulence in the boundary layer and lowered heat transfer is associated with lowered turbulence. They cite visual experiments in a water tunnel using a dye-tracer technique. These observations appeared to show that acceleration reduces turbulence in a boundary layer.

Another well-known situation where acceleration reduces turbulence is in the wind tunnel. Prandtl and more recently Deissler and others have developed analyses which predict this reduction of turbulence in the free stream as the gas is accelerated toward the throat. Obviously the turbulence in the main stream of the tunnel may be significantly different from that in the boundary-layer being considered here. Nevertheless, some estimates have been made of the effect of acceleration on the turbulence in Moretti and Kays' boundary layer by using Deissler's methods for wind tunnels. The dashed curve in figure III-4 is such an estimate. The estimated and observed reductions of heat transfer agree well. Based upon this observation, a major portion of the relative reduction of heat transfer at the throat of a rocket nozzle could be caused by the turbulence reduction that accompanies acceleration.

The accelerating forces acting on a boundary layer influence not only the turbulence, but other properties of the boundary layers as well. In particular, the velocity profile of a boundary layer is sensitive to acceleration, as is shown in figure III-5. A normal turbulent boundary layer is shown on the left side of the figure, where y is the distance from the wall and u is the local velocity. The velocity profile is approximated by a power-law equation, as shown on the right side of the figure, where U is the free-stream velocity and δ is the boundary layer thickness. The value of n for the usual turbulent boundary layer is near 7. If a sizeable accelerating pressure gradient is applied, the profile is stretched into the shape on the right side of the figure, and the value of n might be 20, 30, or higher. The man on the figure represents the accelerating force that distorts the equilibrium boundary layer profile shown on the left side of the figure.

Measured profiles of accelerated boundary layer. - Boundary layer profile measurements have been made at this laboratory in a rocket-type nozzle using heated air (see fig. III-6). The measurements were made in the accelerating flow region upstream of the nozzle throat. The distance from the wall is shown against the local to free stream

velocity ratio. The measured profile for the accelerated flow is considerably steeper at the wall than the nonaccelerated profile, much in the manner described previously. Measurements like these of the profile shapes and the thicknesses of the velocity and temperature layers help the input to the so-called integral boundary layer prediction technique. However, the predicted heat-transfer rates are still substantially higher than those observed at the throat.

Other influences and gas-side summary. - The effects of acceleration on turbulence and on velocity profiles and their possible effects on heat transfer have been discussed. Other things are happening in the rocket nozzle, which are not considered in the usual estimation of heat transfer. In a highly accelerated boundary layer, the usual direct analogy between velocity and temperature profiles no longer holds. (This analogy is called the Reynolds' Analogy.) The curvature of the walls cause centrifugal effects in the boundary layer that may influence heat transfer. These and other effects are being investigated at Lewis and elsewhere. The important experimental observation is that the throat heat-transfer coefficient is approximately 60 percent of the predicted value (see fig. III-3). If a 30° convergent angle nozzle is to be designed, the Bartz Simplified correlation should be multiplied by 0.6 to estimate the throat heat flux.

In summary, a major portion of the reduction of heat transfer at the throat below the expected value is believed to be caused by flow acceleration effects, which include reduced turbulence and altered boundary layer profiles.

Coolant Side Heat Transfer

The problem of cooling the wall is not the lack of heat capacity in the fluid but how to force the heat into the coolant. In fact, there is only a comparatively modest bulk temperature rise across the nozzle because the entire propellant supply is available for cooling the nozzle. This is significantly different from the chemical rocket where only the fuel is used for regenerative cooling, and it experiences a large temperature rise. The hydrogen coolant will be considered in its high pressure condition. Figure III-7 is a phase diagram of hydrogen shown with temperature-entropy coordinates. The narrow shaded region above the saturation line is the operating region for the coolant in a NERVA-type engine. Pressures of 800 pounds per square inch absolute or higher put the fluid state out of range of some of the near-critical effects that cause problems with heat-transfer correlations. The engine diagram in figure III-1 shows that the coolant is flowing at high speed and is being turned rapidly at the throat. Both the straight and curved sections of the coolant passage will be discussed with emphasis on the curvature effects at the throat.

Straight tube results. - Helpful information on convective heat transfer to liquid

hydrogen has come from research experience with straight tubes. Electrically heated straight tube experiments for this fluid state regime have recently been conducted at Lewis. In figure III-8 the results of these experiments are shown as a plot of $Nu_f/Pr_f^{0.4}$ as a function of Re_f. The data appear to correlate well when a 0.021 line of the Nusselt film correlation is used. This is the same correlation used for perfect gases.

The question arises as to whether this straight tube correlation would be applicable to the straight portion of the cooling passages of a nuclear rocket. It is assumed that it would apply wherever the conditions of heat flux and wall- to bulk-temperature ratios were the same. However, in the nuclear rocket, because of the relatively low bulk temperature rise, the wall- to bulk-temperature ratios can be very high (i.e., on the order of 20). In the chemical rocket they would be lower. Although it would be desirable for these higher wall- to bulk-temperature ratios to be studied in the fully developed flow portion of electrically heated tubes, conditions like these are difficult, if not impossible, to simulate. No claim can be made for the correlation shown in figure III-8 above these conditions and the correlation is expected to change for higher heat flux or higher wall- to bulk-temperature ratios.

Curvature effects. - The effect of curvature on the heat transfer into the coolant will be considered next. Figure III-9 illustrates some electrically heated tube results conducted with a 0.2-inch-diameter tube with a radius of curvature of 4.25 inches. The experimentally determined heat-transfer coefficient divided by the calculated coefficient for straight tubes (evaluated at film conditions) is plotted against angular position around the bend. Heat-transfer rates of more than two times that obtained in a straight tube were measured on the outside of the tube bend. The corresponding values on the inside of the bend were about 20 percent below those of the straight tube. The reason that the values at the beginning of the curvature are above the straight tube values is because of entrance effects. A longer heated length ahead of the curved portion of the tube would be required to minimize these entrance effects. The enhancement in heat-transfer coefficient on the outside bend of the tube (which forms the nozzle throat) is attributed to the strong density gradients and secondary flows set up within the tube as a result of turning the high-velocity coolant flow.

Other effects. - Another effect that may be present in the rocket nozzle tubes but not in the electrically heated tube experiments is surface roughness. Other experimenters have noted enhancement in heat transfer caused by rough surface conditions of the rocket nozzle tubes. In addition, effects such as asymmetric heating, heating in varying area passages and heating to higher values of wall- to bulk-temperature ratios are being studied. Considerable experimental work is required to evaluate these effects that may be important in the real nozzle tubes of the rocket engine. The largest effect on the coolant side coefficient at the throat, namely curvature, is emphasized.

Revised Estimates of Wall Temperature

From this enhanced cooling in the curved section of the cooling passage at the throat wall another benefit that reduces the local wall temperature was derived. If this benefit is added to the reduced heat flux from the gas side, the previous pessimistic estimate of wall temperature at the throat (fig. III-2) is significantly altered. As an example, a comparison of three different gas side temperature distributions along the length of the nozzle is given in figure III-10. These distributions are all for the NERVA NRX-A3 nozzle whose contour is shown in the upper part of the figure. The reactor end is at the left followed by a 45° convergent angle, an 8.72-inch throat diameter, and a 17.5° divergent angle. The nozzle is convectively cooled and consists of an AISI 347 stainless steel U-shaped coolant passage brazed into a 347 stainless steel pressure shell. Curve 1 is the same pessimistic temperature distribution as shown previously with temperatures in excess of 2600° R at the throat. Curve 2 results from applying what has been learned about the reduced heat transfer on the hot gas side. This curve indicates a reduction in peak temperatures of about 350° R. If the knowledge about the effect of curvature on the coolant side, the effect of inlet conditions, and the possible effect of high wall- to bulk-temperature ratios is applied, curve 3 results. Examination of the primary region of concern, the throat region, indicates that the peak temperature has been reduced some more and is now down to 1750° R, a more reasonable maximum operating temperature. All these predicted temperatures are for the NERVA NRX-A3-EP-IV hot-firing condition, 3780° R and 568 pounds per square inch absolute. This test was a successful operation of both the reactor and the nozzle; thus credence is given to the assumption that wall temperatures were more nearly in the vicinity of curve 3.

Although the application of the various heat-transfer effects to calculations of wall temperature might change the designer's thoughts of potential failure to thoughts of anticipated safe operation, wall temperatures by themselves are not the sole criterion for predicting either a successful engine firing or a failure. However, a reasonably accurate prediction of wall temperatures is required for any structural analysis.

Structural aspects. - An insight into the structural aspect of nozzle operation can be achieved by examining the mechanics of deformation of the nozzle coolant tubes during steady-state operation. As is portrayed in figure III-11, this deformation is applicable to a tube-and-shell type nozzle, such as the NERVA nozzle. The stiffer and stronger shell is considered to govern the movement and restraint of the thin-walled coolant tubes. The hotter tubes expand more than the shell but are restrained with a deflection force resulting. The upper half of the figure shows the final result of what this does to the coolant tube. The region of greatest concern is the tube crown and at this location an elastic tangential stress can be calculated. This tangential stress is composed of the bending stress resulting from the bending moment imposed by the deflection force, the membrane stress due to both internal pressure and the deflection force, and the biaxial

thermal stress due to the temperature gradient across the tube wall.

The orientation of this tangential stress is shown in the three-dimensional view in figure III-12. This orientation is indicated by the arrow in the circumferential direction and is calculated at both the inside and outside of the coolant passage wall. Shown in the figure is the U-tube configuration of a NERVA nozzle coolant passage. In addition to the tangential stress there is also the longitudinal stress that is caused primarily by the large temperature difference from the hot gas side to the cold shell side.

Note the range of calculated stresses that results from using the temperature distributions shown in figure III-10. Shown in figure III-13 are the inside and outside tangential stresses as well as the average longitudinal stresses. The numbers on the stress curves correspond to the similarly numbered temperature curves in figure III-10.

These stresses are plotted as a function of the nozzle length, just as the temperatures were. The inside tangential stresses are at the top of the figure. For the most part they are all compressive stresses as indicated by the minus sign on the ordinate. The peak value at the throat for curve 3 is about -80 000 psi, while that for curve 2 is almost double that. The peak outside tangential stresses are about the same magnitude, 80 000 psi at the throat, for curve 3, but these are now tension stresses. The longitudinal stresses, shown at the bottom, are compressive stresses and range up to -300 000 psi.

The yield strength of this material is about 20 000 psia at 1500° R and 10 000 psi at 2000° R. Comparing these strength values with those shown for the inner and outer tangential stresses shows that yielding apparently occurs and that the greater portion of the nozzle operates in the plastic range. The calculated longitudinal stresses indicate that the entire length of the nozzle operates in the plastic range with values considerably higher than those of the tangential stresses. Presumably, the usual concept of designing to an allowable stress below the yield strength of the material is not possible.

The calculated values of elastic stress were shown to emphasize the extent to which the material is operating above its elastic limit. This indicates the relatively large amount of strain that would exist and dramatically points out the need for a material with a high value of ductility. This high ductility value is required to prolong the low-cycle, high-strain fatigue failure that would occur.

Tube buckling. - Another factor associated with tube yielding is the aspect of tube buckling similar to that which occurred on some of the earlier nuclear nozzle firings. Figure III-14 shows rather simply how this buckling occurs. The thin-walled tube has to expand on the hot side while the cold back side might even contract. For the actual operation the effect is the same as a constraint being imposed on this expansion with the excessive strain resulting in the formation of a buckled tube for severe conditions. This buckling occurred in the regions indicated in the bottom sketch of figure III-14.

The buckling can be analyzed by applying the assumption that a nozzle tube under a thermally induced strain behaves like a tube under uniaxial compression. Utilizing avail-

able analyses for buckling of thin shells modified for plastic buckling gives the critical stress that would produce buckling as a function of the geometric parameters of the tube, namely the ratio of the tube radius to the tube wall thickness. This radius-thickness factor can then be related to a critical buckling strain. Under the operating conditions being discussed, buckling can usually be avoided through control of the geometry.

The high temperatures that produce high stresses, however, are difficult to reduce by geometric control because of limitations on minimum tube size and feed system delivery pressures. For the present, however, the nozzles are apparently operating satisfactorily despite indications that they are operating near their upper limit.

Techniques for upgrading nozzles. - Reactor engineers feel that reactor power could be increased without major changes in reactor design. If the required conditions were the same as those required to investigate the uprating of reactors, the present nozzles may not be capable of operating successfully. One method that would allow present nozzles to operate beyond their apparent limit is the use of coatings on the hot gas side. The use of coatings in a high-temperature environment has been relatively successful, but their application in convectively cooled tubular nuclear rocket nozzles has not been investigated. Shown in figure III-15 is an indication of the potential gains for applying a coating to an existing nozzle. Again, calculated temperatures are plotted as a function of length for the same nozzle shown previously in figure III-10. The conditions chosen are for the NERVA NRX reactor operating at twice the power rating and at 5000° R and 960 pounds per square inch absolute.

Applying a coating with a thermal resistance of 100 (sec)(in.^{2})($^{\circ}$R)/Btu causes the maximum temperature to be reduced to 1750° R while the coating is operating at 3100° R. This temperature reduction is within the capabilities of coatings that have thermal resistance values of 100. Such coatings could be produced by about 4 mils of zirconia or 8 mils of alumina.

This large reduction in metal temperature by the use of a coating may indicate that nozzles should be designed to utilize this advantage; however, some unanswered questions exist, which only a development program could answer. For example, the very large temperature drop, about 1300° R, across the thin coating layer may cause excessive cracking, which could lead to the loss of the coating in sections. To safely utilize a coating for the initial design, a definite knowledge of the operating characteristics of a specific coating would be required; however, a coating application to an available nozzle does present the potential for extending the useful operating range of the nozzle.

Summary of Steady-State Operation

For steady-state operation, cooling the nozzle is apparently a difficult heat-transfer problem. Fortunately, flow acceleration effects on the gas side and curvature on the

coolant side collaborate to reduce the severity of the heat load.

TRANSIENT STARTUP

This rocket engine gets to its steady-state operating point only by going through a starting transient. The startup transient operation includes some challenging heat-transfer aspects. While there is no critical cooling problem, the heat transfer has a direct influence on pressure drop, which is one of the most significant variables in the transient.

In the discussion of steady-state operation, the propellant was at high pressure, four or five times critical pressure, but in the transient startup entirely different fluid state regimes exist at low pressure.

Startup Mode

For the startup discussion, the entire nuclear rocket engine, which comprises the nozzle, reflector, and core, will be considered. An unfueled configuration similar to that shown in figure III-1 was tested in an altitude simulation facility at the Lewis Plum Brook station.

Before considering data from startup tests, the conditions in the engine when flow is initiated will be discussed. Initially, the components of the engine (i. e., the nozzle, reflector, and core) are essentially at ambient temperature. When flow is started, liquid hydrogen from a storage tank is transferred through a feedline to the engine. For the first few seconds the sensible heat in the feedline causes vaporization of the liquid hydrogen so that the flow entering the engine is gaseous. As flow continues, the hardware upstream of the engine is chilled down, and two-phase hydrogen moves into the nozzle tubes and eventually penetrates the flow passages in the reflector.

In startup, therefore, both gas and two-phase flow in the nozzle and reflector must be considered. For the region of interest during startup, only gaseous hydrogen flows through the core. With the chilldown the pressure, flow rate, and the temperature of the components are changing simultaneously. As a consequence, the state of the fluid changes with both time and location in the engine.

In order to predict pressure drops in the nozzle, reflector, and core during a startup, the surface temperatures of the flow passages in the individual components at each point in time throughout a chilldown must be estimated. Thus, predictions of pressures in the engine are strongly dependent on estimates of heat transfer from the relatively hot components.

To distinguish the operating range encountered during startup with that of steady state, refer again to the temperature-entropy diagram for hydrogen (fig. III-16). The

two-phase dome is shaded. Recall from the steady-state discussion that the hydrogen state was in the supercritical region, well above the two-phase dome. In startup, the hydrogen state is below the critical region, and the fluid state changes with time.

Heat Transfer in Startup

If a point in the region, such as the nozzle tube inlet, is considered and if the state of the hydrogen during startup is traced, the fluid would be observed to change from a superheated gas and to approach a saturated liquid state; that is, with increasing time, the change is from right to left along the dashed trace shown in figure III-16. This trace indicates that in startup two fluid regimes are of concern, the gaseous and the two-phase (liquid-vapor). Adequate gaseous hydrogen correlations have been in the literature for at least 7 years. They are essentially correlations of the familiar Nusselt number-Reynolds number type.

This two-phase region shown in the temperature-entropy diagram was investigated at Lewis by the use of uniformly heated test sections.

The heat-transfer characteristics should be examined for one of the research runs that comes close to simulating an instantaneous hydrogen state in the nozzle cooling passages. A realistic typical condition for the nozzle would be to assume that the hydrogen enters in a subcooled state and exits as a vapor after absorbing the residual heat of the nozzle. The heated-tube run in figure III-17 conforms to these inlet-exit conditions. The local measured heat-transfer coefficient and the estimated local quality are shown as a function of the tube length. Note that the local heat-transfer coefficient falls rapidly in the subcooled region at the tube entrance and then rapidly climbs when the fluid is saturated.

The flow model is assumed to be annular flow with a predominately vapor layer adjacent to the wall and liquid in the core. This model is portrayed in figure III-18. The vapor annulus is assumed to be laminar at the tube entrance. As the thin laminar gas layer at the entrance thickens, the heat-transfer coefficient drops off drastically (see fig. III-17). The annular flow becomes turbulent after quality develops, and the annulus becomes a turbulent mixture of liquid droplets and vapor. Some of these droplets impinge on the wall, and hence cause the increased heat transfer in the portion of tube where quality is developing.

Since this is a forced convection process, the conventional Nusselt-Reynolds number plot, in which an average density of liquid-vapor mixture was assigned, was used in an attempt to correlate the data. The Nusselt number did not correlate well with the Reynolds number, probably because of the complication of droplet evaporation at the wall.

Another approach was to determine if the heat transfer in a Nusselt parameter could be related to the local fluid friction of a two-phase annular flow. Certainly, the turbulent

mixing process of the liquid droplets with the vapor must be related to the interfacial shear. Martinelli worked out a two-phase frictional parameter for isothermal annular flow. As is portrayed in the following equation, two-phase frictional pressure drop has been correlated by multiplying the gaseous pressure drop by a function involving two parameters, gamma and chi:

$$\left(\frac{\Delta p}{\Delta L}\right)_{tp} = \left(\frac{\Delta p}{\Delta L}\right)_{g} \cdot f(\gamma, \chi_{tt}) \qquad (1)$$

where γ is the hydraulic diameter and velocity slip parameter and χ_{tt} is the shear resistance parameter for turbulence in both phases and is given by

$$\chi_{tt} = \left(\frac{1 - x}{x}\right)^{0.9} \left(\frac{\rho_v}{\rho_\ell}\right)^{0.5} \left(\frac{\mu_\ell}{\mu_v}\right)^{0.1}$$

Gamma corrects for the hydraulic diameter and the slip velocity between the phases. Chi is the Martinelli parameter which comprehends the two-phase shear. Chi is the parameter of interest. The variable x is quality, or percent vapor by mass, ρ is density, μ is viscosity, and the subscripts v and ℓ refer to vapor and liquid, respectively.

The Martinelli parameter was derived originally by assuming an annular flow, which was liquid adjacent to the wall and a gas core, the inverse of this flow model. Martinelli's derivation for the gas annulus - liquid core model was repeated, and the parameter came out with the same terms, which represent the shear at the interface and at the wall.

As is shown in figure III-19, an attempt was made to relate the Nusselt number ratio to Martinelli's two-phase shear parameter χ_{tt}. The reference Nusselt number was computed from a Nusselt-Reynolds equation for forced convection by using an averaged density, as described earlier. Low values of χ_{tt} represent a predominance of gas, and high values, a predominance of liquid. The correlation groups most of the data within ±20 percent. Note that the Nusselt ratio exceeds unity where the fluid is mostly gas. This enhancement is attributed to the continued presence of droplets that vaporize at the wall.

The convective film boiling correlation represented by figure III-19 is a tool that enables the heat-transfer rates with two-phase hydrogen flow to be estimated. The correlation has found wide use in startup heat-transfer analyses.

Pressure Drop in Startup

Prediction code. - A general technique (or procedure) used to calculate pressure

drops and heat-transfer rates in a component in the engine is illustrated in figure III-20.

Consider some component in the engine system, which may be either the nozzle, the reflector, or the core. From measurements, a history of the inlet fluid conditions throughout a transient chilldown run was obtained. The inlet conditions are time dependent and include the following: flow rate, pressure, fluid temperature, and in the case of the nozzle and reflector, an estimated inlet fluid quality, or density. These measured inlet conditions are used in a transient digital program to compute the pressure, fluid temperature, and quality at the exit of the component.

A simplified block diagram of a digital code used to analyze the pressure drop - heat transfer characteristics of an engine system component is shown in the lower part of the figure. These measured inlet conditions are used along with a transient conduction subroutine, a pressure drop - heat transfer subroutine, and a hydrogen properties subroutine to predict outlet conditions and material temperature distributions within the components. The predicted values of temperature and pressure are then compared with experimental (or measured) values.

Comparison with experiment. - Some data from a typical test run conducted in the Plum Brook facility will now be examined. The experimental data and data comparisons are for a single liquid hydrogen test run. This particular test had the steepest flow ramp of all the tests run in the Plum Brook test facility. The flow rate for this run was increased from 0 to about 28 pounds per second in the time span from 0 to 12 seconds.

The experimental pressures at the four major stations in the engine plotted against time are shown in figure III-21. In the early part of the startup, for times less than 3 seconds (for this run), the hydrogen entering the engine is gaseous at low pressure, and the major portion of the pressure drop in the engine occurs in the nozzle coolant tubes. As the chilldown progresses, the reflector becomes the major resistance to flow, and in the later portion of the run the pressure difference between reflector inlet and core inlet amounts to as much as 60 percent of the overall pressure drop in the engine. The pressure drop in the core is seen to increase gradually throughout the run. For this test run, as well as other runs made in the Lewis-Plum Brook facility, the hydrogen flow entering the core was gaseous.

An attempt will now be made to predict pressures in the engine during a simulated startup. Beginning with the nozzle, some comparisons will be made of measured and predicted pressures in components of the engine for the particular test run considered. Shown in figure III-22 is a plot of static pressure against time for the nozzle, and a comparison of the measured and predicted pressures at the nozzle tube outlet. As indicated in the figure, the hydrogen entering the nozzle tubes changed from gas to two phase at about $3\frac{1}{2}$ seconds after flow was initiated.

A quasi-steady-state digital program, similar to that described in the previous block diagram (fig. III-20), was used to calculate pressures at the nozzle coolant tube outlet.

The measured inlet pressure, a measured flow rate, and an estimated inlet fluid density were used as input to the digital code. The calculated (or predicted) pressures at the nozzle tube outlet are shown against time by the solid line.

As indicated in the figure, for the time span from 0 to about 8 seconds the calculated and measured pressures at the nozzle tube outlet are in reasonable agreement. For times between about 8 and 12 seconds, the calculated pressure drops across the nozzle tube are about two times the measured pressure drop.

The rather large difference between the calculated and measured pressures at the coolant tube outlet in this time span is believed to be caused partly by an overestimation of the heat transfer from the countercurrent flow of warm gas on the inside of the nozzle. From published data of other two-phase experiments, the Martinelli two-phase pressure drop relations that were used in the analysis appear to have a tendency to overestimate the frictional pressure drop for two-phase flow. In the later portion of the test run, the pressure drop across the nozzle tubes was primarily due to friction. Therefore, this too may partially explain the difference between the calculated and experimental pressure drops near the end of the run.

For the reflector figure III-23 shows a similar comparison of calculated and measured pressures at the reflector outlet. For this test run the flow entering the reflector changed from gas to two phase at about 4.5 seconds. Because of the large reflector mass, the hydrogen flow at the reflector outlet was gaseous throughout the 12-second run time; that is, even though the flow at the reflector inlet was two phase for times greater than $4\frac{1}{2}$ seconds the heat pickup in the reflector caused a transition from two phase to gas flow at some point inside the reflector. As a result, the hydrogen flow at the reflector outlet was a superheated gas throughout the test run.

A quasi-steady-state digital code, similar to that described, was used to calculate the pressures at the reflector outlet. For this run, the calculated and measured pressures at the reflector outlet are in reasonable agreement throughout the test run.

Of the three major components in the nuclear rocket engine system, the core appears to be the easiest to analyze during a chilldown transient. A single tube flow model was used to estimate the pressure drop - heat transfer characteristics of the core for several of the startup test runs. In general, the predicted and measured values of pressure drops for the core were in good agreement. For the particular test being considered, the predicted pressure drops across the core were within about 10 percent of the measured values.

These pressure calculations look reasonably accurate, but this is only a part of the problem. Fluid and material temperatures must be estimated also. In general, our predicted and measured values of fluid and material temperatures in the core assembly were in good agreement. As mentioned before, the hydrogen flowing through the core is in a gaseous state. In the nozzle and reflector, however, some significant differences were

observed between the calculated and measured local material temperatures of these components, especially during the time period in which the hydrogen flow is two phase.

Thus far in the transient discussion, individual components of the rocket engine, where the inlet conditions are experimental, have been considered. The question arises concerning the ability to predict overall pressure drop starting with known conditions at the nozzle inlet only. When the calculated and measured overall system pressure drops are compared for the run shown, the estimated values are found to be as much as 30 percent larger than the measured values. In general, the predictions of pressure drop are high, but it is felt that they could be improved. A part of the difference between predicted and measured values may be caused by nonuniform fluid inlet conditions to the parallel cooling passages of the components, especially when the hydrogen flow is two phase. The effect of nonuniform inlet fluid conditions on pressure drops in parallel cooling channels is discussed in paper IV (STARTUP DYNAMICS AND CONTROL).

SUMMARY

In this discussion some of the heat-transfer problems that relate to the startup and steady-state operation of a nuclear rocket engine have been discussed. The scope of this discussion had to be limited to a few topics, and time permitted only a highlighting of the topic material. As was seen from the discussion of the startup transient, heat-transfer knowledge is important in assessing the transient pressure drop characteristics of the engine components. The nozzle and reflector appear to be the most difficult components to analyze because of the presence of two-phase flow in complicated multipassage geometries. There is some difficulty in adding up the pressure drops of the individual components into an overall estimate.

In the transient phase there are no apparent problems in cooling the system components. For the steady-state operation, the crucial heat-transfer problem lies in the marginal regenerative cooling of the nozzle throat. Two phenomena help the situation. First, the effects of flow acceleration appear to reduce the hot gas heating load in the throat. Second, concave curvature in the throat region of the cooling passage enhances the coolant heat transfer.

The final decision concerning the reliability and integrity of the nozzle is a strength-of-materials decision. Heat-transfer researchers are sometimes enamoured by correlations of heat-transfer coefficient and heat flux, but for a design the correlation must be able to give an accurate prediction of wall temperature.

Introduced into the discussion was reference to the problems associated with making decisions regarding strength and reliability of the nozzle coolant passage material.

BIBLIOGRAPHY

STEADY-STATE OPERATION

Gas Side Heat-Transfer Coefficients

Bartz, D. R.: A Simple Equation for Rapid Estimation of Rocket Nozzle Convective Heat Transfer Coefficients. Jet Propulsion, vol. 27, no. 1, Jan. 1957, pp. 49-51.

Bartz, D. R.: An Approximate Solution of Compressible Turbulent Boundary-Layer Development and Convective Heat Transfer in Convergent-Divergent Nozzles. Trans. ASME, vol. 77, no. 8, Nov. 1955, pp. 1235-1245.

Boldman, Donald R.; Schmidt, James F.; and Fortini, Anthony: Turbulence, Heat-Transfer and Boundary Layer Measurements in a Conical Nozzle With a Controlled Inlet Velocity Profile. NASA TN D-3221, 1966.

Deissler, Robert G.: Effect of Uniform Longitudinal Strain Rate on Weak Homogeneous Turbulence in a Compressible Flow. NASA TN D-2800, 1965.

Elliott, David G.; Bartz, Donald R.; and Silver, Sidney: Calculation of Turbulent Boundary-Layer Growth and Heat Transfer in Axi-Symmetric Nozzles. Tech Rept. 32-387, Jet Prop. Lab., Calif. Inst. Tech., Feb. 1963.

Moretti, P. M.; and Kays, W. M.: Heat Transfer to a Turbulent Boundary Layer with Varying Free-Stream Velocity and Varying Surface Temperature - An Experimental Study. Int. J. Heat Mass Transfer, vol. 8, no. 9, Sept. 1965, pp. 1187-1202.

Prandtl, L.: Attaining a Steady Air Stream in Wind Tunnels. NACA TM 726, 1933.

Ribner, H. S.; and Tucker, M.: Spectrum of Turbulence in a Contracting Stream. NACA TN 2606, 1952.

Schacht, Ralph L.; Quentmeyer, Richard J.; and Jones, William L.: Experimental Investigation of Hot-Gas Side Heat-Transfer Rates for a Hydrogen-Oxygen Rocket. NASA TN D-2832, 1965.

Schmidt, James F.; Boldman, Donald R.; Ehlers, Robert C.; and Coats, James W.: Experimental Study of Effect of Simulated Reactor Core Position on Nozzle Heat Transfer. NASA TM X-1208, 1966.

Taylor, G. I.: Turbulence in a Contracting Stream. Z. Angew. Math. Mech., vol. 15, no. 1/2, Feb. 1935, pp. 91-96.

Coolant Side Heat Transfer

Hendricks, Robert C.; Graham, Robert W.; Hsu, Yih-Yun; and Friedman, R.: Experimental Heat-Transfer Results for Cryogenic Hydrogen Flowing in Tubes at Subcritical and Supercritical Pressures to 800 Pounds Per Square Inch Absolute. NASA TN D-3095, 1966.

Hendricks, R. C.; and Simon, F. F.: Heat Transfer to Hydrogen Flowing in a Curved Tube. Multi-Phase Flow Symposium, Norman J. Lipstein, ed., ASME, pp. 90-93.

Hendricks, Robert C.; Simoneau, Robert J.; and Friedman, Robert: Heat-Transfer Characteristics of Cryogenic Hydrogen from 1000 to 2500 psia Flowing Upward in Uniformly Heated Straight Tubes. NASA TN D-2977, 1965.

Hess, H. L.; and Kunz, H. R.: A Study of Forced Convection Heat Transfer to Supercritical Hydrogen. J. Heat Transfer, vol. 87, no. 1, Feb. 1965, pp. 41-48.

Miller, W. S.; Seader, J. D.; and Trebes, D. M.: Forced Convection Heat Transfer to Liquid Hydrogen at Supercritical Pressures. Paper Presented at Int. Inst. Refrigeration Meeting, Commission I, Grenoble (France), June 9-11, 1965.

Revised Estimates of Wall Temperature

Roark, Raymond L.: Formulas for Stress and Strain. Third ed., McGraw-Hill Book Co., Inc., 1954.

Timoshenko, Stephen P.; and Gere, James M.: Theory of Elastic Stability. Second ed., McGraw-Hill Book Co., Inc., 1961.

TRANSIENT STARTUP

Heat Transfer in Startup

Hendricks, Robert C.; Graham, Robert W.; Hsu, Yih-Yun; and Friedman, R.: Experimental Heat Transfer and Pressure Drop of Liquid Hydrogen Flowing Through a Heated Tube. NASA TN D-765, 1961.

Pressure Drop in Startup

Clark, John S.: Analytical and Experimental Study of Startup Characteristics of a Full-Scale, Unfueled Nuclear-Rocket-Core Assembly. NASA TM X-1231, 1966.

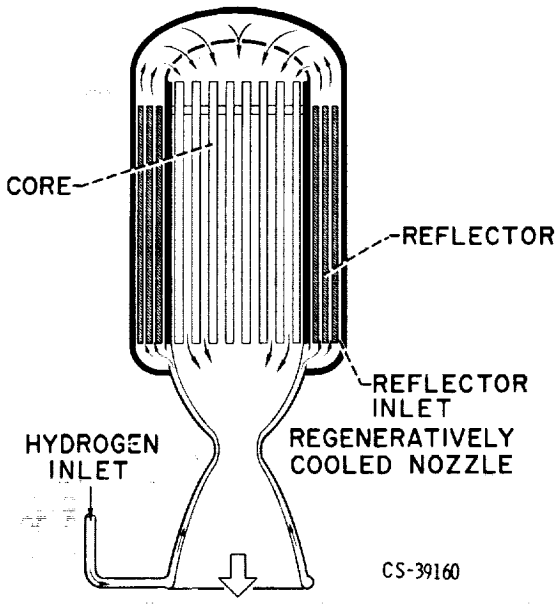

Figure III-1 - Nuclear rocket engine.

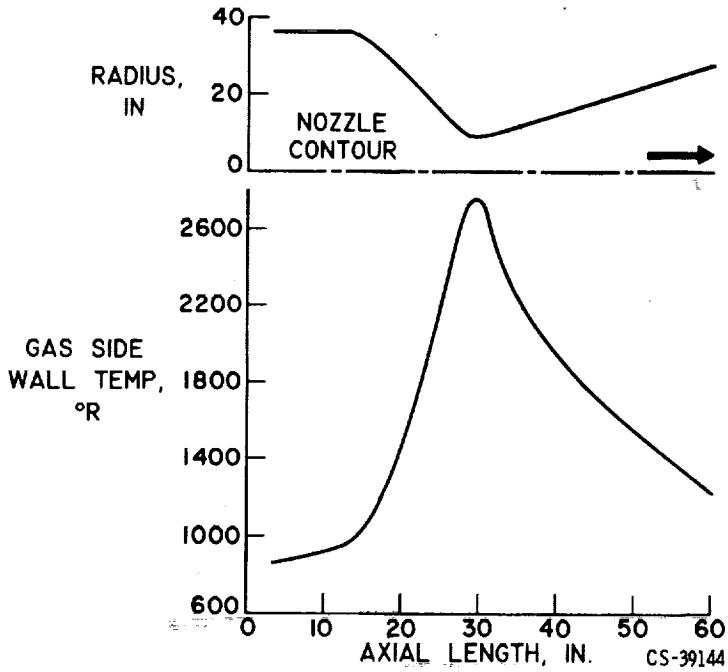

Figure III-2. - Pessimistic wall temperature prediction.

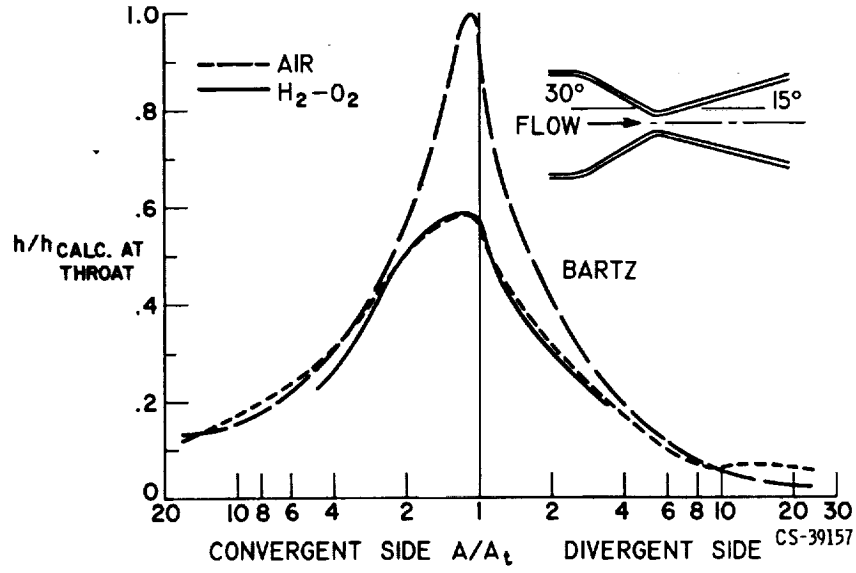

Figure III-3. - Rocket nozzle hot gas side heat-transfer coefficients.

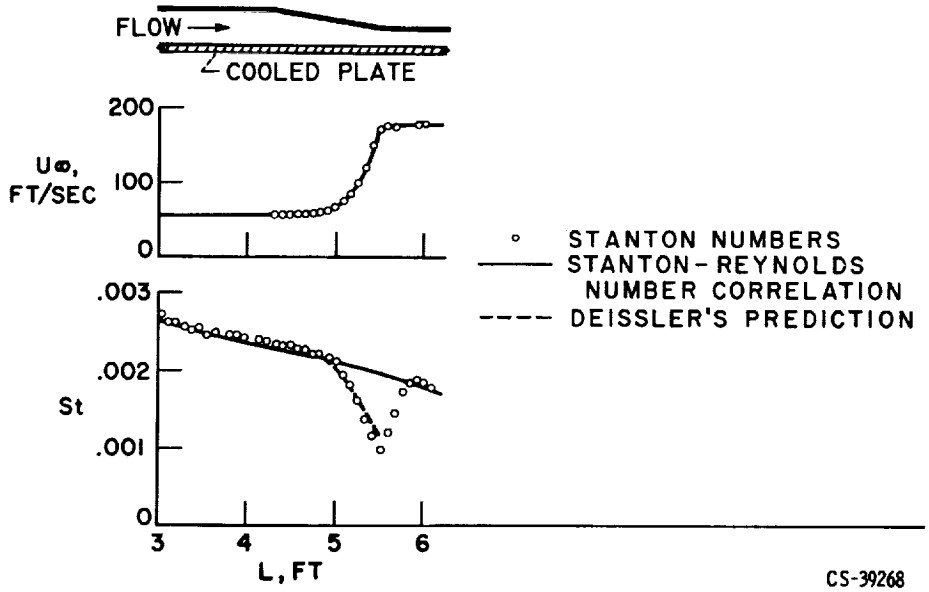

Figure III-4. - Moretti-Kays flow acceleration data.

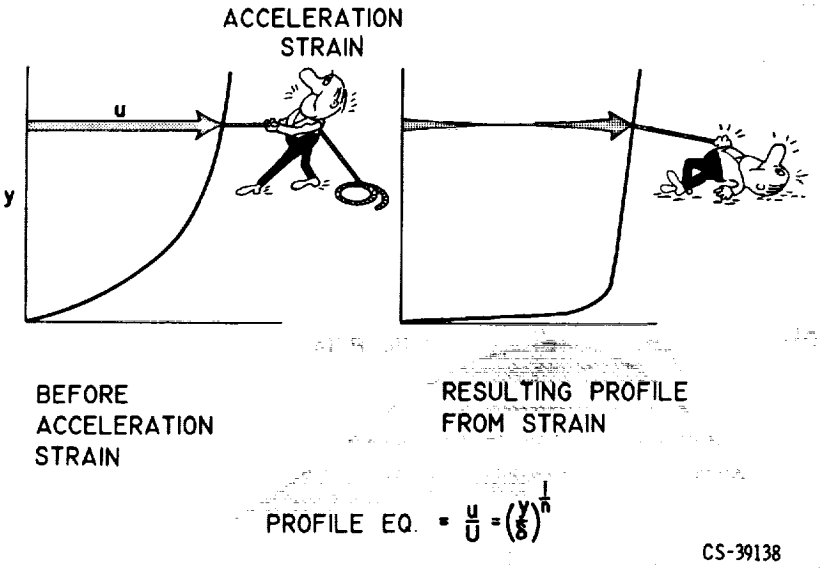

Figure III-5. - Effect of acceleration strain on profile.

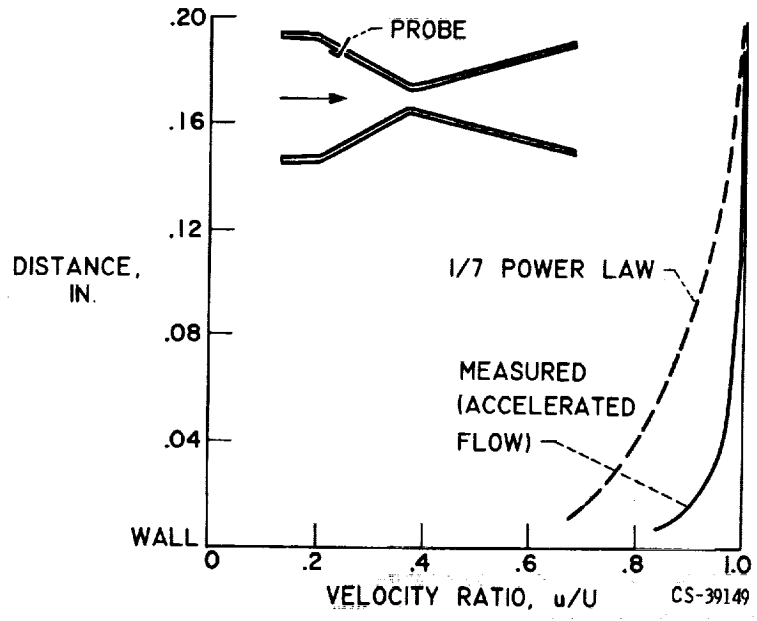

Figure III-6. - Nozzle boundary layer profiles.

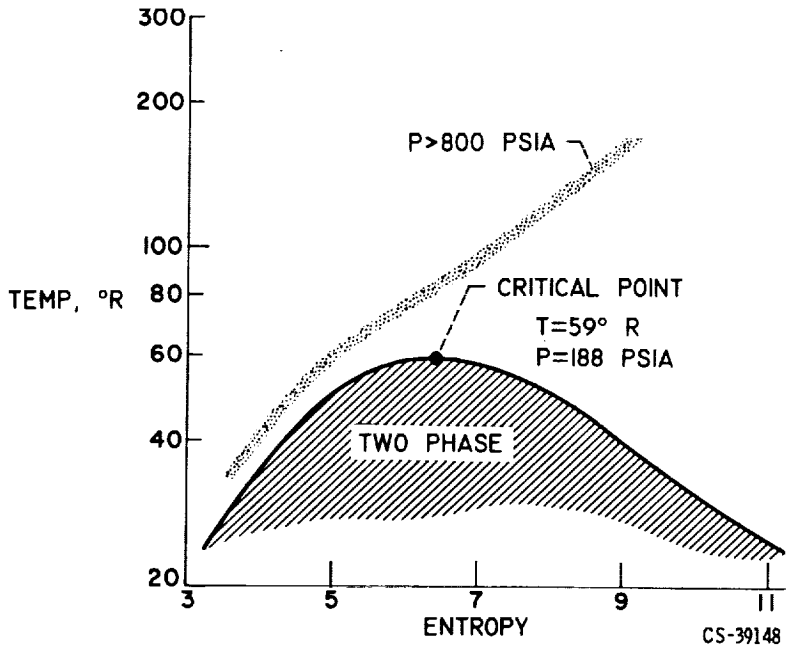

Figure III-7. - Phase diagram of hydrogen.

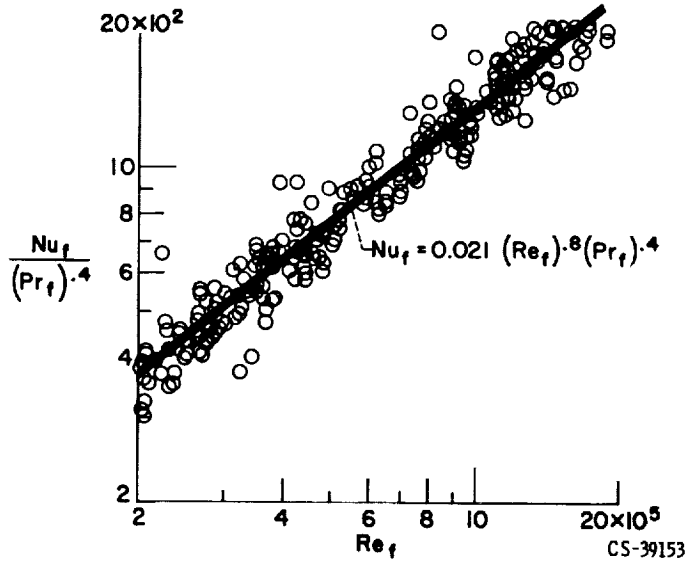

Figure III-8. - Film correlation of high-pressure hydrogen. Pressure, 800 to 2500 pounds per square inch absolute; heat flux, 2 to 10 Btu/(in.^{2})(sec); wall- to bulk-temperature ratio, 11; tube inside diameters, 0.21 to 0.44 inch; length-diameter ratios, 30 to 60.

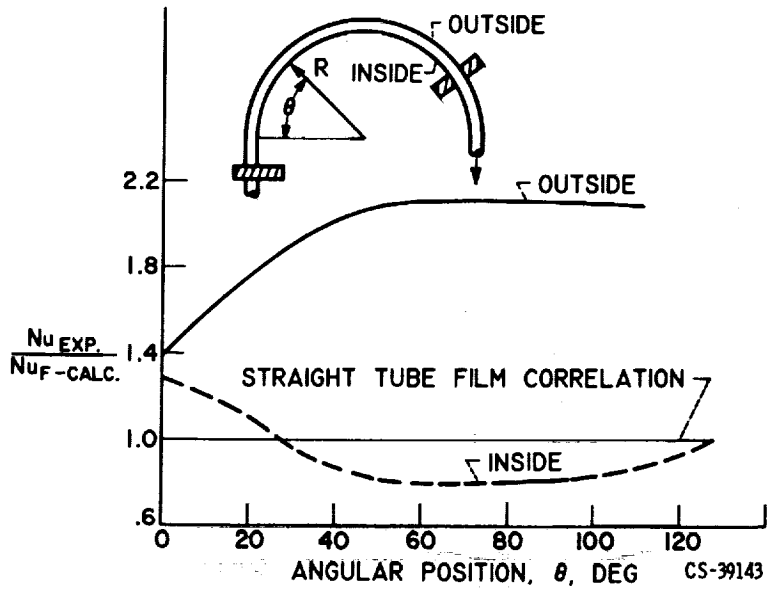

Figure III-9. - Curved tube heat transfer with gaseous hydrogen. Curvature radius, 4.25 inch; diameter, 0.21 inch.

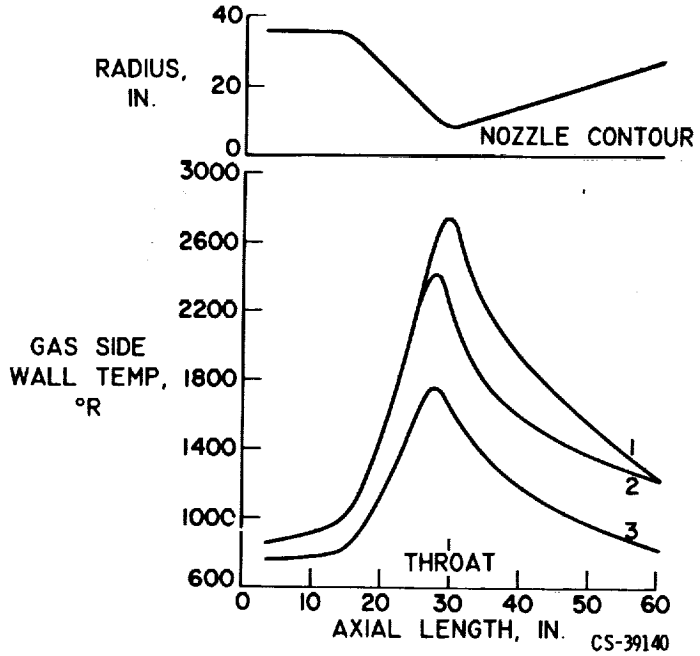

Figure III-10. - Coolant passage gas side wall temperatures.

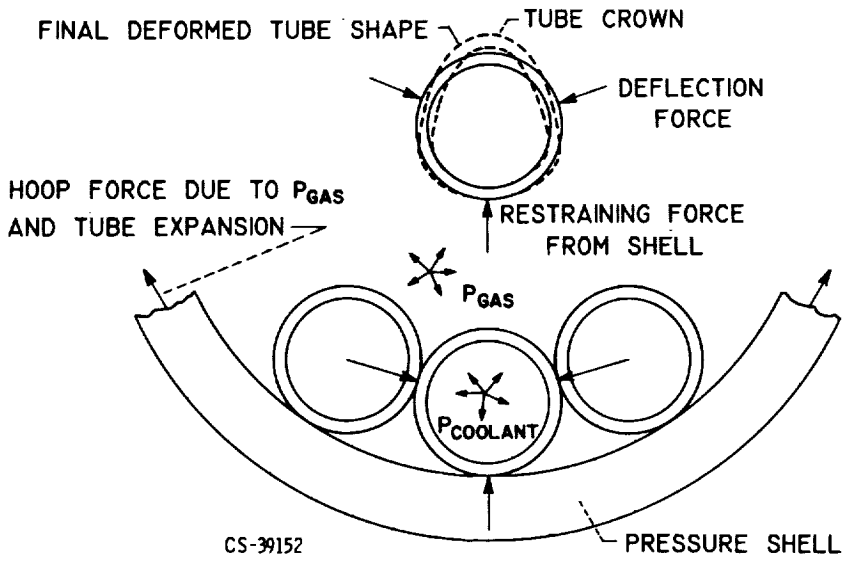

Figure III-11. - Mechanics of tube deformation.

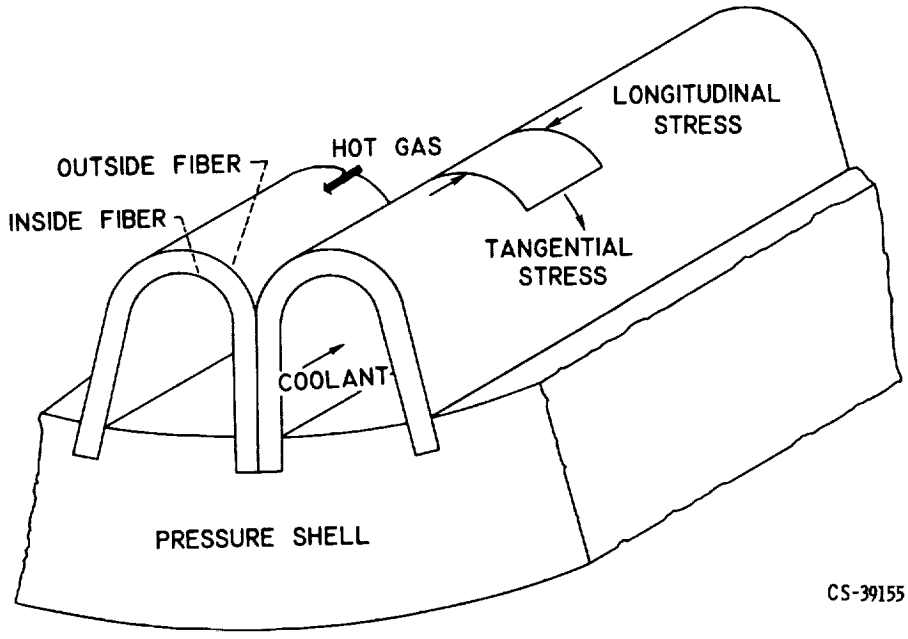

Figure III-12. - Orientation of coolant passage wall stresses.

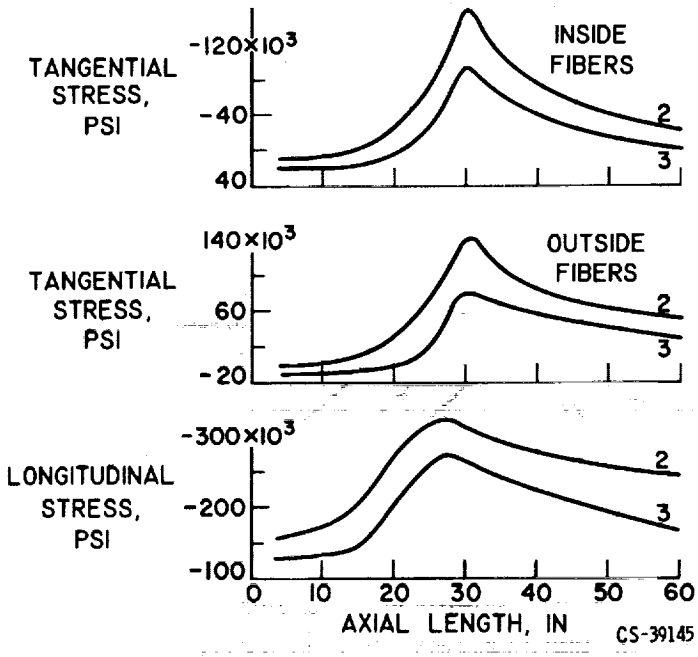

Figure III-13. - Coolant passage stresses.

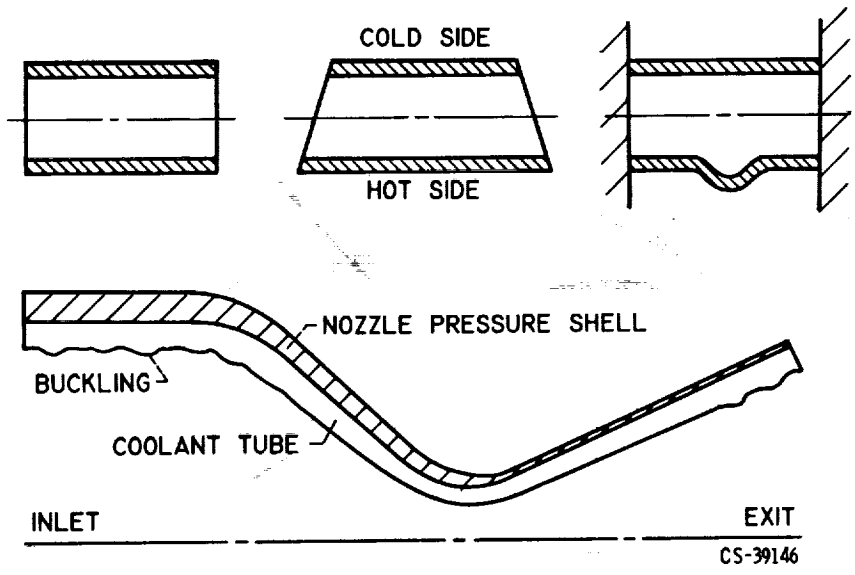

Figure III-14. - Tube buckling.

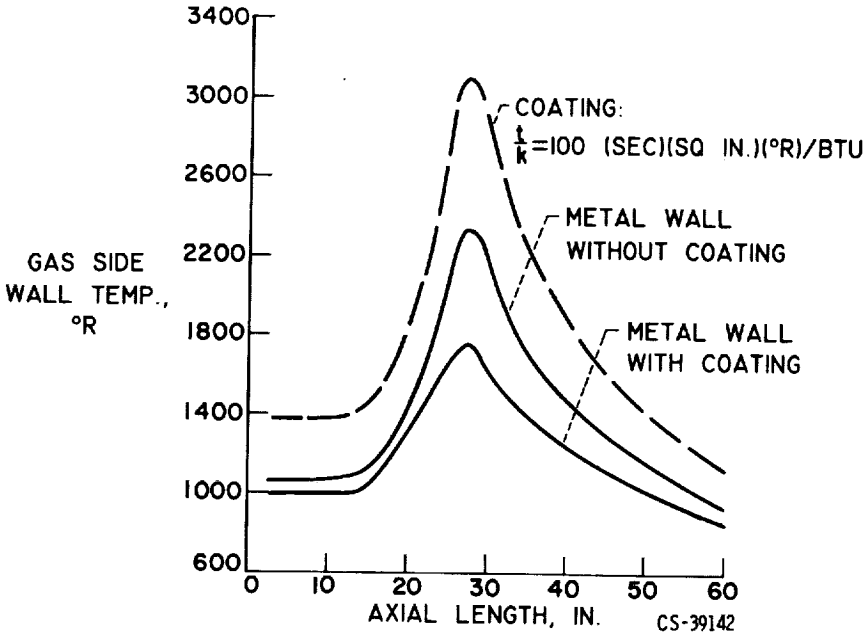

Figure III-15. - Effect of coating on gas side wall temperatures.

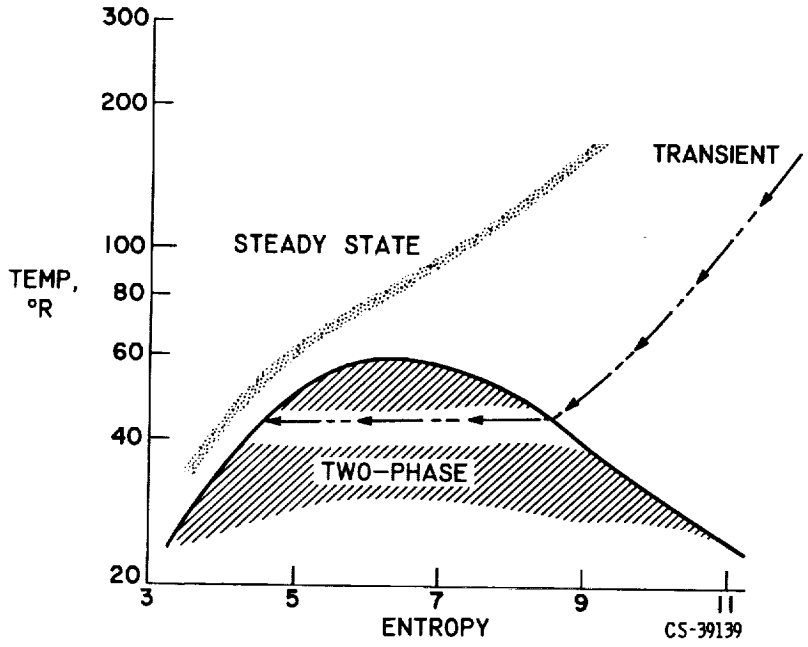

Figure III-16. - Hydrogen state at nozzle coolant inlet during startup.

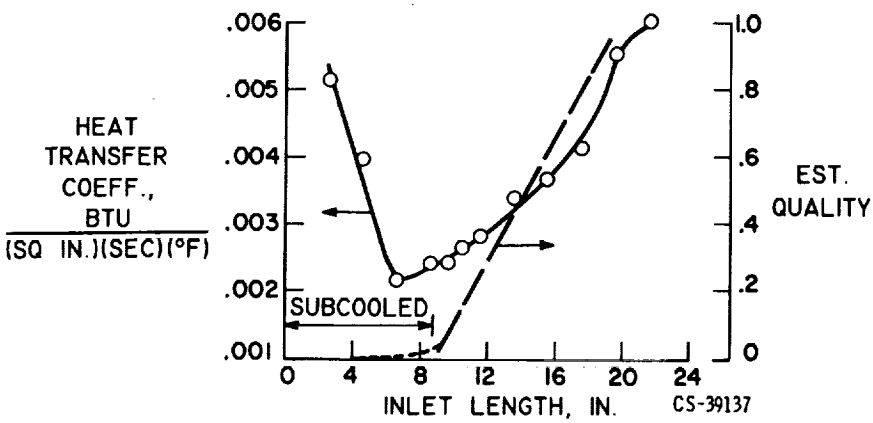

Figure III-17. - Convective film boiling of hydrogen with subcooled inlet. Uniform heat flux, 1.08 Btu/(in.^{2})(sec); inlet temperature, 49.2° R; inside diameter, 0.335 inch.

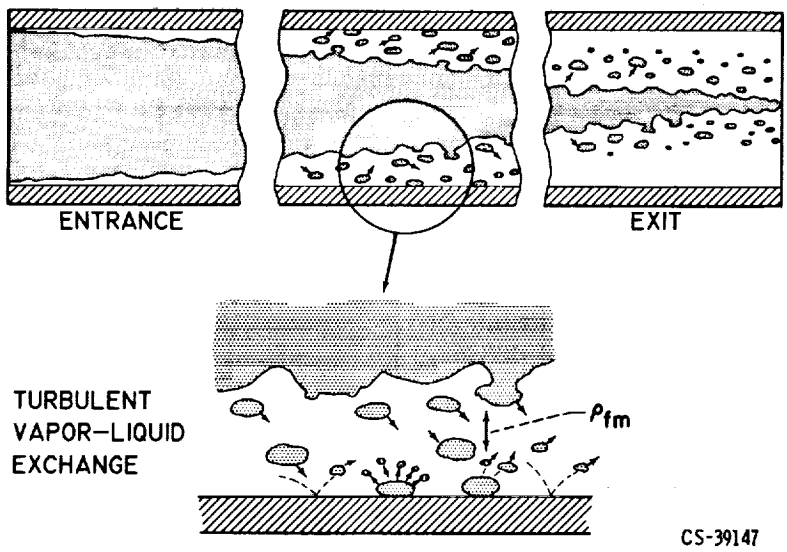

Figure III-18. - Concept of two-phase hydrogen flow model.

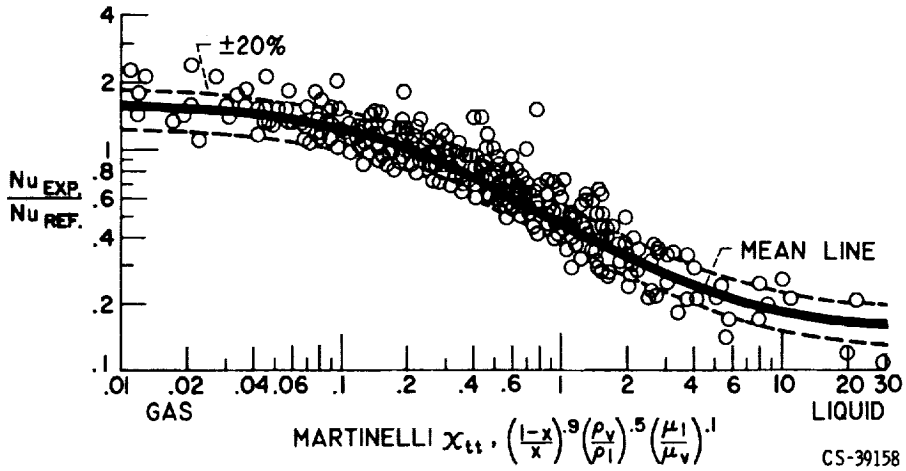

Figure III-19. - Convective film boiling of liquid hydrogen.

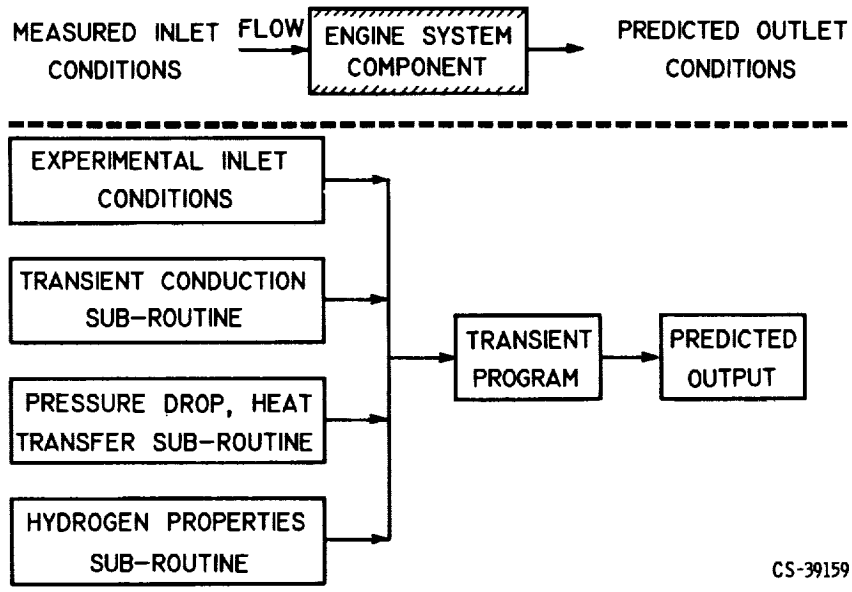

Figure III-20. - Description of prediction technique.

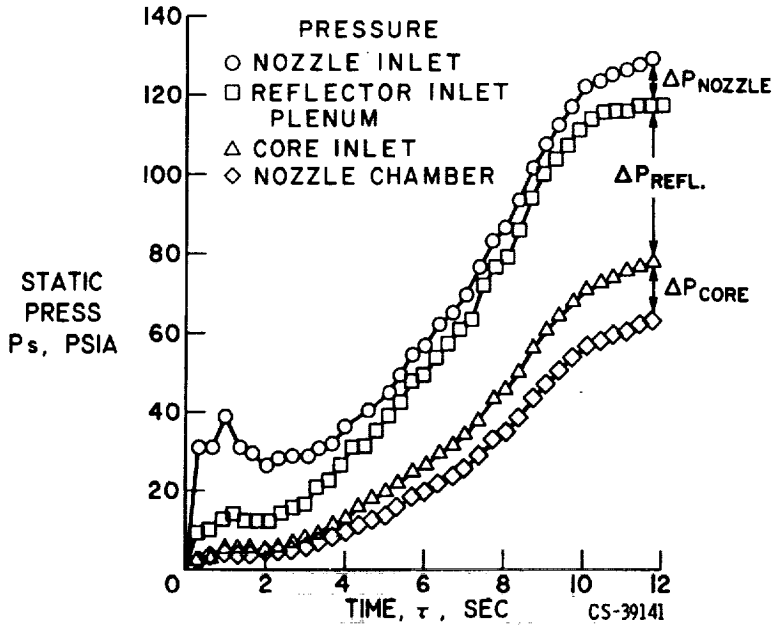

Figure III-21. - Experimental pressures against time at four major stations in engine system.

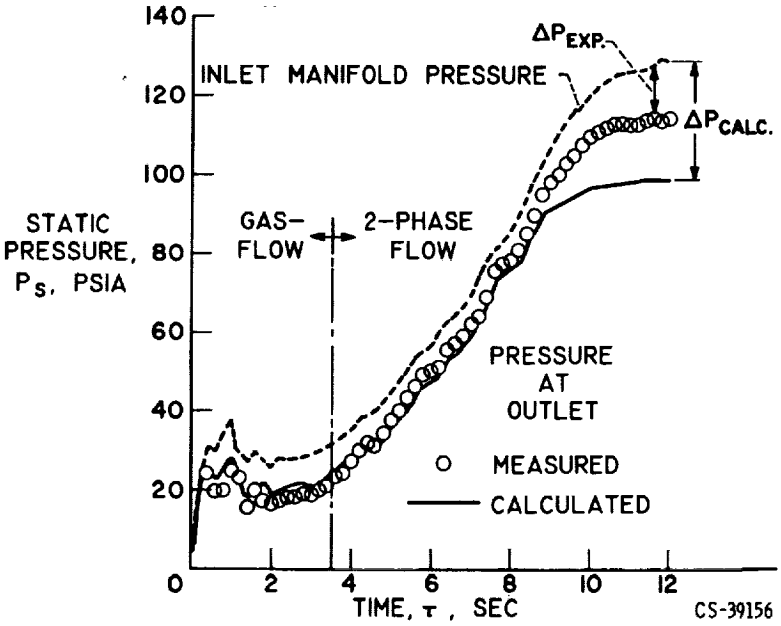

Figure III-22. - Measured and calculated static pressures at nozzle coolant tube outlet.

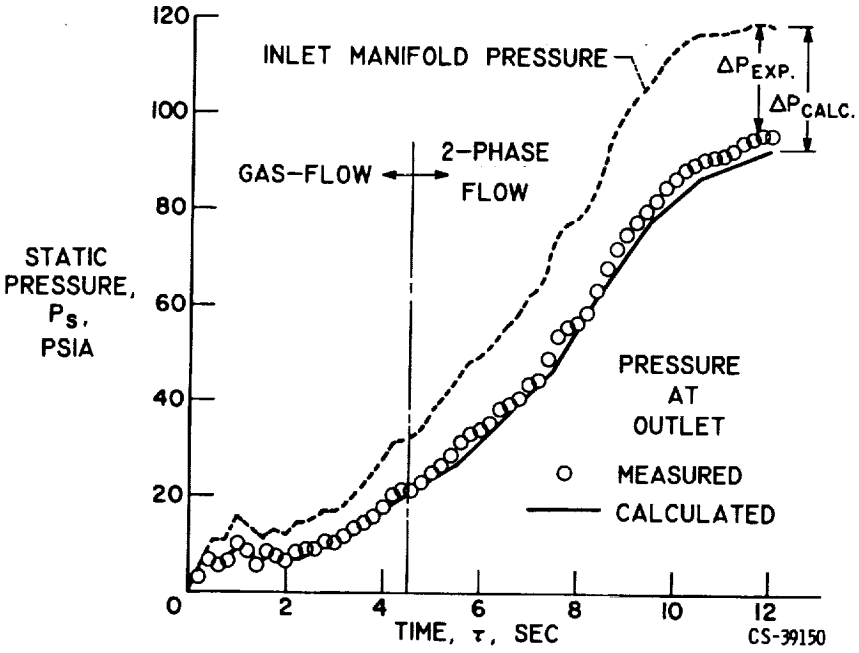

Figure III-23. - Measured and calculated pressures at reflector outlet.

X66-51410

IV. STARTUP DYNAMICS AND CONTROL*

Herbert J. Heppler, Jr., Benjamin H. Colmery,
James J. Watt, and Vernon D. Gebben

Various components of nuclear rockets are discussed in the paper on PROPELLANT FLOW SYSTEM COMPONENTS and the paper on HEAT TRANSFER AND FLUID MECHANICS. A useful propulsion system requires the integration of these components into a single entity whose operation is harmonious and controllable. Some of the Lewis efforts in system investigations and control development are presented in this paper. Specific attention is given to flow system startup characteristics and two-phase hydrogen flow characteristics. In the controls area, the application of pneumatic components, or fluidic devices, is discussed.

NUCLEAR-ROCKET COLD-FLOW STARTUP

Benjamin H. Colmery

INTRODUCTION

A nuclear-rocket engine in space probably will use no special startup equipment; it will rely on a "bootstrap" technique starting procedure. Run-tank pressure drives hydrogen propellents through the flow system. The liquid hydrogen acquires heat from the engine components, and a portion of the heated hydrogen is bled to the turbine. This bleed gas powers the turbine, which in turn accelerates the pump increasing the flow and pressure through the system. Successful bootstrap results in a continuous increase of system flow and pressure.

The bootstrap technique has been used successfully to start chemical-rocket engines, but there are significant differences in the nuclear-engine bootstrap. One difference is the much longer time for the nuclear rocket to be brought to power. Also, all the propellant is utilized, and it follows a more complex hydrogen flow path in the nuclear rocket. These factors coupled with the lack of precise knowledge of two-phase hydrogen flow and boiling phenomena caused concern as to whether unacceptable flow perturbations might

occur during bootstrap startup. Further, there was uncertainty as to whether enough energy could be delivered to the turbine at low pump speeds to cause flow acceleration. Also, there was the usual question of unanticipated problems in new hardware.

Therefore, a full-scale test of the bootstrap startup of a nuclear-rocket engine was undertaken - the first such test ever made. The Nuclear-Rocket Cold-Flow Test Facility used (fig. IV-1) is located at the Plum Brook Station of the Lewis Research Center. The altitude exhaust system shown enabled maintaining a rocket-nozzle-exhaust pressure of nominally 0.5 pound per square inch absolute throughout each run. The rocket engine was mounted in the 130-foot-tall structure at the right in a down-firing position.

SYMBOLS

A	cross-sectional flow area, ft^2
A_{ht}	heat-transfer area, ft^2
C_p	specific heat of wall material, $Btu/(lb)(^oR)$
d	diameter of flow passage, ft
g	acceleration of gravity, ft/sec^2
H	heat-transfer coefficient, $Btu/(ft^2)(^oR)(sec)$
h	fluid enthalpy, Btu/lb
I	turbopump moment of inertia, (ft-lb)(sec)/rpm
K	loss coefficient
K_n	choked-nozzle flow coefficient, $(ft^2)(^oR)^{1/2}/sec$
k	fluid thermal conductivity, $Btu/(ft)(^oR)(sec)$
L_p	pump torque, ft-lb
L_t	turbine torque, ft-lb
M	mass of wall material, lb
N	turbopump speed, rpm
P	fluid pressure, lb/ft^2
ΔP	component pressure drop, lb/ft^2
Pr	fluid Prandtl number
P_{nc}	nozzle chamber pressure, lb/ft^2
ΔP_p	pump pressure rise, lb/ft^2

P_{ti}	turbine-inlet fluid pressure, lb/ft^2
P_{to}	turbine-outlet fluid pressure, lb/ft^2
Q	heat addition from surroundings, Btu
R	gas constant, $ft/^oR$
Re	fluid Reynolds number
T	fluid bulk temperature, ^oR
T_{nc}	nozzle chamber temperature, ^oR
T_s	saturated-fluid bulk temperature, ^oR
T_{ti}	turbine-inlet fluid bulk temperature, ^oR
T_w	wall temperature, ^oR
t	time, sec
V	volume of lump, ft^3
W	weight flow, lb/sec
ΔW	empirical weight flow storage, lb/ft^2
W_n	nozzle flow, lb/sec
W_p	pump weight flow, lb/sec
W_t	turbine weight flow, lb/sec
ΔX	length of lump, ft
ρ	fluid density, lb/ft^3

SYSTEM DESCRIPTION

A schematic diagram of the rocket-engine test package is shown in figure IV-2, and a photograph of some of the hardware is shown in figure IV-3. The test hardware consisted of a turbopump assembly, unfueled reactor, and a supersonic exhaust nozzle. The liquid-hydrogen run tank, which feeds the pump, has a capacity of 2000 gallons and has a servo-controlled pressurizing system. An 8-inch-diameter line, which is equipped with a turbine-type flowmeter, connects the pump to the run tank.

The turbopump assembly consisted of a Rocketdyne MARK-IX turbopump, turbine-power-control valve, and turbine bleed line. The liquid-hydrogen pump is composed of an axial-entrance mixed-flow axial-discharge inducer stage, six identical high-pressure axial-flow stages, and a single-outlet collecting volute. The pump is designed for opera-

tion with liquid hydrogen and is capable of providing the flow rate and pressure requirements of a NERVA type engine.

The turbine is a six-stage pressure-compounded axial-flow unit designed for operation with hot or ambient temperature gaseous hydrogen. The unit was designed to deliver 15 000 horsepower and is capable of deliverying NERVA power requirements with ambient temperature hydrogen.

The pump discharges into a 4-inch-diameter stainless-steel flight-weight feed line equipped with a servocontrolled butterfly valve used for flow control. Approximately 18 feet downstream from the main flow-control valve, the propellant line is divided equally into three $2\frac{3}{8}$-inch-diameter ducts that feed the nozzle inlet manifold.

The regeneratively cooled (liquid hydrogen) tubular-wall nozzle utilizes single-pass cooling. The liquid hydrogen enters the tubes through three equally spaced inlet connections on the manifold and flows toward the reactor end.

On discharging from the nozzle coolant tubes, the fluid enters the reflector inlet manifold section of the reactor assembly. From there it passes through the reflector component that is composed of the inner graphite reflector, an outer aluminum reflector, simulated aluminum control rods, and the aluminum pressure vessel. The fluid then enters the reactor core; flowing through the many parallel coolant passages in the unloaded graphite reactor core.

The warm hydrogen emerges from the core into the regeneratively cooled nozzle thrust chamber where most of it is exhausted into the facility vacuum exhaust (0.5 psia). A small portion of the fluid, however, is bled by a 3-inch-diameter bleed port, turbine-gas bleed line, and servocontrolled turbine-power-control valve, to the turbine. Altogether, the rocket-engine system tested was a full-scale model of what might have been a flight version of a system using the Kiwi B-1 reactor.

One objective of this startup program was to determine the bootstrap capability of the nuclear-rocket engine for a range of tank pressures and the influence of two-phase flow and pump stall on the startup. A second objective was to develop an analytical technique that would dynamically simulate the startup and be useful as a general tool to predict startup characteristics.

EXPERIMENT PROCEDURES

Two kinds of experimental runs were undertaken: cooldown and bootstrap. The cooldown tests were undertaken to examine the problems of boiling and two-phase flow. In these runs, the pump was chilled to liquid-hydrogen temperatures. Then, at zero run time, the pump-discharge valve (fig. IV-2) was opened, and run-tank pressure forced flow through the system to the facility vacuum exhaust. The run was continued until the

engine components had cooled and flow had stabilized. Unlike later bootstrap tests, the turbine-power control valve was kept closed throughout the cooldown run. Hence, it was possible to examine the two-phase flow and boiling instabilities without the additional complications of turbopump-load interactions and the dynamics associated with a rapid increase in flow and pressure. Ten cooldown runs were made with run tank pressures of 25, 35, and 50 pounds per square inch absolute.

In the bootstrap runs, the pump was chilled to liquid-hydrogen temperatures, and at zero time, the pump-discharge valve was opened and flow was established in the system. The turbine-power-control valve was opened at run times varying from 0 to 10 seconds and was controlled by various schemes to maintain desired pump acceleration. The run was continued, generally, until peak values of pump speed, weight flow, and pump pressure rise had been achieved. To date, 15 bootstrap runs have been made.

RESULTS AND DISCUSSIONS

Cooldown Tests

Three cooldown tests corresponding to run-tank pressures of 25, 35, and 50 pounds per square inch absolute are shown in figure IV-4. The time history of the static pressure at the nozzle coolant inlet shows two types of oscillations. There is an initial transient with a nominal disturbance frequency of about 2 cps, which is called initial surge. A second mode of oscillation, called two-phase-flow perturbations, follows with an initial frequency of about 15 cps.

The initial surge was an expected phenomenon. Undoubtedly, it is the result of the introduction of liquid hydrogen at cryogenic temperature into a pipe at ambient room temperature. When the hydrogen flashes into vapor it produces the pressure surge. The phenomenon occurred as soon as the pump-discharge valve was opened, and it died away in about 2 seconds. It originated in the lower part of the pump-discharge line as a pressure disturbance; this disturbance proceeded upstream and downstream from the point of origin and was closely followed by corresponding changes in hydrogen weight flow and fluid temperature. The initial surge, which occurred on both the cooldown and the bootstrap runs, died away with an oscillation frequency of about 2 cps. The initial surge was the largest flow-system perturbation encountered.

Normalized peak surge amplitude is plotted against run-tank pressure in figure IV-5. The initial peak pressure is sensitive to run-tank pressure with the higher tank pressures attenuating the pressure surge. Also shown in the figure is an unexpected effect - an apparent dependence on the weight of the pump-discharge-line flanges and gimbals, as indicated by the two curves.

The flanges and gimbals on the pump-discharge line were changed after the first 12 test runs. Boiler-plate-weight flanges (about 31 lb each) were replaced by flight-weight flanges (about 3 lb each), and lighter gimbals were used. The replacement hardware was made of the same materials as the old. The internal dimensions and finish specifications were unchanged, and the piping was not changed - only the flange and gimbal mass were changed. Prior computations and intuition indicate that the smaller heat capacity of the smaller mass should have negligible effect on heat transfer in the pump-discharge line during the first few seconds of hydrogen flow; hence, it was anticipated that the change in mass would not affect the amplitude of the initial surge.

A possible explanation of the existence of two curves in figure IV-5 is the effect of vibration on the heat-transfer coefficient for fluid flow in a pipe. Literature exists on the interaction between vibration and heat transfer which indicates that lateral oscillations of a pipe containing flowing hydrogen substantially augment the heat-transfer process under some conditions (ref. 1, p. 133). The pipe with the lighter flanges could vibrate with higher lateral velocities. The largest velocities would result sequentially in more fluid turbulence, larger heat transfer, a larger rate of vaporization of liquid hydrogen, hence, a larger pressure surge.

Because the phenomenon was unexpected, the pump-discharge line had not been instrumented for vibration. Hence, verification of the foregoing hypothesis has not yet been made.

The second kind of disturbance (fig. IV-4), termed two-phase-flow perturbation, commenced about 2 seconds after flow initiation. The two-phase-flow perturbations were found to originate as pressure disturbances, and these pressure disturbances were transmitted upstream and downstream from the point of origin.

The pressure disturbances were accompanied by flow and temperature changes. The flow changes occurred out of phase with the pressure disturbances. Temperature variations of the fluid were observed at a given point until the hydrogen temperature reached saturated liquid temperatures at that point; subsequently, flow and pressure disturbances continued, but temperature oscillations were no longer apparent.

As shown in figure IV-4, the amplitude of oscillations appears unaffected by run-tank pressure, but the duration of the oscillation is shortened with higher tank pressure.

Bootstrap Capability

Results of a typical controlled bootstrap run are shown in figure IV-6. The upper curve shows the pump operating map. The pump stall line is depicted as a band, because of hysteresis effects of entering and leaving stall, and because of uncertainties in the precise location of the stall line at low pump speeds. The lower curve shows pump speed as

a function of time. Points A and B in both figures correspond to the same points in time. This test run is termed controlled because a closed-loop control system was used to maintain a desired rate of pump acceleration.

Events in the run occurred as follows: At zero time, the pump metal had been chilled to liquid-hydrogen temperature and the pump-discharge valve was opened. As flow was initiated, there were sharp pressure surges in the regions downstream of the pump-discharge valve. The surges were followed by rapid pressure oscillations at a frequency of about 15 cps, similar to those obtained in the cooldown runs. These oscillations have been omitted during the first 6 seconds of the run in the upper curve of figure IV-6. The pump initially windmilled to point A because of the liquid hydrogen flowing through it, forced by tank pressure.

At 6 seconds, point A, the turbine-power-control valve was opened and commanded to achieve a pump acceleration of 200 rpm per second. It can be seen in the lower curve of figure IV-6 that this acceleration was quickly achieved and held smoothly. In the upper curve (fig. IV-6) buildup of pump pressure rise and of hydrogen flow occurred. There were pressure and flow disturbances, but they were small. The operating point skirted the stall region, reached an operating peak in flow and speed at about point B, and then faded back to the origin.

The peak at point B occurred because the turbine-inlet fluid energy became insufficient to continue accelerating the turbopump. This fluid energy, acquired from the latent heat energy of the engine components, decreases as the system cools. In an actual flight startup, nuclear power would have become the dominant energy source somewhere between times A and B, and the bootstrap acceleration would have continued to the desired system operating point.

Figure IV-7 shows data from a typical uncontrolled bootstrap test plotted on the pump operating map. This run is called an uncontrolled run because both the pump-discharge valve and the turbine-power-control valve were opened fully at zero run time and kept fully open until the end of the run. This uncontrolled bootstrap gave the fastest increase in pump speed, flow, and pressure, and it also gave the largest flow disturbances. Initially, there were rapid appreciable variations in flow and pressure. The pump windmilled for a few seconds until adequate power arrived at the turbine to cause it to accelerate. Then there was a rapid buildup of pump speed, pressure, and flow.

The initial flow and pressure disturbances were damped during the bootstrap acceleration. The pump entered the stall region. Flow and pressure oscillations were observed that continued until the pump left the stall region. Nevertheless, bootstrap continued, and the pump acceleration was nearly constant at 1150 rpm per second. Maximum values for pump speed, pressure rise, and flow (10 000 rpm, 100 psi, and 30 lb/sec, respectively) were achieved in about 12 seconds; these are appreciable values of the rated Kiwi B-1 operating point.

The tests described by figures IV-6 and IV-7 show that, neglecting weightlessness and the complications introduced by nuclear operations, a bootstrap start could be accomplished. They show that appreciable values of pump speed, liquid-hydrogen flow, and pump pressure rise could be achieved by using latent heat of the engine components (at ambient atmospheric temperatures), and that peak values could be built up in as little as 12 seconds.

In tests not illustrated, it was also shown that bootstrap runs could be successfully accomplished at a run-tank pressure of 25 pounds per square inch absolute. The lower the run-tank pressure, the lower the overall tank weight; hence, insofar as the bootstrap operation is concerned, it appears that lighter weight tanks might be used.

Operational Problems

Several system and equipment operating problems were encountered during the runs, and an interesting one is shown in figure IV-8. The interest arises because of the erroneous appearance that the severe oscillations were simply a result of the system operating point being accelerated into the pump stall region. In fact, the oscillations were the result of gas ingestion.

The axial pump used counteracts axial thrust with a balance piston. A bleed line from the region of the balance piston had been installed to empty upstream of the pump inlet. In posttest analysis, it was found that during cooldown, a check valve prevented the bleed line from being fully chilled to liquid-hydrogen temperature. Hence, when the pump acceleration occurred, the bleed line discharged gas rather than liquid into the pump inlet.

The bleed line was modified to enable complete cooling, and the run of figure IV-8 was repeated under otherwise identical conditions. The result is shown in figure IV-9. It is clear that removal of the bleed-line heat source removed the oscillations. The two figures also illustrate what might happen if gas were entrained in the liquid that leaves the run tank during bootstrap.

Other operational problems encountered were straightforward, correctable ones involving cryogenic temperatures or random equipment malfunctions.

Analytical Simulation

The goal of an analytical effort at Lewis has been to develop a mathematical model to simulate the nuclear-rocket-engine startup. The system was studied by dividing the model into spacial lumps, each representing a specific hardware component of the research

apparatus shown in figure IV-2. These lumps can then be grouped, as in figure IV-10, into a system block diagram composed of a pump, feed line, nozzle coolant tubes, reflector, core, thrust nozzle, turbine bleed line, turbine-power-control valve, and turbine. The lumping was done in this manner to take advantage of system geometry and data probe locations and also to limit the amount of necessary analog computing equipment.

The state of the fluid varies throughout the system during the course of a run. With liquid hydrogen flowing into the system, the material of the components begins to cool by giving up latent heat to the fluid. Throughout every experimental run, it was observed that a definite, but changing, portion of the system contained two-phase fluid. The preceding portion was all liquid, while the remaining portion downstream was all gas, as illustrated in figure IV-11. As the run proceeded and the system cooled, the two-phase section moved downstream.

During the time of simulation, the range of the fluid state was specified for each lump; all liquid in the pump, the possibility of liquid, two phase, or gas between the feed line inlet and the reflector exit, and all gas throughout the balance of the system.

The differential equations describing each lump were written and then programmed on the analog computer. For purposes of presenting the system equations, they can be grouped into those pertaining to the turbopump assembly and those concerning the load.

Turbopump Assembly

As stated earlier, the turbopump is a MARK-IX axial-flow liquid-hydrogen pump and six-stage turbine. This unit is described by the following equations:

$$\Delta P_p = N^2 f_1\left(\frac{W_p}{N}\right) \tag{1}$$

$$L_p = N^2 f_2\left(\frac{W_p}{N}\right) \tag{2}$$

$$\frac{dN}{dt} = \frac{30}{\pi I}\left(L_t - L_p\right) \tag{3}$$

$$L_t = W_t f_3\left(N, T_{ti}, \frac{P_{to}}{P_{ti}}\right) \tag{4}$$

$$W_t = \frac{P_{ti}\left[1 - \left(\frac{P_{to}}{P_{ti}}\right)^2\right]}{T_{ti}} f_4 \frac{N}{\sqrt{T_{ti}}} \tag{5}$$

Equations (1) and (2), the pump-head-rise and torque-characteristic equations, respectively, are empirically derived from the manufacturer's rated speed operating data and from experimental low-speed data. The balance of the equations was generated from a more theoretical basis, namely, from torque and momentum considerations.

As stated earlier, the turbine is powered by a controlled flow of gas that is fed through the turbine bleed line from the nozzle thrust chamber. The representation for this bleed line is adequately described by the all-gas-lump equations presented in the following section.

Load

The load segment of the model was broken into five major spacial lumps: feed line, nozzle coolant tubes, reflector, core, and thrust nozzle. In general, the equations for each lump are as follows: the conservation of fluid mass, the conservation of fluid momentum, the conservation of fluid energy, the conservation of thermal energy of the material parts, Newton's law of cooling, and the fluid state properties. The written forms of these equations are, respectively,

$$\frac{dR}{dt} = \frac{1}{V}\left(W_{in} - W_{out}\right) \tag{6}$$

$$\frac{dW}{dt} = \frac{gA}{\Delta X}\left(P_{in} - P_{out}\right) - \frac{K}{2V}\frac{W^2}{\rho} - \frac{1}{V}\left(\frac{W_{out}^2}{\rho_{out}} - \frac{W_{in}^2}{\rho_{in}}\right) \tag{7}$$

$$\frac{dh}{dt} = \frac{1}{\rho V}\left[\frac{dQ}{dt} - W\left(h_{out} - h_{in}\right)\right] \tag{8}$$

$$\frac{dT_w}{dt} = -\left(MC_p\right)^{-1}\frac{dQ}{dt} \tag{9}$$

$$\frac{dQ}{dt} = HA_{ht}\left(T_w - T\right) \tag{10}$$

$$P = f_5(\rho, h) \tag{11}$$

$$T = f_6(p, h) \tag{12}$$

For an all-gas lump, the general equations (6) to (12) apply directly with the following qualifications: First, the fluid temperature (eq. (12)) was assumed to be a function only of the fluid enthalpy. Second, the pressure relation (eq. (11)) was modified into the more conventional gas law:

$$P = R\rho T \tag{13}$$

And finally, the heat-transfer coefficient used in equation (10) was

$$H = 0.021\frac{k}{d}\,Pr^{0.33}Re^{0.8}\left(\frac{T}{T_w}\right)^{0.575} \tag{14}$$

For an all-liquid lump, the general equations (6) to (12) also apply directly, if the appropriate heat-transfer coefficient is assumed. In addition, the fluid-temperature state equation (eq. (12)) can be simplified if saturated liquid hydrogen is assumed:

$$T = f_7(P) = T_s \tag{15}$$

Theoretically, the general equations (6) to (12) could be used for a two-phase lump if homogeneous flow and thermodynamic equilibrium between the phases are assumed. A pressure state relation (eq. (11)) has been derived from existing two-phase-properties tables, and the fluid-temperature state would be that of saturated liquid hydrogen (eq. (15)). Because of the complexities and uncertainties in arriving at a two-phase pressure loss coefficient K and a two-phase heat-transfer coefficient H, experimental data were used to modify empirically the momentum equation (eq. (7)) and the heat-transfer equation (eq. (10)). In the case of the heat-transfer relation, a correlation of the form in figure IV-12 was derived from experimental data and found to be an adequate representation for the overall average heat transfer in a two-phase lump.

However, in an analog simulation employing these two-phase equations, the fluid-pressure relation (eq. (11)) proved to be too cumbersome for practical use. Therefore, a more convenient form of the state relation, one relating the two-phase density to the

pressure and enthalpy (eq. (16)), was used. Unfortunately, the utilization of this equation necessitated alternate forms for the conservation equations of mass and momentum (eqs. (6) and (7)) The modified equations are as follows:

$$\rho = f_8(h, P) \tag{16}$$

$$W_{out} = W_{in} - \Delta W \tag{17}$$

$$\Delta P = \frac{\Delta X}{gA}\left[\frac{K}{2V}\frac{W^2}{\rho} + \frac{1}{V}\left(\frac{W_{out}^2}{\rho_{out}} - \frac{W_{in}^2}{\rho_{in}}\right)\right] \tag{18}$$

Note the missing derivatives of density and weight flow in equations (17) and (18), respectively. The lack of a convenient expression relating pressure to a function of density and enthalpy forced dropping these derivatives. In turn, the flow dynamics that are characteristic of the two-phase lump were thus removed. Detailed investigation has shown that this two-phase dynamic response is a necessary factor in determining low-frequency system dynamics. Hence, the model as presented herein must be considered a quasi-steady-state simulation.

Thus, the system load consists of a thrust nozzle plus four lumps, modeled after the gas described previously, liquid, or two-phase representations. Within a fraction of a second after flow initiation, the gas side of the nuclear-rocket nozzle may be considered choked at the throat. The choked, isentropic nozzle weight flow is given by

$$W_n = K_n \frac{P_{nc}}{\sqrt{T_{nc}}} \tag{19}$$

Simulation of the previously discussed controlled and uncontrolled bootstrap tests are presented in figures IV-13 to IV-16. In the first case, the pump speed was controlled in such a manner that the pump stall was avoided, while in the second case, the system was accelerated in an uncontrolled manner with no attempt made to avoid the stall region.

For the controlled bootstrap tests, after a 6-second period of pump windmilling, the turbine-power-control valve was opened and bootstrapping commenced. There were initial flow oscillations but they were damped out as bootstrapping proceeded. The system operating point steadily increased to a maximum pump pressure rise.

The simulation was initiated 5 seconds after the start of the experimental run because of the range limitations of the analog computer. Most of the initial oscillations had died out by 5 seconds; those remaining, however, could not be duplicated by the model because

of the missing two-phase dynamic terms. The steady-state level approximated the pump map data (fig. IV-13) and the parameter-time data (fig. IV-14); the simulated pump correctly operated out of the stall region during the entire computer run.

The second run was an uncontrolled bootstrap test. It was uncontrolled because the turbine-power-control valve was opened fully at the beginning of the test and kept fully open until the end. The initial flow oscillations were once again damped out as bootstrapping commenced. Stall-induced flow oscillations were observed during a portion of the run as the system bootstrapped through stall to a maximum pump pressure rise and weight flow.

The simulation of the second test began 3 seconds after the actual experimental system startup. The simulated pump entered and operated in the stall region, but the analytical model was unable to produce the stall-induced flow oscillations, as indicated in figure IV-15. The parameter-time data is presented in figure IV-16.

For both tests, the model matched the experimental data for most parameters to within 10 to 25 percent of the measured quantities. The only exceptions to this are the turbine weight flow and certain other parameters that disagreed in the initial low level portions of the runs.

CONCLUSIONS

The conclusions drawn from the experimental bootstrap startup operations conducted to date have the qualifications that nuclear operations and weightlessness were not included, and that there are a number of boiling and two-phase-flow phenomena that still are not explained. With these qualifications, it can be stated that

1. The bootstrap operation was performed successfully. Appreciable percentages of the rated operating conditions of system flow rate, pressures, and pump speed were achieved.

2. Bootstrap was accomplished successfully at a run-tank pressure of 25 pounds per square inch absolute; this may have important implications on run-tank weight.

3. Flow disturbances encountered would not cause concern about the practicability of a nuclear bootstrap startup on a flight mission.

A quasi-steady-state model has been developed to simulate a nuclear-rocket cold-flow system. In general, the experimental data were matched to within 10 to 25 percent of the measured values . The effort demonstrated that a complex system, such as a nuclear-rocket engine, may be simulated with a fairly simple model. It has demonstrated the necessity for including two-phase flow dynamics. The quasi-steady-state model paves the way for more detailed studies in the areas of two-phase flow dynamics, heat transfer, and friction pressure drop.

ANALYSIS OF HYDROGEN FLOW CHARACTERISTICS AT SUBCRITICAL PRESSURES

James J. Watt

INTRODUCTION

Some highlights from a program conducted at Lewis to provide support for the development of the nuclear rocket in the area of component heat-transfer and flow analysis are described. Only two phases of the reactor operating spectrum were considered, the startup and after-cooling phases, both of which involve hydrogen at subcritical pressure.

TRANSIENT ANALYSIS

For startup analysis, the two-phase and gas flow regions were considered. Correlations for local heat transfer and pressure drop were included in a transient-analysis procedure. The purpose of the procedure is to predict as a function of time in a given engine component the following conditions: fluid pressure and temperature profiles along the length, depth of two-phase penetration, wall temperature profiles both axially and longitudinally, and flow distribution when parallel passage components were considered. Input to this transient procedure included the geometry and material properties of the component and the initial distribution of material temperatures. Input provided as a function of time during the transient were the flow rate, inlet fluid pressure, and inlet enthalpy. A quasi-steady-state approach was used in flow analysis, that is, flow and heat-transfer conditions were defined periodically during the transient, and the changes in material temperature were calculated on the interval between flow calculations.

Chilldown experiments were performed on single and multiple channel test sections that simulated conditions in the reactor components during the startup transient. Liquid hydrogen flowing from a pressurized supply tank was introduced into test sections initially at room temperature. Flow continued until the test section was chilled to near liquid hydrogen temperature. Figures IV-17 to IV-19 are photographs of three test sections used in chilldown experiments. A single tube 55 inches long with a 0.75-inch outside diameter and a 0.188-inch inside diameter is shown in figure IV-17. A five-passage test section is shown in figure IV-18, and a 33-passage test section representing 1/24 of a nuclear-rocket reflector annulus is shown in figure IV-19. Tests were performed in an evacuated enclosure to reduce the convective heat transfer from the outer surfaces of the test sections.

The experimental flow rate and test-section-inlet conditions along with the initial

material temperature distribution were then used as input to the transient-analysis procedure. The usefulness of this procedure was then evaluated by comparison of predicted and experimental results.

The results of some of the earlier experiments are included in reference 2 (p. 133). The results of applying the transient-analysis procedure to the reflector during the full-scale nuclear-rocket bootstrap startup tests performed at the Lewis Plum Brook Station are presented in paper III. A more complete description of the transient-analysis procedure and a comparison of its predictions with experimental results obtained from chilldown experiments on a single tube (fig. IV-17) are the subject of a current investigation (unpublished data obtained by F. C. Chenowith, J. J. Watt, and E. L. Sprague of Lewis).

A comparison of single-tube chilldown experimental results with predictions illustrates the current status of transient analysis. The measured wall temperatures along the length of the test section are indicated at 3.0, 8.0, and 13.0 seconds during a chilldown run in figure IV-20. The solid lines are the predicted temperature profiles. Before zero time, the test section had a nearly constant wall temperature of 522° R. At zero time, liquid-hydrogen flow was started into the test section. The thin-walled 3-inch-long dip tube at the inlet chilled rapidly. Because there was no temperature instrumentation until the 7-inch station, the accuracy of prediction in this region cannot be evaluated. There is a dip in the predicted wall-temperature profile that occurs at the point of transition from two phase to all gas in the flow passage. The length at which this transition occurred is indicated by the dashed veritical lines for each time. The tip or disparity in predicted wall temperature increases in both amplitude and length with time. Further into the all-gas region, it may be noted that good agreement between predicted and experimental wall temperatures was obtained.

The reason for the dip in predicted wall temperatures is indicated in figure IV-21, where the heat-transfer coefficients predicted by the two-phase and gas correlations 11.0 seconds after the start of a chilldown run are plotted. Heat is being transferred from the wall to a two-phase fluid for the first 13 inches and to a gas for the remainder of the passage. As shown in figures IV-20 and IV-21, the peak heat-transfer coefficient occurring near the end of the two-phase region causes the dip in predicted wall temperatures, and the decrease in heat-transfer coefficient at the transition to gas (38 percent, in this case) causes the sharp increase in wall temperature. The minimum of the dip lags the two-phase to gas transition point because of time history effects as the two phase penetrates progressively further into the passage during the chilldown

These disparities occur in a region that requires a research effort. The two-phase correlation used (ref. 3, p. 133) was based on an experimental effort that considered qualities less than 0.8. The gas correlation (ref. 4, p. 133) was based on experiments performed with bulk temperature far removed from saturation temperatures. The disparity, therefore, occurs at the intersection of two extrapolated correlations.

Heated-tube experiments performed with hydrogen gas at temperatures near saturation temperature (unpublished data obtained by H. J. Gladden and J. J. Watt of Lewis) have indicated that there is a bulk temperature effect on gas heat transfer. These experiments also indicated a strong increase in heat-transfer coefficient near the entrance of a passage when velocity and temperature profiles develop concurrently.

In summary, the transient-analysis procedure is a useful tool for predicting the general characteristics of flow and heat transfer in passages that contain boiling hydrogen. There are local limitations because conditions occur where current correlations for heat transfer are not directly applicable. These limitations become significant if thermal-stress calculations are to be performed, based on predicted material temperature profiles.

PARAMETRIC STUDY

A system model developed for the cold-flow startup of the nuclear rocket was discussed in the previous section. This model includes the characteristics of the pump, turbine, nozzle, control valves, and reactor. Its weakness was in the areas related to two-phase hydrogen. For purposes of heat-transfer and flow calculations in the model, a series of single passages was used to simulate the flow system. In order to include the two-phase hydrogen heat-transfer and flow characteristics in the model, it was necessary to test the system to gain empirical characteristics. The usefulness of this approach is thus limited because system analysis cannot be performed until the system of interest is built and tested.

A parametric study was made which demonstrates that the overall characteristics of each of the components in a given system could be analytically predicted and that these characteristics could be expressed as functions of fundamental variables over the range of interest. The flow-calculation portion of the transient-analysis procedure (discussed in the TRANSIENT ANALYSIS section) was utilized for the parametric study. The flow calculation procedure evaluates instantaneous steady-state conditions. Continuity is satisfied, but this procedure does not contain the terms required for a dynamic analysis. The parametric study was also performed to provide more insight into the general characteristics of a system containing boiling two-phase hydrogen.

Basically, three parameters change with time during a bootstrap startup: flow rate, wall temperature, and depth of two-phase penetration. The change in depth of two-phase penetration can be considered for a given component as a change in inlet quality. A single-flow passage representing the reflector is illustrated at the top of figure IV-22.

The influence of the three parameters (inlet quality, flow rate, and wall temperature) on the heat transferred to the fluid passing through the channel is shown by the three curves for the range of interest in startup (fig. IV-22). It may be seen that the overall heat transferred to the fluid Q increases almost linearly with increase in flow rate per

unit flow area G, and also with increase in wall temperature. As the heat transfer Q is nearly independent of changes in inlet quality, figure IV-22 suggests that Q in a portion of the system containing two-phase hydrogen might be expressed as a function only of G and wall temperature.

Correlations for overall heat transfer for the reflector and for the pump-discharge line are shown in figure IV-23 as functions of G and $T_{wall} - T_{liquid}$. Points for the reflector were generated by performing a series of steady-state calculations over the range of conditions expected during startup; wall temperatures from 100° to 500° R, inlet qualities of 0 and 0.4, and three flow rates. The points form a straight line and the equation for the line is

$$Q = 0.00123\, G^{0.8}(\Delta T - 30)$$

where $\Delta T = T_{wall} - T_{liquid}$ and T_{liquid} is the saturation temperature for the inlet pressure. The reflector is an efficient heat exchanger in the sense that the passages are long and the ratio of heat-transfer surface area to flow area is large. Even with saturated liquid entering the passage, boiling occurred quickly under most conditions, and the predominate heat-transfer mode was from the wall to a gas.

The correlation for the pump-discharge line took the form

$$Q = 0.82 \times 10^{-4} G^{0.8}(\Delta T)^2$$

This line, 20-feet long and 4.3 inches in diameter, had comparatively little heat-transfer surface area. For the range of conditions considered during startup, the two phase penetrated the entire length. The difference between the correlations for the reflector and pump-discharge line is a result primarily of the fact that the heat transfer was predominately to a gas in the reflector and predominately to two phase in the pump-discharge line. The form of the equation for the discharge line is somewhat surprising, but it merely reflects the characteristics of the local two-phase correlation (ref. 3, p. 133) as applied to the given geometry and conditions to obtain an overall correlation.

The pump-discharge line of the full-scale nuclear-rocket system at Plum Brook was instrumented for heat-transfer studies. The solid points near the curve for the pump-discharge line are experimental values obtained during bootstrap tests. The agreement with the open symbols (calculated points) is most encouraging.

The foregoing discussion indicates that if the single-passage-simulation geometry and range of expected conditions for a component are known, the current prediction techniques are adequate to be used in developing overall heat-transfer correlations for each lump of a system. It also illustrates that the correlations can be expressed as a function of G and ΔT. Correlations for the pressure drop in a lump or portion of the system were

found to be more complex functions of the three parameters.

The influence on the pressure profile in a typical reflector passage of changes in inlet quality is shown in figure IV-24. The depth of two-phase penetration is indicated by a film-boiling model in the upper figures for three inlet qualities X_{inlet} of 0, 0.35, and 0.5. It may be noted that the lower the inlet quality, the greater the depth of penetration into the passage.

The calculated pressures along the length for each of the inlet quality conditions are shown in the lower portion of figure IV-24. The perhaps subtle but significant point of this figure is that there is little change in pressure in the two-phase region but a significant change in the all-gas region. Although there is a change in velocity as the hydrogen evaporates, the forces are really quite small and the resulting pressure gradient is small compared with the pressure drop occurring in the gas region where the fluid temperature and viscosity increase as the pressure decreases. In order to define the pressure profile in a component or a system, it is essential that the end of the two-phase region be well defined. Not because of forces associated with boiling but rather that the significant pressure changes occur in the all-gas region.

The influence of each of the parameters on the pressure drop in a passage is shown in figure IV-25. All three parameters are shown to exert a strong influence on the pressure drop as they are each varied over their expected range during startup. Whether a quality of 1.0 or 0 is assumed entering the passage makes a difference of two to one in the calculated pressure drop for the conditions of a constant wall temperature and flow rate.

Pressure drop is extremely sensitive to flow rate, as indicated in figure IV-25. Flow rate is an especially difficult parameter to handle accurately during system analysis because of the storage of fluid at various points in the system. The nuclear-rocket system at Plum Brook contained over 30 cubic feet of volume. With the system initially at 0.5 pound per square inch absolute, a significant amount of hydrogen is required to fill the system during a bootstrap startup. For the first 5 to 10 seconds, the flow into the system from the tank far exceeded the outflow from the nozzle throat, and it was 10 to 15 seconds before the outflow started to match the inflow (unpublished data obtained by D. M. Straight, J. J. Biesiadny, J. G. Pierce, and G. W. Metger of Lewis). The time period of this storage effect is dependent on the acceleration rate of the turbopump.

The wall temperature is also shown to have a strong influence on pressure drop. This emphasizes the need, in system analysis, to remove the heat from the system components accurately if valid simulation of pressure drop or pump load is desired.

The combined influence of inlet quality and flow rate is illustrated in figure IV-26 for the typical reflector passage. At low flow rates, there is little influence of inlet quality on the pressure drop. At higher flow rates, inlet quality becomes a sensitive parameter. The family of curves in figure IV-26 is for a wall temperature of 400° R. If a higher wall temperature is assumed, the slope of all the constant flow rates will increase.

For system pressure-drop analysis, computed families of curves relating the three parameters to pressure drop could be provided for each component or lump in the system.

PARALLEL CHANNEL PROBLEM

Figure IV-26 brings out another problem in the analysis of two-phase flow. When flow in parallel passages is analyzed, it is assumed that the total flow will be distributed among the passages in such a way that each passage will have the same overall pressure drop. This flow distribution will be a function of the geometry and surface temperature in each of the passages. Figure IV-26 shows one passage and one wall temperature, but for a given pressure drop, for example, a ΔP of 25 pounds per square inch, there are any number of possible flow rates that could occur depending on the inlet quality.

The problem may be clarified by the example in figure IV-27. Two parallel passages are utilized to simulate the reflector. First, two phase leaves the nozzle coolant passage (sketch at the right of the figure) and is separated by turning into the reflector passages at P_1. Liquid could enter the right passage and gas the left.

A curve for pressure drop as a function of total flow for the separated case is shown at the left. This curve was developed by assuming that the two passages had the same surface temperature and geometry. This assumption permitted obtaining points from figure IV-26. For an assumed pressure drop, flow rates for saturated liquid entering and saturated gas entering were obtained. Summing these two flow rates provides a total flow rate for the assumed pressure drop and therefore a point on the curve. By repeating this process over a range of pressure, the solid line representing the separated case in figure IV-27 was generated.

The curve for the mixed case was obtained as follows: From the points used to generate the separated flow curve, an energy balance was solved to obtain a mixed mean inlet quality. A pressure drop was then obtained which satisfied that inlet quality and total flow rate. By repeating this process several times, the curve for the mixed or homogeneous case was defined.

As shown in figure IV-27, the mixed case always results in a higher calculated pressure drop that could be considered as a maximum. The unmixed case is not a minimum because, if subcooled liquid and superheated gas were assumed, an even lower pressure drop for a given total flow rate would result. The uncertainty in inlet conditions is an unresolved problem in the analysis of two-phase flow in parallel passages. No measurements of either flow or inlet quality are available for the individual passages. The tendency for separation of phases has been observed in multipassage component tests. Much higher pressure drops than recorded experimentally have frequently been calculated. This is traced in part to the assumption in the analysis procedures of perfect mixing.

To our knowledge, there have been no thermal-stress-induced failures in either the

nozzle coolant passages or the reflector due to this separation of phases. Despite this success, if it is desired that reasonable heat-transfer and flow analysis be performed, it is desirable that future inlet plenum designs give as uniform a quality distribution as possible.

The results of this parametric study are summarized by the following points:

(1) Correlations for the overall heat transfer and for the overall pressure drop may be expressed in terms of fundamental variables for each lump of the system when the lump is simulated by a single passage. The overall heat transfer may be expressed as a function of G and ΔT, and the overall pressure drop as a function of X_{inlet}, G, and ΔT.

(2) For a flow passage containing a region of two-phase hydrogen and a region of gaseous hydrogen, pressure drop in the two-phase region is small, but pressure drop in the all-gas region is significant.

(3) For flow through parallel passages, separation of two-phase flow into liquid and gas at the inlets to the parallel passages leads to difficult problems in the analysis of pressure drop, flow distribution, and material temperature profiles.

FLOW AND PRESSURE OSCILLATIONS

"Initial surge" and "two-phase oscillations" were identified during the system tests at Plum Brook and were previously discussed in this paper. Various modes of oscillations were observed during chilldown and heated-tube experiments performed at Lewis. In the paragraphs that follow, four modes of oscillation observed during these component tests are described. This information is presented as a matter of general interest and represents our current interpretation of observed phenomena. Cataloging the modes is hazardous at best because each mode is intimately related to the characteristics of the system in which it occurs. A combination of visual observations and the interpretation of continuous recordings of pressure, temperature, and flow rate were utilized in arriving at these classifications.

Nucleation Source

This mode of oscillation was observed during heated-tube experiments. The model is shown in figure IV-28(a). A glass section just before the heated section permitted the observation of gas bubbles periodically approaching the heated length. The frequency of the appearance of bubbles corresponded to the frequency of measured pressure oscillations.

Gas bubbles entering the boiling section increase the inlet quality. This in turn increases the pressure drop through the boiling section as indicated in figure IV-25. The increase in pressure drop in the boiling section causes a pressure rise at the inlet. This decreases the rate of gas generation from the nucleation source. Thus, a periodic varia-

tion in inlet quality results in oscillations in flow and pressure. A nucleation source resulting from a heat leak to the flow line is used as an example here. Periodic gas generation (flashing) at a restriction before the boiling section can have the same effect. This type of oscillation is seldom severe and can be removed by increasing subcooling of the fluid approaching the boiling section.

Oscillation Source

What is called an oscillation source is indicated as a chamber with a heat source off the main flow line in figure IV-28(b). It frequently appears in the liquid portion of hydrogen flow systems. A real example might be the dead ended leg of a tee in the flow line, or on a smaller scale, a pressure-transducer line. The chamber literally breathes in liquid and breathes out gas. When liquid is breathed in, the flow to the boiling section is reduced; when gas is breathed out, the flow rate and quality approaching the boiling section are altered. The result is periodic flow and pressure oscillations. The amplitude is related to the ratio of the flow in and out of the oscillation source to the through flow in the line. The frequency decreases as the heat flow to the oscillation source is decreased. This type of oscillation may be removed by providing a bleed port on the chamber to remove the gas.

Density Waves

This type of oscillation was observed during heated-tube tests. It would occur when two-phase hydrogen penetrated the entire boiling length. As indicated in the model (fig. IV-28(c)) two-phase hydrogen tends to form a slug-mist-type flow model. When these slugs pass through a restriction, the flow characteristics change, and oscillations in pressure in the boiling section occur. This type of oscillation was observed and the term "density wave" was coined during work reported in reference 5 (p. 133).

Initial Surge

The initial surge oscillations observed during component tests were perhaps less complex than those observed during bootstrap tests because the system was cleaner and interfaces were more clearly defined. The basic description of an initial surge may be made with the aid of the model in figure IV-28(d). The basic elements of the flow system are a precooled length of line, a heated or boiling section, and a restriction in the gas region. For simplicity in this discussion, the liquid-penetration depths at uniform intervals of time are shown by dashed lines labeled alphabetically.

At zero time (point A) pressurized liquid is released into a low-pressure system. Initially, in an attempt to fill the system, the liquid will penetrate too far into the boiling section for stable conditions (point B). At this point gas is being generated faster than it can be removed from the system through the line and orifice at the existing pressure. The velocity (kinetic energy) of the liquid column is dissipated in pressurizing the gas. At point C the liquid velocity is zero and maximum pressure is reached. Because the pressure is greater than the supply pressure, the flow reverses to point D. The combination of effects, caused by the reversed liquid flow and the gas outflow through the restriction reduces the pressure in the boiling section significantly below the supply pressure. The liquid again penetrates deeply into the boiling section, and the cycle is started again. Peak pressures 70 percent greater than supply pressure were observed in the boiling section during chilldown tests of a 1/24 reflector annulus shown in figure IV-19.

The flow system for those chilldown tests is shown schematically in figure IV-29. The test procedure was to pressurize the tank and prechill the flow line to a point just ahead of the reflector inlet plenum. When the line was thoroughly chilled to liquid-hydrogen temperature, flow was directed into the reflector inlet plenum starting the chilldown experiment.

With the aid of high-speed motion pictures, it was observed that the fluid would enter the inlet plenum periodically. This periodic penetration of the liquid into the plenum was related to pressure oscillations in the reflector. When the reflector pressure approached its minimum value, liquid flowed into the plenum. The liquid boiled, and the pressure then increased to values significantly higher than the tank pressure. This high pressure forced the liquid back into the supply line. Boiling stopped and the pressure decreased, thereby completing one cycle.

This oscillation results from an interaction of the inertia of the liquid column, the compressibility of the gas, the boiling process, and the pressure-flow characteristics of the exit orifice. The oscillation is started by the initial flow surge, and it is sustained by periodic boiling.

The influence of the exit orifice size was investigated and is also shown in figure IV-29. The smallest orifice caused the highest pressure peak and this occurred at the lowest frequency. For the largest orifice, the pressure peak was negligible. This example is a fairly simple illustration of the initial surge phenomenon because the boiling can be expressed as a function of liquid position alone.

There are some conditions that tend to stabilize a system. In the upper model of figure IV-30, the liquid column contains gas bubbles. When oscillations involving strong interactions with the inertia of the liquid column are considered, the presence of the gas provides some compressibility in the liquid column tending to reduce the severity of the oscillations. While this mechanism would tend to reduce the severity of the initial surge, it could lead the system into the mode of oscillation related to a variation in inlet quality.

Perhaps the most widely used stabilizing influence in boiling systems is indicated in the lower model of figure IV-30. A restriction in the liquid region just before the boiling section will nearly always stabilize a system. It does this either by isolating the inertia of the liquid from the boiling process, or by making the amplitude of the two-phase oscillations small in terms of the total pressure loss through the system.

This approach is difficult to apply to a transient case because the depth of liquid penetration is changing with time making the restriction location a difficult problem. This approach also increases the pump work. As pointed out previously, flashing at the restriction can lead to a mode of oscillation related to the nucleation source.

Summary of Oscillations

The oscillation-source and nucleation-source modes were primarily a result of periodic variation in two basic parameters: flow rate and/or inlet quality. The strong influence of these parameters on pressure drop has been discussed previously. The density wave mode of oscillation is related to boiling primarily in the sense that it reflects the periodicity of the slug-mist flow model as it passes through a restriction. The initial surge mode could be considered as the seeking of a stable depth of liquid penetration that would satisfy the overall applied pressure drop. The variation in boiling rate during this seeking, acts as a forcing function. The significance or importance of each mode of oscillation is dependent on the system characteristics and operating conditions.

It has been the intent of this discussion to convey a physical explanation of the various modes observed in terms of understandable parameters. Analytically it is not this simple. Each mode involves a complex interaction of flow, heat transfer, fluid properties, and system geometric characteristics. Analytical models of systems to evaluate the various modes have met with only limited success because of difficulties in simulation of characteristics and weighting of the interactions.

CONCLUDING REMARKS

Studies related to reactor aftercooling are not discussed in this paper. References 6 and 7 (p. 133) are listed as representative of Lewis effort in this area. Analysis of the transient-flow characteristics in the laminar-turbulent transition region are being continued at Lewis (unpublished data obtained by R. W. Leko).

FLUID CONTROLS

Vernon D. Gebben

INTRODUCTION

The nuclear-rocket engine is composed of two separable but interacting systems. Energy is derived from a nuclear rocket that is controlled by neutron-absorbing material on control drums located in the reflector. Hydrogen flows through the reactor absorbing the heat generated and is expelled through a nozzle producing thrust. The system flow is regulated by the turbopump whose speed is controlled by the turbine-power-control valve. The most significant control parameters for operating the engine are the chamber temperature and the chamber pressure, which are indicative of specific impulse and thrust.

A simplified block diagram of a NERVA type control system is shown in figure IV-31. The programmer provides the reference signals for the reactor-power and the system-flow loops. The system controller contains comparators for measuring the difference between the reference signals from the programmer and the feedback signals, amplifiers for high sensitivity, and compensators for stabilizing the system. Actuation servos are used to position the turbine-power-control valve and the control drums. The chamber pressure P_c and the chamber temperature T_c are the controlled variables that are measured for use by the system controller. Neutron flux signals φ are available for reactor startup and for quick reactor power control.

In the present control system, the elements are controlled by electrical signals, and the actuation servos are electropneumatic servomechanisms. Another approach, under investigation, is to use an all-pneumatic control system; that is, to replace electronic circuits with pneumatic circuits and to use pneumatic control sensors. The pneumatic supply would be hydrogen gas - the working fluid of the engine. In the pneumatic circuits, fluid amplifiers are the counterpart for the transistors, line restrictors are the resistors, and volumes are the capacitors. Integrated circuits can be fabricated by using techniques analogous to the printed circuit used in electronics.

For the past 3 years, Lewis has been evaluating pneumatic components that could be used to improve reliability without affecting the performance of the system. This paper describes the operation of some of the fluid amplifiers that are being used in these developments and presents the status of this work.

FLUID AMPLIFIERS

The fluid amplifier (also called fluidic and flueric) was introduced 6 years ago by the Army's Harry Diamond Laboratories. Figure IV-32 shows the silhouette of passageways

engraved in a block of material. The fluid that flows through the channels is gas, but liquid can be used. As illustrated, the high-pressure-supply flow is deflected to output channel 2. The deflection is caused by a low-pressure signal in control channel 1. Likewise, the supply would be deflected to the other output channel when the pressure in control channel 2 exceeds the pressure in control channel 1. The flow from the outputs would be directed to the control ports of another amplifier or, possibly, to a motor. This type of fluid amplifier can be built to operate as either a bistable or a proportional amplifier. In the bistable amplifier, the supply flow is switched from one output port to the other. In the proportional unit, the supply stream is divided into two outputs that are related to the differential control signal.

Figure IV-33 illustrates some Lewis design improvements (ref. 8, p. 133). In this unit, the control passageways inject the control flow in a direction along the supply stream rather than perpendicular, as shown in figure IV-32. This configuration prevents overdeflection of the supply stream and thereby produces good saturation characteristics.

The side vents provide another feature. Side vents A and the center vent C improve the performance by increasing the linearity and reducing the noise in the output. Side vents B are designed to isolate the amplifier from the load. Operation of side vents B is illustrated in figure IV-34 where the amplifier is driving a piston. As shown, the supply stream is deflected to the lower output passageway and directed into the lower chamber of the actuator. The piston moves upward. The fluid discharged from the upper chamber flows back into the amplifier. This return flow is diverted out the side vent. If, however, the amplifier did not have this special vent, the return flow would be directed into the sensitive interaction region and would interfere with proper operation of the amplifier. Tests have shown that side vents B are very effective buffers for isolating the amplifier from the load.

A photograph of one of our laboratory test models is shown in figure IV-35. This model is approximately 4 inches long and 2 inches wide. The channels are 1/16 inch deep. The width of the supply nozzle is 40 thousandths of an inch. This amplifier can be reduced to one-third of its present size by using photoengraving techniques. Photoengraving techniques have been used to build amplifiers with materials of plastic, glass, and metal.

One of the main features of this jet type of fluid amplifier compared with other fluid amplifiers is its high-frequency response. Fluid logic circuits have been demonstrated to operate with pulse rates of 1000 pulses per second.

Another important device in this field is the vortex amplifier (illustrated in fig. IV-36). It consists of two parts: a cylindrical chamber and a separate tube. The flow enters the chamber through radial inlets for supply flow and through tangential nozzles for control flow. The flow leaves the chamber through an orifice located at the center of chamber end-wall. The flow leaving the orifice is collected by the receiving tube located

a short distance away from the orifice. The flow that bypasses the tube is vented out. The pressure and flow collected in the tube are the output of the amplifier.

First, consider the case where the control flow is zero. The supply flow entering the chamber radially will flow directly to the exit orifice. The flow leaving the orifice will be a jet that flows into the receiving tube. This condition of zero control flow gives the maximum output; 95 percent pressure recovery and 95 percent flow recovery can be obtained. High recovery results because the distance between the exit orifice and the receiving tube is small.

When control flow is injected into the chamber, a vortex is generated. Consequently, the flow leaving the exit orifice is rotational flow that fans outward as the result of centrifugal forces. Because the flow from the orifice is conical in shape, the fluid will partially bypass the receiving tube. The amount of bypass depends on the strength of the vortex established by the control flow. With maximum control flow, all the fluid is vented. This operating condition gives the minimum pressure in the receiving tube, and an output pressure whose value is generally below the vent pressure.

In addition to the amplification characteristics resulting from the exit flow pattern, the vortex amplifier also throttles the flow leaving the exit orifice. (The exit flow equals the total of control and supply flows.) In some designs, the flow leaving the exit orifice is reduced by a factor of 8 when the control changes from zero to maximum flow rate because resistance to vortex flow is much higher than the resistance to radial flow. The combination of throttling and diversion of the fluid leaving the exit orifice provides a useful method for controlling power to a load.

Several other types of fluidic elements have been described in engineering literature. In general, each of these elements operates by a sensitive dynamic trait that controls the flow pattern of the supply (main) stream. Some elements operate by controlling the boundary layer, others use techniques that involve the control of fluid entrainment, turbulence, momentum, and vortex flow.

These elements appear to be well suited for application on the nuclear rocket. They can operate on hydrogen gas, have adequate frequency response characteristics, and can be built rugged for operating near the engine.

Actuation Servos

The actuation servos for the turbine-power-control valve and the control drums have been examined for possible improvements. The major components of the actuation servo are shown in figure IV-37. The servo consists of two assemblies: a control assembly for processing signals and an actuator assembly for power. The control assembly contains a comparator for measuring the difference between the input and feedback signals, ampli-

fiers for boosting signals, conditioners for stabilizing the system, and a speed limiter for preventing the actuator from slewing too fast. In the second assembly, the servovalve provides the pneumatic power to the motor, the motor manipulates the control drum (or turbine-power-control valve), and the position sensor provides the feedback signal. The control assembly, servovalve, and motor are three areas under investigation for improvements.

The new control assembly would use pneumatic circuits designed to tolerate the severe environment of extreme temperatures and radiation. This assembly will be mounted on the actuator assembly to form a single package instead of the two separate units required when electronics are used. The study phase of the contract showed that the servo operated with fluid-amplifier circuits will have the performance equivalent to the present electronic unit. The details on component sizes, amplifier requirements, and the pressure-flow requirements are available in references 9 and 10 (p. 133). Most of the components have been fabricated. Preliminary tests on portions of the compensation networks indicate that the required specifications can be obtained.

The servovalve shown in figure IV-38 operates without the use of moving mechanical parts. This experimental model used vortex amplifiers for controlling the fluid power. It was demonstrated that this type could be designed for use in the control drum actuation servos. Except for linearity and output stability, the performance of this unit is comparable to the flapper nozzle type presented used on the NERVA actuators. Summary of the performance characteristics are given in table IV-1. The final report (ref. 11, p. 133) presents design details, test results, and suggestions for improving the performance.

A second-generation flueric servovalve is presently under development. This new unit also uses vortex amplifiers for controlling the flow. Besides improving the linearity and noise characteristics, it will have higher power gain and will incorporate dynamic pressure feedback. This feedback provides virtual damping characteristics to the actuator and thereby stabilizes the system. This servovalve is being designed to operate in conjunction with the pneumatic control assembly.

The improved motor under development is the pneumatic nutator motor. This motor, shown in figure IV-39, was designed for manipulating the control drums of nuclear-rocket engines similar to NERVA. It is ideal for nuclear-rocket applications because it contains no high-speed sliding parts that require special lubricants.

The motor contains a pair of bevel gears with an unequal number of teeth. The input gear is attached to the housing by a gimbal ring and is driven by eight bellows. The gimbal ring allows the input gear to nutate (wobble) and prevents rotation. The output gear, which is attached directly to the output shaft, is allowed to rotate but not to nutate. By moving the point of force around the circumference of the input gear, the input gear will nutate and its teeth will mesh consecutively with each of the output gear teeth. The output gear has one less tooth than the input gear. Consequently, the output will be displaced

by one tooth for each cycle of the input gear. The bellows that manipulate the input gear are pressurized sequentially by a logic network of vortex amplifiers. A low-power pneumatic input signal controls the logic network, driving the motor in either direction.

The final report (ref. 12, p. 133) on this motor describes the operation and the test results. Some performance deficiencies were noted with the prototype motor. The maximum output speed of 10 degrees per second and the maximum output torque of 235 inch-pounds were too low. It should be pointed out, however, that low performance characteristics were caused by the fluid logic circuits and were not the fault of the mechanics of the motor. Improvements in the circuits are being developed. In general, the motor operated satisfactorily and demonstrated feasibility for use in control-drum systems.

CONCLUSIONS

These investigations for improving the NERVA control system revealed some difficulties in designing new fluid-amplifier circuits. For example, fluid elements were easy to demonstrate, but high performance circuits required extensive development. Exact impedance matching within the circuit is very important and generally requires a major effort to accomplish. Wave reflections can also create problems in high gain operational circuits used in control systems. Results from our work and from developments under other government programs, however, do indicate that fluidic control systems are feasible.

REFERENCES

1. Hendricks, R. C.; Simoneau, R. J.; and Friedman, R.: Heat-Transfer Characteristics of Cryogenic Hydrogen from 1000 to 2500 psia Flowing Upward in Uniformly Heated Straight Tubes. NASA TN D-2977, 1965.

2. Ellerbrock, Herman H.; Livingood, John N. B.; and Straight, David M.: Fluid-Flow and Heat-Transfer Problems in Nuclear Rockets. Nuclear Rocket Propulsion, NASA SP-20, 1962, pp. 27-56.

3. Hendricks, R. C.; Graham, R. W.; Hsu, Y. Y.; and Friedman, R.: Experimental Heat Transfer and Pressure Drop of Liquid Hydrogen Flowing Through a Heated Tube. NASA TN D-765, 1961.

4. Miller, John V.; and Taylor, Maynard F.: Improved Method of Prediction Surface Temperatures in Hydrogen-Cooled Nuclear Rocket Reactor at High Surface- to Bulk-Temperature Ratios. NASA TN D-2594, 1965.

5. Stenning, A. H.; and Veziroglu, T. N.: Boiling Flow Instability. Rep. No. 7 (NASA CR-64319), Miami Univ., Coral Gables (Fla.), May 1965.

6. Harry, David P., III: A Steady-State Analysis of the "Laminar-Instability" Problem Due to Heating Para-Hydrogen in Long, Slender Tubes. NASA TN D-2084, 1964.

7. Turney, G. E.; Smith, J. M.; and Juhasz, A. J.: Steady-State Investigation of Laminar-Flow Instability Problem Resulting From Relatively Large Increases in Temperature of Normal Hydrogen Gas Flowing in Small Diameter Heated Tube. NASA TN D-3347, 1966.

8. Griffin, W. S.: Bistable Fluid Jet Amplifier with Low Sensitivity to Receiver Reverse Flow. Proceedings of the Fluid Amplification Symposium, Harry Diamond Labs, Oct. 1965, vol. 3, pp. 17-35. (Available from DDC as AD-623457.)

9. Boothe, W. A.: Feasibility Study - Application of Fluid Amplifiers to Reactor Rod Control. Rep. No. 63-GL-134 (NASA CR-54005), General Electric Co., Nov. 25, 1963.

10. Cardon, M. H.: Replacement of Electronics with Fluid Interaction Devices. Rep. No. BRLD-2946 (NASA CR-54758), Bendix Corporation, Aug. 31, 1965.

11. Anon: Design, Fabrication and Test of a Fluid Interaction Servovalve. Rep. No. BRLD-2978(NASA CR-54463), Bendix Corporation, May 17, 1965.

12. Howland, G. R.: Pneumatic Nutator Actuator Motor. Rep. No. BPAD-863-16719R (NASA CR-54788), Bendix Corporation, Oct. 17, 1965.

TABLE IV-1. - SIGNIFICANT PERFORMANCE CHARACTERISTICS

Item	Specified	Measured
Supply pressure	5.16×10^5 N/m^2 g air (75 psig)	5.16×10^5 N/m^2 g air (75 psig)
Pressure recovery	3.1×10^5 N/m^2 g (min.) (45 psi)	3.1×10^5 N/m^2 (45 psi)
Rated no-load output flow	0.0113 kg/sec (0.025 lb/sec)	0.0131 kg/sec (0.029 lb/sec)
Flow recovery	0.55 min	0.44
Quiescent supply flow	0.0204 kg/sec (max.) (0.045 lb/sec)	0.030 kg/sec (0.067 lb/sec)
Input signal pressure	2.75×10^5 N/m^2 g (max.) (40 psig)	1.72×10^5 N/m^2 g (25 psig)
Input signal bias pressure	1.38×10^5 N/m^2 g (max.) (20 psig)	1.17×10^5 N/m^2 g (17 psig)
Input signal power	30 W (max.)	55 W
Differential input signal power change for output pressure change from -0.69×10^5 N/m^2 to 0.69×10^5 N/m^2 (-10 to 10 psi)	5 W (max.)	5 W
Linearity $\frac{\text{Gain maximum}}{\text{Gain minimum}}$	3	15
Output stability	0.034×10^5 N/m^2 (max.) (0.5 psi)	0.27×10^5 N/m^2 (4 psi)
Transient response	0.25 sec	0.10 sec

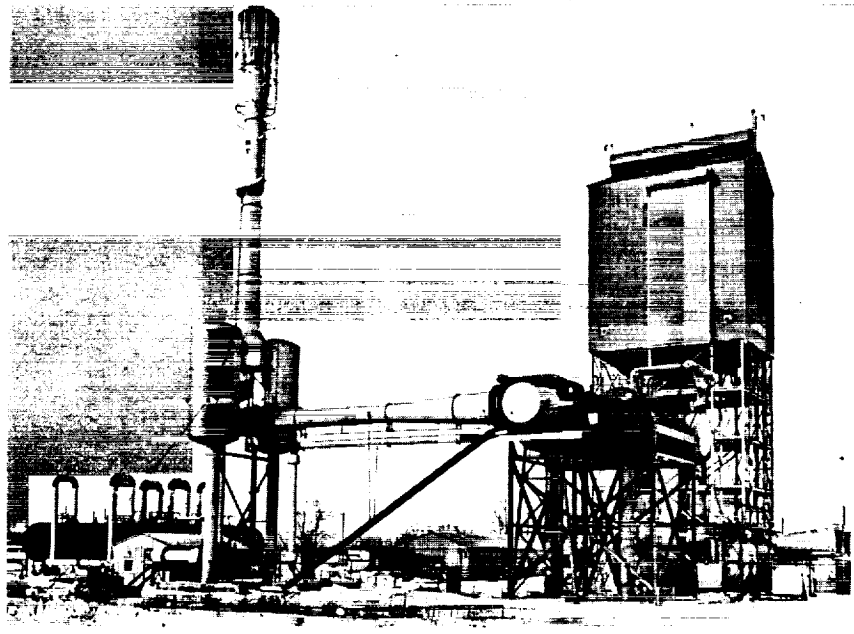

CS-39163

Figure IV-1. - Nuclear-rocket cold-flow test facility.

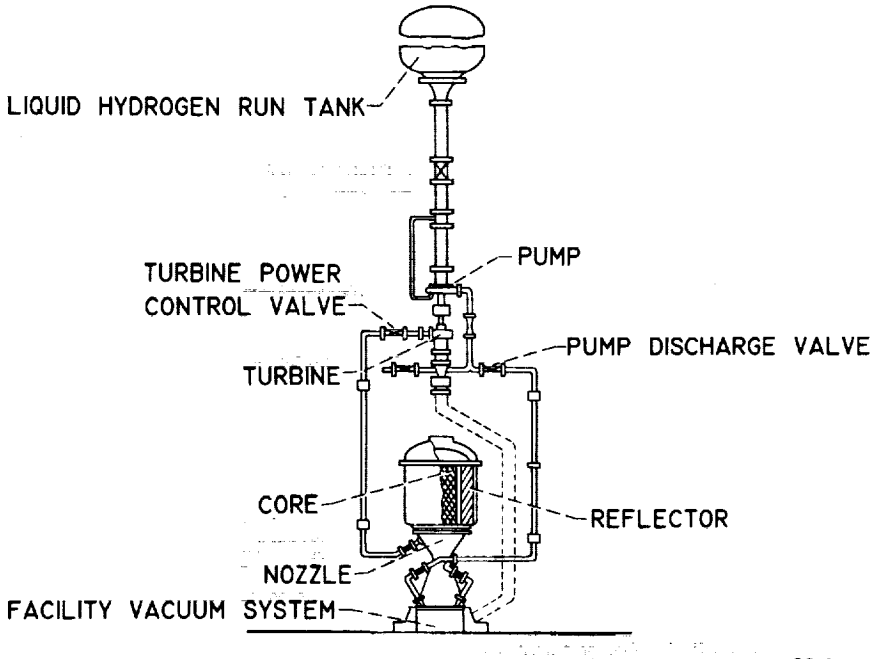

CS-39190

Figure IV-2. - Nuclear-rocket cold-flow-test hardware.

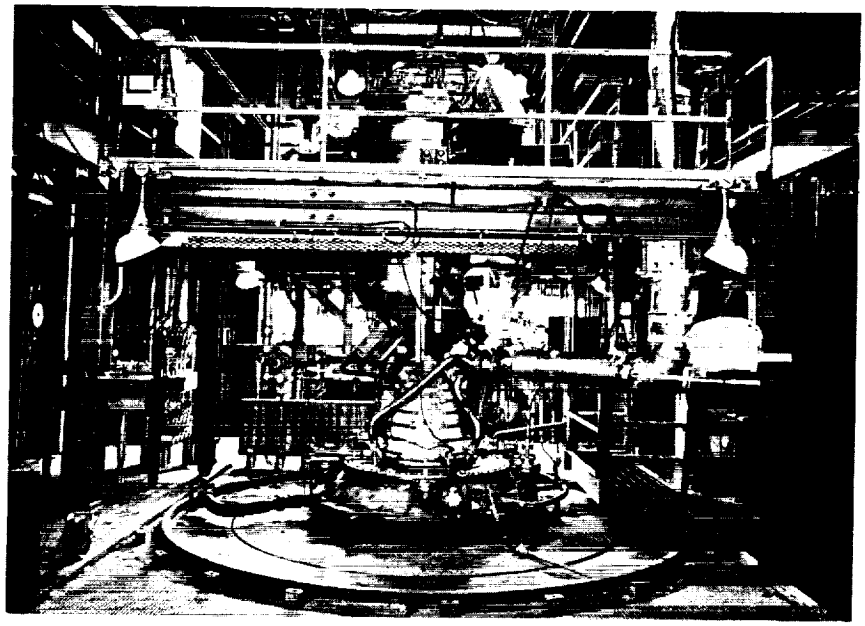

CS-39164

Figure IV-3. - Cold-flow startup test hardware.

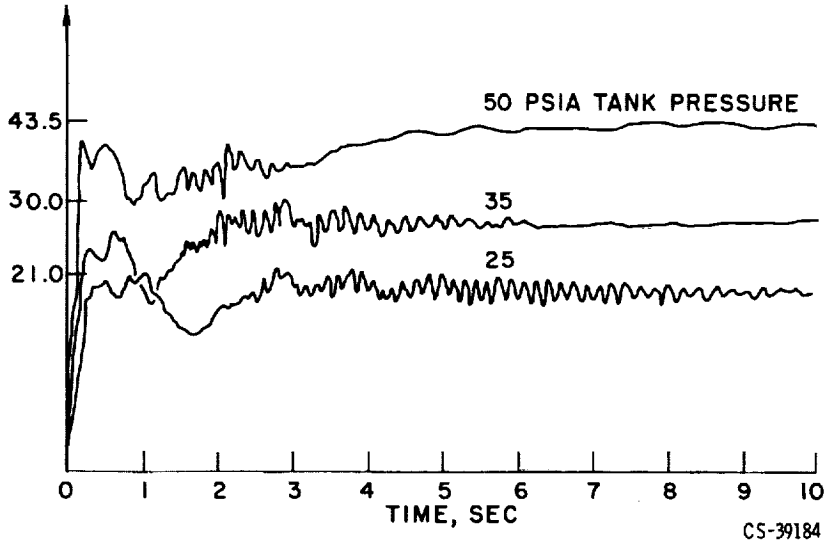

CS-39184

Figure IV-4. - Flow perturbations.

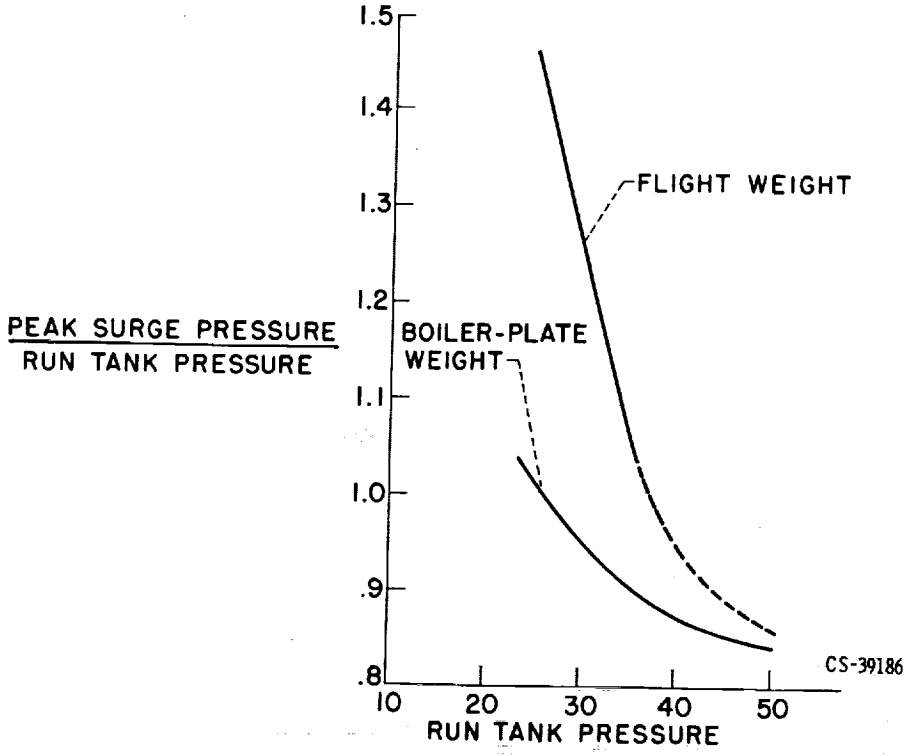

Figure IV-5. - Effects of tank pressure and flange weight on initial pressure surge.

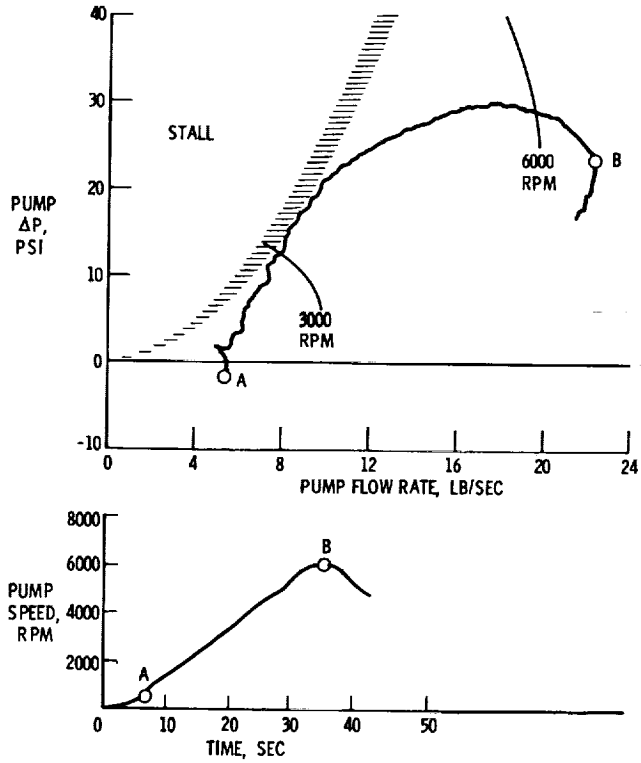

Figure IV-6. - Controlled bootstrap. Tank pressure, 35 pounds per square inch absolute.

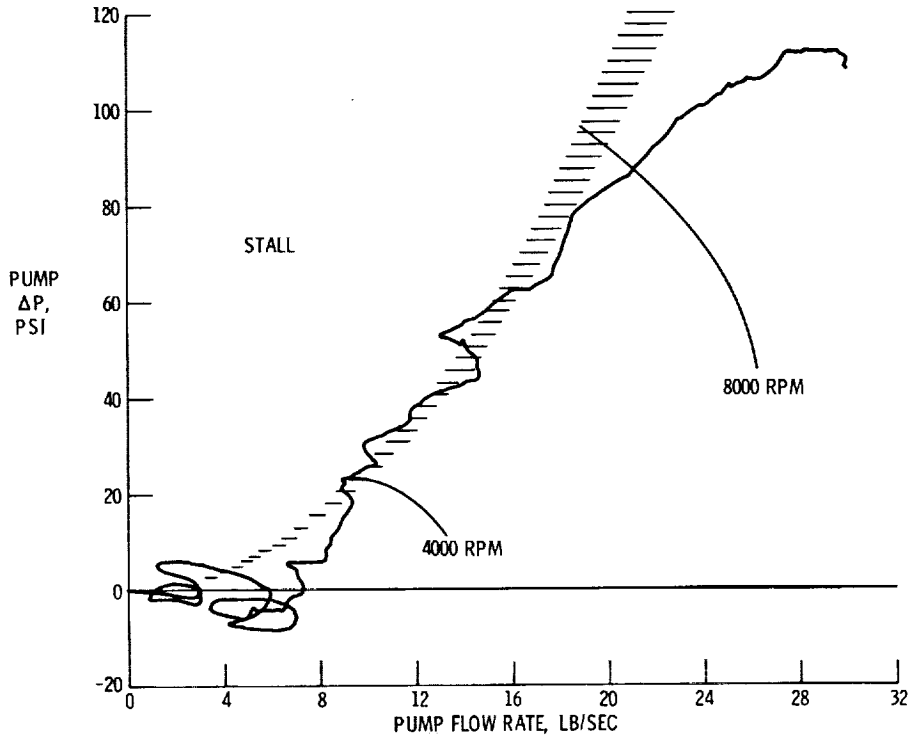

Figure IV-7. - Uncontrolled bootstrap. Tank pressure, 35 pounds per square inch absolute.

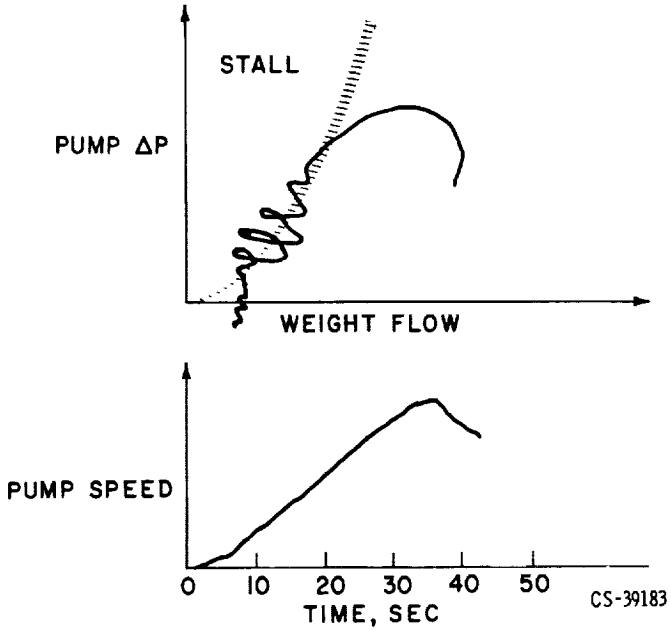

Figure IV-8. - Equipment operation problems.

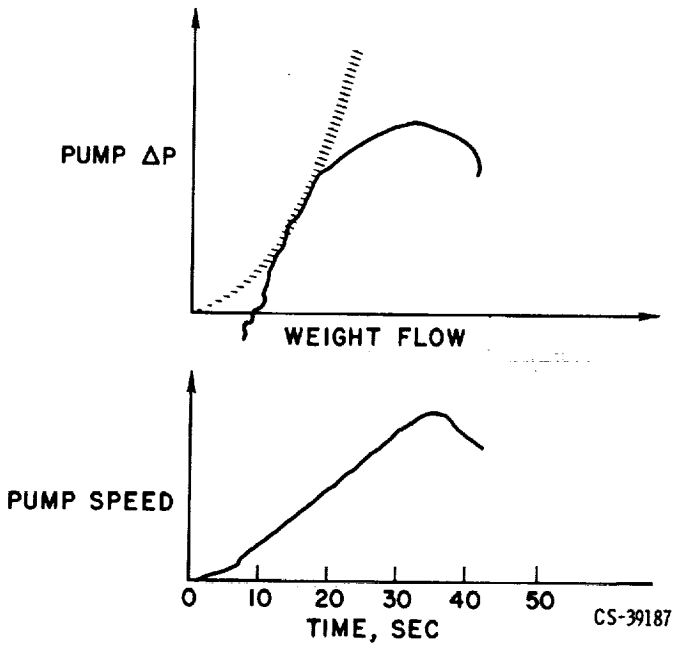

Figure IV-9. - Rerun with modified cold bleed line.

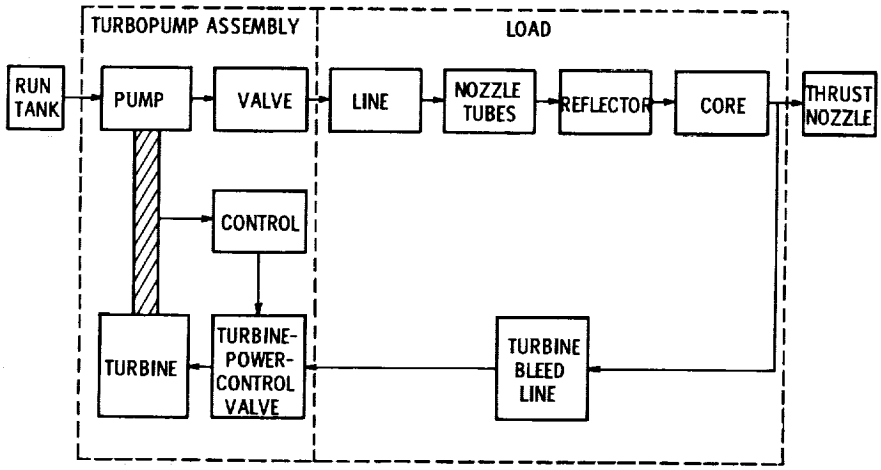

Figure IV-10. - System block diagram.

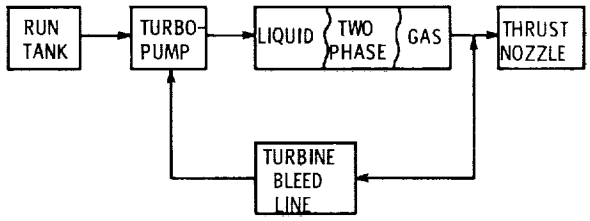

Figure IV-11. - Simplified model showing variation of fluid state throughout system.

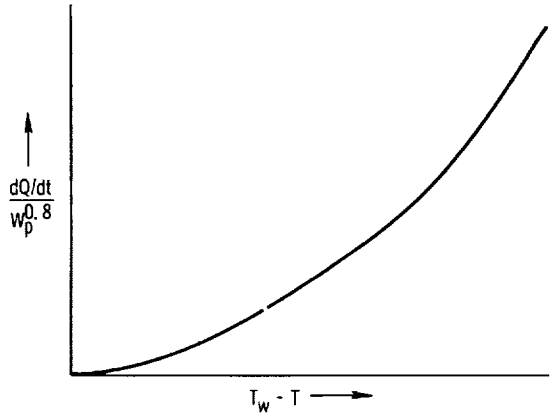

Figure IV-12. - Form of empirical heat-transfer correlation.

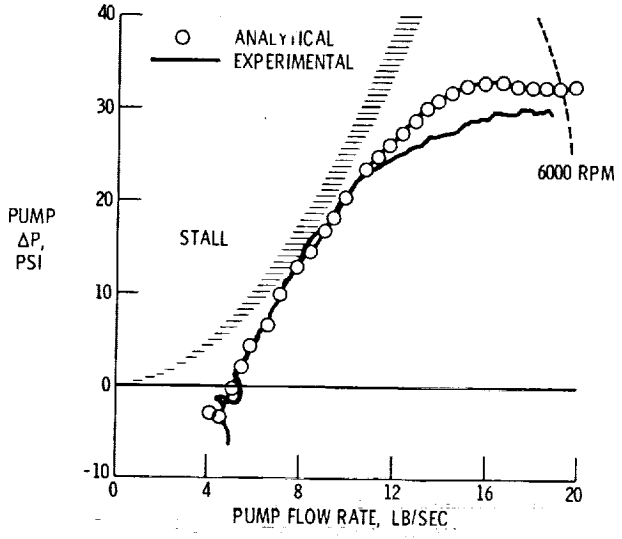

Figure IV-13. - Comparison of analytical and experimental controlled bootstrap data.

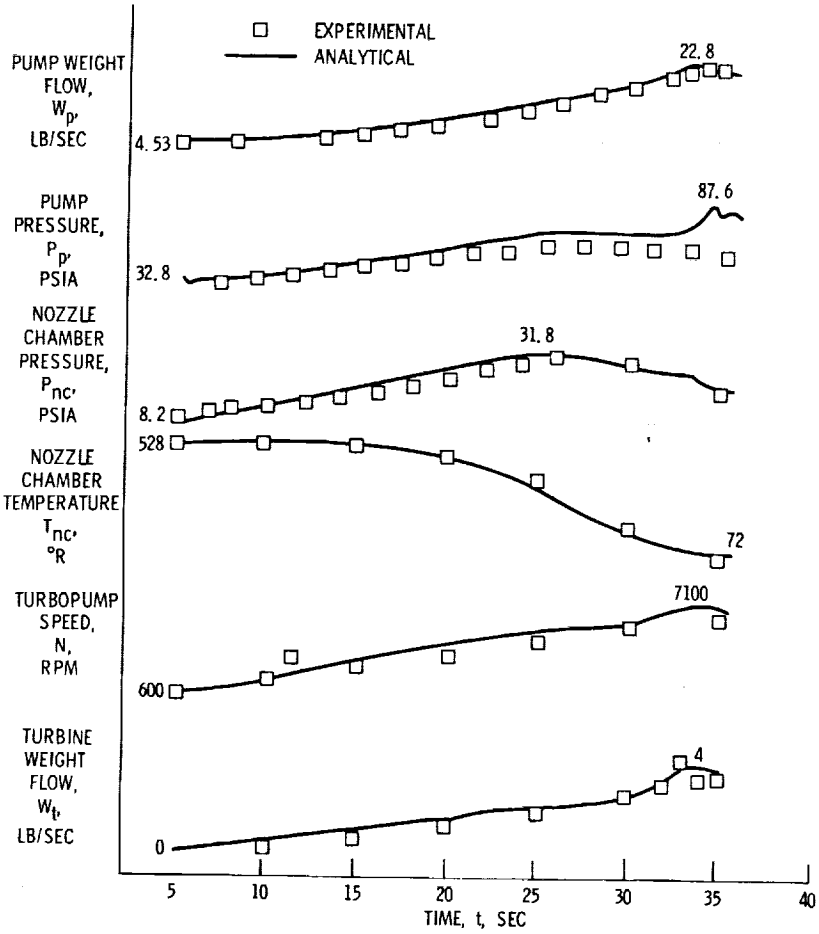

Figure IV-14. - Parameter-time comparison of analytical and experimental controlled bootstrap.

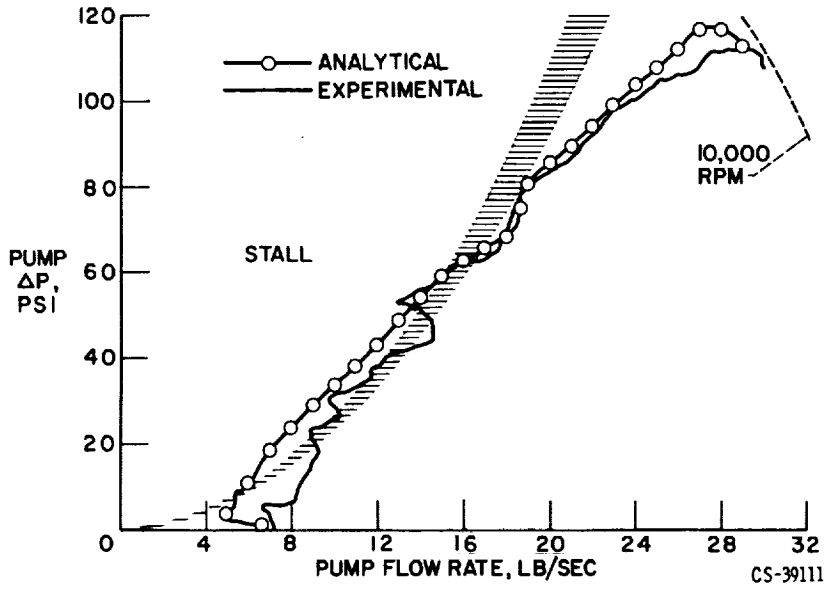

Figure IV-15. Comparison of analytical and experimental uncontrolled bootstrap data.

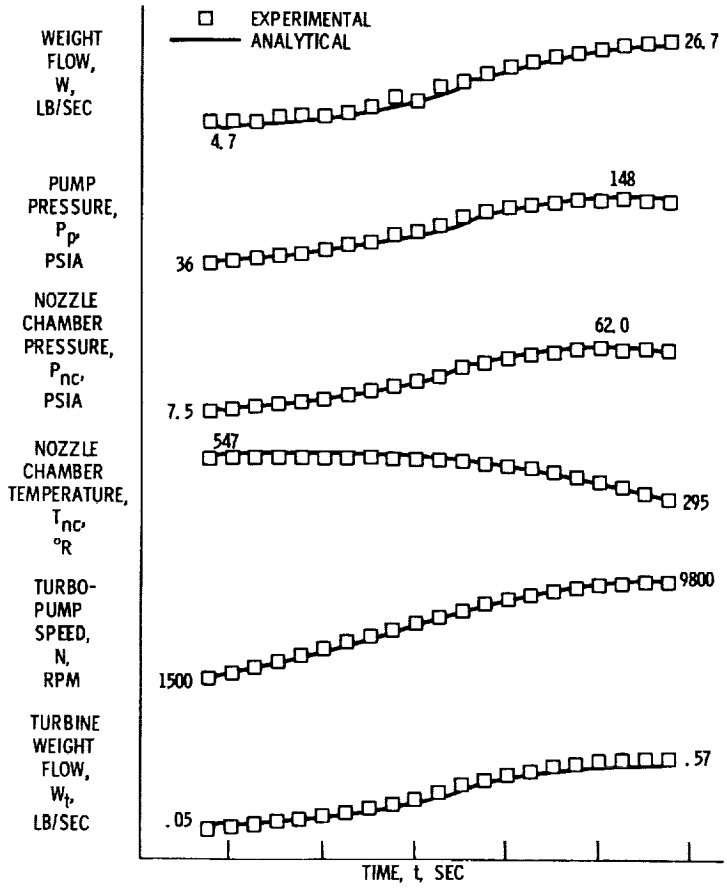

Figure IV-16. - Parameter-time comparison of analytical and experimental uncontrolled bootstrap.

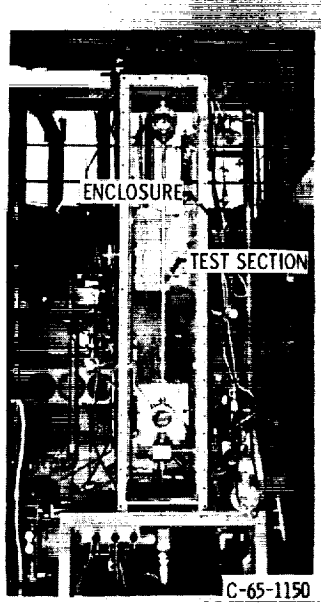

Figure IV-17. - Single thick walled tube.

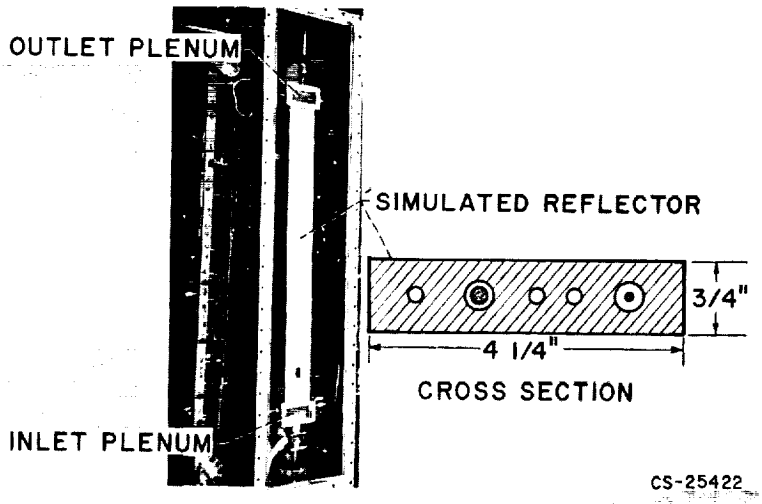

Figure IV-18. - Simulated reflector for flow maldistribution studies.

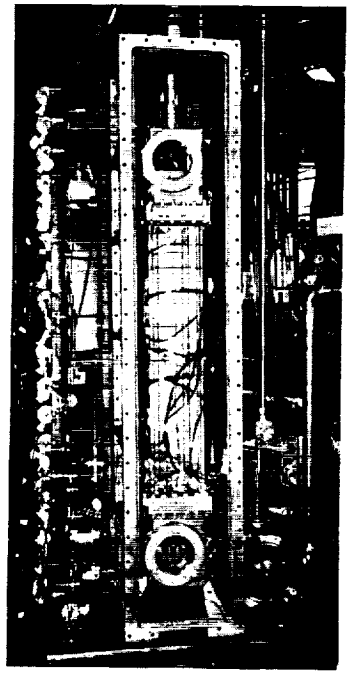

C-63961

Figure IV-19. - 1/24 reflector annulus.

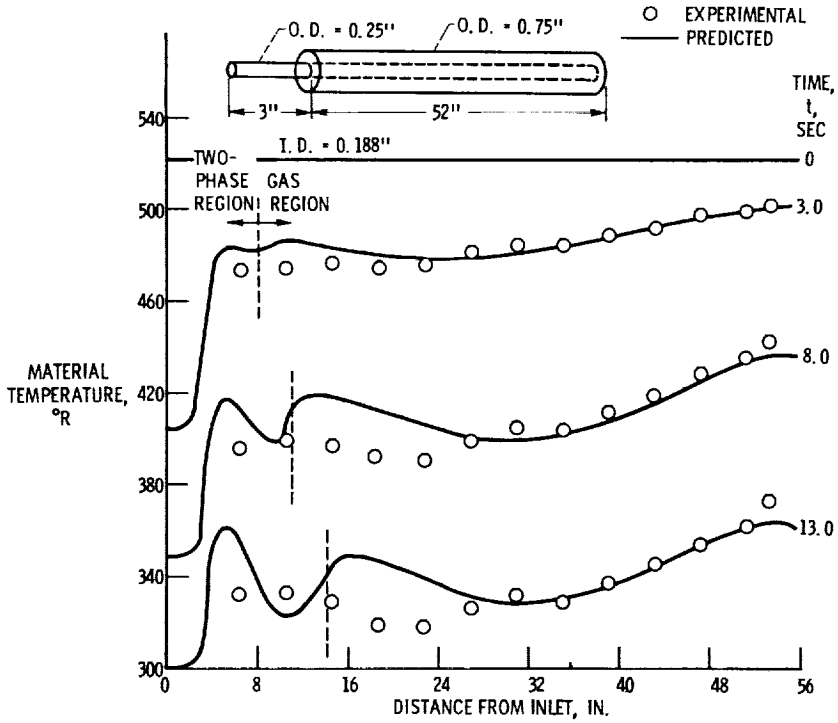

Figure IV-20. - Comparison of experimental and predicted wall temperatures as function of time during chilldown run.

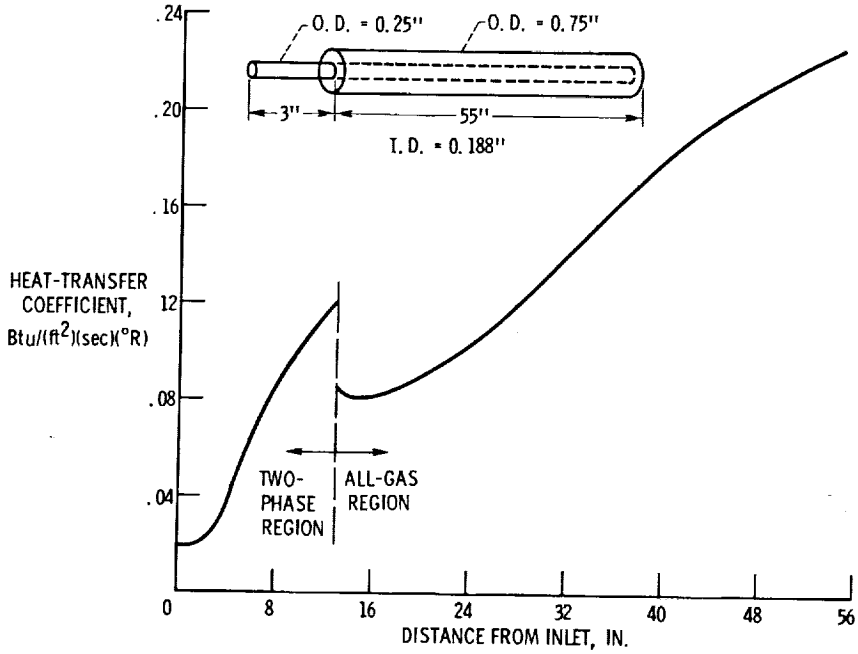

Figure IV-21. - Predicted heat-transfer coefficient as function of length. Chill-down run at 11.0 seconds; inlet pressure, 47.0 pounds per square inch absolute; 0.00644 pound per second; inlet enthalpy, 90.61 Btu per pound.

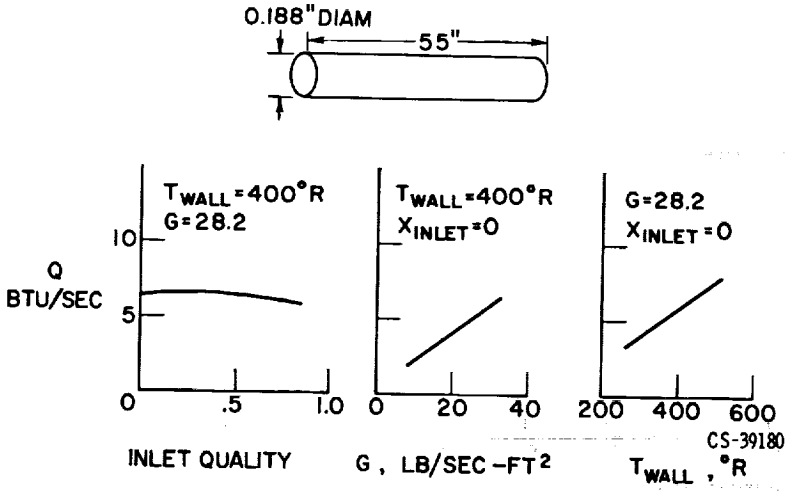

Figure IV-22. - Influence of quality, flow rate, and wall temperature on heat added to fluid.

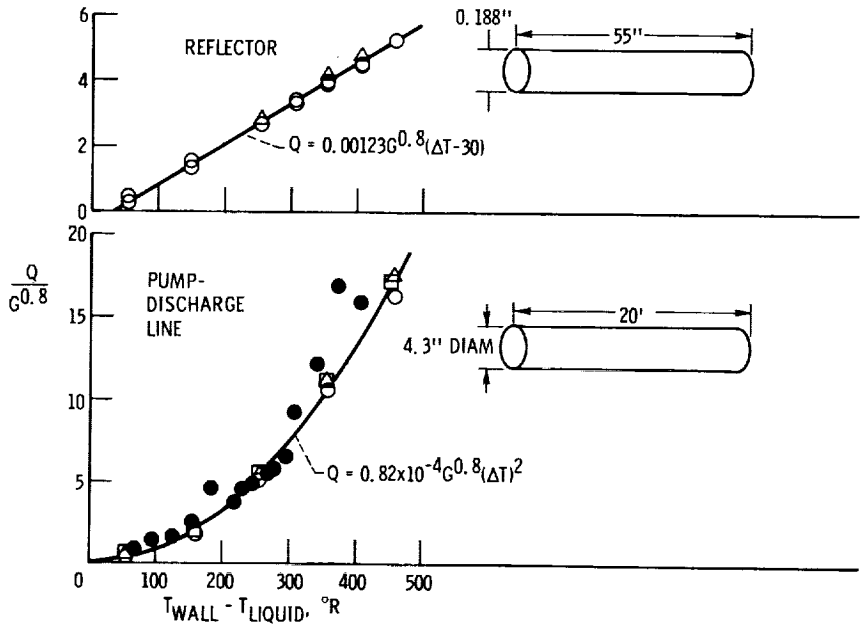

Figure IV-23. - Overall heat-transfer correlations.

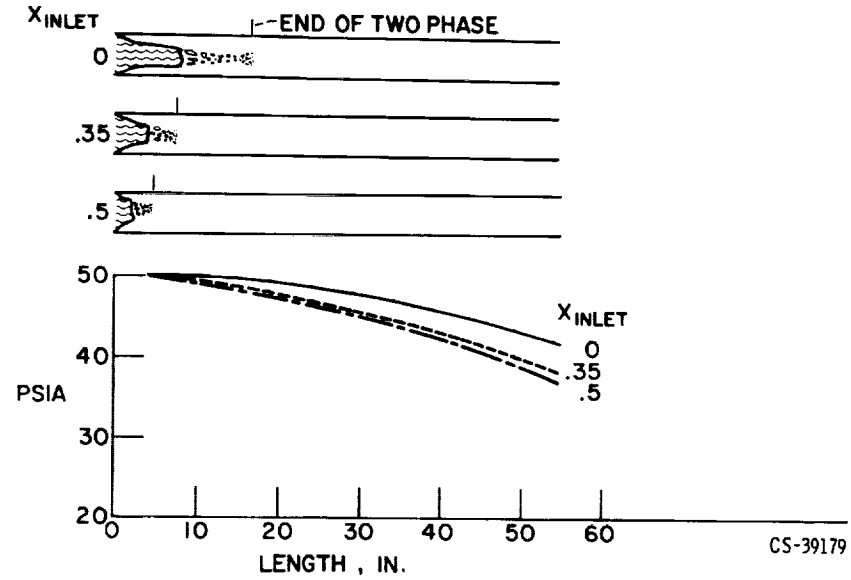

Figure IV-24. - Effect of inlet quality on pressure profile. Length, 55 inches; diameter, 0.188 inch; wall temperature, 300° R; inlet pressure, 50 pounds per square inch absolute; flow rate, 0.0052 pound per second.

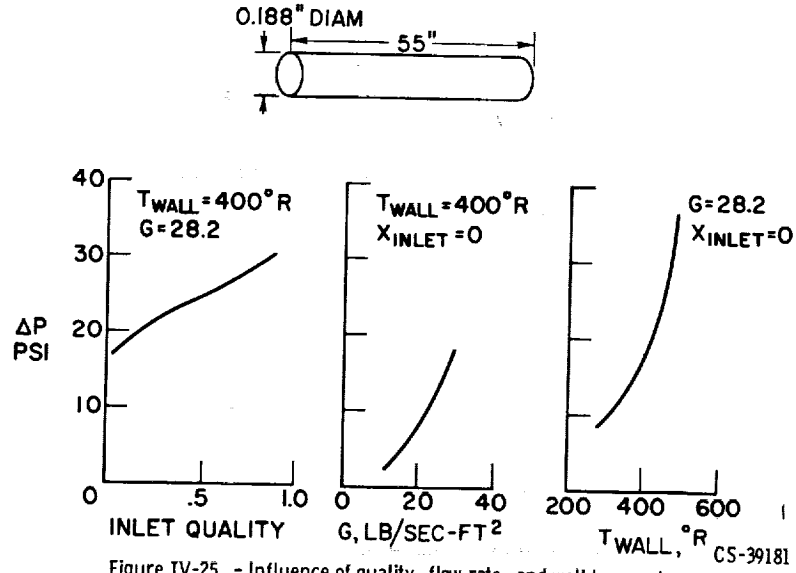

Figure IV-25. - Influence of quality, flow rate, and wall temperature on pressure drop.

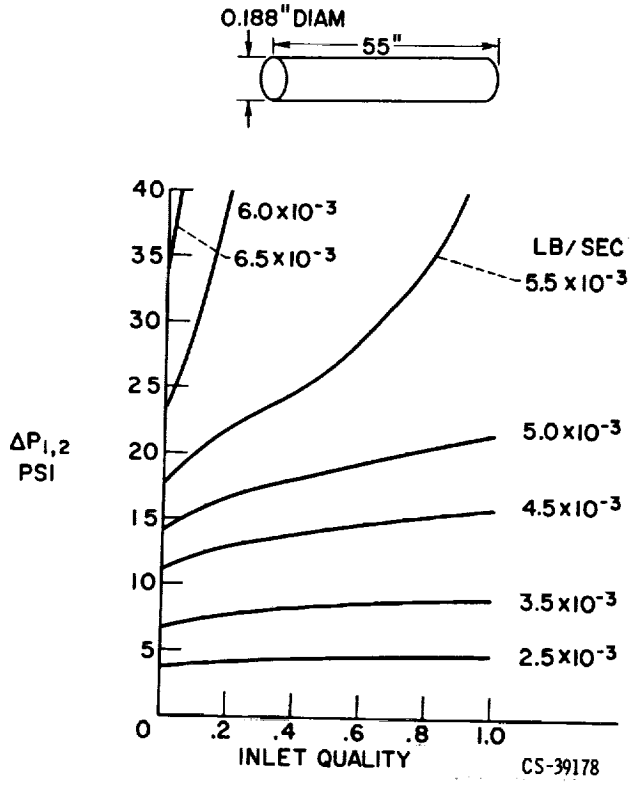

Figure IV-26. - Combined influence of inlet quality and flow rate. Wall temperature, 400° R.

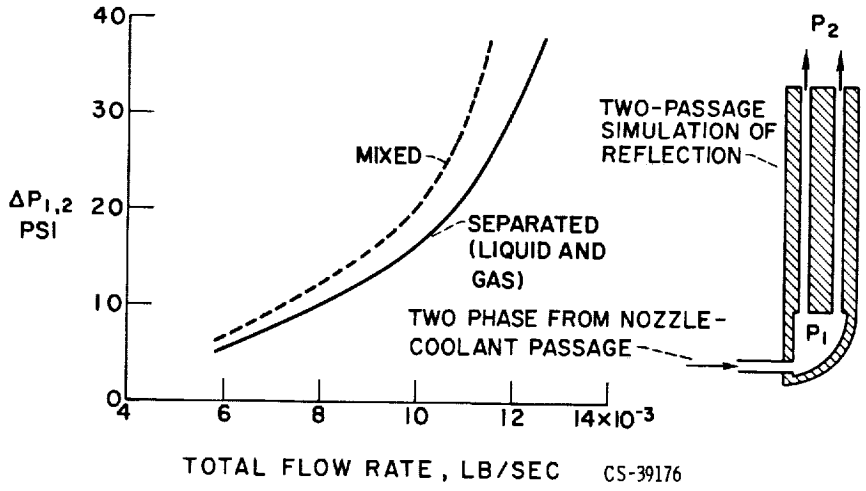

Figure IV-27. - Pressure drop as function of flow rate for separated and mixed inlet quality.

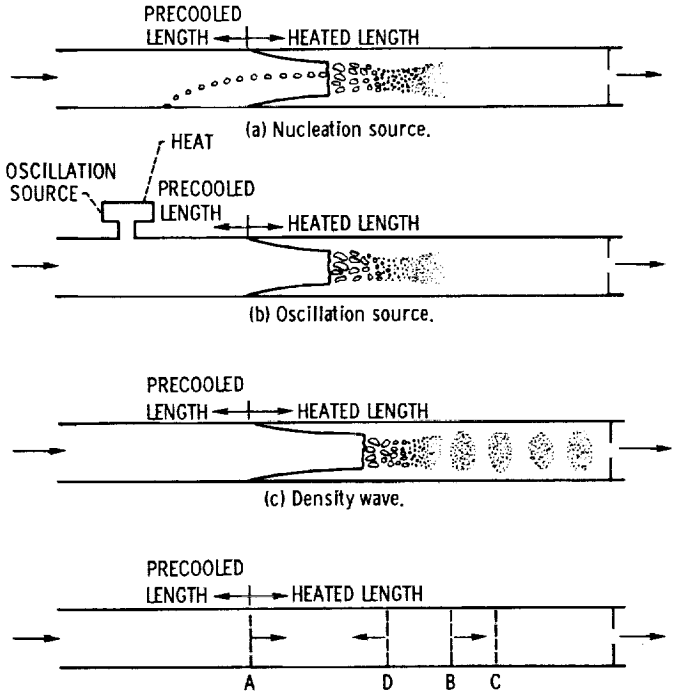

Figure IV-28. - Oscillation models.

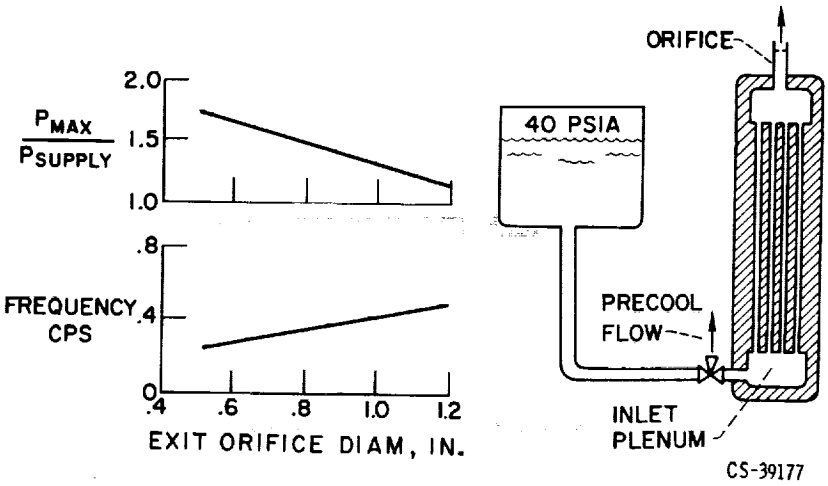

Figure IV-29. - 1/24th Reflector segment.

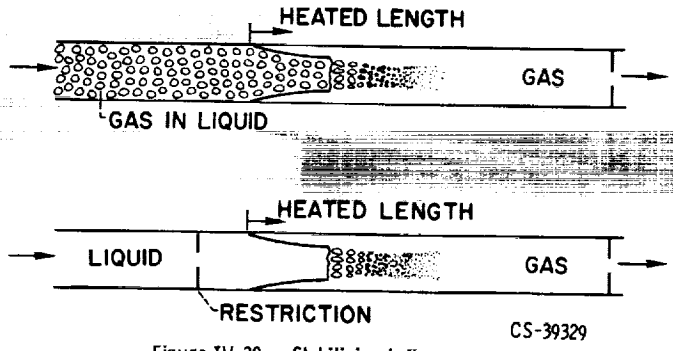

Figure IV-30. - Stabilizing influences.

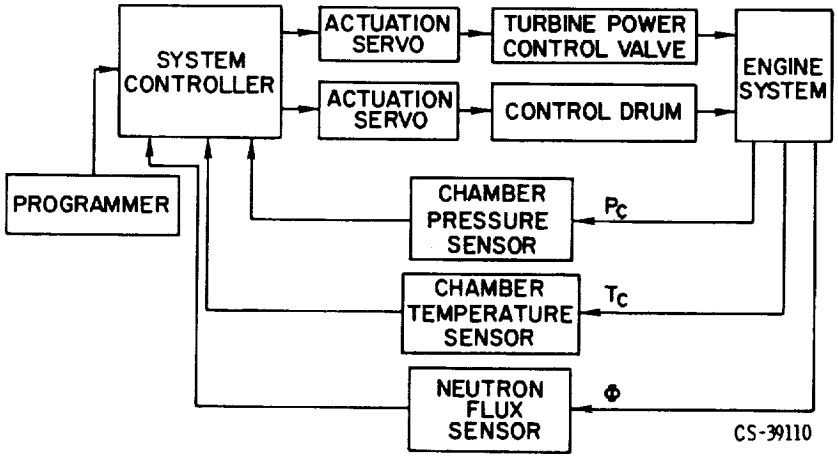

Figure IV-31. - Nuclear-rocket-engine control system.

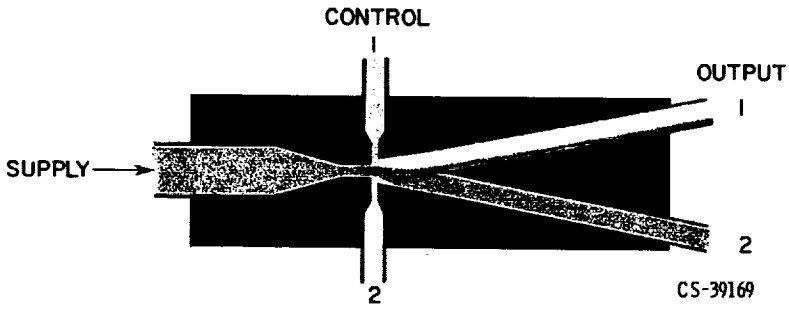

Figure IV-32. - Original fluid jet amplifier.

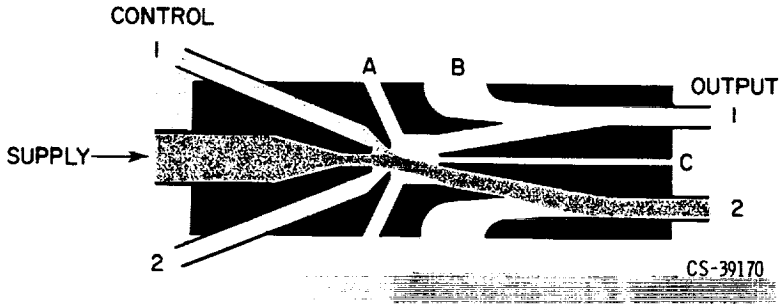

Figure IV-33. - Improved fluid jet amplifier.

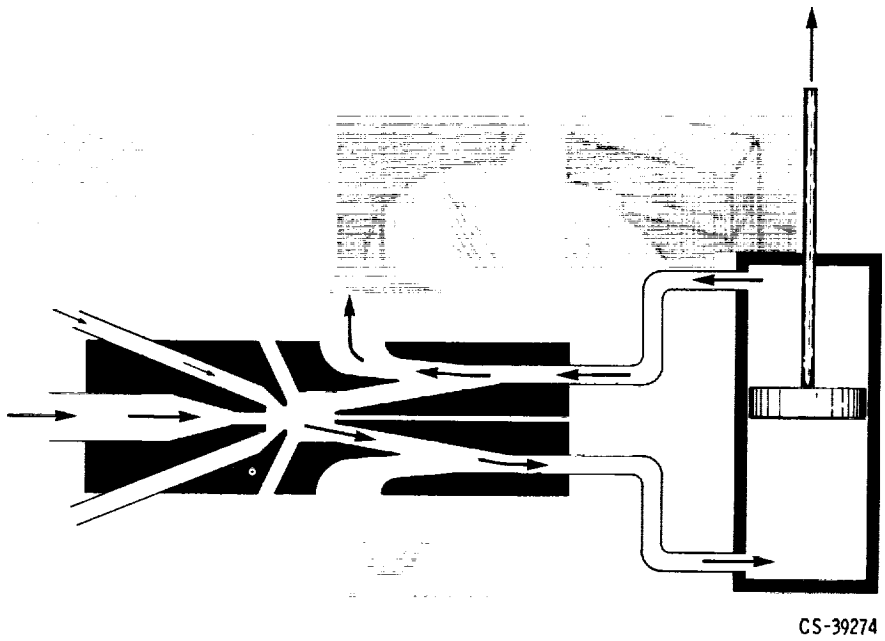

Figure IV-34. - Piston driven by fluid jet amplifier.

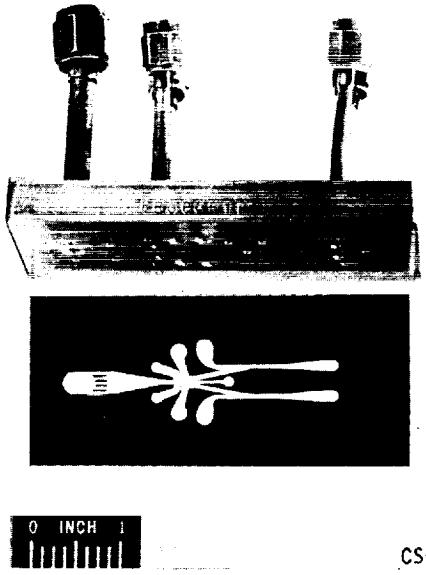

Figure IV-35. - Laboratory model of proportional amplifier.

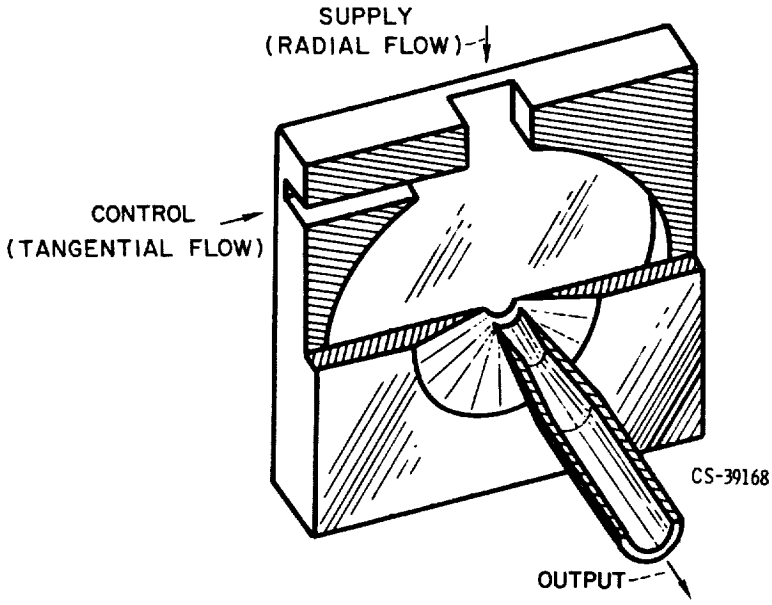

Figure IV-36. - Vortex amplifier.

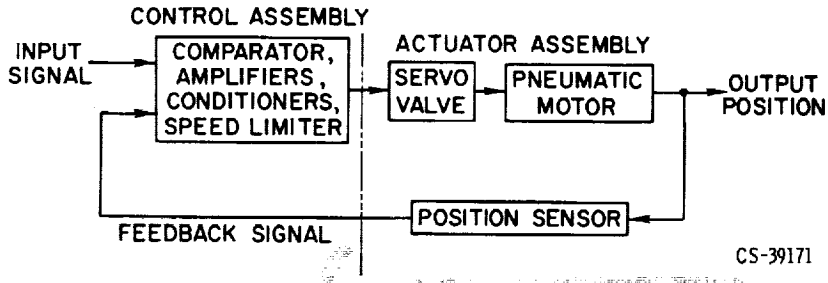

Figure IV-37. - Actuation servo for control drums and turbine-power-control valves.

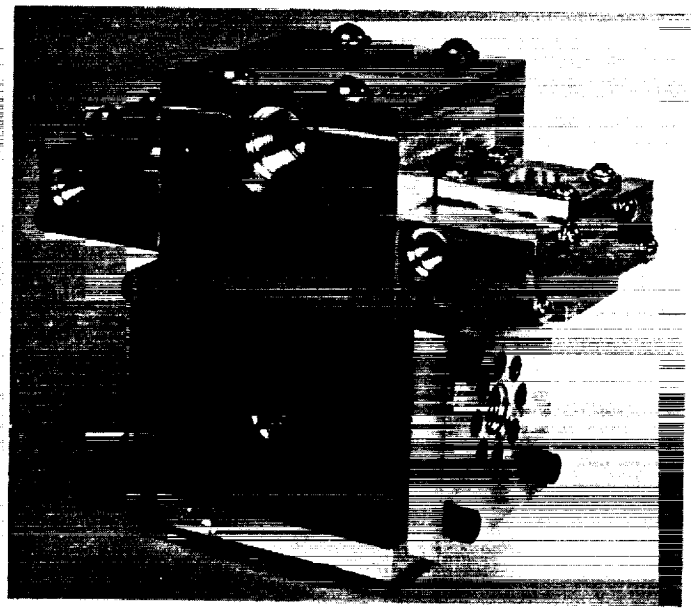

CS-39172

Figure IV-38. - Flueric servovalve.

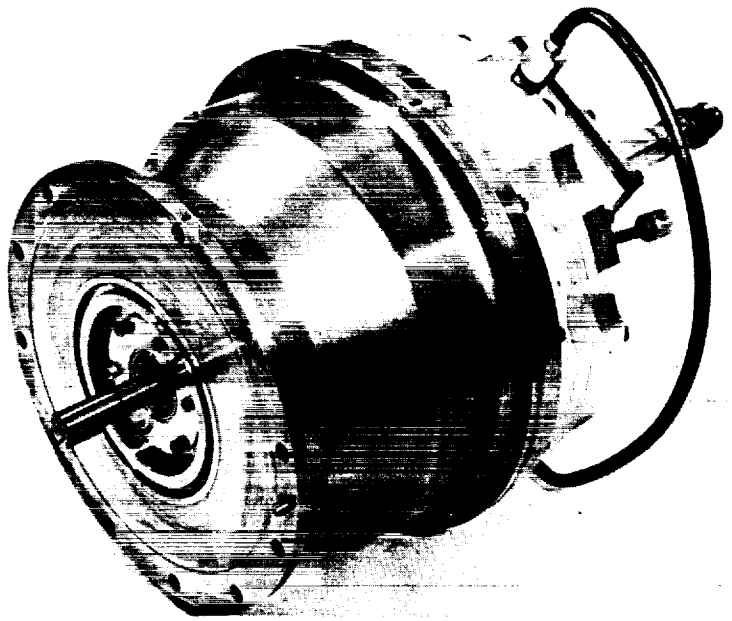

CS-39173

Figure IV-39. - Pneumatic nutator motor.

TUNGSTEN WATER-MODERATED NUCLEAR ROCKET

INTRODUCTION

The Lewis Research Center has been studying tungsten-matrix fuel elements at a modest research level since about 1956. The early studies used lithium hydride and other solid moderators for these thermal reactors. A switch to light water was made around 1958. By 1960, the concept of a tungsten water-moderated reactor was well defined. The necessary research required to establish the engineering feasibility and the performance of such a nuclear rocket system was then organized.

This program was accelerated in late 1961 and 1962 by Dr. Silverstein and Mr. Finger. A sizeable contract effort was initiated to augment the Center's in-house capabilities. Answers were required to such questions as (a) can uranium be contained in tungsten-matrix fuel elements, (b) can fuel elements be constructed in the shapes required for optimum strength and heat transfer, (c) are the neutronics acceptable, (d) can a reliable control system be included, (e) can the water moderator be cooled by the hydrogen propellant without freezing difficulties, (f) what will the performance, lifetime, and restart capability of such a reactor be, and (g) can the tungsten water-moderated reactor (TWMR) demonstrate sufficient performance gains over graphite to make its development worthwhile.

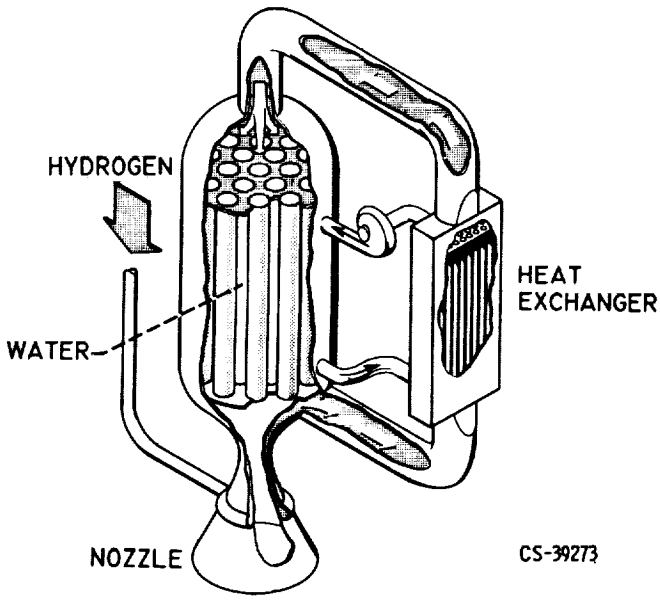

(a) Tungsten water-moderated reactor concept.

The research and the technology contributions that have been made to the tungsten water-moderated reactor program are summarized in papers V to VIII. Reasonable confidence now exists that useful tungsten water-moderated reactors can be developed. Whether they should be developed or not is beyond the scope of the research-oriented activities described herein.

Basically, the tungsten water-moderated reactor is a thermal reactor (sketch (a)). It utilizes water as the

moderator, uranium dioxide as the fuel, and tungsten as the fuel element structural material. As is common to all nuclear rocket systems, hydrogen is used as the propellant. The reactor consists of a tank pierced by a number of pressure tubes which are attached to tube sheets at the inlet and outlet ends of the reactor. The space inside the tank between the tubes is filled with water, which serves both as the moderator and a coolant for the structure. Heat is generated in the water by neutrons and gamma rays and is also transferred to the water from the hot fuel elements, which are located in each of the pressure tubes. The removal of the heat is provided for by pumping the water through the core and through a heat exchanger in a closed loop. The water is regeneratively cooled in the heat exchanger by the hydrogen propellant, which flows from the supply tank through the nozzle and heat exchanger into the core. As the hydrogen flows through the core and over the fuel elements, it is heated to a high temperature and is expanded out the nozzle to produce thrust.

The potential advantages of the concept lie in the following areas:

The use of tungsten provides a material with good thermal shock resistance and good tensile and compressive strength. Tungsten is not subject to corrosion by the propellant, and it permits the fabrication of fuel elements with very thin web thicknesses.

The use of water as the moderator provides a good low-temperature coolant for the pressure vessel and structural members.

The heterogeneous core allows for structural independence among the fuel assemblies and makes independent development of these components possible.

The desirable characteristics of a nuclear rocket system are reliability; high specific impulse; low weight, small size; growth potential; ease of development; long running time; and restart capability. High specific impulse requires high gas temperature and, therefore, high fuel element temperature. The size not only affects the weight of the powerplant itself but also affects the shielding requirements. Growth potential includes both a range of sizes and specific powers. Ease of development requires that the interaction between components be small so that each component can be developed independently. Long running times for nuclear rockets would be of the order of hours. Restart capability is desirable from a testing as well as an operational standpoint.

In order to study these requirements in depth, a reference design system was chosen. This reference design system focused attention on the actual engineering problems as well as on the limits for analysis and tests and established relations among the various components. The results of these studies are included in papers V to VIII, which are summarized as follows:

A REFERENCE DESIGN FOR THE TUNGSTEN WATER-MODERATED NUCLEAR ROCKET - A description is given of the design used as a reference in planning and executing the Lewis program of investigations of a thermal nuclear rocket propulsion system. Arrangement and types of component, normal operating conditions, and ma-

terials of construction are discussed.

REACTOR PHYSICS - The neutronics of water-moderated heterogeneous reactors using tungsten enriched in the 184 isotope is discussed. Analytical methods have determined and critical experiments have confirmed the margins of reactivity required for design. Separated and natural mixtures of tungsten isotopes are used to adjust radial- and axial-power distributions for best heat transfer. The desirable features of finely distributed in-core control systems are discussed.

MATERIALS AND FUEL ELEMENT - The properties of the tungsten - uranium dioxide fuel-element material, selection of fuel-element configurations, and methods of fabrication are discussed. Methods of stabilizing the fuel-element material under conditions of thermal cycling so as to ensure fuel retention at operating temperature have been studied. The limiting conditions of operation are presented.

FLUID SYSTEMS AND CONTROL - A discussion of the heat-transfer and fluid-flow characteristics is presented. The problem areas for major components in the hydrogen propellant system and in the water moderator loop are reviewed. With the use of analog representation, the performance of the components as an overall system has been studied and the stability and control of the system investigated. Finally, the size and weight variation of a family of reactors with the same general configuration is given.

A bibliography of the reports on the tungsten water-moderated nuclear rocket program published by NASA and by NASA contractors is included at the back of this report following paper VIII.

V. A REFERENCE DESIGN FOR THE TUNGSTEN WATER-MODERATED NUCLEAR ROCKET

Morton H. Krasner

Lewis Research Center

INTRODUCTION

Most of the information gained in the program has been used in the reference design. Design solutions to particular problems, other than those incorporated, were investigated during the program, and some of them are discussed in later papers. A final design for a specific mission may look quite different from this one, the principal purpose of which was to explore the concept.

This nuclear rocket concept includes the same general types of components as those in the graphite system described in papers II to IV. In figure V-1, which shows a block diagram of the tungsten nuclear rocket, these components can be identified as the reactor, the reactor control system, and the hydrogen flow system. In addition, this system requires a water flow loop and a heat exchanger for cooling the water. The reference design not only incorporates these new components but also introduces certain innovations into the propellant flow and the reactor control systems.

The performance characteristics of the system are as follows:

Reactor power, Mw	1500
Average outlet gas temperature, ^{o}F	4000
Hydrogen flow rate, lb/sec	93
Number of fuel assemblies	121
Maximum fuel element surface temperature, ^{o}F	4500
Fuel element outlet dynamic head, psi	12.6
Nozzle chamber pressure, psia	600
Specific impulse, sec	830
Maximum heat flux in fuel elements, Btu/(sec)(sq in.)	7.2
Hydrogen flow area, sq ft	2.1
Core power density, Mw/cu ft	40

The power level was arbitrarily set for the design and is in the range of the early graphite systems. The outlet gas temperature was also set as a design objective. From these two conditions, both the hydrogen flow rate and the number of fuel assemblies result. Operating limits for the various components which are assumed or demonstrated are fuel-element temperature, propellant dynamic head, and nozzle chamber pressure. Other factors achievable in the reference design include specific impulse, maximum heat flux, hydrogen flow area, and core power density. Specific impulse is based on a 40:1-area-ratio nozzle with an efficiency of 98 percent. For the calculation of core power density, the volumes of the metal reflectors were included.

REACTOR ASSEMBLY

Fluid Flow

Since the problems peculiar to the tungsten water-moderated nuclear rocket are principally in the core, this component received the most study.

The reactor arrangement is somewhat complicated because all the system elements converge in this region. Figures V-2 to V-8 simplify its description by showing the various parts. Figure V-2 is a cross section through the reactor assembly taken normal to the flow at midlength. The two radial cutting planes shown in figure V-2 create the axial section shown in figure V-3; the lower half results from the vertical plane and the upper half from the plane at 30° to the vertical.

These two views show an arrangement very similar to the concept schematic described in the preceding paper and shown in figure V-4. The pressure vessel is 52 inches in diameter, and the core region is about 55 inches long. The fuel assemblies are contained in $2\frac{1}{2}$-inch-diameter aluminum pressure tubes in which hydrogen flow is from left to right. These tubes are fastened to two tube sheets and arranged as shown in the cross section in figure V-2. Thermalization of the neutrons resulting from the fissioning of the fuel in the assemblies takes place in the water surrounding the pressure tubes. The tube sheets and the cylindrical pressure vessel, also made of aluminum, contain the water moderator. A beryllium side reflector and an inlet end reflector are also included in the core. The diameter of the outer surface of the side reflector is 43 inches. This side reflector reduces neutron leakage and helps distribute the power radially in the core. A flat distribution would result in maximum power output of the reactor. Then each of the assemblies could put out as much power as heat-transfer characteristics would permit. The inlet end reflector is used to shape the axial power distribution in the fuel assemblies. The goal in this shaping is to match the local power generation with the changing heat-transfer characteristics of the hydrogen and fuel elements for maximum effectiveness.

The water-to-hydrogen heat exchanger required in the concept to remove radiation induced heat from the water is also included inside the pressure vessel in order to couple this component closely with the active core both in time and space flow paths. This is done by dividing the heat exchanger into six shell and tube sections and placing them in an annular space just outside the side reflector. The rest of this annulus forms a water flow path and acts as a reflector. The water moderator is circulated between the core and the heat exchanger by a pump located outside the pressure vessel. The arrows in figure V-3 show water flow paths. Water leaves the pressure vessel near the outlet end and returns from the pump near the inlet end of the reactor. Water flow through the core region is in the same direction as the hydrogen flow. Water not only passes outside the pressure tubes to act as a coolant and moderator, but also passes through the side and top reflectors to cool them. Water flows in the shell portions of the heat exchangers from the outlet end of the core toward the inlet end of the core.

Because of gamma radiation, all materials in the vicinity of the reactor core require cooling. The flowing moderator is in contact with most of the pressure vessel walls and performs this cooling function. The pressure vessel head forms a plenum for distribution of the propellant to the pressure tubes. Gas is heated by the fuel elements inside the tubes and discharges into the nozzle chamber.

The arrows in figure V-5 indicate the hydrogen flow in the core region in more detail. In a nuclear rocket, the reactor fuel elements serve as heat-transfer devices for heating the propellant. Before ending up in the head region for distribution to the fuel assemblies, the hydrogen must pass through the tubes of the water heat exchangers. These components receive the cold propellant directly from the cooling passages of the nozzle at a temperature of -290^{o} F. There may be understandable alarm at the use of such a cold gas to cool water. However, it was possible to design and test a heat exchanger to operate at design conditions with a comfortable margin between the tube outer surface temperature and the freezing point of water. After flowing through the six units, the gas can be conveniently collected. The energy deposited in the gas in both the nozzle and the heat exchangers is then used to supply part of the power required to feed the propellant through the system. This is done by piping the gas out of the pressure vessel and through a turbine. The gas leaving the turbine reenters the pressure vessel through the head. A shadow shield can be located inside the head and conveniently cooled by the gas flowing over and through it on the way to the fuel assemblies. Of the 121 assemblies included in the core, 117 are used to heat most of the propellant to 4000^{o} F before it is discharged into the nozzle chamber. Insulation protects the outlet tube sheet from the hot gas. The rest of the hydrogen is used to provide the additional system pumping power requirements. As is indicated in paper II, some of the gas in the graphite system is also diverted from the main nozzle flow to supply pumping power. High-temperature gas, in that case, is diluted with cold gas to reach acceptable turbine inlet temperatures. The reduced-

temperature bleed gas for the tungsten system is supplied by using four special fuel assemblies in the central part of the core. The fact that the fuel assemblies are rather individual units makes this possible. The four units discharge at the inlet end of the core into separate ducts which carry the flow to the turbopumps.

Control System

With fuel assemblies, moderator, and coolant, all that is required to make the power source operational is a control system. Figure V-6 is an axial section through the core including both the hydrogen and water flow and the reactor control systems. Figure V-7 is an end view of the pressure vessel with the head and shield removed. This control system was designed to maintain a good power distribution in the core. In order to do this the thermal neutron absorber required for regulation of reactivity was distributed fairly uniformly across the core area. Figure V-6 shows the control devices used. These are fixed tubes extending down into the water moderator and interspersed among the fuel assemblies as shown in figure V-7. The tubes are Zircalloy and contain an aqueous solution of cadmium sulfate; the cadmium is a strong neutron absorber or poison. The result, in effect, is a core containing about 200 stationary small control rods. The amount of cadmium in the solution must be varied to control the reactor. This is done by connecting them to a flow loop in which the solution concentration can be adjusted. A schematic drawing of this control solution loop is shown in figure V-8. One control tube is used in this schematic to represent all the tubes. It contains an inner tube for bringing solution into the core. Flow out of the core is in the annular space between the tubes. The large number of tubes requires careful manifolding for good poison distribution. The rest of the control solution flow system is outside the pressure vessel. A heat exchanger using propellant gas as a coolant removes the heat deposited in the fluid by radiation, and a pump circulates the fluid at a constant rate around the loop. If a decrease in poison concentration is desired, a portion of the flow is bypassed through a mixed bed ion exchanger. The bypass flow reenters the main flow and reduces solution concentration before the core is reached. Bypassing continues until the required increase in core reactivity is established. Cadmium concentration in the solution is increased by injecting a cadmium sulfate concentrate into the main flow from a pressurized storage container. A combination pressurizer-accumulator rides on the main flow line to accommodate such volume changes and to maintain 600 pounds per square inch in the system. Solution temperatures range from 125^{o} to 215^{o} F.

Structure

Figure V-3 shows that the pressure vessel consists essentially of two containers. One of these is for hydrogen and is formed by the head, the inside surfaces of the pressure tubes, and the tube sheets. The other is for water and is formed by the pressure vessel cylinder, the outer surfaces of the pressure tubes, and the tube sheets. Since most of these members are water cooled on at least one side, temperature differences in the structure and thermal stresses should be low. In order to reduce the loads across the walls shared by these two containers, the water system pressure is regulated to match the hydrogen pressure. This is done specifically in the region of the outlet tube sheet since cooling is most difficult in the vicinity of the hot gas. With little or no pressure drop across the tube sheet, its thickness can be minimized and the cooling problem reduced. The principal load on the inlet tube sheet results from the aerodynamic forces on the fuel assemblies. In this arrangement the tube sheet is supported by the inlet end reflector. This 3-inch-thick beryllium member thus serves a dual purpose. The load is transferred by means of a collar attached to each pressure tube which bears on the reflector. A forged beryllium disk would be used in its fabrication. Forged beryllium has reasonable room temperature ductility and high strength, and forgings of this general size were produced for early project Mercury capsules. The cooling of the reflector is very important. Water is not only in contact with both flat surfaces, but also flows through the thickness in holes provided for the pressure tubes. This distribution of cooling assures very low temperature gradients resulting from gamma heating, and thus, the thermal stress problem common to heavy support grid plates is avoided.

The pressure tubes, the inlet and outlet tube sheet, and the inlet end reflector form an independent structural network; its integrity does not depend on fuel assemblies inserted into pressure tubes.

The principal functions of the fuel assemblies are to hold the fuel material in position and to provide flow passages for the propellant, but they must also reduce heat leakage from the hot fuel element to the aluminum pressure tubes. All these functions must be accomplished with minimum restraint of relative thermal expansion of fuel assembly components and the aluminum structure.

Figure V-9 is a section through one of the propulsion type fuel assemblies in which the inlet and outlet tube sheets, the pressure tube, the load transfer collar, and the inlet end reflector are again located. The fuel element is broken into 26 fuel element stages, $1\frac{1}{2}$ inches long, to prevent possible maldistributions in long parallel flow paths. The spaces between stages allow some flow redistribution. The stages are attached to an axially continuous support tube. The thin tube is made up primarily of tungsten and is attached to the inlet tube sheet for axial support. To keep the 55-inch-long tube and attached stages from excessive vibrations, lateral supports are located along its length.

The main lateral support is at the hot end and consists of a spline and keyway arrangement which allows relative axial and radial expansion between the pressure and support tubes. Auxiliary lateral spring supports are located at various points in the hot region and allow the same freedom. The pressure tube is also laterally supported near its midlength by an orifice plate used for water distribution.

The cold end support tube attachment incorporates a seal which enables the establishment of a stagnant hydrogen zone between the pressure and support tubes. The low conductivity of this gas coupled with the presence of the support tube acting as a radiation shield thermally insulates the pressure tube. Pressure tube temperatures can be kept below 300° F with reasonable cooling water velocities. The same technique of radiation shields and insulative gas spaces is used to protect the outlet tube sheet.

A beryllium reflector plug is located at the inlet end of each fuel assembly. These make up for the holes in the inlet end reflector provided for the pressure tubes.

NONNUCLEAR COMPONENTS

Figure V-10 is a schematic drawing of the overall engine system. The control solution loop previously described is omitted for simplicity (fig. V-8). Figure V-11 shows the water flow loop and includes design point operating conditions. It consists of the reactor region, with parallel flow through the side beryllium reflector, the heat exchanger, and the pump. Only the pump is outside the pressure vessel. System pressure is maintained at 600 pounds per square inch at the outlet tube sheet of the core. The total flow rate is 1040 pounds per second, and temperatures range from 240° F at the core exit to 195° F at the heat-exchanger exit. The flow through the active core region is 946 pounds per second.

Figure V-12 shows the flow of hydrogen propellant. The propellant must be forced from liquid storage at 35 pounds per square inch through the reactor to pick up the energy of the power source and through the nozzle to convert the energy to thrust. Since the hydrogen is also used to cool the nozzle, the water moderator, and the control solution, it must also be forced through various heat-exchanger passages. All pumping is done by two pumps in series, each with a different source of power. The pumps raise the pressure of the 93-pound-per-second hydrogen flow to 1180 pounds per square inch. The hydrogen then cools the nozzle walls and the water moderator in the heat exchanger in succession. In the process the temperature is raised to -160° F. The controlled bypass line around the heat exchanger provides flexibility of operation at off-design conditions, as is explained in paper VIII. The heat picked up in this necessary process of cooling the nozzle and water is used to supply two-thirds, or 6000 horsepower, of the required pumping power by passing the hydrogen through a topping turbine. Turbine control is achieved

with throttling and bypass valves. On leaving this topping turbine, the gas performs its other secondary cooling function when part of the flow is diverted through a heat exchanger to cool the control solution. The entire flow reenters the pressure vessel at 712 pounds per square inch and -140° F. The flow through the propulsion type fuel assemblies, 90.5 pounds per second, is heated to 4000° F and discharges into the nozzle chamber at 600 pounds per square inch to create thrust.

As mentioned previously, the rest of the flow is heated to a lower temperature in special fuel assemblies to supply the remainder of the system pumping power. Figure V-13 shows the path of this bleed flow. The division of flow occurs in the reactor head region, and 2.5 pounds per second of bleed gas leaves the pressure vessel at 1400° F and 600 pounds per square inch. It then flows through three turbines in series before discharging to the atmosphere. The turbines drive the control solution circulating pump, the water moderator circulating pump, and the first stage propellant feed pump. Each turbine is supplied with a controlled bypass line and a throttling valve for control during operation.

SYSTEM STARTUP

As mentioned previously, the conditions given in the figures are for operation at design power. The startup of the graphite system is discussed in paper IV. Since the tungsten system contains additional components and since the design incorporates modifications in the propellant feed and reactor control systems, this operational phase was also considered in the tungsten program at Lewis. Although there is more discussion of this in papers VI and VIII, the effect of the water moderator on the way in which the system is brought to power is discussed here. For this discussion, a likely startup sequence is described.

Small startup pumps for the control solution and water moderator systems are used to circulate these fluids slowly. The pumps require about 1 horsepower. With no hydrogen flow, the reactor is brought critical and to some low power level by reducing the poison concentration in the control solution. With no hydrogen flow the fuel elements increase in temperature, and heat is transferred to the circulating water moderator. The low power condition is maintained until water is at about normal operating temperature. At that point the liquid hydrogen tank shutoff valve is opened and hydrogen flow starts through the system under tank pressure to initiate the same sort of bootstrap procedure discussed in papers III and IV. The mass of warm water in the reactor system has two effects on this operation. First, it is a source of stored energy which can be transferred to the propellant in the heat exchanger upstream of the topping turbine to help the bootstrap operation. Second, it not only tends to keep up the hydrogen flow, but also starts

to increase reactor power. (The second effect is due to the negative water temperature coefficient of the core.) Hydrogen flow and water flow are rapidly increased as power increases until design conditions are established at rated power and full thrust is developed.

OTHER POWER LEVELS

As stated previously, the rated power for the reference design was an arbitrary choice. The discussion in this section has demonstrated the way in which the basic simple system schematic diagram shown in figure V-4 was translated into a feasible 1500-megawatt system. Certain variations would be required for a nuclear rocket with a different power level.

Obviously, a different power level would require a different number of fuel assemblies. Any required number of pressure tubes could be incorporated into a structure similar in nature to the one described. Fuel assemblies of exactly the same size and design could be used in this structure to produce the new power. The heat exchangers could be sized to handle the energy deposited in the water moderator. Modification of the pressure vessel diameter would be required to house the required components. The other system components depend primarily on fluid flow rates and pressure drops. These conditions, then, would set sizes of turbopumps, nozzles, valves, and piping required for different power levels.

The structurally important inlet end reflector would be expected to vary in thickness as core diameter would change. However, since its function as a reflector depends on thickness, it may be desirable to maintain that dimension at a minimum of 3 inches even at lower powers.

Reactor physics considerations also enter into this process of varying design power in other ways. As core sizes become larger, required excess reactivity becomes easier to achieve. This would indicate greater flexibility in the manipulation of nuclear parameters and the possibility of better performance. Conversely, as core sizes decrease, neutron leakage from the core increases and required reactivity becomes a more difficult and finally a limiting problem. Design flexibility therefore decreases as power is reduced. Reactor control system possibilities may also change as power varies. A more detailed discussion of many aspects of reactor physics appears in the next paper.

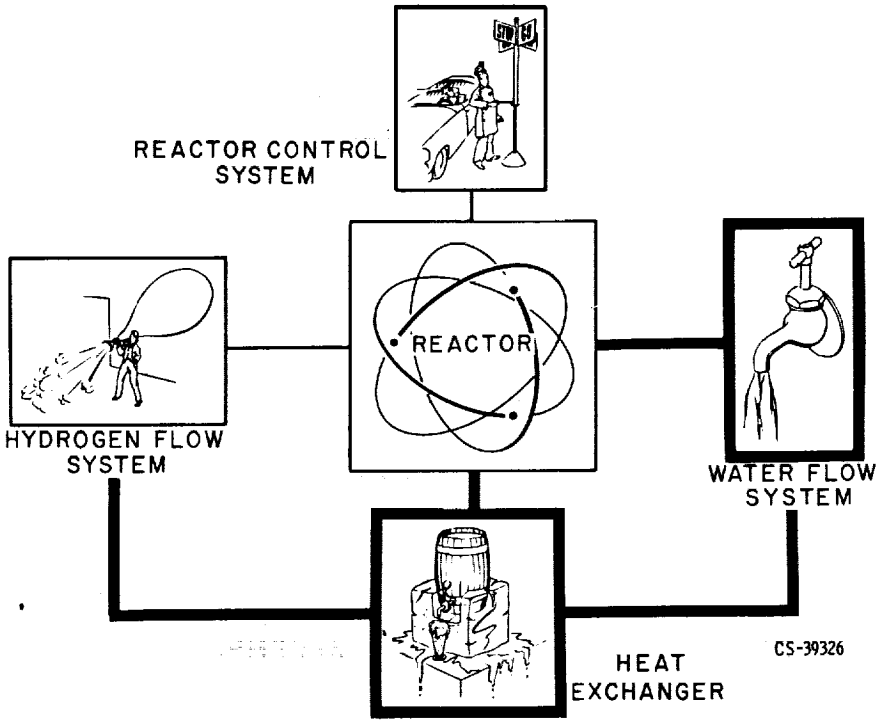

Figure V-1. - Component block diagram for tungsten nuclear rocket.

This figure UNCLASSIFIED

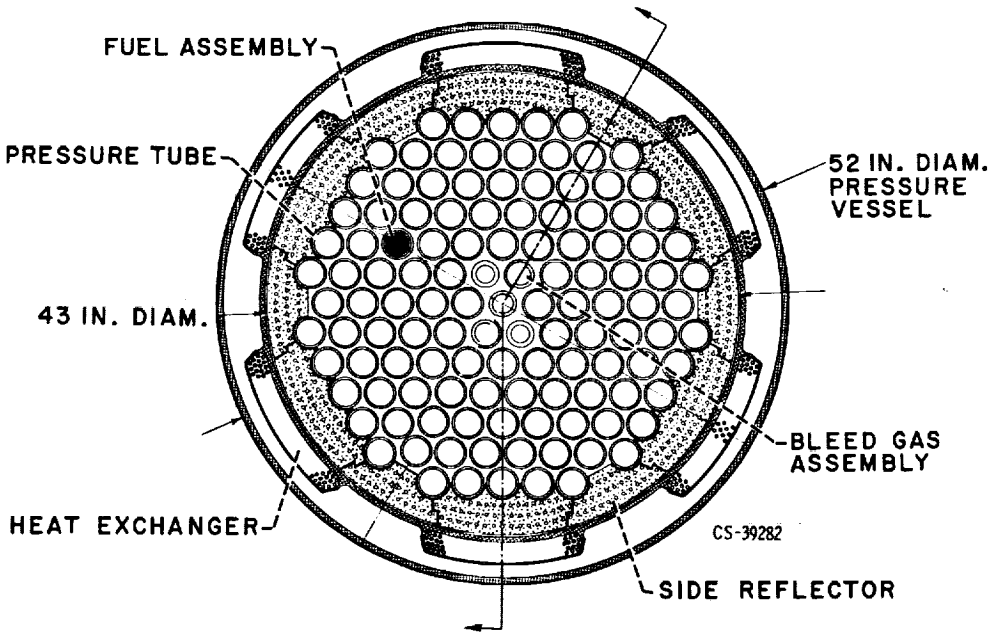

Figure V-2. - Cross section of reactor assembly.

This figure CONFIDENTIAL

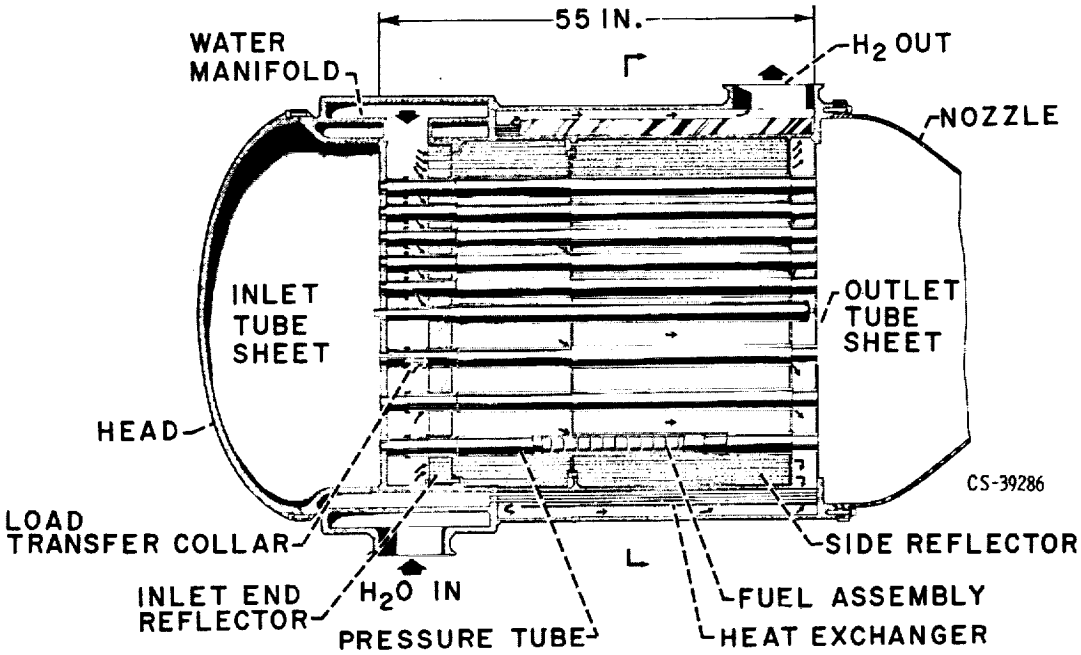

Figure V-3. - Axial section of water region in reactor assembly.

This figure CONFIDENTIAL

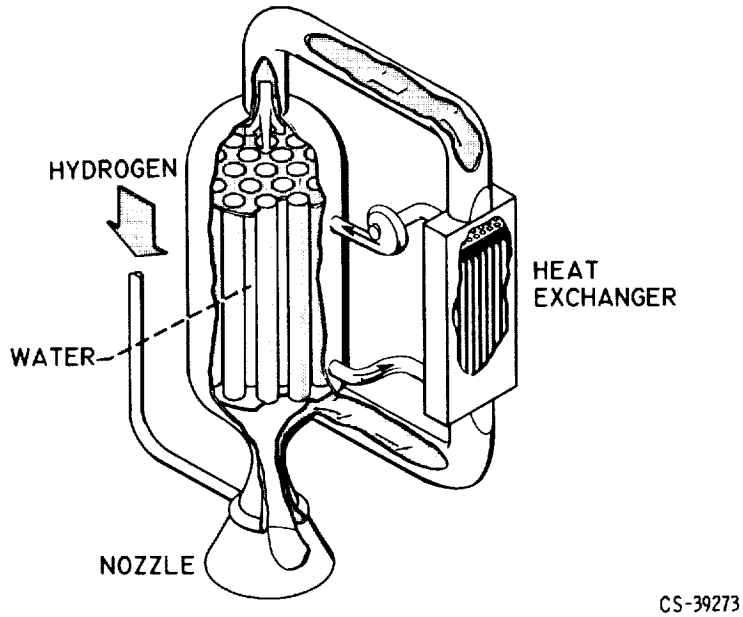

Figure V-4. - Tungsten water-moderated reactor concept.

This figure UNCLASSIFIED

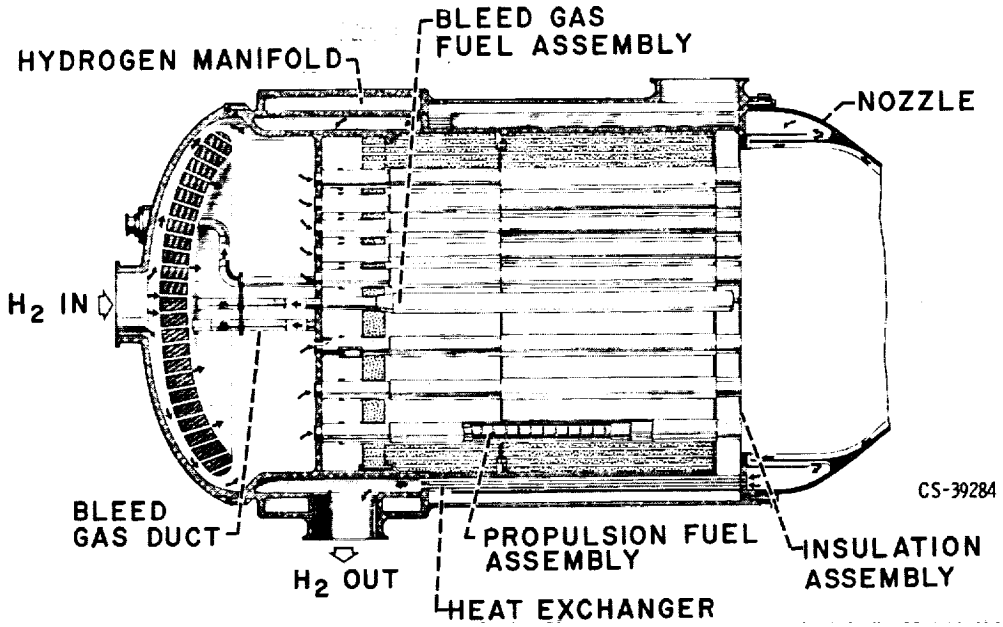

Figure V-5. - Hydrogen flow in axial section of reactor assembly.

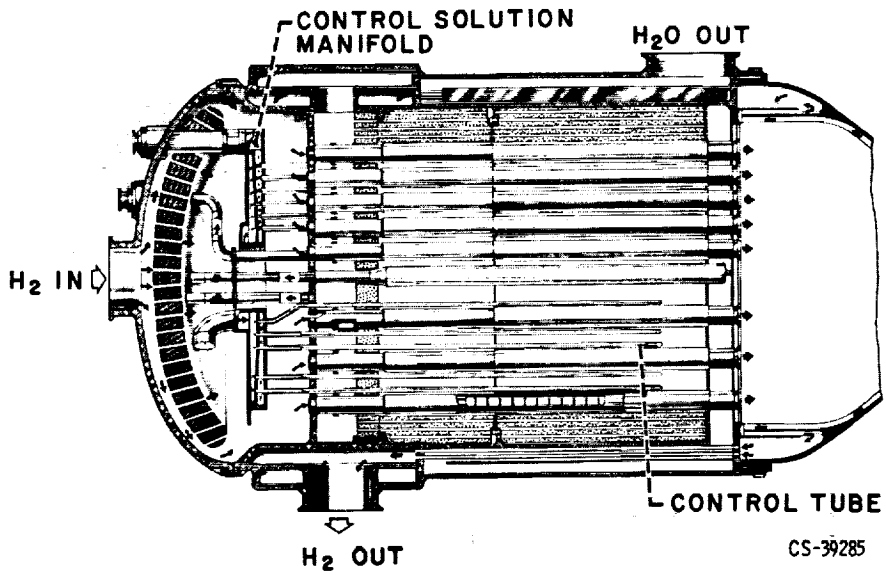

Figure V-6. - Axial section of reactor assembly.

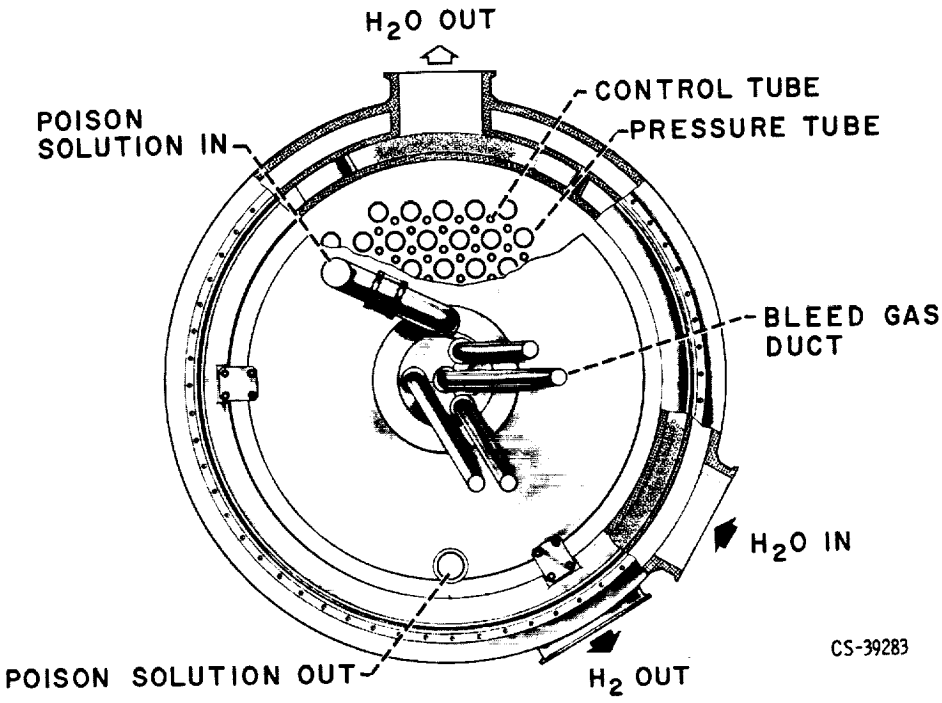

Figure V-7. - End view of reactor assembly.

This figure CONFIDENTIAL

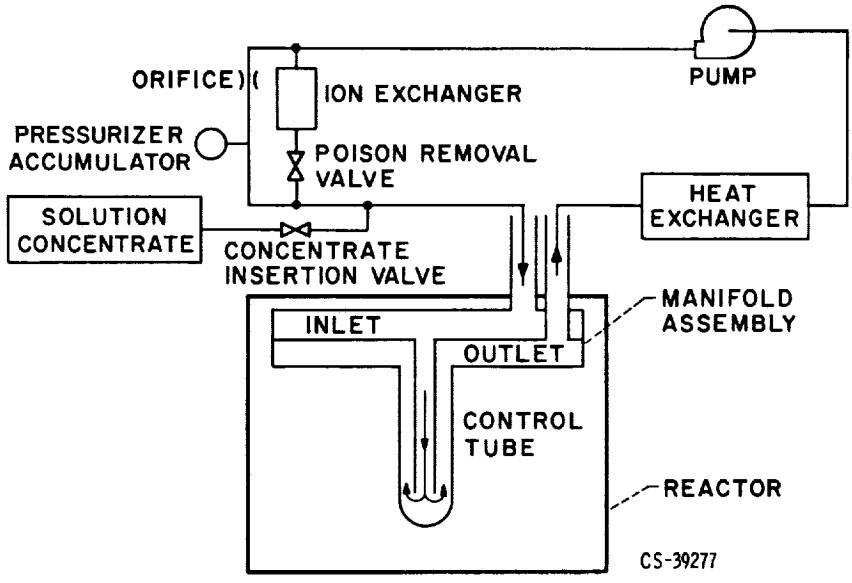

Figure V-8. - Schematic diagram of reactivity control solution system.

This figure UNCLASSIFIED

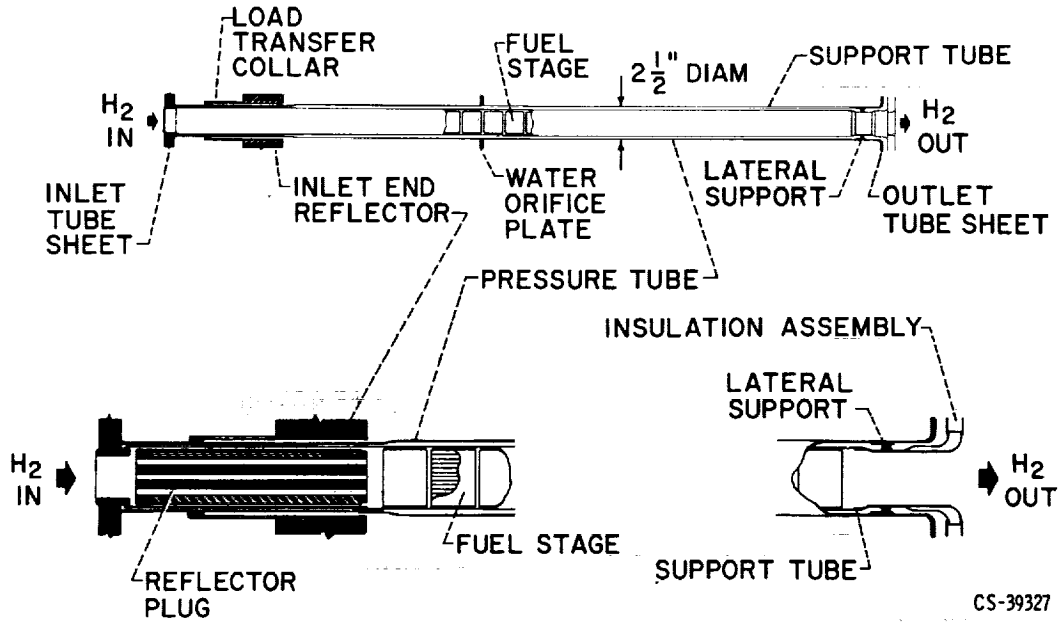

Figure V-9. - Propulsion fuel element assembly.

This figure CONFIDENTIAL

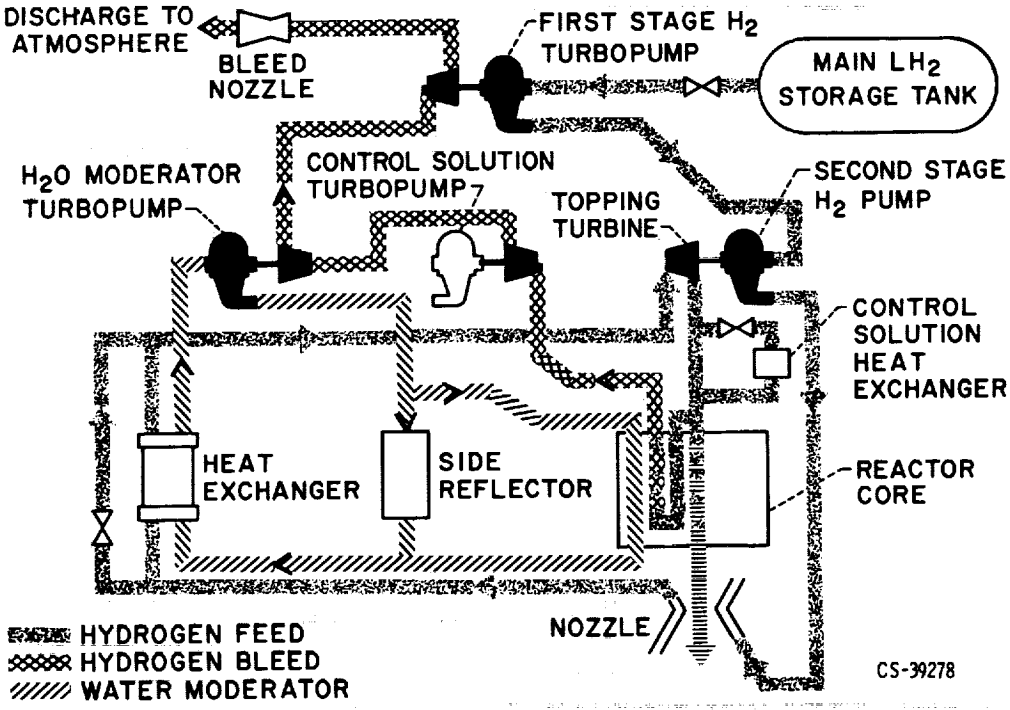

Figure V-10. - Schematic diagram of overall system.

This figure UNCLASSIFIED

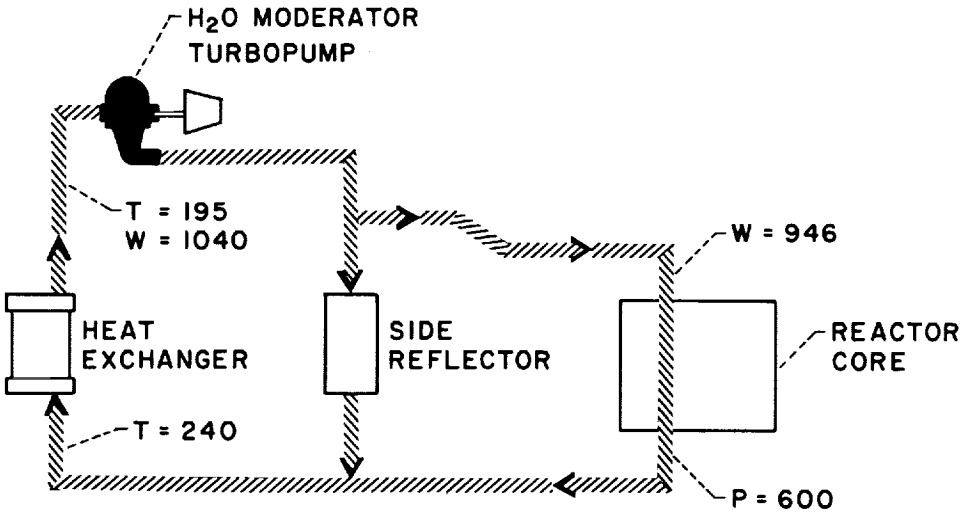

Figure V-11. - Schematic diagram of water system. Pressure, P, pounds per square inch absolute; temperature, T, °F; weight flow, W, pounds per second.

CS-39280

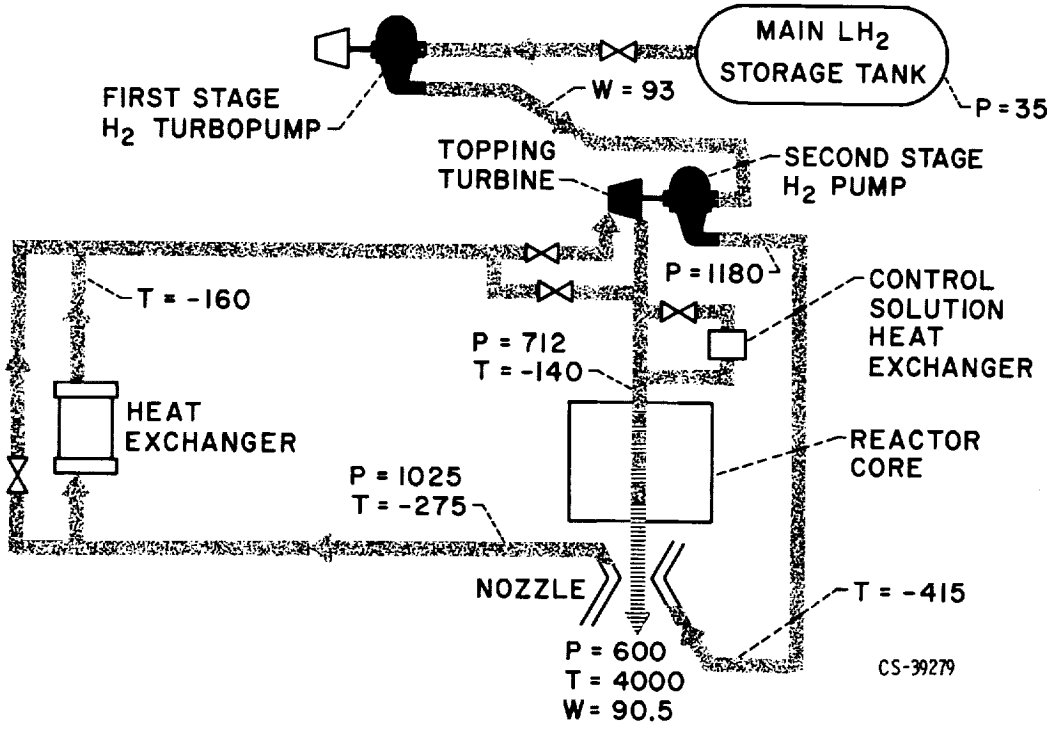

Figure V-12. - Schematic diagram of hydrogen propellant system. Pressure, P, pounds per square inch absolute; temperature, T, °F; weight flow, W, pounds per second.

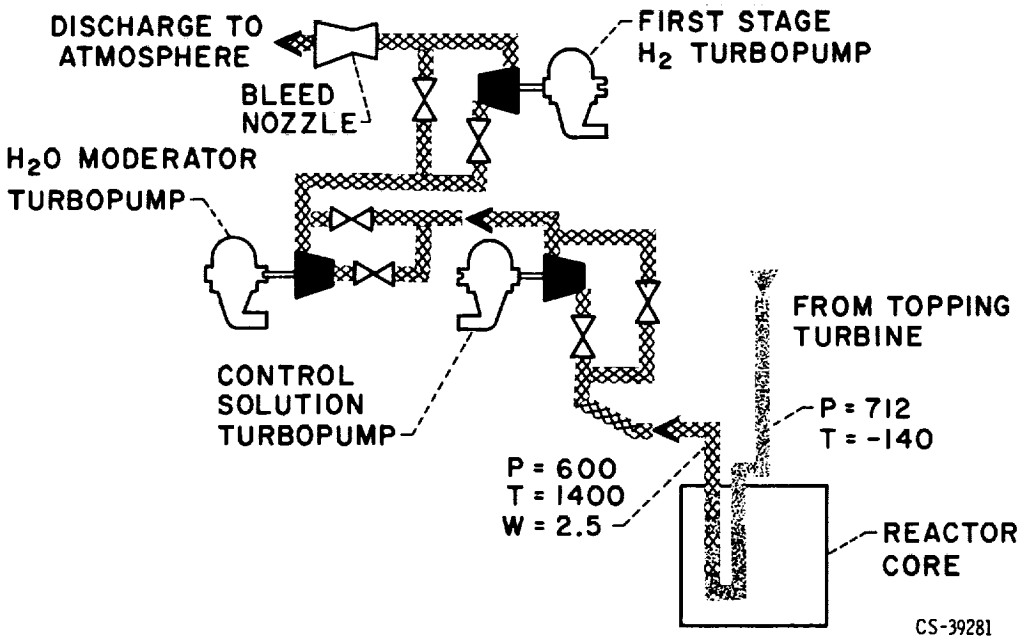

Figure V-13. - Schematic diagram of hydrogen bleed system. Pressure, P, pounds per square inch absolute; temperature, T, °F; weight flow, W, pounds per second.

X66-51412

VI. REACTOR PHYSICS

Donald Bogart, Edward Lantz, Wendell Mayo, and Paul G. Klann

Lewis Research Center

INTRODUCTION

The reactor physics work performed for the tungsten water-moderated reactor is described herein. In the other papers, the mechanical design of the reactor and dynamic aspects of the system are discussed. This paper deals with the neutronic behavior of the reactor as designed within the mutual limitations imposed by the other phases of the concept. It is shown that analytical methods have determined and critical experiments have confirmed the margins of reactivity required for the design which uses separated tungsten enriched in the 184 isotope. As a means for tailoring the radial and axial power distributions for desirable heat transfer, mixtures of natural tungsten and a single mixture of enriched tungsten have been considered and their use is illustrated.

At the outset, an understanding of the core geometry is necessary. In figure VI-1 a cross section of the reactor is shown. The fuel assemblies through which the hydrogen propellant flows are arranged in an hexagonal array and are surrounded by a light water moderator. Most of the fissions in this reactor take place at essentially thermal energies because of the unique neutron slowing down properties of the water moderator. The core is reflected by a primary beryllium and a secondary water reflector. A water-to-hydrogen heat exchanger is located in the secondary reflector.

A sector of this reference reactor is shown in figure VI-2. The fuel elements have a 2.5-inch outside-diameter aluminum pressure tube. For structural strength, tungsten is used that is enriched in the 184 isotope which has one-tenth of the absorption cross section of natural tungsten. The center-to-center distance between fuel elements is about 3.1 inches; this fuel-element spacing is a measure of the amount of water in the core. The hydrogen propellant density in the fuel-element regions is very small compared to the hydrogen density in the water and contributes negligible moderation.

The reference reactor employs a finely distributed in-core control system. The reentrant control tubes containing dilute absorptive solutions are distributed throughout the entire core and are shown in figure VI-2 as small circles spaced among the fuel-element tubes. Because the control tubes affect neighboring fuel assemblies only, the amount of

control that can be obtained becomes virtually independent of core size. The radial beryllium reflector is an average of 2.5 inches in thickness and contains about 10 percent by volume of cooling water. The beryllium is scalloped to displace water near the outer fuel assemblies in order to minimize circumferential power peaking.

In the reference reactor, the fuel-element spacing is kept constant so that the entire core is made up of hexagonal cells as shown in figure VI-2. The initial objective of the neutronics work to determine the multigroup parameters of these cells. These cell parameters are then used to arrive at a reactor design that allows each fuel element to operate near its best condition for transferring energy to the hydrogen propellant.

The incentive for flattening and shaping the power distribution is to produce maximum gas and propellant temperature in each fuel assembly. These must be consistent with the limiting maximum metallic fuel temperatures and the maximum dynamic loads on the fuel-element stages.

There are many methods that may be exploited to shape the power distributions to that desired. In particular, there is the method that distributes the fissionable materials nonuniformly throughout the core and the method of varying the water spacing between fuel assemblies. These techniques have been used in reactor designs in the past.

In the present reference design, the available range of fuel loadings of uranium dioxide in the tungsten - uranium dioxide matrix has been employed to flatten the power across the individual fuel cell. The method of flattening power across various fuel cells in the core in the radial direction employs natural tungsten as a distributed parasitic absorber. This is accomplished by making some of the tungsten support tubes that support the fuel-element stages out of natural tungsten rather than separated tungsten.

The method of adjusting the axial power distribution to one that is desirable for heating the propellant up to the required temperature in the shortest length of time requires a combination of heat-transfer and neutronic calculations. Here too natural tungsten is used as a distributed parasitic absorber. Since the reference design uses separated tungsten in the fuel element, replacing part of the separated tungsten by natural tungsten in strategic fuel stages of the fuel assembly can shape the axial power. With the judicious use of these special stages in conjunction with the use of inlet reflectors, the desired axial power distribution has been approached quite closely. In the reference design shown in figure VI-1 the core has uniformly spaced fuel assemblies, which are identical to each other in geometry and composition, in a hexagonal array.

The selection of the fuel-assembly center-to-center spacing is reserved so as to fulfill a very important requirement of the reactor design. This requirement is that the reactor should be inherently self-stabilizing during power operation. The requirement can be achieved by designing for a negative water temperature reactivity effect. The center-to-center distance between fuel assemblies shown in figure VI-2 is all important in establishing the desired negative effect.

The reactor shown in figure VI-1 is about 4 feet in diameter and represents the reference reactor for which an indepth study has been made. Its power level is approximately 1500 megawatts. These reactors can be increased in power level by adding more of these identical fuel assemblies with a resultant increase in core diameter. However, the tantalizing prospects lie in going in the other direction - that is, in exploring the possibilities of designing very small cores. These compact cores will be discussed later.

It is recalled that the reference reactor has a finely distributed in-core control system, which consists of reentrant tubes in the water spaces between fuel assemblies. These tubes contain a flowing cadmium-water solution of low concentration. Such a dilute system is capable of controlling the core with a minimum of perturbation to the power distribution in the neighboring fuel assemblies. Although reactors that employ a rotating drum control system in the radial reflector are familiar, such reflector control systems are inadequate for the larger cores. It will be shown that for large reactors an in-core finely distributed control system is independent of core site and has many advantages. The first area to be discussed concerns the neutron cross sections. The reactor concept requires precise neutron cross sections for all of the tungsten isotopes. Therefore, considerable emphasis was placed on cross section measurements early in the program.

The second area will be the development of reactor analysis methods. Ordinarily, reactor designs depend heavily on the results of critical experiments. Because of the unavailability of the required amounts of separated tungsten, semiempirical approaches that rely on critical experiments to a large extent have been rejected in the present study. Reliance has been placed on neutron transport calculations using the S_n transport programs for the core cell calculations. The basic separability of the axial and radial neutron flux distributions and the relative uncoupling of the fuel-element cells permit the use of one-dimensional multigroup programs for gross criticality calculations. The validity of this approach has been checked by two-dimensional calculations.

The third area is the establishment of the reference reactor design that has been previously described. Although a range of reactor sizes was looked at, one reference reactor was adopted for detailed study.

In the final area, the analytical design method has been confirmed by a series of critical experiments which simulate the reference reactor. Because of the relative completeness and precision of the microscopic neutron cross sections for the materials of the reference reactor, a high degree of confidence can be placed in the accuracy of fuel-element cell calculations. Critical experiments have been performed to check the overall accuracy of the calculations and to confirm the desired negative temperature coefficient of reactivity.

CROSS SECTIONS

Tungsten has many large resonances in the intermediate neutron energy range (fig. VI-3), and an accurate knowledge of the resonance parameters is required for precision neutronic calculations. The major competitors for neutrons in the tungsten water-moderated reactor are tungsten and uranium 235. The competition is in proportion to the amount of each material and to the magnitude of their respective cross sections. In order to maximize absorptions in the fuel, uranium enriched to 93 percent in uranium 235 is employed. Absorptions in the tungsten should be minimized in so far as is practical. Natural tungsten has a thermal cross section of 18.3 barns, which may be reduced by almost an order of magnitude by enriching in the tungsten 184 isotope. Since tungsten 184 has no significant resonances below 185 electron volts, enrichment is even more attractive. Even with large enrichment, a significant fraction of the neutrons may be expected to be absorbed in separated tungsten. The resonances may be effectively bypassed, however, by slowing the neutrons down in the water outside of the fuel elements and thereby keeping neutrons away from the tungsten.

TABLE VI-1. - CROSS SECTIONS FOR TUNGSTEN ISOTOPES

Cross section	Remark	Instrument
Capture to 10 eV	±3 percent	General Atomic linac
Resonances to 2100 eV	20 levels	Oak Ridge National Laboratory fast chopper
Resonances to 2200 eV	125 levels	Rensselaer Polytechnic Institute linac
Inelastic scattering to 1.5 MeV	14 levels	Argonne National Laboratory, Van de Graaff accelerator

Table VI-1 summarizes some recent work on cross sections for the individual tungsten isotopes. Capture cross sections at low energies below 10 electron volts have been measured recently at the General Atomic linac with a precision of ±3 percent.

The resonance region to 2100 electron volts has been studied at the Oak Ridge fast chopper facility; 16 resonance levels in tungsten 184 above 185 electron volts have been measured and 4 major levels of non-184 isotopes have been remeasured.

The resonance region to 2200 electron volts was covered by the Rensselaer linac, and parameters for a large number of resonance levels in all of the isotopes are being measured.

Finally, the high energy inelastic scattering cross section to 1.5 million electron volts are being measured at Argonne with the Van de Graaff accelerator. The partial cross sections for many inelastically excited levels in tungsten 184 and natural tungsten have been reported and tungsten 182 and 186 isotopes are being measured.

As a check on the precision and completeness of these available microscopic cross sections, several integral experiments were undertaken at the Lewis Research Center. The first of these is the measurement of effective resonance integrals for the isotopes of tungsten.

A reactor that is used as a reactivity measurement facility is shown in figure VI-4. The unreflected aluminum reactor vessel is 12 inches in diameter and contains a uranyl-fluoride-water solution. The neutron slowing down flux in this core is similar to that provided in the concept reactor. Isotopic samples are enclosed in cadmium covers at the center of the core and criticality is achieved at a particular solution height that is accurately measured. The change in solution height for samples of various thickness is related to that for a standard reference such as thin gold for which the resonance integral is known.

Figure VI-5 shows effective resonance integrals I_{eff} for gold. Values of I_{eff} are in barns and represent the average epicadmium resonance capture cross section per atom as a function of sample size. The sample size is given by the parameter $(\text{surface-to-mass ratio})^{1/2}$ of the sample. This parameter correlates results for most sample geometries and corresponds to an inverse thickness for a slab sample. Large values of surface-to-mass correspond to very thin samples in which very little self-shielding of neutrons occurs. The epicadmium reactivity and activation data points show that I_{eff} decreases as samples get thicker. The reference dilute integral or unself-shielded value of 1585 barns for thin gold has been used as a standard.

The solid line is the calculation of these epicadmium values of I_{eff} by the Nordheim method, which follows the data very well giving credence to the experimental and analytical methods.

The effective resonance integrals for separated tungsten 184 mixtures are shown in figure VI-6. The data points are for tungsten samples made of isotopic mixtures that are highly enriched to approximately 94 percent in tungsten 184. In the reference reactor, the geometries of the tungsten 184 samples correspond to values for $(\text{surface-to-mass ratio})^{1/2}$ of 0.50 to 1.00. The Nordheim calculations using the known resonance parameter data for the tungsten isotopes predict the experimental data very well. Interestingly, the 184 contribution to I_{eff} by itself is only approximately 25 percent of the total integral even for these highly separated tungsten 184 mixtures. This shows the importance of the large resonances of the non-184 isotopes.

Another integral measurement that has been made is shown in figure VI-7. This is a tungsten-water age experiment. The age for fission energy neutrons is proportional to the mean square distance a neutron will travel from the point of fission to where it becomes a low energy neutron. An array of natural tungsten rods in a water tank with a radioactive neutron source and detector foils located in the array of rods was used. The magnitude of the experimental age is an indirect measure of the high energy cross sections.

Therefore, comparison of the experimental and calculated values of the age is a check on how well high energy elastic and inelastic cross sections are known.

The age results are shown in figure VI-8 for plutonium-beryllium source neutrons. The age to 1.44 electron volts in square centimeters is plotted as a function of percent tungsten in tungsten-water mixtures. Three tungsten-water mixtures were measured and the ages for these mixtures are less than the age for pure water. This immediately indicates the importance of the tungsten inelastic cross sections because the inserted tungsten rods slow down fast neutrons better than the displaced water. The calculated curves are from the GAM-II cross section multigroup compilation that is used for reactor studies. Although the plutonium-beryllium source spectrum has been measured above 1 million electron volts, it is generally known that there is a low energy component that has not been measured. The plutonium-beryllium source spectrum that was used required a 20±5 percent component at approximately 0.5 million electron volts in order to normalize the calculation and experiment for pure water. When this spectrum with its 20 percent component is used, the calculated results are shown by the solid line, which is about 10 percent lower than the ages measured for the tungsten-water mixtures. This difference is believed to be due to the use of the evaporation model at high energies which exaggerates slightly the inelastic scattering effects due to tungsten. If the ±5 percent uncertainty in this component is used, the bottom and top dashed lines, respectively, are obtained.

REACTOR ANALYSIS METHODS

The analytical part of the reference reactor study program serves several functions. It provides a vehicle for the understanding and interpretation of physical phenomena, for the design and specification of pertinent experiments, and for the extension of experimental data into areas not specifically covered by the experiments.

Figure VI-9 indicates very briefly how the neutronic calculations proceed. The basic problem is to obtain an adequate approximation to the solution of the Boltzmann transport equation. Of course, calculational methods have not evolved to the point where the general reactor problem can be solved in one package. Rather, it is solved in a series of steps. Iterative numerical methods programmed for the digital computer are used.

The basic calculation for the reference reactor is the solution of the fuel-cell problem. The GAM-II and GATHER programs are used to obtain multigroup spectrum averaged microscopic cross sections for the materials in the fuel element. The Nordheim resonance calculation is done within the GAM-II program for the tungsten isotopic and uranium 238 resonances.

Spatial neutron flux solutions for the fuel-element cells are obtained using an S_n transport theory program. The cells are usually cylindricized on an equal area basis which permits detailed one-dimensional calculations to be made. Two-dimensional (x, y) cell solutions may be obtained when required. For example, cell self-shielding factors due to the pressure of the liquid poison control tubes are most accurately computed using two-dimensional programs. The self-shielding factors resulting from these cell calculations are used in the GAM-II and GATHER programs to recompute the neutron spectrum and macroscopic average cross sections.

These cross sections are then used in full core spatial calculations to obtain the reactor multiplication factors and gross radial and axial power distributions. A radial-axial buckling synthesis technique is used with one-dimensional programs, although two-dimensional (r, z) calculations also have been performed.

Another analytical problem that is important to the tungsten water-moderated reactor is that of gamma heating. Since the magnitude of the water temperature plays an important part in the system operation, accurate calculations of the energy deposition in the water by gamma rays is required. Figure VI-10 indicates the technique used for solving the gamma ray problem. The basic task is to determine the origins, capture locations, and energies of the gamma rays. The Monte Carlo program ATHENA was developed for this purpose. Neutrons and gamma rays, both primary and secondary, are tracked by Monte Carlo methods in three-dimensional geometry to provide heating rates in any part of the reactor. Up to 81 energy groups may be used. Also, a statistical estimator is used to compute heating rates and fluxes at point detectors inside or outside of the core in reasonable computing times.

REACTOR DESIGN AND CRITICAL EXPERIMENTS

Reference Reactor Design Considerations

The basic calculation in the reference reactor is the estimation of the multiplication factor for the fuel cell. This cell consists of a fuel element, its pressure tube, and the proportional amount of surrounding water moderator.

The multiplication factor as a function of water thickness for several concentrations of tungsten 184 is shown in figure VI-11. The water thickness parameter shown is the distance between adjacent pressure tubes. The multiplication factor, in the absence of any leakage of neutrons, is just the number of neutrons produced per neutron absorbed in the cell. The bottom curve is for natural tungsten with 30.7 percent tungsten 184. Results for enriched tungsten containing 78.4, 87, and 94 percent of tungsten 184 are also shown.

The general similarity of the shape of the curves is noted. As the water thickness is increased from small values, the number of neutrons slowing down past the resonances increases and the multiplication increases. A point is reached, however, where an additional water moderator acts as a parasitic absorber and the multiplication decreases. This corresponds to an overmoderated condition; the region to the left of the peak multiplication corresponds to the under-moderated region.

A substantial gain in multiplication with increased enrichment in tungsten 184 is obtained. This increase is due to the decreasing thermal absorption cross section which goes from 18.3 to 2.9 barns with enrichment, while the effective resonance integral goes from 38.6 to 10.7 barns. This accounts for a major part of the increase in multiplication. It is clear that some enrichment of tungsten 184 is required. The availability and cost of tungsten enriched in the tungsten 184 isotope are therefore of prime importance.

The aspects of separated tungsten 184 production have been considered in detail at Oak Ridge. The K-25 gaseous diffusion plant at Oak Ridge is capable of separating tungsten isotopes. This plant has been mothballed, but the results of a technical and economic study for producing tungsten 184 that was conducted by the K-25 people are shown in figure VI-12. The unit costs are shown on the right for various enrichments in tungsten 184. This unit cost curve rises very rapidly above 90 percent enrichment. The choice of the 87 percent enrichment for the reference isotopic mixture shown has a reasonable unit cost and the annual production shown on the left for this enrichment is indicated to be 10 000 pounds.

Figure VI-13 again shows the neutron multiplication as a function of water thickness for the reference cell using tungsten enriched to 87 percent in tungsten 184. The maximum multiplication is about 1.39, and it occurs at a water thickness of a little more than 1/2 inch and decreases for less water due to increased resonance absorption in the tungsten.

The lower curve shows the neutron multiplication for the core with 121 of these fuel elements inside the beryllium reflectors that were previously described. This curve takes into account the neutrons leaking out as well as those absorbed in the reactor. For a water thickness of 1/2 inch, the multiplication is decreased to about 1.18. The reason for the interest in the under-moderated region to the left of the maximum is that this is the region where significant negative temperature reactivity coefficients can be obtained. With a negative coefficient, as the core temperature increases, the core loses reactivity. As a result of this behavior, the reactor power is self-stabilizing. Since temperature is the key parameter that must be controlled for reliable rocket reactor operation, it will be shown that this negative temperature coefficient of reactivity can be a very useful feature for taking the reactor up to power and for power regulation.

Preliminary calculations indicated that a water thickness of about 0.54 inch might give a sufficiently negative coefficient. However, the calculation of the exact water temperature coefficient of reactivity is difficult because of the many variables that are temperature dependent. Also, the use of isotopically enriched tungsten in a thermal reactor was without precedent. Therefore, an experimental critical program was initiated to determine the precise amount of excess reactivity available and to determine if the water temperature reactivity was sufficiently negative.

Critical Experiments

The reference reactor design was neutronically and physically simulated for a series of critical experiments. Figure VI-14(a) shows the critical assembly. The core is contained in a $6\frac{1}{2}$-foot-diameter water tank, and the pressure tubes that contain the fuel assemblies are shown. These tubes are inserted through the upper grid plate.

A cutaway view of the critical assembly is shown in figure VI-14(b). The upper and lower grid plates that space the 121 fuel assemblies in a hexagonal array are shown. Before the reactor is made critical, water is pumped into the tank filling the spaces between the fuel elements and around the core.

The beryllium reflector used consisted of a 4-inch inlet reflector (not shown) that was assembled in the area below the core and the $2\frac{7}{8}$-inch beryllium side reflector. This side reflector was backed by 1/4 inch of boral sheeting to reduce the reactivity effects of the exterior water. It is noted that the reference core is upside down in the experimental configurations, that is, the inlet beryllium reflector is at the bottom. The beryllium side reflector was faced by a scalloped aluminum plate which mocked up the true shape of the reflector.

The dilute poison control tubes are located at the midpoints of the triangular water gaps between the fuel elements. These tubes contained cadmium solution to hold down the excess reactivity of the core.

The isothermal temperature coefficient was measured in these cores by heating the moderator water in a series of steps to 180° F and measuring the reactivity using calibrated control rods.

The first two experiments were made at two different fuel-element spacings to study the change of the core excess reactivity and temperature coefficient with fuel-element spacing. These experiments were made with the core reflected with water only, because of the flexibility of water reflectors to permit changes in fuel-element spacing. One of these fuel-element spacings was then selected for the beryllium reflected experiment which was a mockup of the reference design.

Since large quantities of separated isotopes were not available for construction of fuel elements, the neutronic characteristics of the fuel element had to be simulated in the mockup core. Figure VI-15 presents a cutaway view of the fuel element to show how the simulation was accomplished mechanically. The outside diameter of the aluminum pressure tube is 2.56 inches. The fuel stages contain the correct amount of uranium 235 but required substitute materials for the tungsten 184 mixture. The two views on the right show schematically how the simulation materials are distributed. A uranium-aluminum alloy is used as the fuel. The enriched tungsten is simulated using natural tungsten in reduced amounts to match the correct thermal cross section. In order to match the correct resonance region capture, a single ring of depleted uranium 238 was employed. A total of 121 of these fuel assemblies were used in the critical experiments. The final sizes of the simulating materials were based on numerous calculations so as to assure an accurate neutronic simulation.

The calculated results showing the precision of the simulation are given in table VI-2. The results are given in terms of absorptions per source neutron for the reference and simulated cores. The hydrogen, oxygen, and uranium 235 absorptions agree very well. Since the separated tungsten is simulated by using a combination of natural tungsten and uranium 238, the sums in both cores must be compared. The sum is 0.150 for the reference core and 0.153 for the simulated core. The aluminum shows some mismatch although the total absorptions per source neutron compare very well. The total for the reference core is 0.851 and the total for the simulated core is 0.854. The difference of the absorption from unity is due to the neutron leakage. The thermal utilization quantity shown is the ratio of thermal absorptions in fuel to total thermal absorptions, and the match in this parameter is indicative of how precise the simulation is at the thermal energies. The slowing down ages may be compared as an indication of the match of the slowing down properties of the two cores. The difference shown is due to a small high energy scattering mismatch.

TABLE VI-2. - PRECISION OF FUEL-ELEMENT SIMULATION

Absorption		
Material	Reference core	Simulated core
Hydrogen	0.071	0.069
Oxygen	.002	.002
Aluminum	.001	.014
Uranium 235	.617	.616
Tungsten	.146 } 0.150	.095 } 0.153
Uranium 238	.004 }	.058 }
Total	0.851	0.854

Core	Thermal utilization	Age, cm^2
Reference	0.7857	95.16
Simulated	.7820	90.56

These comparisons of reference and simulated cores are on the basis of calculations. In order to obtain experimental confirmation of the simulation, several kilograms of calutron separated tungsten isotopes were obtained from Oak Ridge. These isotopes were used to fabricate 5 special stages which were substituted for five of the stages in the center fuel assembly

TABLE VI-3. - COMPARISON OF REFERENCE AND SPECIAL FUEL STAGES

Fuel stage	Tungsten isotope			
	182	183	184	186
	Weight in fuel stage, g			
Reference	6.18	38.82	339.61	5.52
Special:				
5-Ring	6.15	38.91	162.16	5.63
8-Ring	7.92	40.30	244.20	7.84
11-Ring	9.78	41.75	332.00	10.15

of the mockup core and the resulting change in reactivity was measured. The special stages were in the form of concentric rings of metallic tungsten isotopes.

The isotopic tungsten composition of the reference fuel cell could not be exactly matched with these special stages. However, its expected reactivity worth was bracketed by varying the number of rings. This can be seen in table VI-3, which shows the number of grams of each isotope in a reference stage and in three configurations of special stages. It is seen that the 5-ring stage closely matches the reference stage in every isotope except 184. Due to the deficiency in 184, this 5-ring special stage must be less absorptive than the reference stage. As more rings are added to increase the 184 content, the amounts of the other isotopes also increase. Consequently, when the amount of 184 is closely matched, as it is in the 11-ring case, there is too much of the other isotopes, which make this configuration more absorptive than the reference stage. Therefore, the reactivity of these 5- and 11-ring special states will bracket the reactivity of the reference tungsten stage.

The results of the experiment are shown in figure VI-16. The ordinate gives the reactivity which would result from a total replacement of all the mockup stages in the core by special stages which have the number of rings listed in the abscissa. The reactivities measured with the special fuel-element stages were converted to their full core counterparts by an analytically derived constant. It is noted that the reactivity of the mockup stages is experimentally found to lie in between that of the 5- and 11-ring special stages. Thus from the extremes of this experiment it can be expected that the reactivity of the mockup core is within ±2 percent of that of the reference core.

Actually, the agreement is considerably better than this. The comparative deviation between the mockup core and the core built of 8-ring special stages was calculated. The result of this calculation is shown by the triangle. It is seen that it agrees to within 1/2 percent in reactivity with the measured value. This close agreement lends strong support to the method of treating the individual isotopes of tungsten in the calculations used in establishing the mockup core.

The results of the critical experiments on the mockup core are given in figure VI-17. The multiplication factors are shown as functions of the center-to-center spacing between the fuel elements. Measured multiplication factors for the three critical configurations investigated are plotted. The values obtained at the 2.9- and 3-inch fuel-element spacings

with water reflectors are indicated. When the beryllium reflector is added, a 5-percent increase in multiplication was obtained for the 3-inch spacing.

The precritical calculated values are shown by the solid lines. The lower curve is for water-reflected cores while the upper one is for beryllium-reflected cores. It is noted that the reactivity of all cores was consistently underestimated initially by about 2 percent in reactivity.

More detailed calculations were subsequently performed for the water-reflected configuration with 3-inch spacing. These calculations included two-dimensional calculations of the fuel-element cell and the total core, and improved treatment of the resonance effects. These refined results are shown as the dashed line on the figure and were found to agree with experiment to within 1/2 percent in reactivity.

Because a negative water temperature coefficient was desired, spacings on the undermoderated side of the multiplication curve were investigated. On the left side of the curve a reduction in the amount of water between the fuel elements results in a loss of multiplication. This is indicated by comparing the 3-inch water-reflected configuration with the 2.9-inch configuration. A negative temperature coefficient is therefore suggested on the left side of the curve since the multiplication is decreased as the water density is reduced by heating.

The purpose of the first two critical experiments with the 2.9- and 3.0-inch water-reflected configurations was to find the fuel-element spacing that had a suitably negative temperature coefficient with sufficient overall core reactivity. The 3-inch spacing was found to be most satisfactory. The beryllium-reflected reference core was then built using the 3-inch spacing.

Power Distributions

The detailed radial power distributions within a fuel element are very important in the reactor design since the maximum exit gas temperature can only be obtained if each fuel ring is operating near the maximum allowable temperature. Therefore, the spatial distribution of the power in the fuel-element cell must be accurately known. An experiment conducted to measure the radial power distribution within a simulated fuel element is shown on figure VI-18. The relative power density is plotted as a function of the radius of the fueled region. The simulated fuel element, shown in the insert, is similar to that previously described. The fuel consisted of seventeen 1-mil uranium 235 sheets wrapped with fission fragment catcher foils interspersed so to measure relative power. The catcher foils and fuel sheets are shown schematically along the abscissa. These are distributed in the region between the 0.25- and 1.00-inch radius shown. Natural tungsten and uranium 238 were distributed similarly to represent enriched tungsten. The thin

natural tungsten ring shown represents the support tube. The circles are the experimental data points. They are normalized to 1.0 at the outside radius of the fuel. The power decreased from this point to a value of 0.46 at the inner radius. The triangular points are calculated values using multigroup transport theory, and the agreement is very good.

The radial power fall off is due primarily to the attenuation of the thermal neutron flux. Neutrons slowing down in the water constitute nearly the entire source of thermal neutrons. Therefore, the power, which is proportional to the fission cross section times the flux, falls off. The distribution shown is typical of an unzoned fuel element. This power distribution would require orificing of each propellant channel within the fuel element in order to operate at maximum exit temperature. The more desirable alternative is to flatten the power in the fuel element by fuel zoning. The flux will still decrease toward the center of the element but the fuel is distributed so that the power is relatively flat. Since the calculation and experiment are in good agreement for the experiment shown in figure VI-18, the same calculation can be used to compute the loading schedule for uniform power.

Figure VI-19 shows the radial power in a zoned 10-ring fuel element. The power distribution relative to the average power in the cell is shown for each of the 10 fuel rings. The ring numbers correspond to the fuel rings indicated on the insert. The loading schedule used is given for each fuel ring. A loading of 32 volume percent uranium dioxide in tungsten is assumed to be the metallurgical limit for these fuel elements and was used in the center ring. The loading decreases to 12.9 volume percent at the outside. This zoned distribution of fuel compared to the unzoned fuel element results in a reduction of about 1 percent reactivity. The variation of the power through the fuel ring is not serious because of good fuel ring thermal conductivity. In ring number 8, the calculated variation is ±5 percent relative to the average in the ring. If the power were flat through the ring, the metal temperature would be decreased only 14° F.

However, the power distribution is still not quite perfect. Note the slight dip in power in rings 6, 7, and 8. An increase of 0.2 volume percent uranium dioxide in these rings would correct this. However, this is well within the ±0.5 volume percent estimated uncertainty in the manufacture of any given fuel ring.

Another type of power distribution that is important within the fuel element is the circumferential power distribution.

A sector of the reference reactor is shown in the upper sketch of figure VI-20. It is noted that the amount of water varies around the perimeter of the fuel element. The greatest amount of water is in the triangular gaps where the control tubes are located. There are two competing effects here - there is an effect causing flux peaking where the most water exists and an effect causing flux depression due to the cadmium in the control tubes. These two effects tend to cancel one another.

The rectangular cell used to compute the circumferential power distribution is shown on the lower half of figure VI-20. The left half is shown as it is represented in the two-dimensional S_n transport calculations in (x, y) geometry. The circular boundaries are necessarily represented as steps. The area of each region is conserved. If advantage is taken of the 180^o symmetry that exists, only the left half of the cell need be specified. Even with this savings in mesh size, a 15-group 400-point problem will just about overflow a computer with a 32 000-bit storage. The reactivity of the cadmium solution is also obtained from this type of calculation.

The data points in figure VI-20 indicate the circumferential power for the case with pure water in the control tubes. The values given are the power in the specified mesh interval relative to the cell average power. The variation circumferentially amounts to about 4 percent from the smallest value of 1.47 to the maximum of 1.53 near the control tube which contains water only. Peaking is reduced when the control poison is present as it will be under normal operating conditions. This point was checked experimentally, and it was found that there is negligible circumferential peaking around the central fuel element when reference cadmium concentration is in the poison tubes. Figure VI-21 shows the results of activation measurements made with foils circumferentially placed around two of the fuel elements in the critical assembly. The purpose of the measurements was to determine the effects of the poison control tubes and of the reflector on the circumferential power distributions. The ratio of the power at the angle φ to the average power around the fuel element is plotted as a function of φ. For the center fuel element, negligible circumferential power variation was observed with the dilute reference concentration in the control tubes.

The results of circumferential power measurements made on a fuel element located at the edge of the core indicate a power peaking of about 6 percent in the direction of the water gaps between the fuel elements at the reflector. These water spaces between the fuel elements and the reflector can be reduced and still allow adequate cooling. This should reduce the power peaking at the reflector. The power peaking is included as a local factor in heat-transfer calculations.

Of equal importance to the radial and circumferential power distribution within the fuel element are the gross radial and axial power distributions in the core.

Figure VI-22(a) shows the radial power density in the uniform or unzoned core. The measured local to average radial power for all the fuel elements in a 1/12 sector of the core is shown plotted as a function of the radial position of the fuel element. The measurements were made by counting the fission product gamma activity of the middle axial fuel stage of each fuel assembly.

The values calculated by a one-dimensional cylindricized representation of the core are shown by the solid line. It is noted that good agreement is obtained except near the edge of the core. The deviations here are believed to be due to the cylindrical approxi-

mation of the hexagonal boundary of the core employed in the calculation.

Since the power generation of the core is not uniform across the core radius, not all of the fuel assemblies are operating at the limit of their heat-transfer capability, and consequently, there would be a reduction in the hydrogen gas exit temperature. This could be compensated for by orificing the hydrogen flow to the outer fuel assemblies to maintain the required exit temperature. However, this would result in a reduction of total core power.

Another way of maintaining the exit temperature would be by decreasing the fuel loading in the center fuel assemblies. However, there are manufacturing advantages in keeping all the fuel assemblies identical.

Water-moderated reactors designed with fuel-element spacings that increase with core radius were investigated early in study. In this method of zoning, water is removed from the center of the reactor and a flatter radial power generation is obtained. The fuel cells that result are not uniform.

The method of flattening the radial power that was chosen for the reference design was the use of natural tungsten support tubes in central fuel assemblies. In this way it is possible to keep the fuel loading and the fuel assembly spacing constant and to flatten the radial power distribution by placing an additional parasitic tungsten absorber around the central fuel assemblies.

The reference reactor design is particularly adaptable to this method, since the tungsten absorber can be incorporated by replacing the enriched tungsten support tubes with natural tungsten support tubes.

Figure VI-22(b) shows an example of radial zoning in which the relative power generated in the fuel assemblies is plotted as a function of radius in the core. The effect of replacing the tungsten 184 support tubes in the central 19 fuel assemblies with the more absorptive natural tungsten support tubes is shown by comparing the curve for the uniform core to a calculation and the measured values for the zoned core. The power generated in the outer fuel assemblies is significantly closer to that generated in the central assemblies in the zoned core. This means that the propellant hydrogen flow to these outer fuel assemblies does not have to be orificed as much in the zoned core to maintain the maximum exhaust gas temperature from all assemblies. This zoned core has about 2 percent less reactivity than the uniform core.

In order to discuss the axial power distribution, recourse must be made to figure VI-23, which was originally discussed in paper V. This figure shows the fuel assembly and a cutaway sketch of one of the stages. The axial power distribution is concerned with the distribution of power between the axial stages. The composition of materials in some of these fuel stages can be adjusted to make the amount of power generated in the stage closer to that which is desired for efficient heat transfer. In addition, the axial power distribution is shifted by use of a neutron reflector at the inlet end of the core.

It consists of a beryllium plug with axial holes that are sized to set the hydrogen flow to the fuel assembly, a beryllium plate that supports the fuel assemblies, and the water in and around the inlet plenum.

Figure VI-24(a) shows the axial power density in a uniform core. The power measured in each of the stages of three fuel elements is shown. One of the fuel elements measured was located at the center of the core, one at an intermediate position, and one at the edge of the core. The measured power in each stage normalized to the average of all the stages in that assembly is shown plotted against the axial location of each stage. The inlet beryllium reflector is at the left, and the outlet water reflector is at the right.

The normalized results for the three fuel elements are seen to coincide closely. Thus, the similarity of the axial power distributions for all the fuel elements is seen to be an indication that the axial and radial power distributions are separable.

The solid line shows a diffusion theory calculation for the axial power distribution. Good agreement is found everywhere except near the inlet beryllium reflector where a 10 percent underestimation occurs. Better results might be obtained at the inlet beryllium reflector with transport theory calculations.

In figure VI-24(a), it is noted that the power is shifted slightly toward the inlet end by the beryllium reflector. This shift toward the inlet is desirable because for a given fuel surface temperature more heat can be transferred to the cold entering hydrogen at the inlet than to the hot hydrogen further along the core.

Since separated tungsten is being used in this reactor, the use of some natural tungsten as a parasitic absorber provides a convenient means by which the axial power distribution may be further shifted to the inlet to better satisfy heat-transfer needs. The axial power distribution in the core, that is, the power in each of the fuel stages, is shown in figure VI-24(b). The power distribution for each stage of uniform composition is again shown as the dashed line. However, by using a mixture of 30 percent natural tungsten and 70 percent separated tungsten in these 10 stages, this more absorptive mixture shifts the axial power distribution to the solid line shown. The effects obtained are the results of using zoning with epithermal absorption rather than changing the fuel loading. This technique eliminates thermal spiking at zone boundaries and gives a smooth power distribution, which is much better suited for efficient heat transfer as will be in paper VIII. However, the introduction of some natural tungsten to accomplish this power shift reduces the available reactivity by about 4 percent relative to an unzoned core.

Reactivity and Reactivity Control

From a control standpoint, the two important reactivity effects are those due to the water and to the fuel temperatures. The reference core was designed with the small fuel-element spacings so that a negative water temperature coefficient of reactivity would be

obtained. In addition, a small water thickness magnifies the resonance absorption which, in turn, magnifies the negative fuel temperature coefficient.

Figure VI-25(a) shows the change in reactivity from the room temperature value as a function of the average water temperature in the core. The curve is from early calculations for a zoned core that appeared to be desirable and was used for the control system studies. The points plotted in this figure are experimentally measured values for the unzoned isothermal critical assembly with a beryllium reflector.

There are two effects that are not accounted for in the experiments. One is the effect of zoning the core for a better power distribution. It should be noted that in this calculation the radial power was flattened by varying the fuel-element spacing. The other is the effect of having the cadmium solution in the control tubes at a lower temperature than the water temperature, as will be the case in the rocket reactor.

From the curve shown in figure VI-25(a), it is seen that about 1 percent in reactivity is used in taking the water from room temperature up to the nominal operating temperature. This loss in reactivity must initially be compensated for by a control system. However, once the reactor is in this hot critical condition, the reactivity in the hot water can be regained by dropping the water temperature.

To understand how this reactivity can be used to advantage in getting the reactor up to power and for self-stabilization of power, it is recalled from the discussion in paper V that the heat which is absorbed by the water in the reactor is transferred to the cold hydrogen propellant in the heat exchanger. For steady-state operation at a particular power level, the heat absorbed in the water must equal the heat carried away. Consequently, for steady-state operation there must be a constant hydrogen flow through the heat exchanger. Otherwise, the hydrogen in the heat exchanger will either take away more or less heat than is put into the water in the reactor, and the water temperature will tend to go up or down. However, as seen in figure VI-25(a), as soon as the reactor water temperature deviates from this equilibrium operating value, the reactor will go on either a negative or positive period to get the water temperature back to the operating point. Thus the reactor power will follow the hydrogen flow to maintain a given water temperature. The power will follow at a fast rate without reliance on temperature sensors or external reactor control of any kind. A similar situation exists for the reactivity feedback accompanying variations of the fuel temperature. However, in this case the effect is more prompt because the hydrogen cools the fuel directly rather than hydrogen cooling the water through a heat exchanger.

The reactivity change with fuel temperature is a result of the absorptive tungsten resonances undergoing Doppler broadening with increasing fuel temperature and thereby interacting with a larger part of the neutron slowing down flux. The result is an instantaneous increase in resonance absorption with an increase in fuel temperature. Figure VI-25(b) shows the decrease in reactivity that promptly accompanies increasing fuel

temperature. The negative reactivity resulting from a change in core average fuel temperature from 68° F to any temperature is shown. About -1.5 percent reactivity is introduced by the fuel coming up to its average temperature of 3300° F. Although the maximum fuel temperature is 4500° F, this net Doppler effect is an average over the entire core.

The major part of this prompt negative feedback of reactivity arises from the resonances of the non-184 isotopes, in particular from tungsten 183. The slope of the line at 3300° F is negative and corresponds to the coefficient of reactivity that is chiefly responsible for the self-stabilizing properties of the reactor at rated power. Experimental Doppler coefficients for separated tungsten isotopes are presently being measured.

Another reactivity effect that must be accounted for is that due to transient fission products. The most troublesome of these is xenon 135, particularly for high flux thermal reactors. The thermal flux for the reference reactor is somewhat greater than 10^{14} newtons per square centimeter per second. During full power operation the core reactivity worth gradually decreases about 0.4 percent reactivity at the end of 1 hour due to xenon poisoning. If a reactor is shut down after a period of operation, the decay of this iodine to xenon results in a buildup of transient xenon which then decays with its own characteristic half life.

Figure VI-26 shows the reactivity of this transient xenon as a function of time after shutdown. For this calculation, the reactor is shut down after 1 hour of full power operation; consequently, the reactivity starts at a steady-state value of -0.4 percent reactivity and rises to a peak of about -8.5 percent reactivity 12 hours after shutdown. This curve assumes 100 percent retention of the iodine and xenon in the fuel stages. There is evidence that fission product gases diffuse through the tungsten clad at high temperature. Results of preliminary in-pile experiments are presented in paper VII. If it is assumed that about 30 percent of the iodine and xenon is lost through the clad by diffusion at the high operating temperature of the fuel, the transient xenon reactivity has a peak value of 6 percent reactivity, which means that this amount will be required to override peak transient xenon.

TABLE VI-4. - SUMMARY OF REACTIVITY EFFECTS

	Reactivity, Δk/k, percent
Reactivity for power tailoring	-7.4
Temperature defect	-2.5
10 Hours of operation in 1-hour cycles	-1.7
Transient xenon override	-6.0
Design and manufacturing tolerance	±1.5
Propellant hydrogen reactivity	0
Total	-19.1

A summary of all reactivity effects is given in table VI-4. These effects total up to 19 percent so that this amount, which was available in the unzoned critical assembly, is indeed necessary.

The 7.4 percent for power tailoring is made up of a little over 1 percent for flattening the power distribution within the fuel element, about 2 percent for the gross

radial power flattening, and about 4 percent for the axial power adjustment required for the reference core.

The 2.5 percent for the change of reactivity with temperature is made up of 1 percent for the water temperature and 1.5 percent for the fuel temperature change.

The reactivity required for operating the reactor for 10 hours is about 1.7 percent. This consists of 0.4 percent for the xenon poisoning accrued in an hour run, 0.8 percent for long-lived fission product poisoning including samarium, 0.3 percent for fuel transmutation, and 0.2 percent for an assumed fuel loss of 1 percent through the clad in 10 hours.

The 6 percent required for complete transient xenon override assumes 30 percent loss of iodine and xenon through the clad. If this is a good assumption and this 6 percent were available, the reactor could be restarted any time after full power runs up to 1 hour in duration.

An allowance is always required for design and manufacturing tolerances. The 1.5 percent can be plus as well as minus, but it is the minus contingency that is of concern. The positive reactivity can always be shimmed out, but a new set of fuel elements or redesign of the core might be required if a negative allowance is not made.

The propellant hydrogen reactivity is very small in this reactor. There is so much more hydrogen in the water than in the propellant that the hydrogen propellant has an insignificant effect on reactivity.

It is noted that not all of these reactivities need to be controlled. The reactivities that do need to be controlled are shown in table VI-5 along with the assumed reactivity control rates.

The 4.5 percent is for taking the reactor from the cold shutdown to the hot critical condition; 2 percent of this 4.5 percent is the shutdown margin and the other 2.5 percent is the loss in reactivity with temperature. The 0.057 percent per second rate, which is a nominal reactivity control rate, is sufficient to allow getting to hot critical in about 80 seconds; however, in starting up a rocket reactor a lot of hydrogen can be wasted in 80 seconds.

TABLE VI-5. - CONTROL CRITERIA

	Reactivity, Δk/k, percent		Rate, Δk/k/sec, percent
Cold shutdown to hot critical	4.5		±0.057
Temperature control (10-hr operation)	1.7	12.2	±.0035
Shutdown reactivity insertion	---		-.057
Transient xenon override	6.0		±.014
Emergency shutdown	15.0		-5.7

To shorten the time for getting up to full power after the hydrogen flow has been started, without increasing the 0.057 percent per second control rate, the reactor can be brought to this hot critical condition at a very low power level without the propellant hydrogen flowing. The temperature reactivity defect of 2.5 percent can be used to take the reactor from the low-power no-flow con-

dition to 95 percent of full power in about 15 seconds by accelerating the hydrogen flow.

After the hydrogen flow reaches its nominal value, this temperature reactivity will maintain the core temperatures during hydrogen flow fluctuations by its self-stabilizing reactivity characteristic. Also, once the reactor temperatures are set at their maximum operating values, it will be desirable to keep them there throughout the power run. Thus, the only function a reactivity control system will have during steady-state operation is to compensate for the slow change in reactivity that occurs during 10 hours of operation. The 1.7 percent for this will only require the low rate of change of 0.0035 percent per second. This will allow a fine control of temperature.

Due to the transport delay time in the water system, a larger and separate reactivity insertion rate may be required for shutting down the reactor at the end of a timed power run. A delay in achieving this rate can be compensated for by initiating it earlier in the sequence.

For the transient xenon the 0.014 percent per second rate can put in the 6 percent in about 7 minutes. This rate is also sufficient to feed in negative reactivity when the transient xenon is burning out.

Thus, it is seen that the total needed from a reactivity control system is about 12 percent. Also, the largest rate of increase of reactivity needed for this rocket reactor is no greater than is presently used in operating power reactors.

In order to make the finely distributed in-core control systems that are under consideration completely fail safe, independent stored-energy emergency shutdown methods will probably be required. These should be able to insert 15 percent at this fast rate of 5.7 percent per second. It can then be removed at the slower rate of 0.057 percent per second.

Investigations have shown that if conventional rods are used to control the 12 percent in reactivity the axial power distribution is completely distorted. Also, the control rods investigated caused considerable circumferential power peaking. As a result, the thrust to weight ratio and the specific impulse of a rocket reactor with control rods would be less than could be obtained with a finely distributed control system.

On the other hand, reflector control drums distort the radial power distribution, and large cores cannot be satisfactorily controlled by drums. Figure VI-27 shows various reactor reflector control effects. The reactivity of a thick beryllium reflector is plotted as a function of core diameter. The worth of the reflector is large for small diameter cores and is indicated to be worth about 35 percent in reactivity for a 20-inch-diameter core.

As the diameter of the core increases, the percentage of neutrons that leak out decreases and, consequently, the reflector worth decreases. For a 50-inch-diameter core, the reflector is worth only about 6 percent in reactivity.

If the reflector control method is used, the percentage of neutrons that return to the

core is varied by rotating control drums in the reflector. About 40 percent of the total reflector worth can be obtained by rotating control drums. The estimated control swing available from control drums as a function of core diameter is shown on the lower curve of figure VI-27. It is seen that rotating drum control in the thermal reactor can provide up to 20 percent reactivity control swing for a 15-inch-diameter core. For the 32-inch-diameter reference core only about a 5 percent swing can be attained. This is much less than the desired 12 percent. As a result of this limit and other advantages, the liquid poison control system, which is described in paper V, was chosen for the reference design.

The control worth of the finely distributed soluble poison system is shown on figure VI-28. The reactivity of the cadmium solution in control tubes is shown plotted against the cadmium concentration in the tubes.

It is shown that the required reference reactor poison concentrations for a 12 percent control swing can be attained by very dilute poison solutions without approaching this assumed solubility limit of 2.38 moles per liter.

The concentrations measured in the clean critical experiments are also shown. The poison concentrations required for the zoned reference design will be lower because some of the core reactivity is held down by the parasitic poisons added for power tailoring. The control swing for these lower poison concentrations have been calculated and are shown as the solid line. It is seen that the experimental points can be smoothly faired into the calculated curve.

In order to verify the uniformity of the poison concentration throughout the 210 poison tubes in the core under actual flow conditions, the flow loop shown in figure VI-29 was made. This consisted of the poison injection point, the inlet pipe, the distribution plenum, the reentrant control tubes, and the outlet pipe. The construction past the injection point is identical to that proposed in the reference reactor design.

The results of the experiments showed that the poison concentration in any tube varied from the average concentration by less than 5 percent at any time. Calculations showed that a 5 percent decrease in the cadmium concentration in two central poison tubes would result in only a 0.1 percent rise in the power of the center fuel element. This change is negligible.

The experimental assembly shown was also used to check the speed of response of changing poison concentration throughout the control tubes in the core. From calibrated electrical conductivity cells it was determined that the poison entered the core within 0.2 second after opening the injection valve. The core poisoning transient lasted for 2 seconds, which is slightly less than one loop time. This means that the full effect of a given rate of change of poison insertion is seen in 2 seconds.

In order to make this system fail safe, an additional independent system will probably

be required, which when triggered, would inject gadolinium nitrate under pressure directly into the water in the center of the core.

As previously indicated, the soluble poison control system was not the only one investigated. Quite a few other systems were considered, but it is felt that aerospace systems should take advantage of lightweight components whenever possible. A reactor control system using a strong neutron absorbing gas could be a very lightweight and simple system.

The helium 3 isotope has a thermal absorption cross section of about 5000 barns and is obtained from the decay of tritium. Control tubes containing gaseous helium 3 could be located in the same interstitial positions as proposed for the liquid poison control system.

Figure VI-30 shows a schematic of a noncirculating gaseous helium 3 control system. The broken lines represent the in-core control tubes. The helium 3 pressure in them is controlled by operating supply and exhaust valves. Helium 3 is now sufficiently inexpensive so that it can be exhausted to space when an increase in core reactivity is required. Only one exhaust valve is shown, but more could be added in series to prevent leakage. Two completely separable systems are indicated. These would be radially interwoven through the core so that either system could control the core.

A key component of the system is this 5-mil orifice. There would also be small orifices at the feed end of each control tube. Since flow velocity is limited to sonic velocity, these orifices can reduce the maximum speed of response of this system to a very reasonable rate. Another safety feature is that the gas pressure in the control tubes and feed lines inside the main orifices would always be less than the water pressure which surrounds it. The minimum water pressure is 100 psi.

In the insert of figure VI-30, it is noted that the control elements are thin annuli of gas. This geometry prevents excessive heating in the control gas and makes the system thermally stable in the high neutron flux. From a reactivity excursion standpoint, the reactor can be made fail safe by having loss of helium pressure in all systems trigger a spring-loaded water dump valve.

Two examples have been shown of systems which could control the required amount of reactivity without seriously perturbing the distribution of power throughout 10 hours of full power operation. Since these systems function almost entirely by changing the parasitic neutron absorption in the core rather than by changing the leakage from the core, they should be satisfactory for cores of any size.

Large and Smaller Cores

Much of the tungsten water-moderated reactor feasibility study effort has been devoted

to the 121-element reference reactor design, which acts as the focal point for the many technical disciplines involved. However, other reactor sizes are possible using the same reference fuel-element design. Some analyses were therefore performed for larger and smaller core sizes to define the effects on major nuclear design variables.

The axial power distribution and local radial fuel stage power distribution are relatively independent of size and well defined by the previous analysis for the reference core. The gross radial power distribution and neutron multiplication, which are the major design variables affected by size, are now considered.

The characteristics of larger reactor cores are shown in figure VI-31. The sketch at the right illustrates the gross radial power flattening technique used for the reference reactor size. The heavy circles in the central part of the core indicate that some of the fuel elements utilize the neutronic poisoning of natural tungsten support tubes to improve the gross radial power distribution. For larger reactors, core size is increased by simply increasing the number of reference fuel elements. The number of fuel elements containing the more absorptive tungsten isotopic mixture also increases with the core size. The criterion used to establish a power flattened core is that the peak-to-average power should be equal to or less than that of the reference core.

The neutron multiplication factor as a function of core diameter is given in the upper graph of figure VI-31 for both radially uniform and radially zoned cores. The lower graph shows the peak-to-average radial power as a function of core diameter. For every core size, the fuel-element spacing, fuel-element length, and beryllium reflector thickness are the same as for the reference reactor.

For the uniform cores, the multiplication factor increases with core size as expected due to reduced neutron leakage. For the zoned cores, the radial peak-to-average power actually decreases somewhat, showing some improvement over the reference reactor power distribution. This zoning decreases the multiplication factor at every size, but nevertheless results in a net gain over the reference core value.

The large cores with low leakage will require the use of some or all of this excess reactivity gain to obtain a negative temperature coefficient. One means to achieve this would be to reduce the amount of water in the core by reducing the fuel-element center-to-center spacing. The temperature coefficient and the stability of the power distributions in very large cores are areas that should be investigated.

The characteristics of two of the smallest possible separated tungsten cores are shown in table VI-6. Both these cores are unzoned radially in that natural tungsten support tubes have not been used to improve the gross radial power distribution. The fuel-element spacing and length are the same as for the reference reactor. In each case, the beryllium radial reflector has been sized to minimize the value of maximum-to-average power across the core. This reflector thickness results from a compromise between power peaking at the core-reflector interface at large reflector thickness, and power

TABLE VI-6. - CHARACTERISTICS OF SMALL CORES

[Pitch, 3.16 in.; 20 volume percent uranium dioxide.]

Fuel	Number of fuel elements	Core diameter, in.	Beryllium thickness, in.	Factor, k_{eff}	Radial power, $P_R/\overline{P}_R$
Uranium 235	37	21.0	4.0	1.11	1.19
Uranium 233	19	15.2	3.4	1.16	1.16

peaking at the center of the core for small reflector thickness. The radial reflectors on these small cores have sufficient reactivity for reflector drum control systems.

The smallest uranium 235 core, listed first in table VI-6, is a 37-element core that is 21 inches in diameter. With a 4.0-inch beryllium radial reflector it has a neutron multiplication of 1.11 and a maximum-to-average radial power of 1.19. This core would not have sufficient reactivity for overriding peak xenon, but it would have a sufficient amount for axial power tailoring so that 39 inches of fuel will give the same 4000° F exhaust gas temperature as the reference core.

The second core uses neutronically superior uranium 233 as fuel so this core can be made smaller. It has 19 fuel assemblies in a core diameter of 15.2 inches. With a 3.4-inch beryllium reflector it has a neutron multiplication of 1.16 and a maximum to average radial power of 1.16. This core is close to having sufficient reactivity for both axial power tailoring and transient xenon override.

Figure VI-32 shows a cross sectional view of this core. Only 15 kilograms of uranium 233 fuel are required for the 19 fuel assemblies. A water-cooled beryllium reflector with 12 rotating control drums is indicated.

Although this reactor is shown schematically, it is the actual size of a reactor capable of producing a power of 250 megawatts and hydrogen exit temperature of 4000° F from its 19 fuel assemblies. The core diameter is 15 inches and primary reflector diameter is 22 inches. If it were desirable to incorporate the water-to-hydrogen heat exchanger, a secondary water reflector would be added. This would increase the pressure vessel diameter to about 30 inches. The weight of such a reactor, pressure vessel, pumps, nozzle, and piping is only 2500 pounds.

Since the dynamic head limit and therefore the power per fuel element of the reference concentric ring fuel element can be increased by employing the honeycomb type of fuel-element design (see paper VIII), the 250 megawatt power mentioned may be uprated to as much as 360 megawatts.

SUMMARY

By combination of analysis and experiment, the required margins of reactivity for a reference tungsten water-moderated reactor design have been confirmed. The ability to achieve the negative water temperature reactivity required for self-stabilization in the reactor startup and at operating power has also been confirmed.

Use has been made of a single separated mixture of tungsten isotopes enriched in the 184 isotope in conjunction with natural tungsten. With these mixtures, it has been shown that the radial and axial power distributions in the core can be adjusted for good heat transfer. The features of finely distributed in-core control systems have also been considered.

In conclusion, it appears that the nuclear aspects of the tungsten water-moderated reactor are well understood and that the technology is advanced to the point where reactor designs for any power level may proceed.

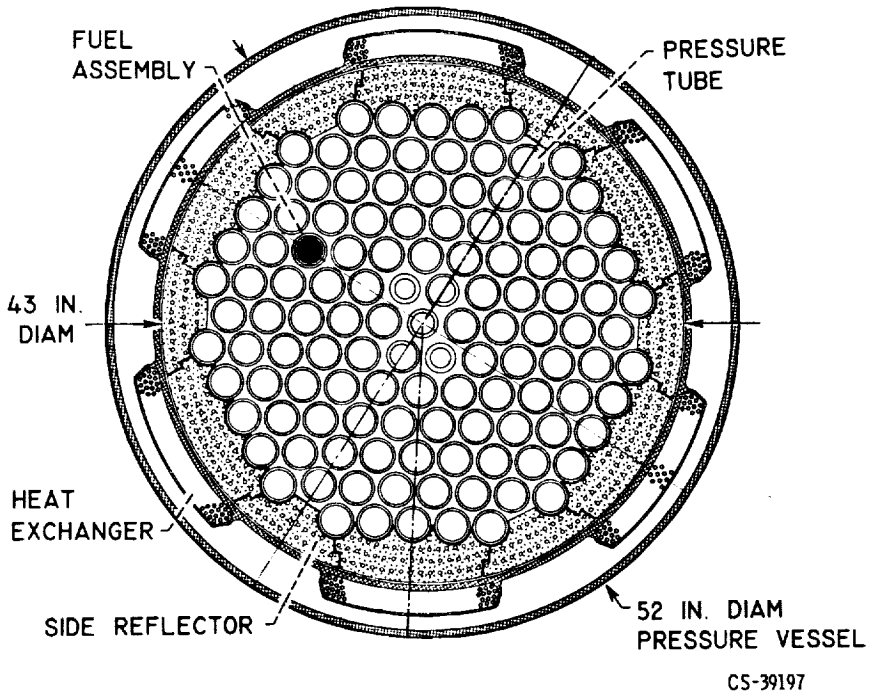

Figure VI-1. - Cross section of reference reactor.

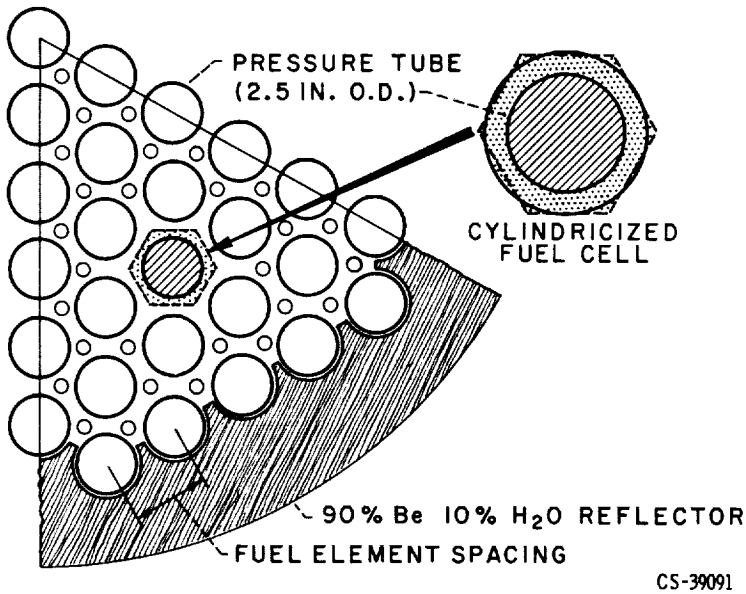

Figure VI-2. - Radial section of reference reactor.

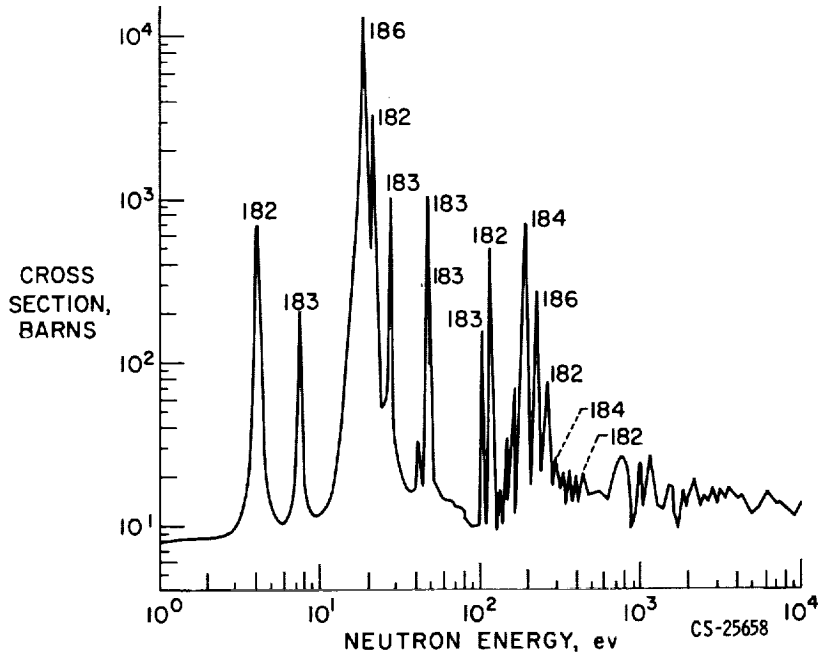

Figure VI-3. - Tungsten total cross section.

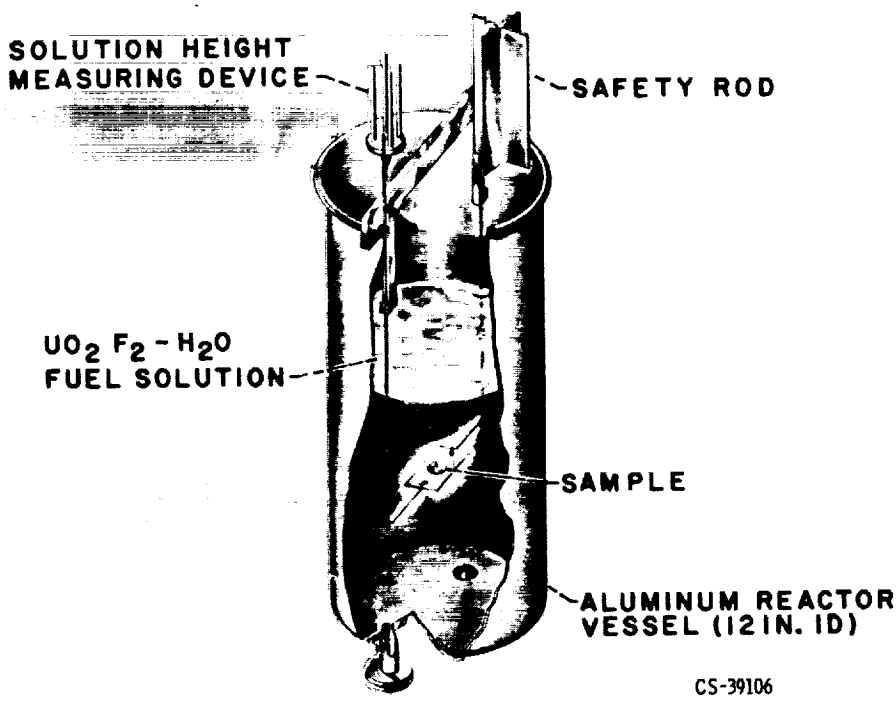

Figure VI-4. - Reactor used as a reactivity measurement facility.

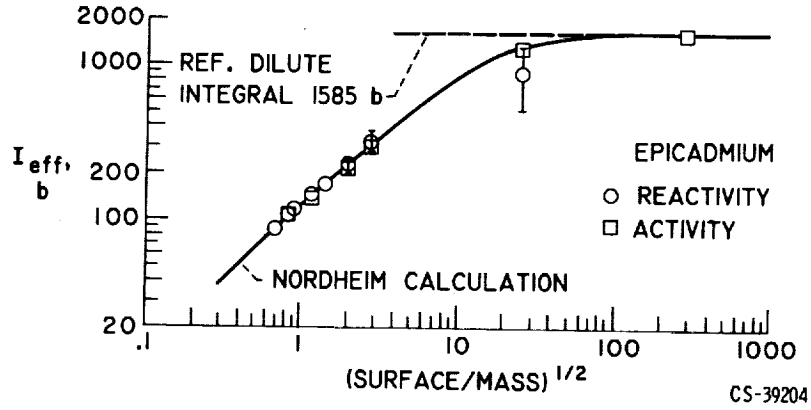

Figure VI-5. - Effective resonance integrals I_{eff} for gold.

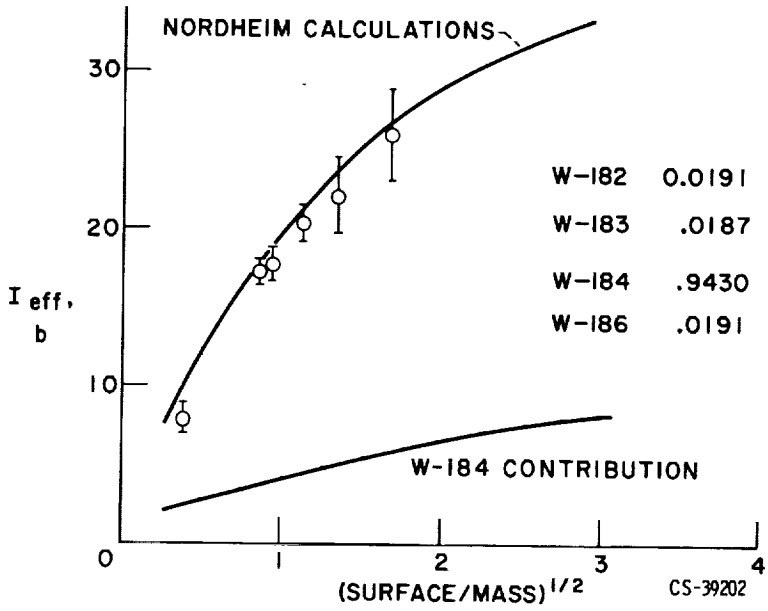

Figure VI-6. - Effective resonance integrals I_{eff} for tungsten mixtures.

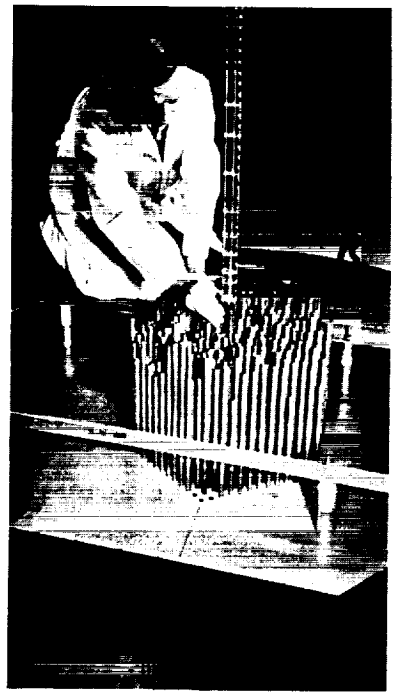

CS-39107

Figure VI-7. - Tungsten-water age measurement.

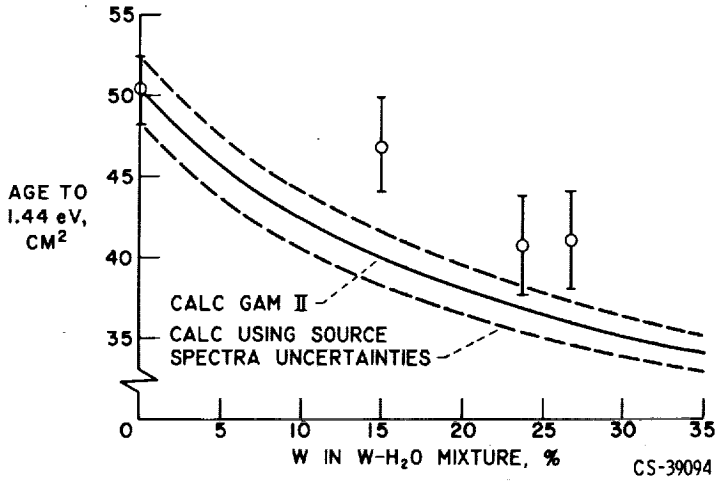

Figure VI-8. - Fermi age in tungsten-water mixtures. Plutonium-beryllium source neutrons.

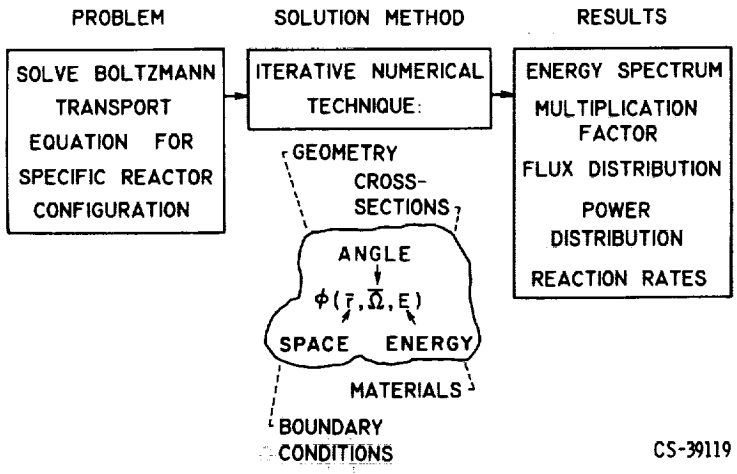

Figure VI-9. - Neutronic calculations.

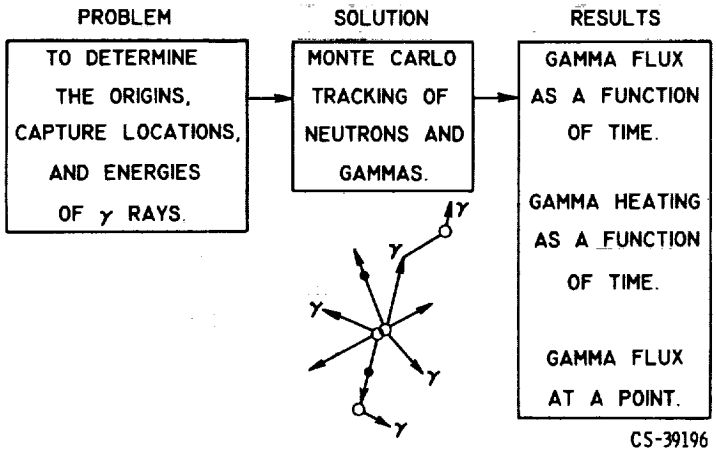

Figure VI-10. - Gamma heating calculations.

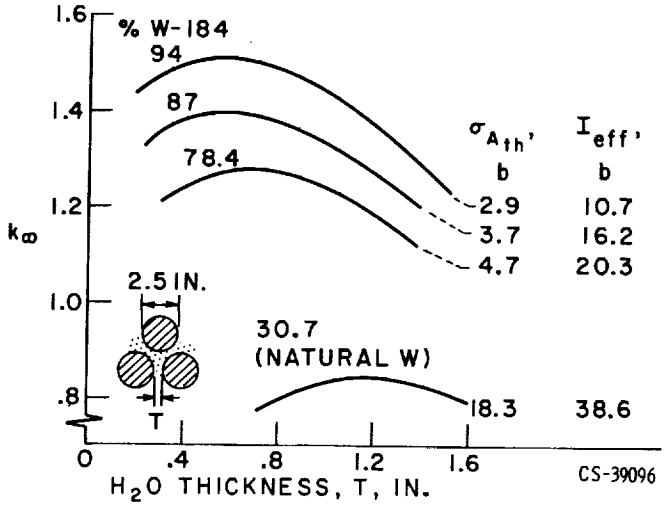

Figure VI-11. - Cell multiplication k_∞. Tungsten - 20 volume percent uranium dioxide fuel.

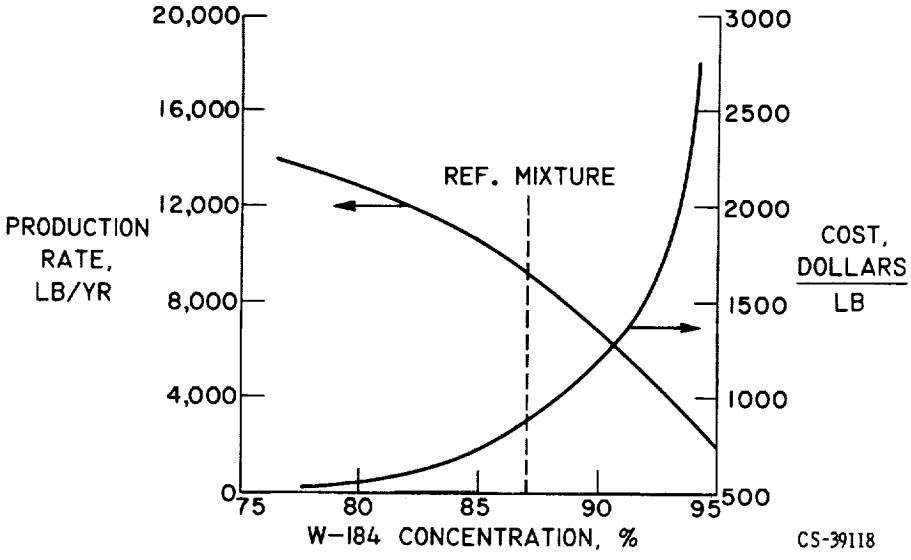

Figure VI-12. - Separated tungsten 184 production.

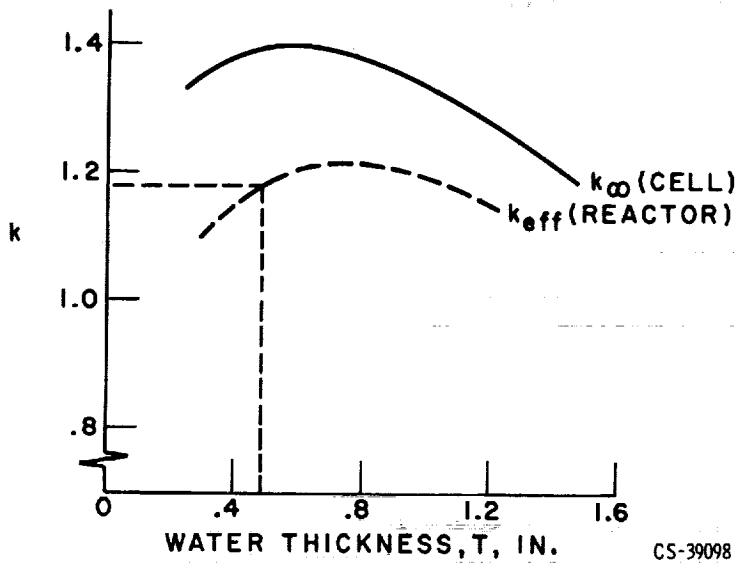

Figure VI-13. - Reactor multiplication k.
Reference mixture, 87 percent tungsten 184.

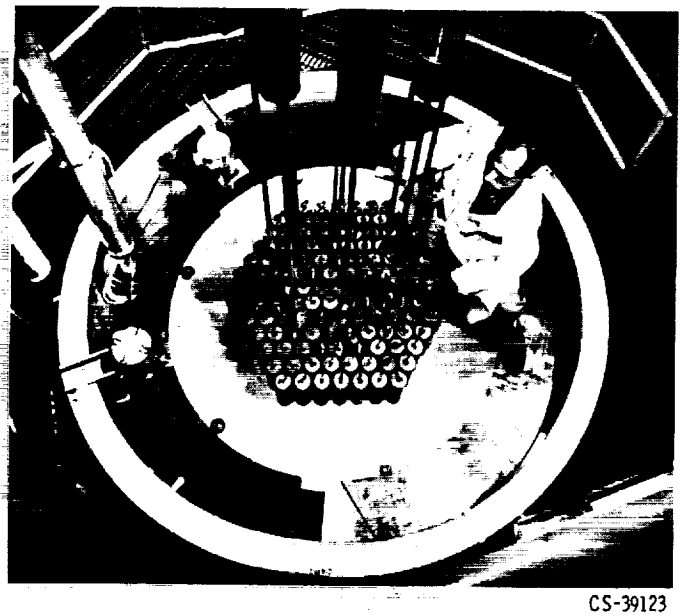

CS-39123

(a) Critical assembly.

Figure VI-14. - Reference reactor critical experiment.

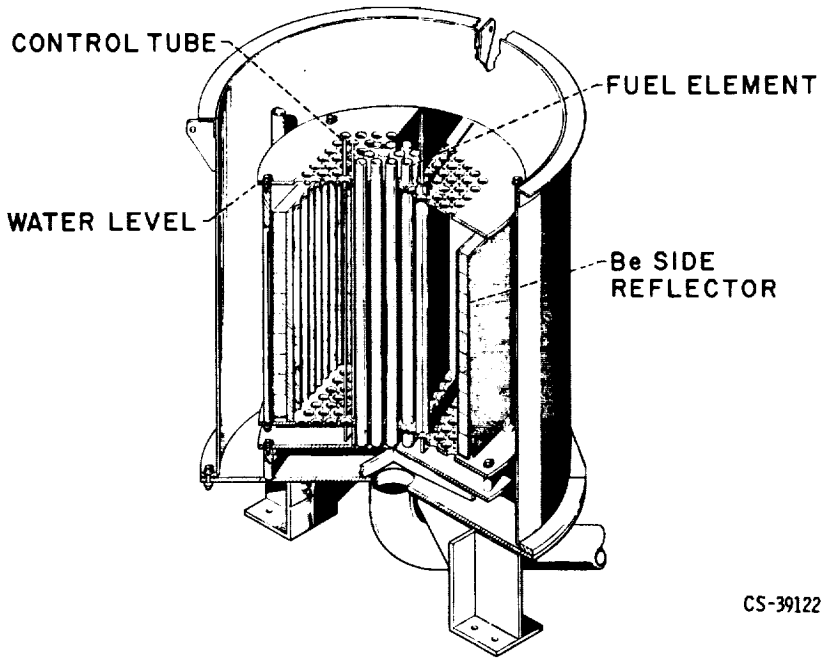

(b) Cutaway view of assembly.

Figure VI-14. - Concluded.

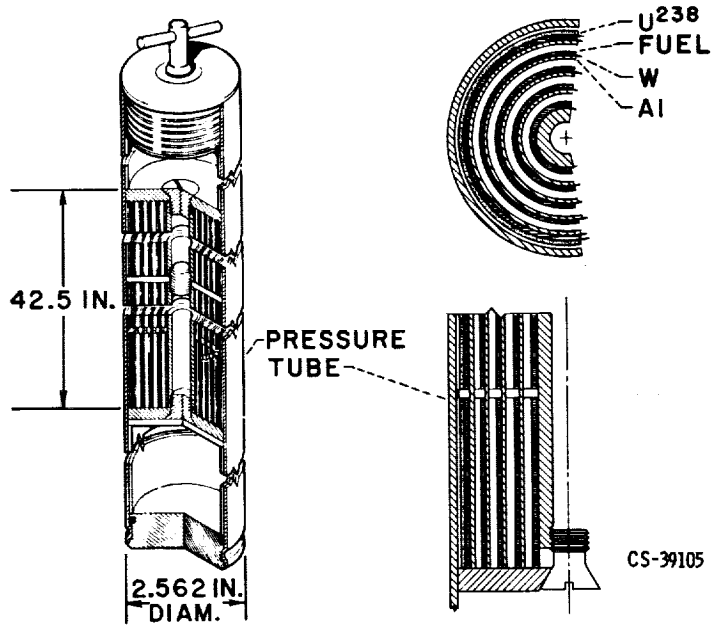

Figure VI-15. - Simulated fuel element.

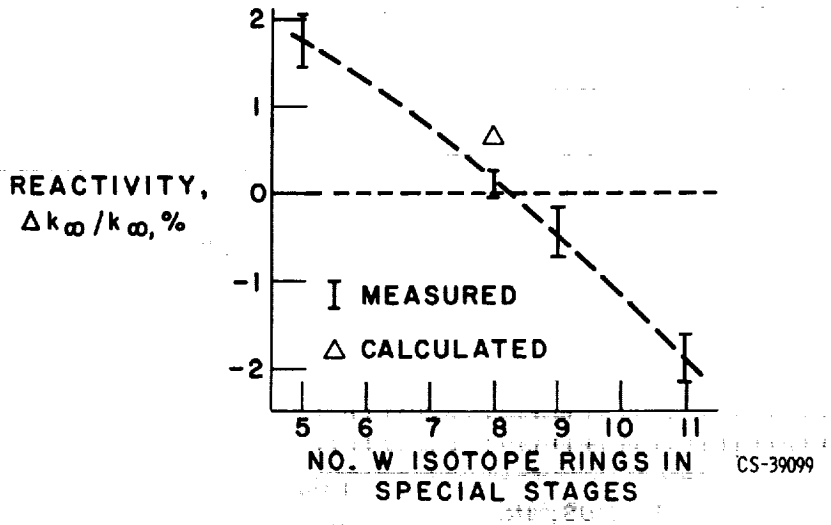

Figure VI-16. - Experimental check of simulation.

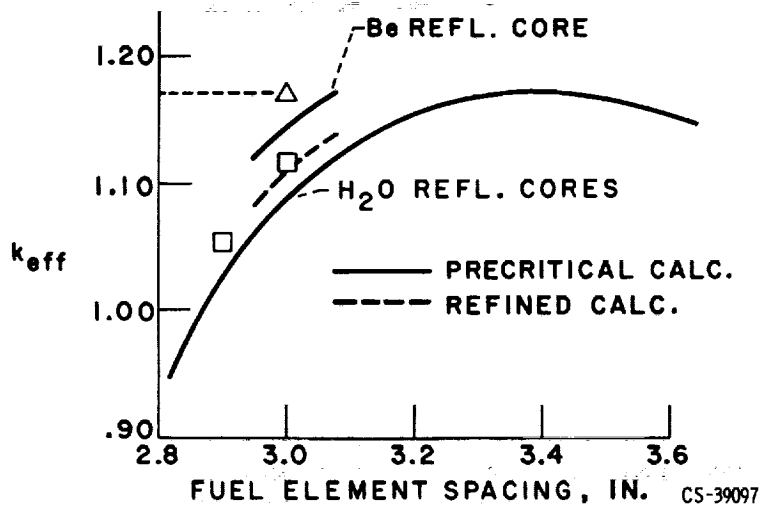

Figure VI-17. - Results of critical experiments.

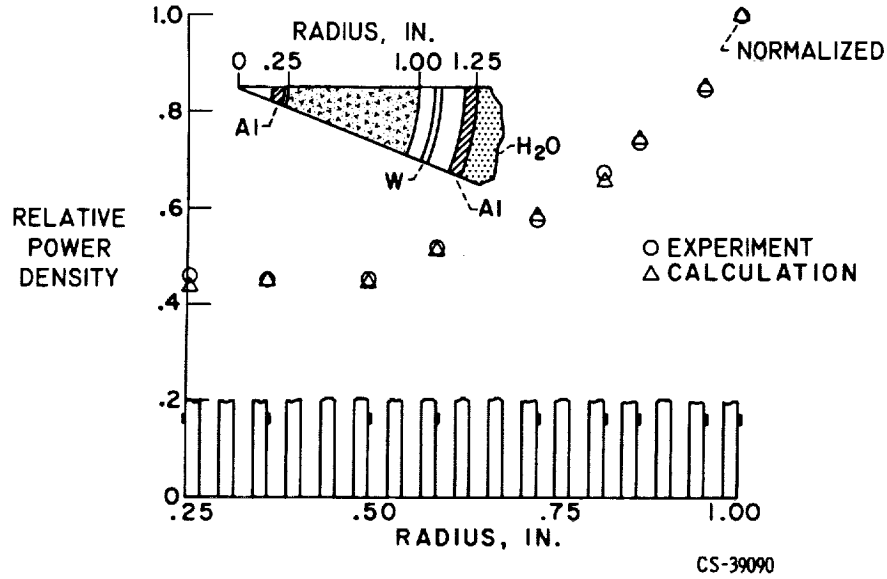

Figure VI-18. - Radial power density in simulated fuel element.

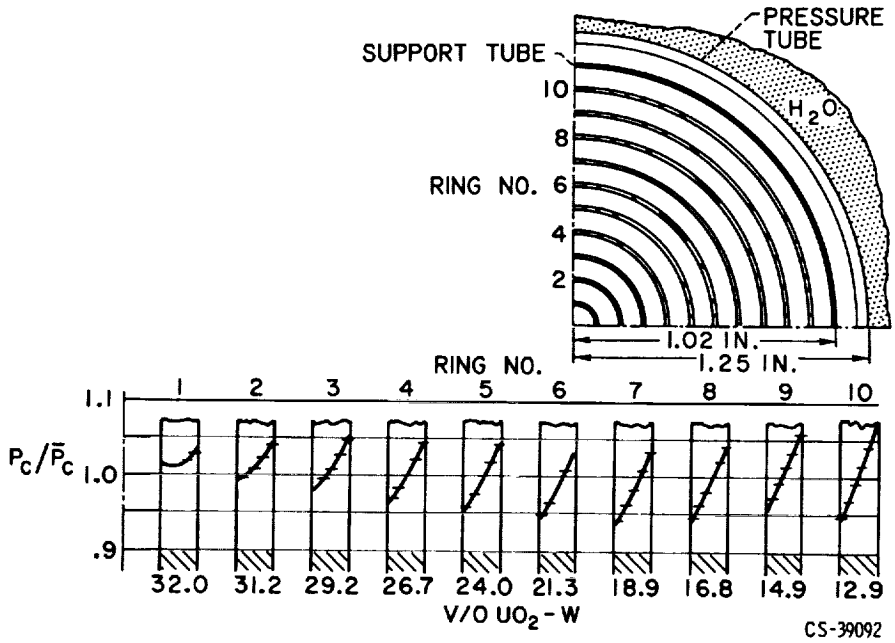

Figure VI-19. - Fuel-element zoning for uniform radial power density.

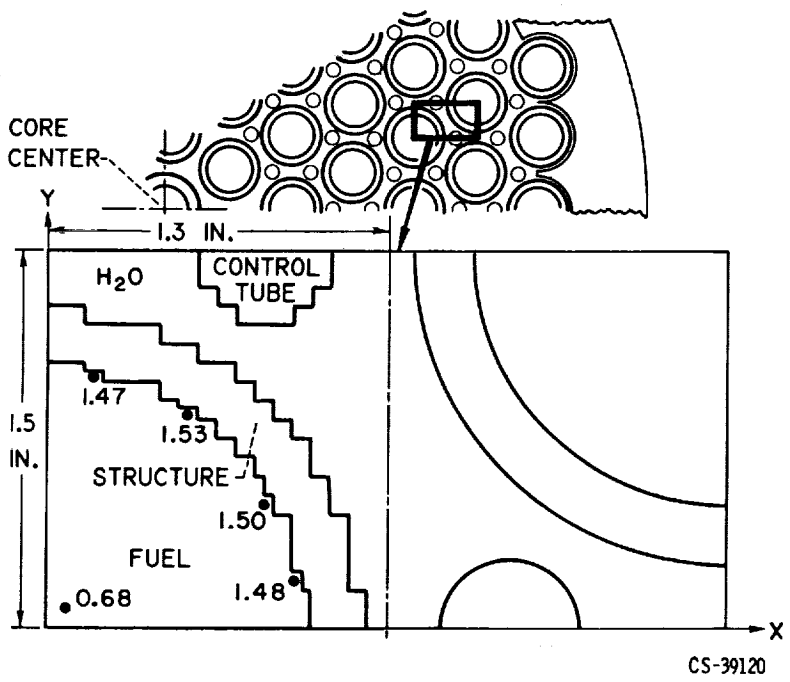

Figure VI-20. - Two-dimensional cell geometry.

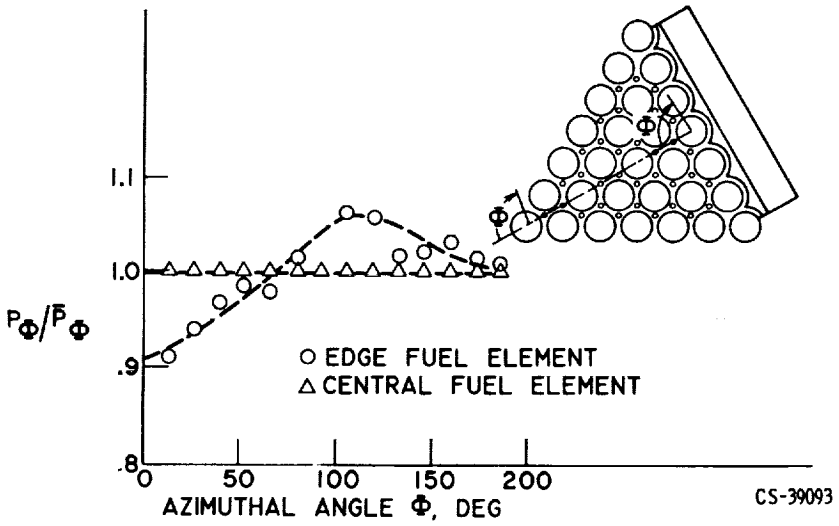

Figure VI-21. - Circumferential power $P_\Phi/\bar{P}_\Phi$.

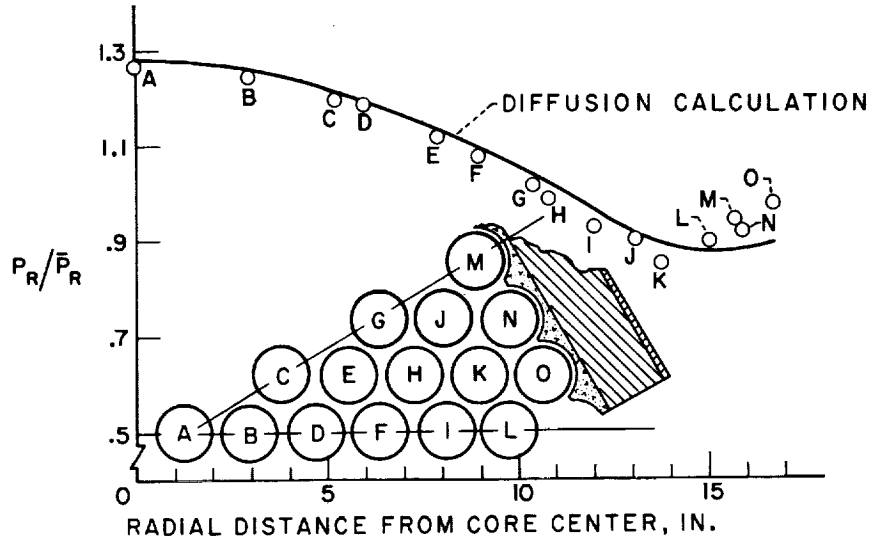

(a) Uniform core.

This figure UNCLASSIFIED

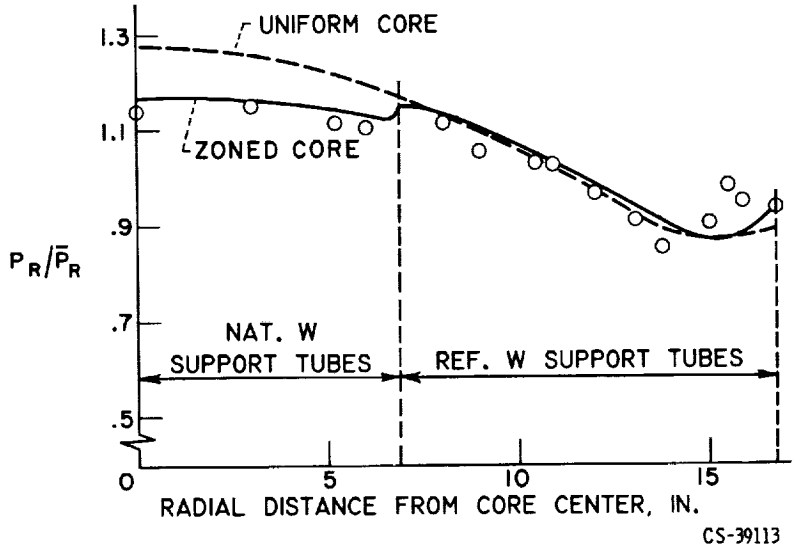

(b) Zoned core.

Figure VI-22. - Radial power $P_R/\bar{P}_R$.

This figure CONFIDENTIAL

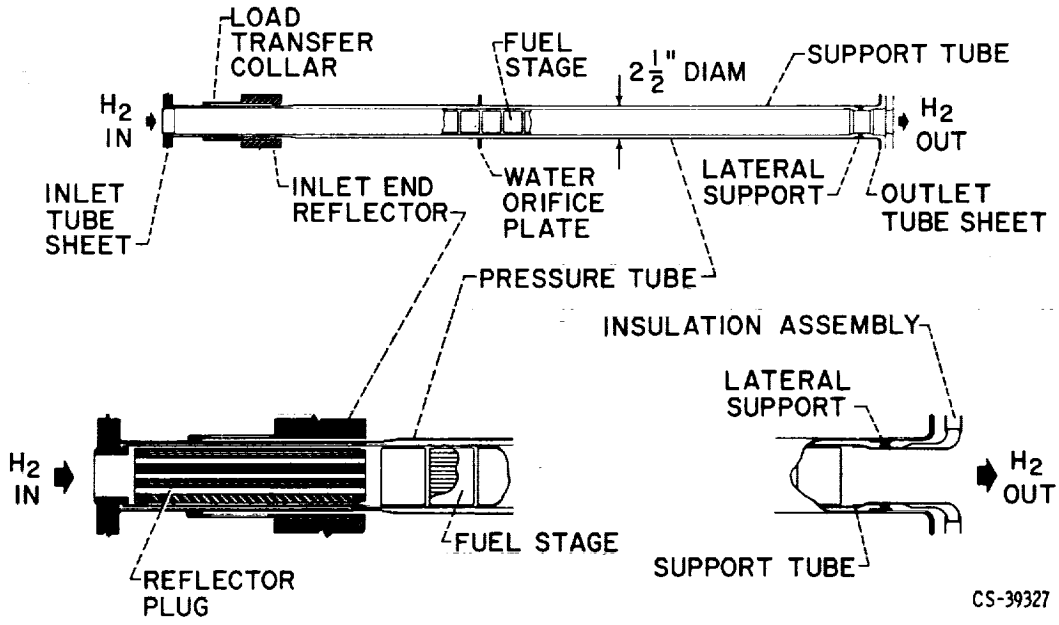

Figure VI-23. - Propulsion fuel-element assembly.

This figure CONFIDENTIAL

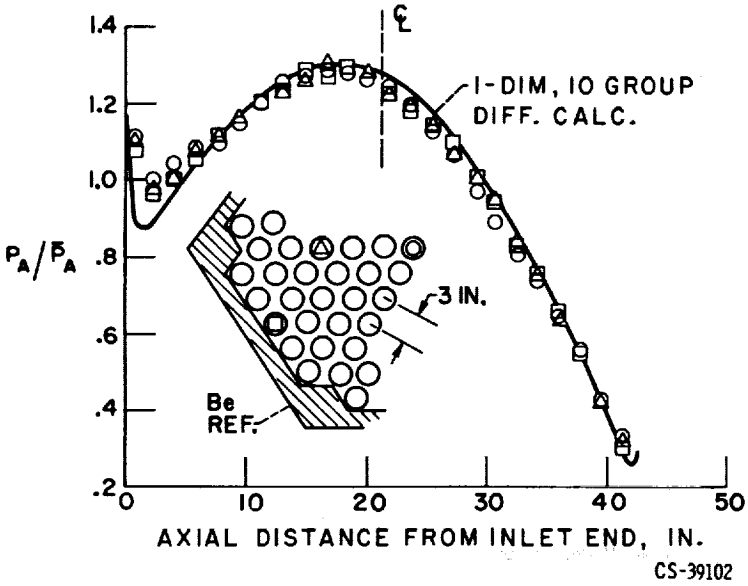

(a) Uniform core.

Figure VI-24. - Axial power $P_A/\bar{P}_A$.

This figure UNCLASSIFIED

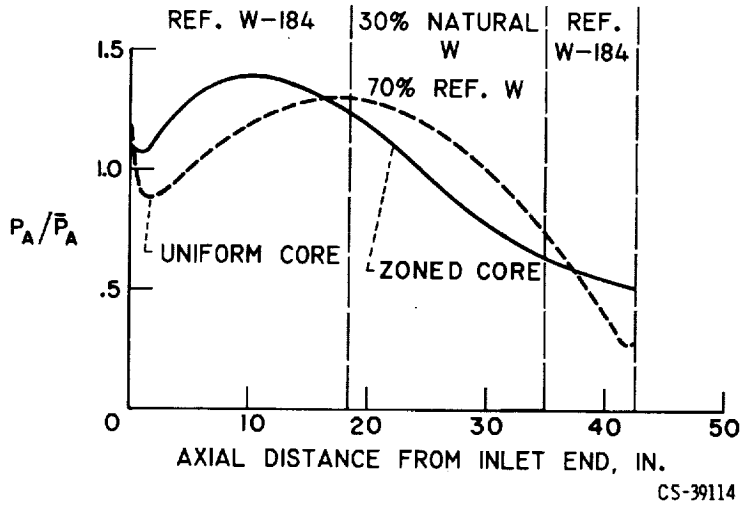

(b) Zoned core.

Figure VI-24. - Concluded.

This figure CONFIDENTIAL

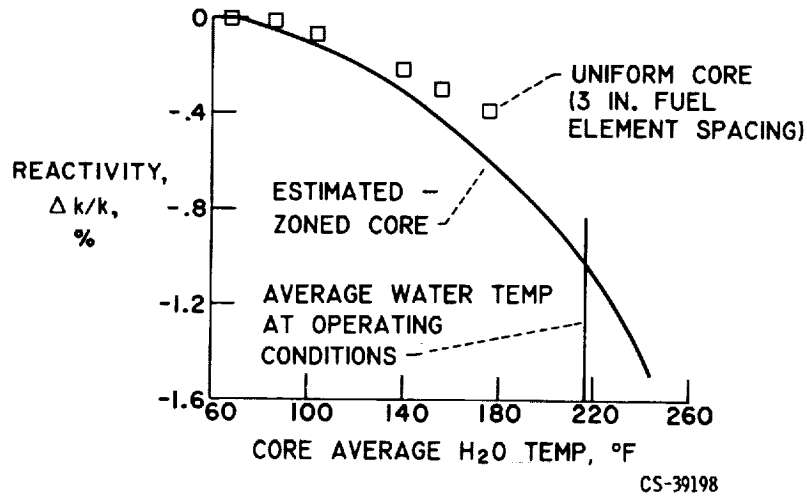

(a) Effect of water temperature.

Figure VI-25. - Reactivity effects.

This figure UNCLASSIFIED

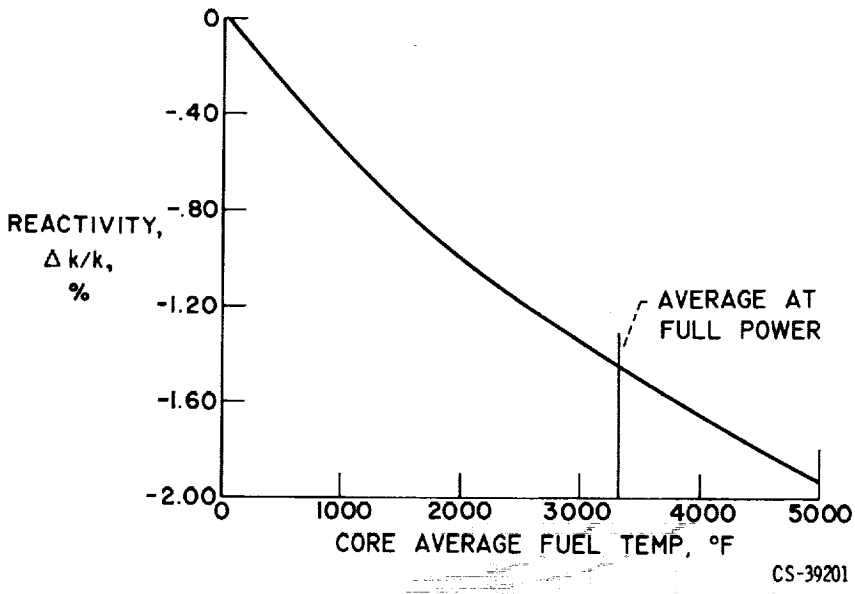

(b) Effect of fuel temperature.

Figure VI-25. - Concluded.

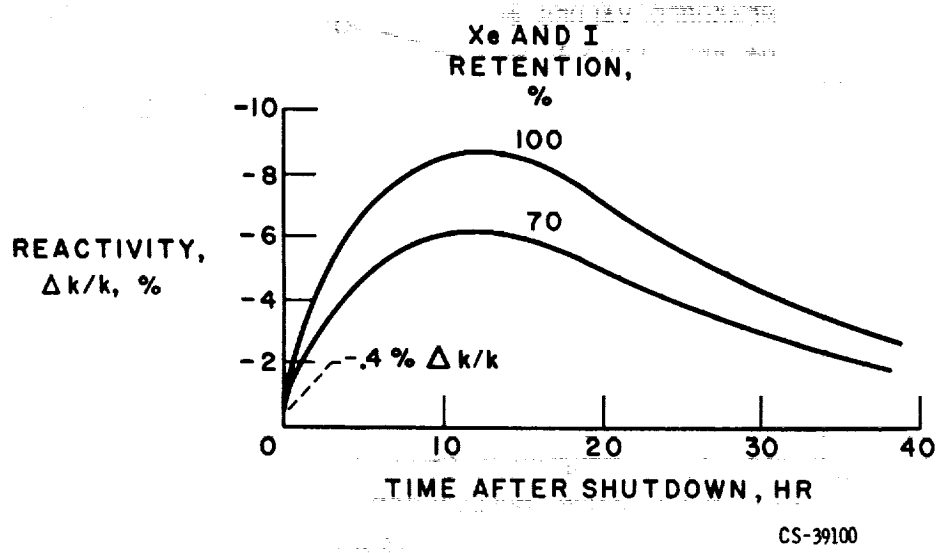

Figure VI-26. - Xenon generation after shutdown. 1-Hour full power run.

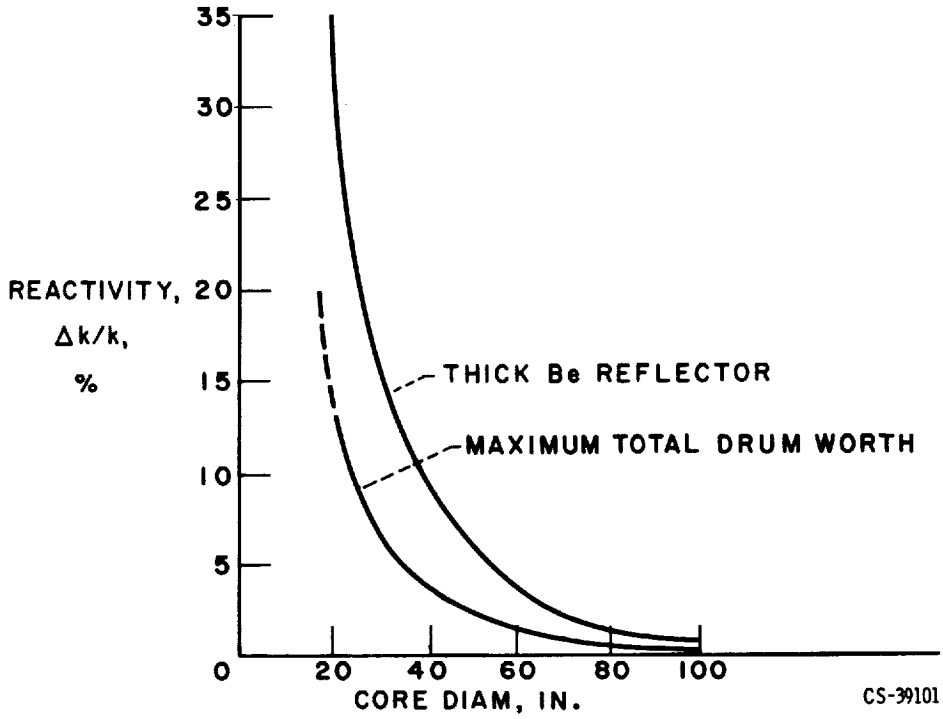

Figure VI-27. - Reflector reactivity.

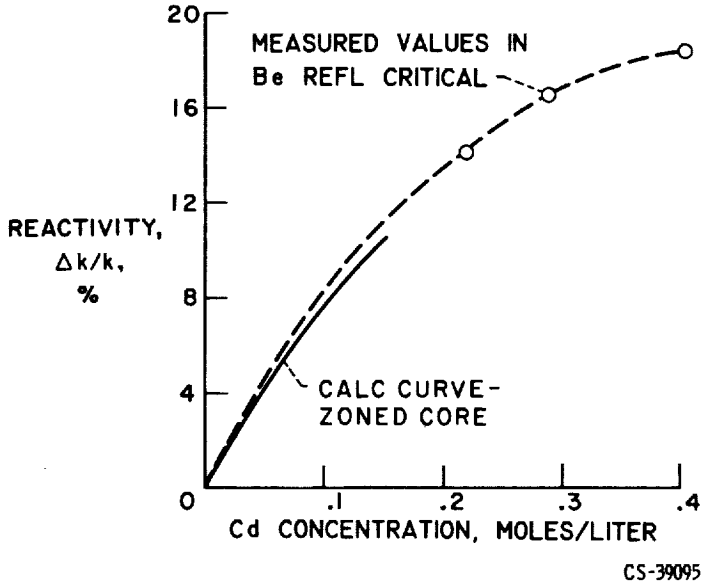

Figure VI-28. - Reactivity of cadmium.

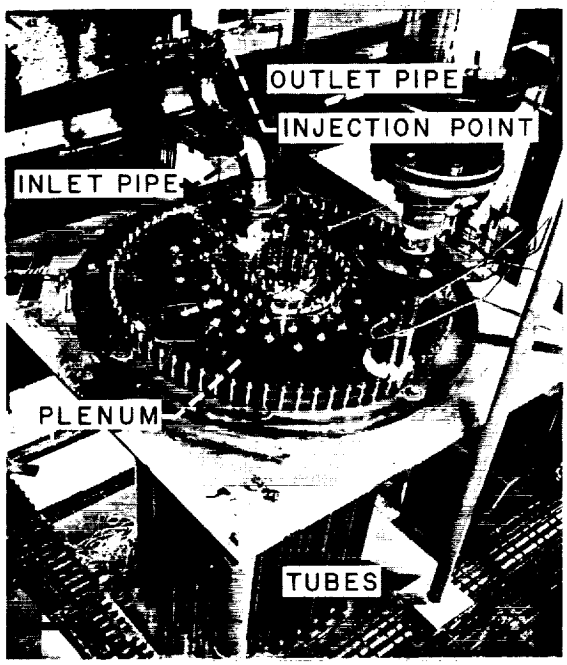

Figure VI-29. - Poison tube assembly flow test.

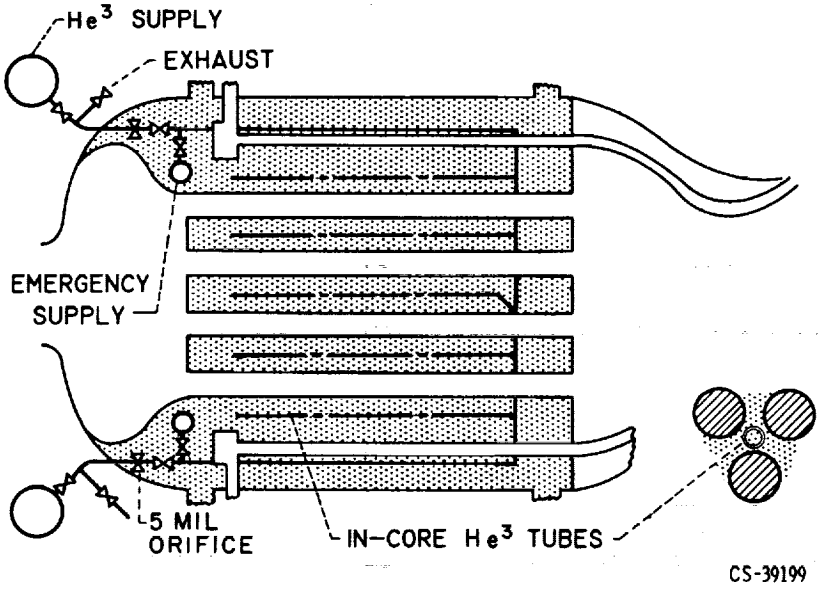

Figure VI-30. - Noncirculating gas control system.

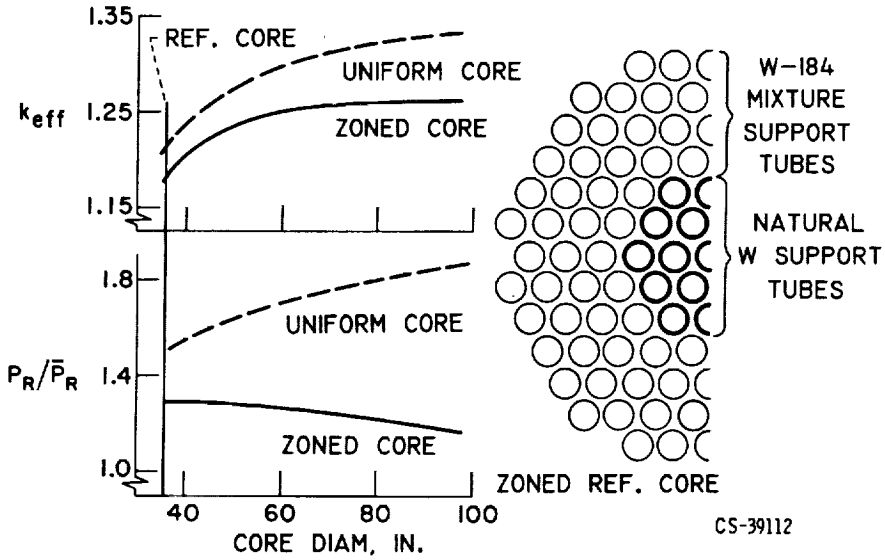

Figure VI-31. - Characteristics of larger cores. Tungsten - 20 volume percent uranium dioxide fuel.

This figure CONFIDENTIAL

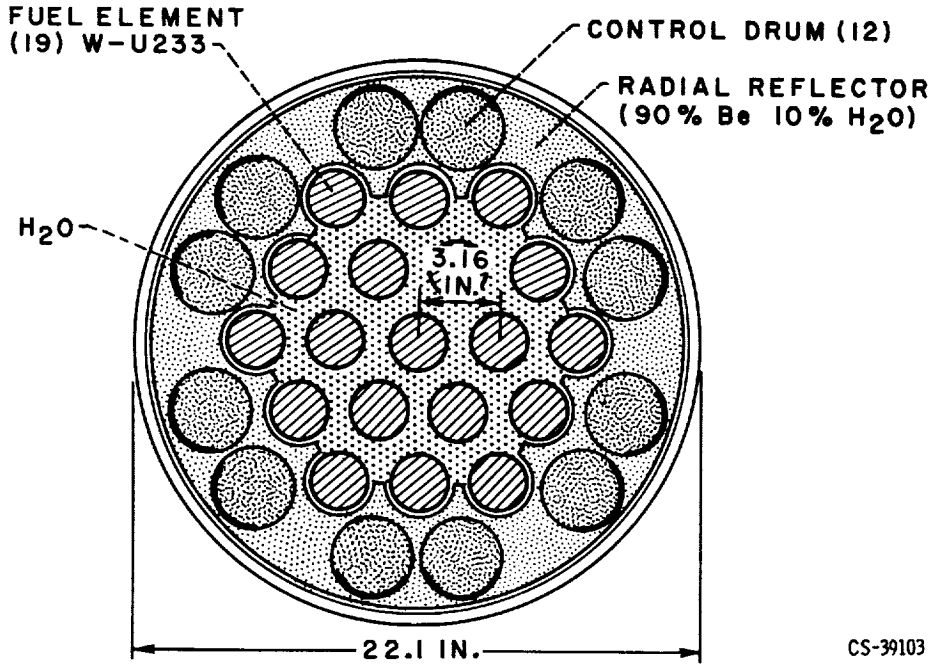

Figure VI-32. - Cross section of small tungsten reactor.

This figure UNCLASSIFIED

X66-51413

VII. FUEL ELEMENTS AND FUEL-ELEMENT MATERIALS

Armin F. Lietzke, Neal T. Saunders, Gordon K. Watson,
Richard E. Gluyas, and Jack G. Slaby

Lewis Research Center

INTRODUCTION

Fuel elements and fuel-element materials have been investigated both by NASA and by contractors to NASA as part of the overall tungsten water-moderated rocket reactor program. This investigation has included a study of the behavior of uranium-bearing tungsten composites in terms of the ability of tungsten to contain the less refractory fuel and the properties of these composites. The investigation has also involved the selection of fuel-element configurations, techniques for fabricating these shapes, and the capability of the configurations to operate under the conditions of interest.

As a basis for the work, certain goals were established early in the program as follows:

Operating temperature, ^{o}F	4500
Operating time, hr	10
Thermal cycling capability, cycles	25
Fuel retention, percent loss	<1.0

High-temperature fuel-element operation is essential if the specific impulse potential of the nuclear rocket is to be realized. The nominal operating temperature was chosen to be 4500^{o} F. Although no specific space mission has been defined, the operating time is assumed to be short and consistent with high-thrust propulsion and small gravity losses. To allow for development testing, operating time was fixed at 10 hours. Without a specific mission, the number of startups and shutdowns are also unknown. Again to allow for development testing, the thermal cycling capability goal was set at 25 cycles. Some fuel losses can be tolerated, but to keep the excess reactivity necessary to compensate for fuel loss in line, the allowable fuel loss was taken to be less than 1 percent. In addition to the goals listed, good high-temperature strength is necessary; that is, the presence of fuel should not compromise the strength of tungsten any more than is necessary.

At the outset of this program, it was decided that these goals could be met best with dispersion-type fuel composites with a continuous matrix of tungsten. Tungsten has the highest melting point of all the metals, almost 1700° F above the selected fuel-element operating temperature. In addition, it has relatively good strength and excellent thermal conductivity over the entire operating temperature range. In fact, its room-temperature conductivity is nearly equal to that of aluminum. Another advantage is that tungsten does not react at all with hydrogen, which was the propellant in this system.

However, tungsten also has some drawbacks for use in this type of reactor. First of all, tungsten is extremely brittle at room temperature, but at a few hundred degrees above room temperature, tungsten transforms to a ductile state and remains ductile at temperatures between this "transition temperature" and its melting point. Because of its room-temperature brittleness and its stiffness at higher temperatures, tungsten is difficult to fabricate. To overcome this, rather novel fabrication techniques and very high temperatures must be used to fabricate tungsten.

Uranium dioxide was chosen as the fissionable fuel to go with the tungsten matrix of the dispersion-type fuel elements. This selection was based primarily on the following factors:

(1) Uranium dioxide is one of the most refractory fuels, having a melting point of about 5000° F (approx. 500° above the selected fuel-element operating temperature).

(2) It has a fairly high uranium density of 9.6 grams per cubic centimeter.

(3) It is, for the most part, not reactive with either tungsten or hydrogen.

Of course, uranium dioxide also has some disadvantages. Its poor high-temperature strength and thermal conductivity are partially compensated by the use of uranium dioxide as a dispersoid in a continuous matrix of tungsten. The dispersion takes full advantage of the good strength and thermal conductivity of tungsten. There are two other problems associated with uranium dioxide that are not as easily solved: its high vapor pressure at high temperature and its tendency to dissociate at high temperature. Both these characteristics can lead to gross loss of fuel from the fuel elements. Because of these two problems, much effort has been directed toward finding methods to keep fuel losses to tolerable levels.

In addition to the fuel retention problem, studies were made of two specific fuel-element configurations. The configurations were examined from the standpoints of fabrication, the ability to withstand the aerodynamic forces of the high-velocity hydrogen, and thermal stresses within the element. Support of the fuel elements under axial drag loads and vibratory lateral loads was studied also.

FUEL RETENTION

In order to evaluate the effects of fuel vaporization and dissociation and to develop

methods for controlling fuel loss due to these factors, it was first necessary to fabricate suitable test specimens. These specimens could also be used to determine the mechanical properties of the fueled composites.

Fabrication and Cladding of Flat Plates

Several methods were developed to produce fueled test specimens that had uranium dioxide particles dispersed in a continuous tungsten matrix. These methods included powder metallurgy techniques that use mixtures of tungsten and uranium dioxide particles and techniques that involve the consolidation of tungsten-coated uranium dioxide particles into dense bodies.

Early in the program, it became obvious that uranium dioxide was being lost from the composites during continuous heating. This problem is caused by the fact that, at the operating temperature of 4500° F, uranium dioxide has a vapor pressure of about 3 millimeters. This high vapor pressure can cause large amounts of fuel loss from tungsten - uranium dioxide composites by vaporization of all surface-exposed uranium dioxide particles and also interconnected, internal uranium dioxide particles. Since a large amount of fuel loss cannot be tolerated in reactor fuel elements, methods to prevent fuel vaporization had to be developed in addition to the development of fabrication methods. One method of reducing loss is the use of a thin (0.001 in.) layer of unfueled tungsten on all the surfaces of the composite. The use of tungsten-coated uranium dioxide particles also has been shown to reduce the vaporization losses.

The method developed at Lewis for the fabrication of flat plates from mixtures of tungsten and uranium dioxide powders is basically a powder metallurgy and hot-rolling operation, which is shown schematically in figure VII-1. Weighed amounts of 0.88-micron tungsten powder and uranium dioxide powder are blended together, and 2 percent (by weight) of stearic acid is added as a binder. The mixture is then cold compacted into flat plates and sintered at 3100° F to yield a cermet plate with a density in excess of 90 percent of theoretical. Additional densification is achieved by rolling at approximately 3500° F. The finished cermet plates are about 20 mils thick and have a density in excess of 99 percent of theoretical. This hot-rolling technique has been successful in the fabrication of plates that contain up to about 40 volume percent uranium dioxide.

The top and bottom surfaces of the plates may be clad during the rolling operation with a thin layer of unfueled tungsten by roll bonding wrought tungsten foil to the cermet, as shown in figure VII-1. This method has proven quite useful since high quality cladding can be easily bonded to the major surfaces of the fuel plate. The resultant cladding is fully dense, very uniform in thickness, and metallurgically bonded to the core.

Several photomicrographs of rolled fuel plates are shown in figure VII-2. These fuel plates contained 10, 20, 30, and 40 volume percent of uranium dioxide. The white areas in the photomicrographs are tungsten, and the darker areas are uranium dioxide particles. The high density of the tungsten matrix and the uniformity of the tungsten cladding that was applied by roll bonding should be noted. The fuel particles were initially spherical and about 50 microns in diameter before consolidation, but they were elongated somewhat during rolling.

With the roll-bonding technique, however, the edges of the plates are still unclad, and some fuel can be lost at high temperatures from these edges. Various cladding methods, such as powder sintering and plasma spraying, have been effectively used to clad the edges of the fuel plates, but these methods are essentially limited to composites of simple geometry.

Other techniques were investigated, therefore, for cladding all exposed surfaces with one process, and vapor deposition techniques were found to be the most promising. Vapor deposition employs the hydrogen reduction of a tungsten halide (WF_6 or WCl_6) at elevated temperatures to deposit tungsten metal on heated surfaces. This deposition results from either of the two following reactions: $WCl_6 + 3H_2 \rightarrow W + 6HCl$ or $WF_6 + 3HCl \rightarrow W + 6HF$. A typical etched photomicrograph of a clad composite is shown in figure VII-3. The vapor-deposited cladding is fully dense and metallurgically bonded to the fueled core. The prime advantage of this cladding method is that the edges of the cermet as well as the major surfaces can be clad by vapor deposition in one operation. This method has been used primarily on flat plates, but it is felt that, with further development, the method can be applied to more complex configurations.

Consolidation of Coated Particles

The use of tungsten-coated uranium dioxide particles is also effective in the reduction of fuel vaporization losses, because each uranium dioxide particle is completely encapsulated in tungsten. This encapsulation prevents contact of adjacent uranium dioxide particles and prevents exposure of the uranium dioxide particles at the surfaces of the composites. In addition, the tungsten coating on the uranium dioxide particles results in a more uniform fuel dispersion in the composites.

The consolidation of tungsten-coated uranium dioxide particles is complicated by the fact that ordinary sintering techniques cannot be used because the large tungsten - uranium dioxide particles do not sinter well. Two techniques, however, have been developed for the consolidation of these particles. These two methods, hot roll compaction and hot isostatic compaction, are quite similar, as shown in the process outline in figure VII-4. In both processes, the tungsten-coated uranium dioxide particles are loaded into flat

molybdenum cans and vibratory compacted to a density of about 65 percent of theoretical. The canned particles are then heat treated in hydrogen at 2000° F to remove any surface oxide on the particles.

In the roll-compaction process, densification of the particles is achieved by hot rolling at about 3100° F. Five roll passes are required to obtain the desired reduction of about 60 percent in thickness.

The molybdenum cans for isostatic compaction must be evacuated and sealed prior to compaction. This is accomplished in an electron-beam welder. Compaction of the sealed cans is then achieved by a combination of temperature (3000° F) and pressure (30 000 psi) in an autoclave. The molybdenum canning material in both processes is removed with a nitric acid solution, which attacks the molybdenum but does not harm either the tungsten or the uranium dioxide particles encapsulated in tungsten.

Typical microstructures of plates produced by both methods are shown in figure VII-5. The dispersion of fuel in the plate produced by roll compaction is quite uniform, but the uranium dioxide particles are rather elongated, which could result in anisotropic properties in the fuel element. The uranium dioxide particles in the isostatically compacted plate are no longer spherical, but the amount of distortion is much less than that obtained with roll compaction, and therefore, hot isostatic compaction is felt to be the more promising process.

Fuel Vaporization Results

Various types of tungsten - uranium dioxide composites were heated to 4500° F in flowing hydrogen, and the resulting fuel loss was measured. The results of these tests are summarized in bar graph form in figure VII-6. The first bar indicates the large amount of fuel that was lost from unclad composites produced from mixtures of tungsten and uranium dioxide powders. This fuel loss was reduced to less than 1/2 percent by cladding the surfaces of similar composites with about 1-mil-thick tungsten, as indicated by the second bar. The loss from unclad samples produced from coated particles also was less than 1 percent. These results indicate that the use of either surface claddings or coated particles is effective in keeping fuel vaporization at tolerable levels. The combined use of these methods yields even better results and should improve the reliability of the fuel elements, since a fuel element with a defective surface cladding can still have the continuous tungsten matrix that prevents extensive fuel losses. It is recommended, therefore, that the fuel elements be fabricated from coated particles and clad with a thin surface cladding of tungsten.

Fuel Loss During Thermal Cycling

Tungsten - uranium dioxide fuel elements must be able to operate under thermal cycling conditions such as those that would be encountered in preflight ground testing or in successive reactor startups and shutdowns during flight. The effect of thermal cycling on fuel loss and on the microstructure was determined on tungsten-clad tungsten - uranium dioxide composities. The fuel loss in weight percent against the total time at 4500° F was measured for such composites in a hydrogen atmosphere. Two curves are shown in figure VII-7. One curve shows the fuel loss that results from constant heating conditions (i. e., no cycling), while the other curve shows that a substantially greater amount of loss resulted where successive 2-hour thermal cycles were used. Typical photomicrographs of cross sections of specimens tested in each way for a total of 10 hours at 4500° F are shown in figure VII-8. The specimen on the left was continuously heated for 10 hours, and the one on the right was cycled for five 2-hour cycles. The cycled specimen shows gross degradation. The grain boundaries of the unetched structure are well defined because of the migration of fuel through these paths. The invasion of the tungsten grain boundaries by the fuel weakened the matrix so much that several tungsten grains were pulled out during polishing, even though very careful polishing techniques were used. The weakened structure eventually allows exposure of uranium dioxide to the atmosphere, and vaporization occurs subsequently.

Cause of Migration and Fuel Loss

The cause of this fuel migration problem can be described best by part of the uranium-oxygen phase diagram shown in figure VII-9 (from ref. 1). In this diagram, the axes represent temperature and composition expressed in terms of the oxygen-to-uranium ratio. For stoichiometric uranium dioxide, the ratio of oxygen to uranium is 2. Heating uranium dioxide to 4500° F and holding the material at this high temperature level cause the uranium dioxide to lose oxygen, as represented by the reaction - $UO_2 \rightleftharpoons UO_{2-x} + O$, and the composition changes to a substoichiometric composition. The loss of oxygen occurs whether a specimen is heated continuously or thermally cycled. On cooling, however, a reaction occurs that can account for the accelerated fuel loss on thermally cycling. As the temperature decreases, the solvus line is crossed where liquid uranium metal separates out, as represented by the reaction $UO_{2-x} \rightleftharpoons UO_2 + U$. The molten uranium migrates into the grain boundaries of the tungsten matrix, where it can reoxidize or hydride in the hydrogen atmosphere. These hydriding and oxidation processes can result in volume changes, which can then pry apart the grains of the tungsten matrix. Thermal cycling

aggravates this problem, since each additional cycle causes more uranium to be transferred by this mechanism from the uranium dioxide particles to the grain boundaries.

It is obvious that this reduction and disproportionation of the fuel cannot be tolerated to any appreciable extent in reactor fuel elements. Therefore, a search has been made for methods that would reduce these degrading effects.

Methods for Control of Fuel Loss

Three promising methods have been found for the reduction of fuel loss during thermal cycling. The first method consists of the addition of thorium dioxide particles of less than 1-micron diameter to the tungsten matrix. The second method utilizes uranium dioxide particles of about 1-micron diameter instead of the 50-micron-diameter particles usually used. The third method consists of the addition of other oxides in solid solution with the uranium dioxide.

The improvements that result from each of these approaches are thought to be due to different causes. The role of oxides, like calcium oxide, in solid solution with the uranium dioxide is to increase the thermodynamic stability of the uranium dioxide to decomposition. Where fine particles of uranium dioxide or thorium dioxide are used in tungsten - uranium dioxide composites, the decreased rate of fuel loss probably is associated with an increased area of interface between the ceramic particles and the tungsten matrix. This area is increased by a factor of about 5 for the amount of thorium oxide added to the tungsten matrix to a factor of about 50 where micron size uranium oxide is used.

The relative effectiveness of these three methods is compared in figure VII-10, which shows the fuel loss as a function of the number of 10-minute cycles to 4500^{o} F in flowing purified hydrogen at 1 atmosphere. Flowing hydrogen is used to remove continuously reaction products and to provide continuously a pure hydrogen environment around the specimens. The curve for an ordinary composite is shown for comparison. All specimens contained the same amount of uranium dioxide (20 volume percent of the composite was uranium dioxide in fig. VII-10). It is important that the amount of uranium dioxide be the same since, in all specimens, it is known that the rate of fuel loss increases with fuel loading. Although each method extended the composite lifetime, the longest lives in terms of fuel loss were obtained through the use of either micron-size uranium dioxide or by additions of calcium oxide in solid solution with the uranium dioxide.

Since the fuel losses from composites with micron-size uranium dioxide and from those with uranium dioxide stabilized with calcium oxide are about comparable, other properties of the composites were studied to choose the better of the two methods of

stabilization. One property that showed a significant difference was the tensile strength.

On the basis of tensile strength data presented later in this paper in the section on mechanical properties (see fig. VII-11), composites with oxide stabilizers in 50-micron uranium dioxide particles were selected as most promising for further study. The use of fine uranium dioxide, however, should not be ruled out completely. Composites with fine uranium dioxide are probably worthy of further development, but the present effort has been concentrated on the use of oxide additives.

A series of screening studies has been carried out on a large number of oxides. Most of these oxides were selected on the bases of solubility in uranium oxide, absence of low melting point eutectics in the concentration range of interest, and stability to decomposition. The amount of each additive used was 10 mole percent in the uranium dioxide. All the composites tested contained 35 volume percent uranium dioxide. In figure VII-12, the relative fuel losses are plotted against the number of 10-minute cycles to 4500° F in hydrogen. The additives fall in several classes of effectiveness as stabilizers. The curve for unstabilized uranium dioxide is given for comparison. The addition of titanium dioxide has no stabilizing effect on components. Calcium oxide falls in the same class with thorium oxide. In this case, the thorium dioxide is added in solid solution in the uranium dioxide, not in the tungsten matrix. As can be seen in figure VII-12, a number of rare earth oxides perform better than calcium oxide. On the basis of the screening runs, yttrium oxide and cerium oxide were selected for further study because they were representative of the two best groups of oxides.

An oxide from each of the two best groups was selected primarily to make sure that the oxides that were in the best group under the conditions of the screening test are the oxides that are best under all conditions, particularly in the case of specimens completely clad with tungsten. It is of interest also that yttrium oxide and cerium oxide are different in that cerium can have a fairly stable valence state of +4 as well as a stable valence state of +3; it is possible that some difference in stabilizing behavior can occur because of this.

Figure VII-13 shows the results of more extensive tests that used either yttrium oxide or cerium oxide as a stabilizer of uranium dioxide in fully clad composites to see if the objective of 1 percent or less of fuel loss could be met after 25 thermal cycles to 4500° F. The loss of uranium dioxide in weight percent is plotted against the number of 10-minute cycles to 4500° F in flowing, purified hydrogen at 1 atmosphere pressure. The curve for composites with unstabilized uranium dioxide is included for comparison. Fuel loss curves are given for composites stabilized with 5 and 10 mole percent of each additive. For both additives at both concentrations tested, the goal of 1 weight percent or less of fuel loss after 25 cycles is easily met. To get a measure of the relative effectiveness of the yttrium oxide and cerium oxide additives and of the additive concentration levels studied, the cycling was carried beyond 25 cycles. Of the concentrations of addi-

tives tested, the 10 mole percent level gave the longest life. Although these data seem to indicate that greater amounts of additives might give even better results, 10 mole percent of additive was not exceeded because an increase in ceramic loading has an adverse effect on the mechanical properties of the composites. Comparison of these fuel loss curves shows that composites with cerium oxide lose somewhat less fuel under the conditions of this test than composites with yttrium oxide; further testing of composites with these additives, however, is needed before a final choice can be made.

Effect of Operating Variables on Fuel Loss

Although the results look quite promising under the test conditions used, actual operating variables could be quite broad. The fuel loss curves, for example, have been shown for a maximum cycling temperature of 4500° F, but "hot spots" conceivably could cause higher temperatures in an actual operating reactor. Also, cycling conditions may involve longer or shorter holds than the 10 minutes at temperature that were used in the tests discussed. Furthermore, the tests were made at 1 atmosphere hydrogen pressure, whereas an element in a reactor would experience much higher pressures (e.g., about 600 psi). Finally, the effects of fission heating must be considered.

The effect of maximum temperature during cycling is shown in figure VII-14, where the fuel loss is plotted against the number of cycles for two different temperatures. Comparison of these curves shows that fuel loss is increased by an increase in temperature from 4500° to 4700° F. The loss after 25 cycles to 4700° F, however, is not more than 2 percent.

The effect of time at temperature during each cycle appears in figure VII-15. The fuel loss in weight percent of uranium dioxide is plotted against the number of cycles for different hold times at temperature for each cycle. The hold times represented are 120, 10, and 2 minutes. (The 1-percent fuel loss level is indicated by the horizontal dashed line.) The 1-percent fuel loss level is reached after 6 cycles for the 120-minute cycles, after 60 cycles for 10-minute cycles, and after 80 cycles for 2-minute cycles. The bar graph shown at the bottom of figure VII-15 shows the total operating time to 1-percent loss for the three different cycles. For the 120-minute cycle, the total time to 1-percent loss is 12 hours; for the 10-minute cycle, it is 10 hours; and for the 2-minute cycle, it is about 3 hours. Thus, for long hold times, the total operating time goal of 10 hours is met, but the number of cycles is small, and for short operating cycles, the total time to reach 1-percent fuel loss is less than 10 hours, but more than 25 cycles can be completed. When 10-minute cycles are used, both 10-hour total operating time and more than 25 cycles are possible. Therefore, reactor operating cycles, particularly during ground testing, should be carefully selected.

The effect of hydrogen pressure on fuel loss has been measured on fully clad composites with 35 volume percent uranium dioxide stabilized with 10-mole-percent cerium oxide. The percent of fuel loss is plotted against the number of cycles to 4500° F in hydrogen at 1 atmosphere and at 600 pounds per square inch in figure VII-16. Thus far, data in 600 pounds per square inch hydrogen have been obtained through 25 cycles. Before these data were available, it was thought that increased hydrogen pressure might cause an increase in fuel loss. Obviously this problem did not materialize; the loss up to 25 cycles is essentially the same at 600 pounds per square inch as it is at 15 pounds per square inch and well below the 1-percent level indicated by the horizontal dot-dash line.

Apparently, no serious fuel loss problem is introduced by temperature excursions, changes in cycling program, or high-pressure hydrogen. All the fuel loss results discussed so far, however, have been in out-of-pile furnace tests. Now it is important to know if irradiation in a reactor can have adverse effects on tungsten - uranium dioxide composites.

The nuclear rocket application requires relatively low values of total exposure (nvt) and low values of burnup. The total burnup for a high-thrust mission is on the order of 0.2 percent. Therefore, one would not expect any noticeable radiation damage or fission product pressure buildup for this application. In-pile capsule tests nevertheless have been conducted on fuel-element material specimens to check the validity of furnace tests. A typical capsule used in these tests is illustrated in figure VII-17. A fueled specimen that measures approximately 1- by 1- by 1/32-inch is held by tungsten wires inside a molybdenum thermal radiation shield. The radiation shield is supported from the capsule walls. The capsule is made of stainless steel and sealed in a vacuum by electron-beam welding.

The specimen is heated by fission of the fuel in the specimen, and the heat is removed by thermal radiation to the capsule walls, which are cooled by water flowing over the outside surface of the capsule. Test temperature is established by fuel loading, the number of radiation shields, and the incident thermal flux. Fuel loss tests were conducted for 4 hours at temperatures from 3500° to 5000° F. Weight loss measurements and metallographic examination indicate no difference between fission heating and furnace heating. No special effort was made to determine the effect of clad thickness, but it was noted that a clad thickness of 1 mil is sufficient to contain the uranium dioxide. Although in-pile tests to date do not include thermal cycling in hydrogen, fission heating by itself does not appear to pose any new problems.

Fission product retention was also of interest because this concept utilizes a thermal reactor and must therefore contend with transient xenon poison if an immediate restart is required. Although xenon 135 is the fission product poison of concern, its primary source is from the decay of iodine 135. Any xenon 135 or its precursors released from the fuel

elements during operation do not have to be considered in the ΔK required for restart. Because iodine is a gas at the proposed operating temperatures, measurable loss of iodine as well as xenon might be expected, especially when considering the diffusion rates at high temperature.

The amounts of iodine present in the capsules after 4-hour irradiation were measured for temperatures from 3000° to 5500° F. Only preliminary data are available, and these results are in figure VII-18, where percent iodine release is plotted against specimen temperature. The percent release was found to increase as the temperature was increased. At the reference design temperature of 4500° F, about 12 percent of the iodine was released. No swelling of the test specimens was observed. The gas release shown in figure VIII-18 as well as the low burnup apparently account for the absence of swelling.

MECHANICAL PROPERTIES

Knowledge of the mechanical properties of fuel-element materials is necessary in the design of the reactor. All the current mechanical property data were obtained on rolled plates prepared by the hot-rolling powder metallurgy techniques. The use of tungsten-coated uranium dioxide particles compacted by either hot rolling or isostatic pressing, rather than individual tungsten and uranium dioxide powders, could possibly result in changes in the data. This possibility is currently being investigated.

Tensile Properties

The results of tensile tests conducted at 4500° F on fuel plates with 0 to 50 volume percent uranium dioxide are shown in figure VII-19. The strength of unfueled tungsten (shown on the left) is about 3700 pounds per square inch. The ductility (not shown) associated with this is about 10- to 15-percent reduction in area. As the fuel loading is increased to about 30 volume percent uranium dioxide, the strength of the composites increases slightly, and very little change in ductility occurs. As more fuel is added, however, the strength begins to decrease rapidly. From these results, it appears that the loading of the fuel elements should be less than about 35 volume percent uranium dioxide in order to avoid the region of rapidly decreasing strength. If more strength is required, it might be possible to use a stronger tungsten alloy in place of the unalloyed tungsten used in these studies.

The effect of test temperature on the tensile strength of several different tungsten - uranium dioxide composites with 20 volume percent uranium dioxide is shown in figure VII-11. It should be noted that the strength of the composites with fine (~1μ) uranium

dioxide particles is relatively low at high temperatures as compared with composites with 50-micron-diameter uranium dioxide particles, which were also tested at a high temperature. This low strength is believed to be due mainly to interconnection of the fine uranium dioxide particles. Very little change in strength was observed in these tests when a metal oxide stabilized fuel (calcium oxide stabilized) was used in place of the standard uranium dioxide. A significant increase in the strength of the composites containing 50-micron-diameter uranium dioxide was achieved by the addition of 2 volume percent of fine (1μ) thorium oxide particles to the tungsten matrix. Thus, a thoriated matrix might be used in combination with a metal oxide stabilized fuel to increase the strength of the composites. If tungsten-coated uranium dioxide particles are to be used, however, methods would have to be developed for the introduction of fine thorium oxide particles into the tungsten.

Creep-Rupture Properties

A series of creep-rupture tests was performed on the tungsten - uranium oxide composites over a range of temperatures and fuel loadings corresponding to those intended for use in the tungsten water-moderated reactor. Some of the results of this study are shown in figure VII-20. It can be seen that, as fuel is added to the composite, the maximum allowable stress that will give a 10-hour rupture life decreases.

Modulus of Elasticity

The deflection of a fuel element under a given load, Young's modulus, is another important design property. A contracted effort has been completed recently in this area, and the results of this study are shown in figure VII-21. The modulus values shown here for tungsten are higher than other static test data reported in the literature. Test conditions in this study were very carefully controlled, and a great deal of care was taken to ensure that creep did not affect the results of these tests.

Composite plates containing 10 to 40 volume percent uranium dioxide were tested, and all the results fall in the shaded area of the figure with very little difference in the values for the different fuel loadings. The rapid decrease in the moduli of the composite materials between 3500^{o} and 4000^{o} F is not fully understood, but one possible explanation is that in this temperature range the modulus of the uranium dioxide decreases rapidly and contributes less and less to the overall moduli of the composites.

DESIGN PARAMETERS

In addition to containing fuel, the fuel elements also transfer the heat energy to the propellant. The designer has certain parameters under his control that should be selected to accomplish, most effectively, the transfer of heat and to provide sufficient mechanical strength in the fuel elements for the operating conditions.

Length-to-Diameter Ratio

In order to achieve maximum propellant temperature, the fuel elements must operate at the maximum temperature consistent with the materials of construction, and the heat-transfer flow passage must have a length-to-diameter ratio large enough that the propellant temperature approaches the fuel-element surface temperature.

The smallest length-to-diameter ratio is attained when the entire fuel element operates at the maximum allowable temperature. The length-to-diameter ratio required is shown in figure VII-22. The propellant-to-surface-temperature ratio is plotted against axial position for Reynolds numbers of 10 000, 20 000, and 60 000. As the gas enters the reactor, the temperature ratio is low, and it increases as shown in figure VII-22. In order for the propellant temperature to approach within 10 percent of the fuel-element surface temperature, it is apparent that a flow passage with a length-to-diameter ratio of 240 or greater is required. If a reactor is 3 feet long, the equivalent diameter should be 150 mils at a Reynolds number of 10 000 and 100 mils at a Reynolds number of 60 000. Actually, slightly larger length-to-diameter ratios than shown here will be required because axial power distributions corresponding to constant surface temperature may not be practical from a reactor physics viewpoint. Nevertheless, an equivalent passage diameter of 1/8 inch is about the size of interest.

Interrelation of Operating Parameters

The Reynolds number is affected by the mass velocity, or the flow rate per unit flow area. The mass velocity is most significant because, with a fixed outlet temperature, it determines the power and thrust from a given size reactor. The interrelation of reactor parameters is shown in figure VII-23. Core pressure drop and outlet Mach number are plotted against mass velocity for several chamber pressures. The variation in dynamic head at the reactor outlet is also shown in figure VII-23. The dynamic head $\rho V^2/2g$ is a measure of the aerodynamic forces acting on the fuel elements. As the mass velocity is increased, the thrust increases. (The thrust per unit flow area is the product of mass

velocity and specific impulse.) There is obviously some limit on flow rate through a given size reactor; this flow rate is dictated by core pressure drop, aerodynamic loads on the fuel elements, or a Mach number limit as a result of flow sensitivity at high Mach numbers.

Although it is impossible to choose an optimum set of operating conditions from a plot such as this, figure VII-23 does provide an insight into the requirements for various operating conditions. For example, any effort to increase performance by operation at high values of mass velocity poses three requirements evident in the figure.

(1) A fuel element capable of withstanding high dynamic head is required.

(2) A core structure capable of supporting high pressure drop is necessary. Core pressure drop rapidly reaches excessive values unless high pressure levels are used.

(3) High inlet pressure results. The inlet pressure is the sum of the outlet pressure and the core pressure drop. The significance of high inlet pressure is that the pumping power may exceed the pumping power available from a topping turbine unless special provisions are made.

From a fuel-element viewpoint, the dynamic head is of the most concern, because it is desirable that this parameter does not severely limit the performance. The aerodynamic forces that a fuel element can withstand depends on the mechanical properties of the materials and the fuel-element configuration.

Fueled Material Composition

The composition of the fueled material to be used in this reactor concept involves the compromise of a number of design factors. These factors can be discussed by writing the uranium dioxide loading as some fraction α of the total volume of solid material in the fuel element, such that

$$V_{UO_2} = \alpha\left(V_{UO_2} + V_W\right) \tag{1}$$

where V represents the volume occupied by the material identified in the subscript. The total volume of solid can be written in terms of the geometrical dimensions. Considering that the material has two major surfaces, the total volume is given by

$$\left(V_{UO_2} + V_W\right) = \frac{S}{2}\, t \tag{2}$$

where S is the surface area and t is the thickness of the fueled material. By using the definition of equivalent diameter

$$D = \frac{4\,AL}{S}$$

where A is the flow area and L is the length of the heat-transfer flow passage, equations (1) and (2) can be combined to yield

$$\frac{V_{UO_2}}{A} = 2\frac{L}{D}\,\alpha t$$

The fuel elements must contain sufficient uranium dioxide in a given size core, represented by A, to satisfy criticality requirements plus enough additional fuel to allow for excess reactivity associated with startup or restart, loss of fuel which may occur during operation, and nonuniform loading to tailor the power distribution.

The increase in average fuel loading, which is included to tailor the power distribution, offers some room for compromise. The fuel elements must, however, contain sufficient uranium dioxide to provide the necessary reactivity. The minimum volume of uranium dioxide is, therefore, established by nuclear considerations. The length-to-diameter ratio is established by heat transfer, as previously mentioned. Consequently, the product αt is essentially fixed.

The interplay between α and t is of concern, therefore. As α is decreased, a greater portion of the material is tungsten. As t is increased to keep the product αt constant, the quantity of tungsten is increased further. Tungsten is present only to serve as a structure to hold the fuel. It is desirable to use a minimum quantity of tungsten consistent with this need for two reasons; the reactor will be unnecessarily heavy otherwise, and tungsten is a parasitic absorber of neutrons, even when enriched.

As α is increased and t is decreased, the mechanical properties are affected adversely, and the structure becomes too thin to withstand the aerodynamic forces of the high-velocity hydrogen. The minimum value of t will, of course, depend on the fuel-element configuration.

The selection of values for α and t, therefore, involves a number of disciplines; that is, nuclear, heat transfer, material properties, and structure. Preliminary studies have shown that a reasonable compromise for this reactor concept is a thickness t of 20 mils, an average uranium dioxide loading of 20 volume percent and, to allow for variable loading to tailor the power distribution, a maximum uranium dioxide loading of about 30 volume percent. Core size and fuel-element configuration may alter this compromise to some extent.

FUEL-ELEMENT CONFIGURATIONS

Various fuel-element configurations have been considered. Among these are elements made of flat plates, concentric cylinders, tube bundles, and fine grids such as a honeycomb. Most of these configurations were considered only briefly because of expected performance limitations or fabrication difficulty. Two configurations, however, the concentric cylinder and the honeycomb, were selected for further study. These geometries are discussed in the following paragraphs. Both elements are the same size, each has flow passages with an equivalent diameter of 1/8 inch, and both require variable fuel loading to compensate for the self-shielding effects discussed in section VI.

Concentric Cylinder Elements

Early in the program, fueled material was available only in the form of flat plates. One of the primary reasons for considering the concentric cylinder element illustrated in figure VII-24 was that this element could possibly be made from plate stock curved to form cylinders of various diameters. The cylinder wall thickness would be about 20 mils, and the annular gap between cylinders would be 1/2 the equivalent diameter or about 1/16 inch. Each cylinder would have a different uranium dioxide loading to achieve uniform radial power within the element. The number of cylinders could vary, and fewer elements would be required in a given size core as the element diameter is increased. As the fuel elements get larger, however, the self-shielding effects increase, and a greater variation in fuel loading is required. The maximum number of cylinders that can be used without exceeding a uranium dioxide loading of 30 volume percent is approximately 11 cylinders. This corresponds to a fuel-element diameter of 2 inches.

Fabrication of Concentric Cylinders

Several tungsten - uranium dioxide cylinders are shown in figure VII-25. These cylinders were easily formed at 1700° F from tungsten - 20 volume percent uranium dioxide plates. Cylinders from 1/2 inch up to several inches in diameter can be formed by this method. However, the joining of these tungsten - uranium dioxide composites was a very difficult problem because dispersed uranium dioxide melts about 1200° F lower than the matrix. Thus, ordinary fusion welding techniques, such as electron-beam or tungsten - inert-gas welding, could not be used without extensive gas bubbling and resultant porosity in the weld zone. Therefore, several other joining techniques were investigated under contracted programs, and the results indicate that the two most promising

techniques are gas-pressure bonding and tungsten - inert-gas brazing with an alloy of tungsten - 25 percent osmium. The gas-pressure bonding method best met the specifications. This process uses a technique similar to that used in hot isostatic compaction. A joint of the type that can be obtained with this method is shown at the right of figure VII-25. It should be noted in the photomicrograph that grain growth has occurred across the interface and clad-to-clad bonding has been achieved. Tensile tests at 4500° F on joined plates have shown that gas -pressure bonding and the brazing method both result in joints that are as strong as the base metal. On the basis of these results, it is thought that tungsten - uranium dioxide cylinders can be successfully fabricated and used to construct a concentric cylinder fuel stage.

Dynamic Head Limitations of Concentric Cylinders

The aerodynamic forces a concentric cylinder fuel-element stage could withstand were not known, but this limit was determined experimentally by noting the dynamic head necessary to cause failure during test. High-temperature tests are difficult to conduct, so tests were first conducted with a substitute material at room temperature. High-temperature property data for tungsten at the time suggested that a lead-antimony alloy at room temperature would simulate fairly well tungsten at high temperature.

Lead-antimony elements were placed in an air duct, and the flow rate was increased until failure occurred. Three elements of the type tested are shown in figure VII-26.

The first fuel-element stage had two support combs at the leading edge soldered to each of the cylinders. The fuel-element stage failed at a dynamic head of 13 pounds per square inch. Additional supports were added at the leading edge, as indicated in the other two photographs. These lead-alloy fuel-element stages failed at dynamic heads of 26 and 30 pounds per square inch.

Tests on tungsten stages were also run at operating temperature. For these tests, hot gas from an arc jet was used in place of room-temperature air. The hot tungsten results are compared with the lead-antimony test results in figure VII-27. Both the tungsten and the lead-antimony results are for fuel elements with leading-edge supports at 90° intervals, as shown in the figure. As previously mentioned, the dynamic head at failure for lead-antimony elements was about 13 pounds per square inch, while the actual average value was 12. 6 pounds per square inch.

The highest dynamic head available from the arc jet rig used for hot tungsten was 12 pounds per square inch. A tungsten element of the type shown here did not fail at 4700° F and 12 pounds per square inch dynamic head. Failure was induced by increasing the temperature, and the element failed during a transient from 4700° to 5100° F.

Lead-antimony, therefore, appears to simulate tungsten quite well, but the simulation

is best at a temperature somewhat higher than the nominal design temperature.

One other effect noted during the lead-antimony tests was that elements tested for long duration failed at lower dynamic heads than those under short-time tests. This indicates that creep contributes to failure. No long-duration hot tungsten data have been obtained to date.

The lead-antimony and tungsten fuel-element stages both failed in the same manner. Figure VII-28 illustrates the type of failure. Failure of the element shown started at the upstream end. As more leading edge supports were added, failure started at the downstream end. Thus, further supports must be added at the downstream end.

These data indicate that the concentric cylinder configuration may be suitable for the reference design conditions, but this configuration imposes a severe dynamic head limit unless many supports are added to the cylinders. Because of the many supports required, it is desirable that these supports also be fueled so that they may contribute most effectively to heat transfer. This obviously leads to a fine grid in which all the webs are fueled. Such a configuration is represented by the honeycomb element of figure VII-29.

Honeycomb Elements

The honeycomb is a very rigid structure and may well satisfy the desire for thin fueled sections discussed earlier without imposing dynamic head as a limiting parameter. The web thickness is about 20 mils, and the distance across flats of each hexagonal flow passage is about 1/8 inch. The outside diameter of the stage is about 2 inches.

Fabrication of Honeycomb Elements

Various fabrication methods were investigated under contracted programs in an attempt to solve the very difficult problem of producing tungsten - uranium dioxide honeycombs. The state of the art in fabrication has now advanced to the point at which it is felt that fabrication of complex geometries is feasible.

Typical honeycombs fabricated with the three most promising methods investigated are shown in figure VII-30. The isostatic compaction method is a combination of temperature and pressure in an autoclave to achieve the compaction of tungsten-coated uranium dioxide particles around expendable hexagonal mandrels. In the powder metallurgy process, tungsten-coated uranium dioxide particles are blended with fine tungsten powder as an aid to sintering. A binder and a plasticizer are added to the mixture, which is then rolled in the green, unsintered condition into thin sheets. These sheets are corrugated and glued together to form a honeycomb, and the entire structure is then densified by

sintering. The pneumatic impaction technique is very similar to the isostatic compaction method in that tungsten-coated uranium dioxide particles are hot compacted around expendable mandrels; in this process, however, compaction is achieved by closed die impaction in a high energy rate forming machine.

All the honeycombs shown have several features in common:

(1) They were all consolidated from tungsten-coated uranium dioxide particles.

(2) They all have a density in excess of 98 percent of theoretical.

(3) The fuel loading of each honeycomb was varied from 30 volume percent in the center to 10 volume percent at the periphery.

Nondestructive testing techniques for honeycombs were also developed under a contracted program. Use of these techniques on honeycombs showed, in general, that relative close dimensional tolerances with regard to web thickness and flow channel size could be achieved. These tests also showed that it is possible to fabricate honeycombs that have a high degree of integrity and no cracks.

Isostatic compaction is thought to be the most reliable of the three fabrication methods. The method used in assembling this type of honeycomb is shown in figure VII-31. The photo-etched molybdenum template is fitted to the plastic jig, and the hexagonal mandrels are installed. The honeycomb is divided into zones of various fuel loadings by Mylar sleeves placed around the mandrels, and a sintered tungsten sleeve is placed around the assembly. The various fuel loading zones are filled with tungsten-coated uranium dioxide particles of the desired fuel loading. During loading, the assembly is vibratory compacted. The Mylar sleeves are then removed, and the top template is installed. The assembly is ejected from the plastic jig and placed in a molybdenum can, which is subsequently evacuated and sealed. The entire assembly is then densified by isostatic compaction. The molybdenum canning material is subsequently removed with nitric acid.

All the honeycombs shown in figure VII-30 are the actual size required for the current reactor design. Thus, no scaleup in size is required to produce actual reactor fuel elements, but an increase in production rates would be necessary. Some additional development of the fabrication processes is required before actual reactor fuel elements could be produced. In particular, improvements are needed to control dimensions and fuel distribution of these structures better. In addition, further development of cladding techniques is needed to clad all the surfaces of the complex fuel-element structure. However, the feasibility of fabricating complex tungsten - uranium dioxide configurations has been demonstrated.

Thermal Stress in Honeycomb Elements

The rigidity of the honeycomb essentially eliminates the dynamic head problem, but this inherent stiffness could become a liability where internal stresses enter in.

Although a design for uniform temperature is attempted, some temperature gradients would be present. Also, dissimilar materials would cause thermal stresses, that is, materials with different thermal expansion coefficients, such as fueled and unfueled tungsten or various amounts of fuel and tungsten in the honeycomb stage itself.

It was felt that the honeycomb could withstand thermal stresses at temperature without difficulty. The combination of strength and ductility for tungsten was believed to be adequate for any reasonable reactor situation. Plastic flow at high temperature would essentially preclude high stresses.

The end result of such plastic flow or inelastic strains, however, was of concern. The problem could occur as follows: Thermal stresses would cause inelastic strain at temperature (1) by plastic flow as the stresses are applied and (2) by creep under these stresses during reactor operation. Because these strains are inelastic, when the honeycomb is cooled, low-temperature stresses would appear as the honeycomb would try to return to its original unstrained condition.

At room temperature, tungsten is strong but brittle, and the internal stresses might cause the honeycomb to crack. The situation is aggravated by thermal cycling where thermal fatigue enters in. It was not known how the honeycomb would deform in this inelastic manner, so no estimates could be made of the low-temperature stresses.

In order to evaluate the thermal stress problem, stresses were imposed on a uniformly loaded honeycomb stage by temperature gradients, as shown in figure VII-32. Hot gas from a tungsten preheater was forced to flow through the 19-hole central region of the honeycomb, indicated by the hatched area. The outer region of the honeycomb was cooled by the flow of cold gas through the hexagonal passages, shown by the dotted area. The temperature gradient was controlled by the amount of cold gas flowing through the outside region. This gradient was predominantly confined to a three-row nonflow zone located between the hot and cold flow regions. The typical radial temperature profile that results is shown in figure VII-32. This radial temperature profile imposes thermal stress in the radial, tangential, and axial direction, as indicated.

Figure VII-33 shows a honeycomb fuel element as it would be tested. Thin members hold the element in position to avoid external constraints. The fuel-element stage is held against a manifold to guide the cooler gas into the passages around the outside element. Hot gas enters through the center from below and is not shown. Thermal stresses were introduced in this manner at high temperature. The fuel-element stage was thermally cycled to determine whether low-temperature stresses and thermal fatigue would cause the honeycomb to crack.

The test conditions were as follows: The maximum heated zone temperature was purposely limited to 4000° F, because the honeycomb specimens with the best oxide additives were not yet available for testing. The maximum temperature gradient was 1200° F per radial inch, and this occurred at the edge of the heated zone. This temperature gra-

dient is considerably in excess of the largest gradient anticipated in the reactor. A total of 25 thermal cycles was run with cooling rates around 20° F per second. Inadvertently, during one of the 25 thermal cycles, a rapid shutdown occurred. This resulted in a cooling rate in excess of 1000° F per second.

Inspection of the element before and after testing with an eddy current probe showed that the honeycomb fuel-element stage had not been affected by the stresses imposed. This test indicates that the honeycomb can withstand both the high-temperature stresses imposed and the low-temperature stresses resulting from inelastic strain, and that thermal fatigue does not set in for 25 cycles.

Cylinder and Ligament Configuration

There are other fine geometry configurations that could be considered. For example, the element shown in figure VII-34 could, with some development, be fabricated by the same process used for the honeycomb. It may have some advantages from a thermal stress viewpoint and it conforms more readily to the cylindrical support tube without compromising the flow passages at the periphery of the element. Since the initial thermal stress tests on the honeycomb have not as yet revealed a thermal stress problem, however, the configuration was not pursued.

FUEL-ELEMENT SUPPORT

The last area of concern is fuel-element support. Figure VII-35 shows the arrangement of the fuel-element components. The fuel-element assembly is housed inside the aluminum pressure tube, as described in paper V, and it consists of a tungsten support tube and a series of fuel-element stages. The support tube fits inside the aluminum tube and runs the full length of the core. Its functions are to keep the hot hydrogen flow away from the aluminum tube and to support the fuel-element stages. The proposed full-length fuel element is made up of short stages arranged in series with each stage individually attached to the support tube. This arrangement is intended to ease fabrication of the element and also to provide mixing of the hydrogen between stages to minimize hot channels.

The support tube is fixed to the cold end of the reactor. Additional lateral support is necessary along the length to center the fuel-element assembly inside the aluminum tube. This will be discussed in more detail later.

Axial Support

Two types of attachments to fasten the fuel-element stages onto the support tube have

been considered: mechanical joints and metallurgical bonds. As an example of mechanical joints, tungsten pins could be used to connect the stage to the support tube but these will not be discussed further. Instead, one method of attachment that uses metal bonding is described herein. Metal bonding could include welding or brazing but, because of the encouraging results obtained with vapor deposition, it was decided to try vapor depositing the tungsten support tube directly onto the fuel-element stages.

Although no fuel element was developed during this program, some hardware was built under contract. The vapor deposition attachment method is illustrated in figure VII-36. A three-step procedure, which uses vapor deposition to form the tungsten support tube on one honeycomb fuel-element stage, is shown. More than one stage would, of course, be used for the full-length fuel element, and the support tube would run the full length of the core.

The three-step procedure starts with the honeycomb stage, which has an unfueled tungsten ring as an integral part of the fuel-element stage. Sacrificial molybdenum is then used to provide a mandrel for the vapor deposition of a tungsten tube as follows: The element is converted to a uniform diameter mandrel by covering the exposed part of the honeycomb with a thin-wall molybdenum cylinder. Molybdenum is added at both ends to extend the support tube and to cover the ends. Actually, a series of honeycomb stages would be used instead of the single stage shown in figure VII-36. The only exposed tungsten is the unfueled tungsten ring and, when the tube is plated onto the mandrel surface, the attachment is achieved in this area. The tungsten tube is vapor deposited by the hydrogen reduction of tungsten hexafluoride, and the outside diameter is machined to the desired dimension at this stage of fabrication. All the molybdenum is then leached out including the thin-wall molybdenum cylinder, which leaves the element, as shown at the top of figure VII-36. The unfueled band used for attachment does not have to be continuous; it could be slit or consist of portions of a band. Also, the axial position of the band is not restricted to an end of the honeycomb stage.

Elements of this type were tested at temperature under axial loads. The maximum-support tube temperature in the reference design is 3550° F, and it occurs at the last stage in the reactor. This temperature was achieved experimentally by induction heating, as shown in figure VII-37. The induction coil, the support tube, and the fuel-element stage are evident in the figure. The maximum aerodynamic drag load also occurs on the last stage of the fuel-element assembly. At the reference reactor design condition, the dynamic head is 12.6 pounds per square inch, which corresponds to a drag force of 25 pounds. A 25-pound load was applied for 10 hours at 3550° F, consisting of five thermal cycles of 2 hours each. The load was then increased 100 percent to 50 pounds, and 10 additional hours were run at 3550° F, consisting of five thermal cycles. Only minor dimensional changes were noticed. These changes occurred only at the attachment. The bond achieved by vapor deposition is therefore sufficient to support the stage for at least

twice the load of the reference design conditions.

Lateral Support

Lateral support requires a means of centering the hot tungsten support tube inside the cold aluminum tube without overheating the aluminum. The lateral support structure must, in addition, be able to accommodate relative thermal expansion between the aluminum and tungsten tubes.

This problem was solved by the use of a thin, corrugated, tungsten support spring shown on figure VII-35. This structure can withstand the high temperature of the support tube and yet provide only very small heat conduction. Heat-transfer calculations show that the heat that is transferred is rapidly dissipated in the aluminum tube, and it raises the aluminum tube temperature only about 30° locally at the point of contact.

The amount of differential expansion that the tungsten support spring must accommodate depends on the axial position, because the tungsten support tube temperature follows close to the propellant temperature. The propellant temperature increases as it passes through the reactor. The aluminum tube temperature, in contrast, is essentially independent of axial position. At the midcore position, the differential expansion is approximately 5 mils compared with an annular gap of 125 mils.

The ability to accommodate relative thermal expansion was determined by a test illustrated in figure VII-38. The tungsten support spring was placed between an outer tungsten cylinder and a tantalum inner cylinder. The difference in thermal expansion between tungsten and tantalum provides a differential expansion when the entire assembly is heated to a uniform temperature in a furnace. The relative expansion of tantalum and tungsten closely simulates the reactor conditions.

A 5-mil-thick corrugated tungsten support spring with 12 lobes resulted in a 1-mil permanent set at 4000° F; that is, there was a 1-mil clearance after cooling to room temperature. No other deformations were noticed. At temperatures lower than 4000° F, no clearance was apparent. The corrugated tungsten support spring, therefore, appears to offer a satisfactory means of maintaining concentricity.

Tungsten is known to be very brittle at room temperature. Therefore tests were conducted to determine whether or not this brittleness would present a problem during lateral vibration. The thin corrugated spring was chosen for this purpose because, in addition to providing a small heat conduction path between the tungsten support tube and the aluminum pressure tube, the thin cross section allows appreciable deflection without introducing large stresses. This deflection introduces friction to damp out any induced vibration.

Tests were first conducted to determine the spring characteristics. These tests, which used a tantalum ring as the mass in a spring mass system, indicated that the corru-

gated spring has a dynamic spring constant that is 50 to 75 times the static spring constant. Also, it possesses damping as high as 50 percent of critical damping.

Such a spring was utilized in a vibration test of a full-length support tube. Strain gages were located at various axial positions. The tube with simulated fuel-element masses was mounted on a shake table, and tests were run first with no lateral support springs, then with one, two, and finally three springs. Tube bending stresses resulting from 1g lateral forced vibration are shown in figure VII-39. Data obtained with two and three springs are not presented.

The maximum stress with no springs was approximately 27 000 pounds per square inch at the resonant frequency of 41 cps. With one spring between the aluminum pressure tube and tungsten support tube, the maximum stress was reduced to about 8000 pounds per square inch at the resonant frequency of 53 cps. When water was added on the outside of the aluminum tube, the resonant frequency decreased to 39 cps because some of the water moving with the tube had increased the effective mass of the system. The maximum stress remained about the same.

The high dynamic spring constant of the corrugated tungsten support spring in effect provides one additional point of support to reduce the maximum stress from 27 000 to 8000 pounds per square inch.

SUMMARY

Results indicate that tungsten - uranium dioxide composites are quite capable of operating under constant heating conditions at 4500^{o} F for 10 hours or more with less than 1-percent fuel loss if the exposed surfaces are clad with a thin layer of unfueled tungsten. The use of tungsten-coated uranium dioxide particles to form the composite is also helpful in reducing fuel losses. Thermal cycling conditions, however, aggravate the fuel retention problem by causing partial decomposition of the fuel. This problem appears to be controllable by the use of uranium dioxide stabilized with other metal oxides, particularly cerium or yttrium oxides, but more extensive testing of composites with stabilized fuel is necessary to completely define the operating potential of tungsten - uranium dioxide composites.

The property measurements that have been made indicate that tungsten - uranium dioxide composites have sufficient high-temperature strength and ductility to be used as self-supporting components in nuclear rocket fuel elements if the fuel loadings are kept relatively low (i. e., less than about 35 volume percent uranium dioxide).

In addition to accomplishing the aforementioned goals, the difficult problems involving fabrication of tungsten - uranium dioxide into suitable fuel-element structures have been largely solved. Fabrication techniques have advanced from the preparation of flat plates

to the consolidation of complex configurations such as honeycombs. Furthermore, methods have been developed for radially varying the fuel loading from 30 volume percent at the center to 10 volume percent at the periphery. It is now felt that fabrication, joining, and nondestructive testing of complex tungsten - uranium dioxide configurations are feasible. Further development and optimization of the various processes are needed, however, before actual fuel elements can be produced.

Fuel-element performance tests have shown that the concentric cylinder element can operate at the reference design conditions, but this element imposes severe performance limitations unless many supports are incorporated. High performance requires a fine grid, such as the honeycomb element. Although the thermal stress problem for these elements has not been completely resolved, the fine grid element appears to offer the best approach to operation at high power density. Methods of supporting these elements against axial and lateral loads are available.

The interrelation of operating parameters is shown in figure VII-23 with a reference design point indicated by the symbol at a mass velocity of 50 pounds per second per square foot and an average dynamic head of 10 pounds per square inch corresponding to a maximum value of 12.5 pounds per square inch mentioned earlier. Without a dynamic head limit, the mass velocity could be increased. It is felt that a fine grid fuel element such as the honeycomb would not present the limit on mass velocity, but rather some other factor such as core pressure drop would enter in. The thrust, therefore, could be increased accordingly.

REFERENCE

1. Martin, A. E.; and Edwards, R. K.: Uranium - Uranium Dioxide Phase Diagram at High Temperatures. J. Phys. Chem., vol. 69, no. 5, May 1965, p. 1788.

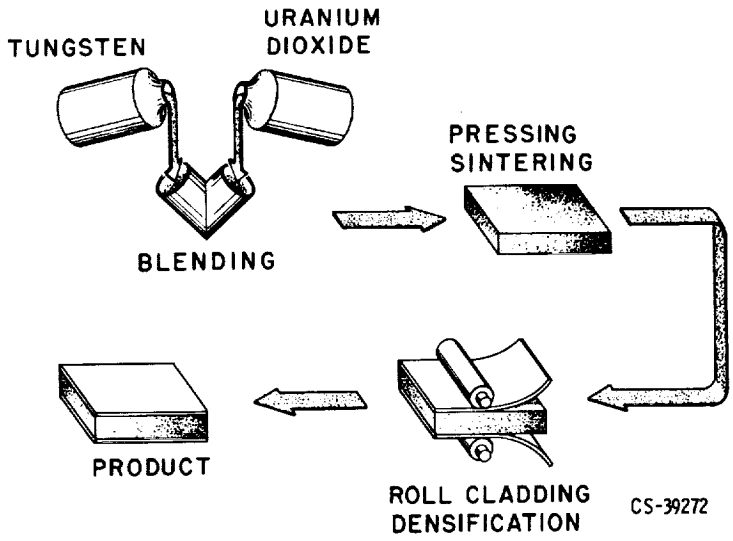

Figure VII-1. - Fabrication of tungsten - uranium dioxide composites by powder metallurgy techniques.

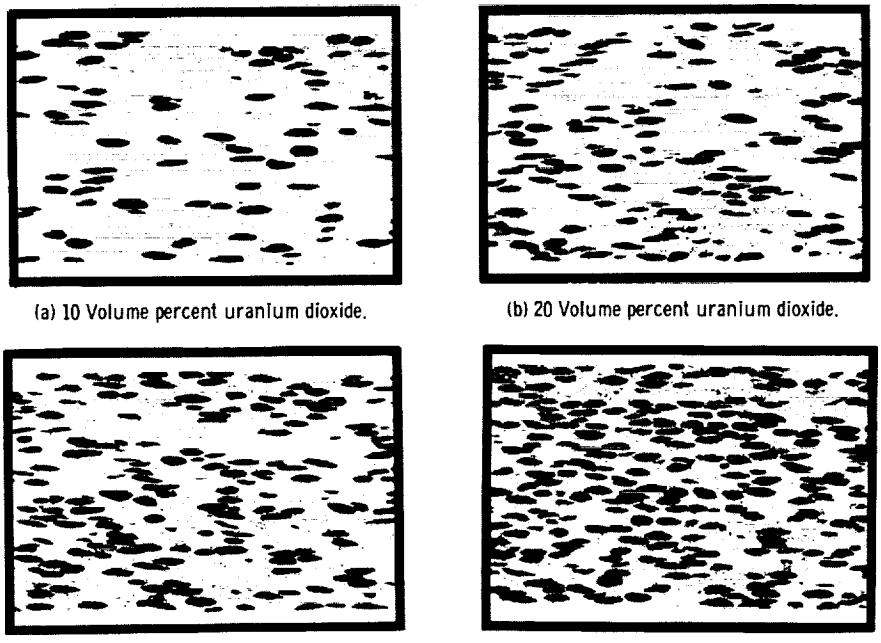

(a) 10 Volume percent uranium dioxide.

(b) 20 Volume percent uranium dioxide.

(c) 30 Volume percent uranium dioxide.

(d) 40 Volume percent uranium dioxide.

Figure VII-2. - Tungsten - uranium dioxide plates of various fuel loading. (Sections are parallel to rolling direction.)

CS-29782

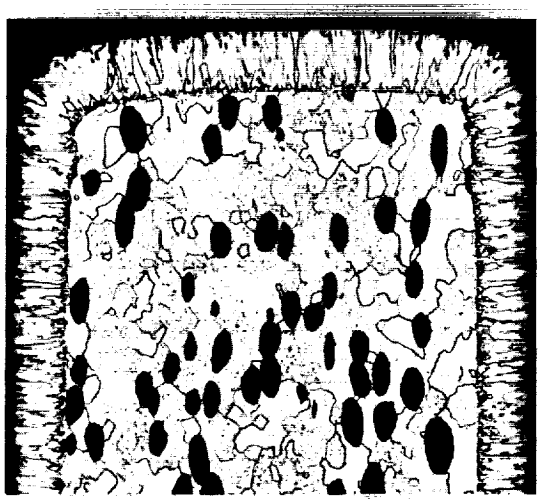

CS-38964

Figure VII-3. - Tungsten - uranium dioxide composite surface clad by vapor deposition.

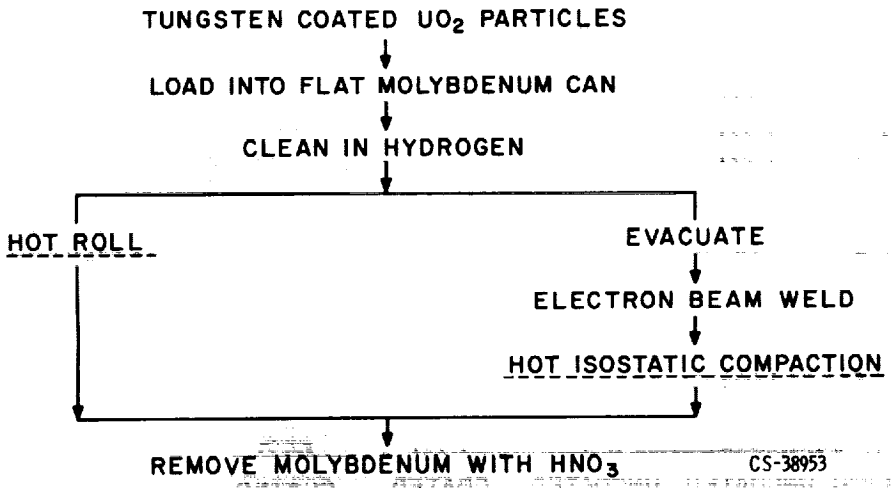

Figure VII-4. - Consolidation techniques for tungsten-coated uranium dioxide particles.

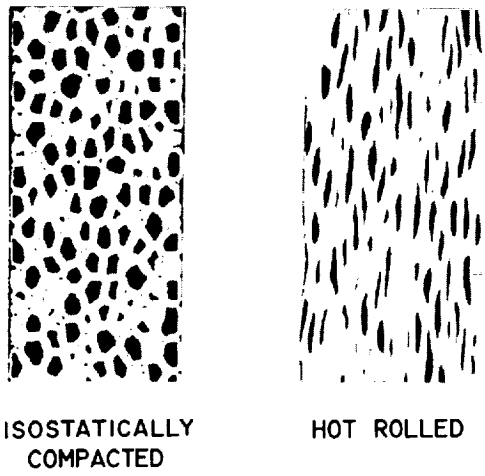

Figure VII-5. - Tungsten - uranium dioxide plates compacted from coated particles.

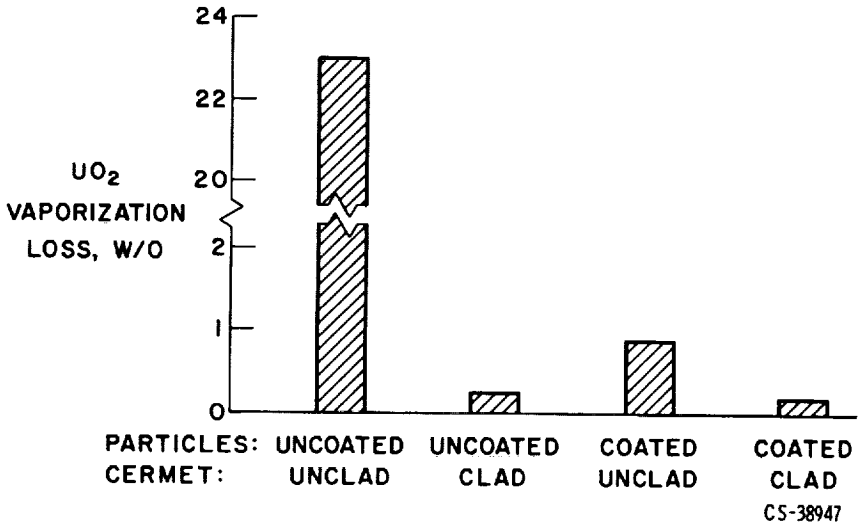

Figure VII-6. - Vaporization fuel loss from tungsten - uranium dioxide composites. Test conditions, 2 hours at 4500° F in hydrogen.

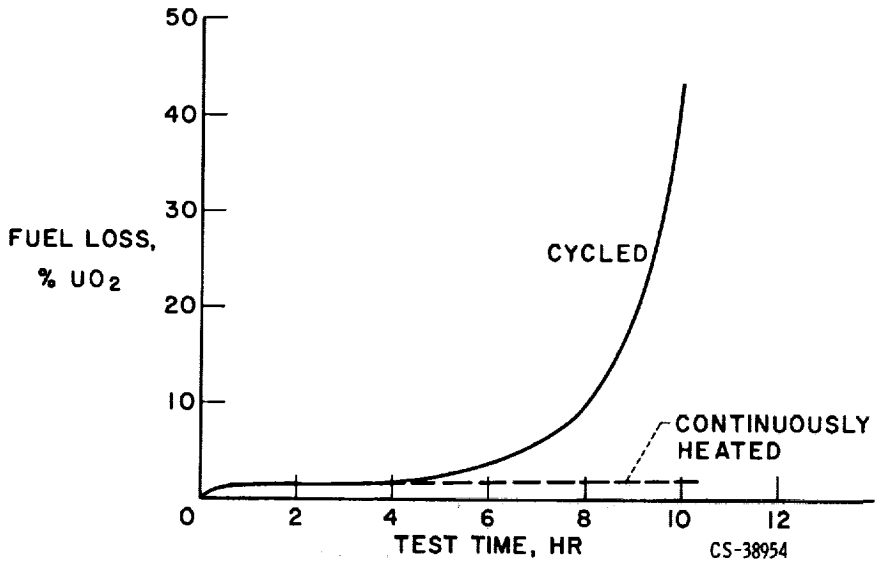

Figure VII-7. - Effect of thermal cycling on fuel loss at 4500° F.

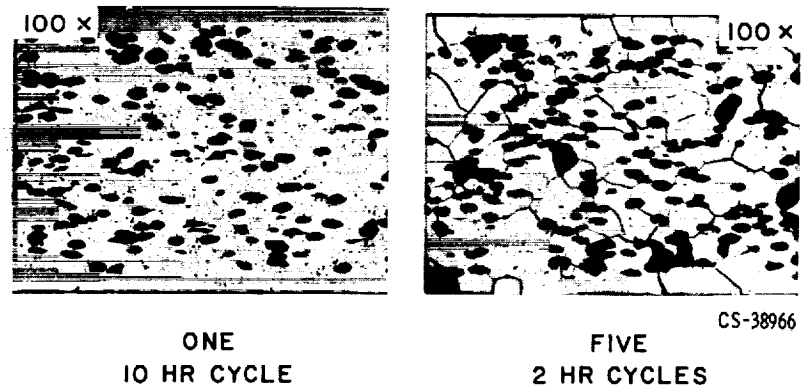

Figure VII-8. - Effect of thermal cycling at 4500° F on tungsten - uranium dioxide composites.

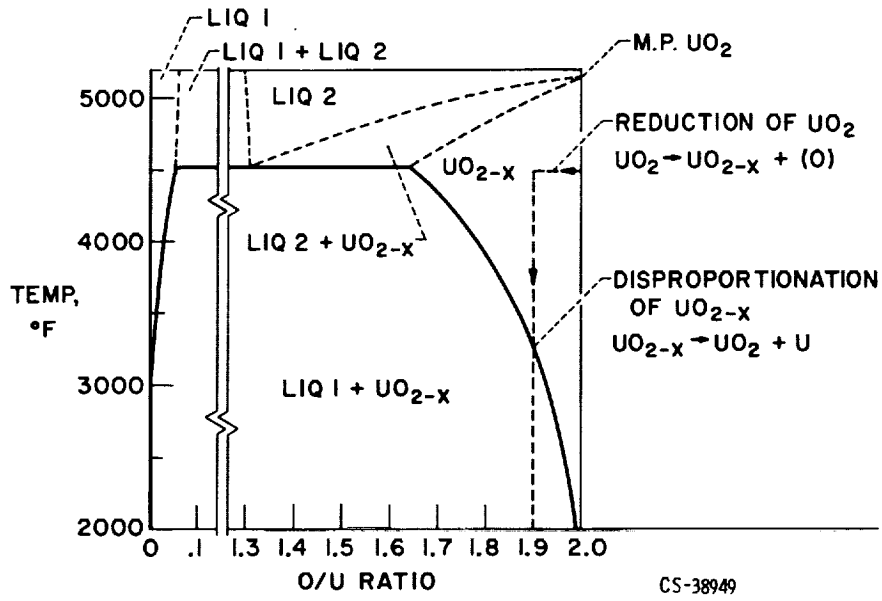

Figure VII-9. - Oxygen-uranium phase diagram.

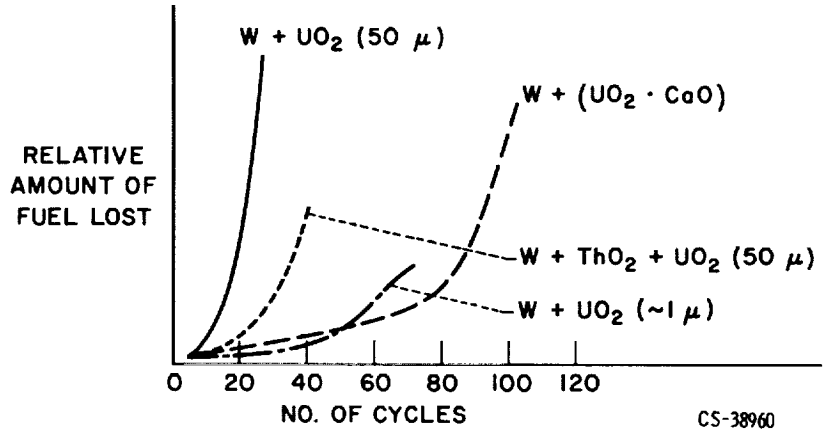

Figure VII-10. - Effect of cycling on various tungsten - uranium dioxide composites. Cycle time, 10 minutes; temperature, 4500° F; pure hydrogen environment.

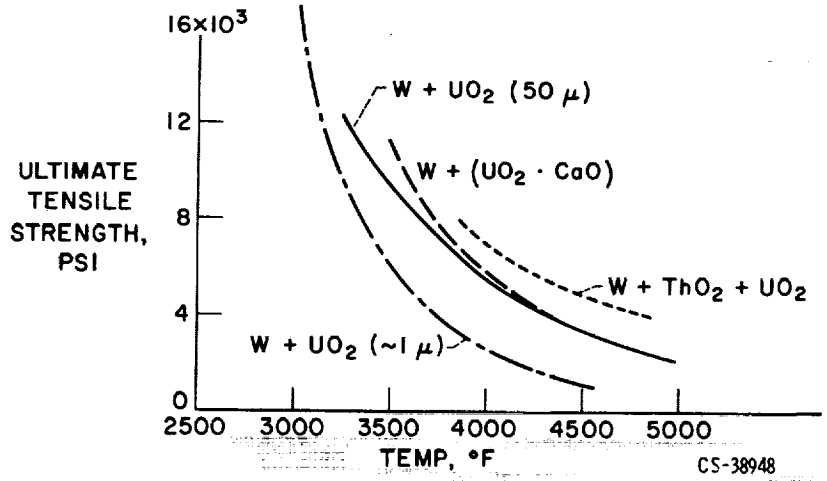

Figure VII-11. - Effect of core material changes on strength of tungsten - uranium dioxide composites.

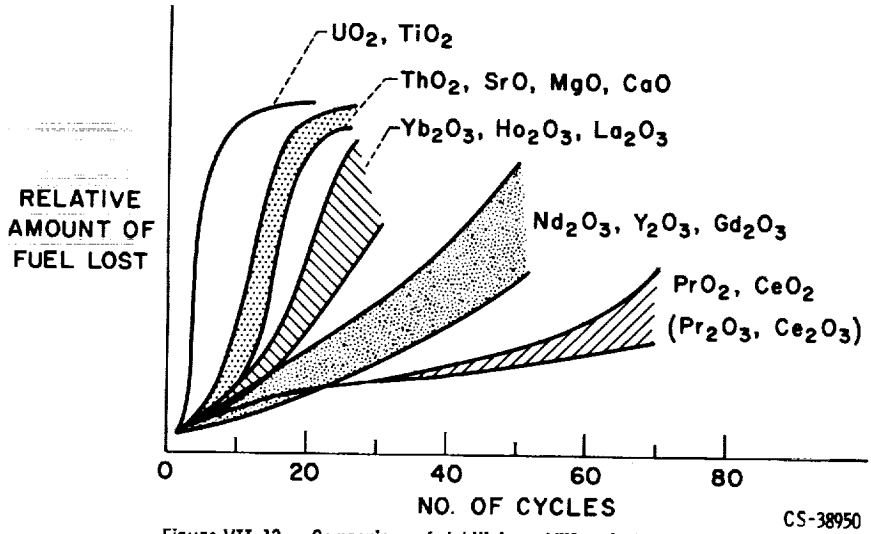

Figure VII-12. - Comparison of stabilizing additives in tungsten - uranium dioxide composites. Cycle time, 10 minutes; temperature, 4500° F; pure hydrogen environment.

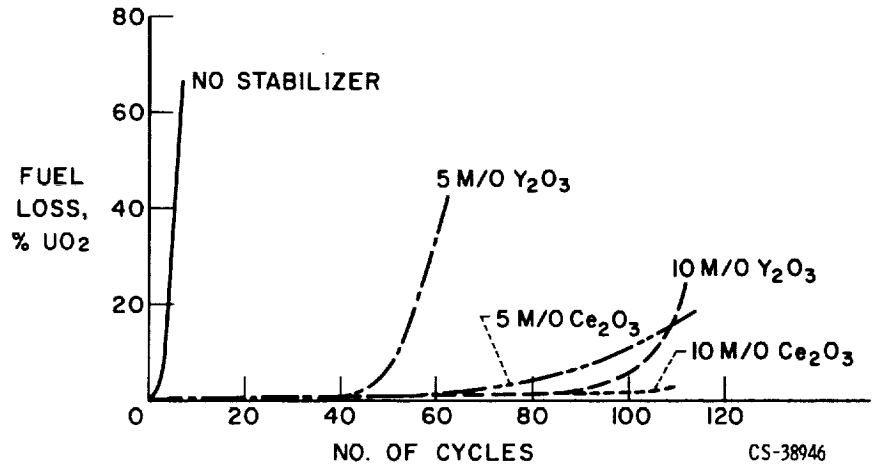

Figure VII-13. - Effect of cerium oxide and of yttrium oxide as stabilizers of uranium dioxide in tungsten - uranium dioxide composites. Cycle time, 10 minutes; temperature, 4500° F; pure hydrogen environment.

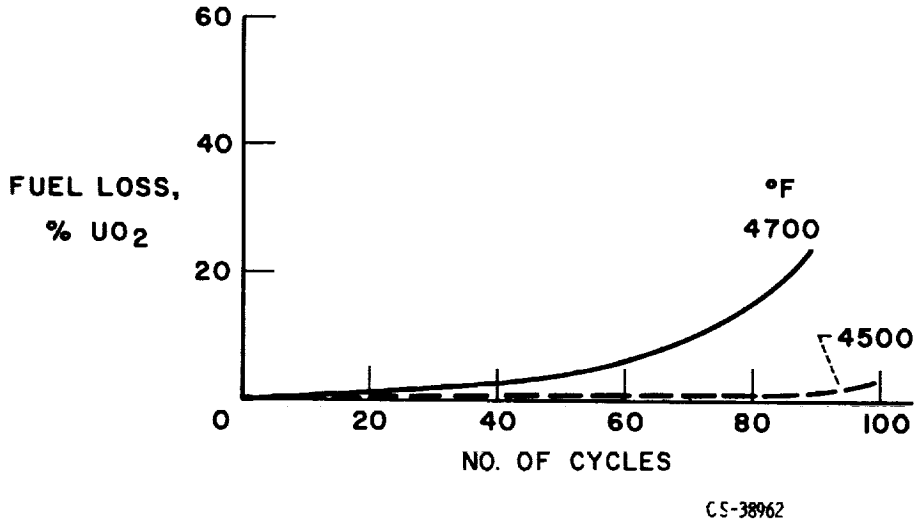

Figure VII-14. - Effect of temperature on tungsten - uranium dioxide composites stabilized with cerium oxide. Cycle time, 10 minutes; temperature, 4500° F; pure hydrogen environment.

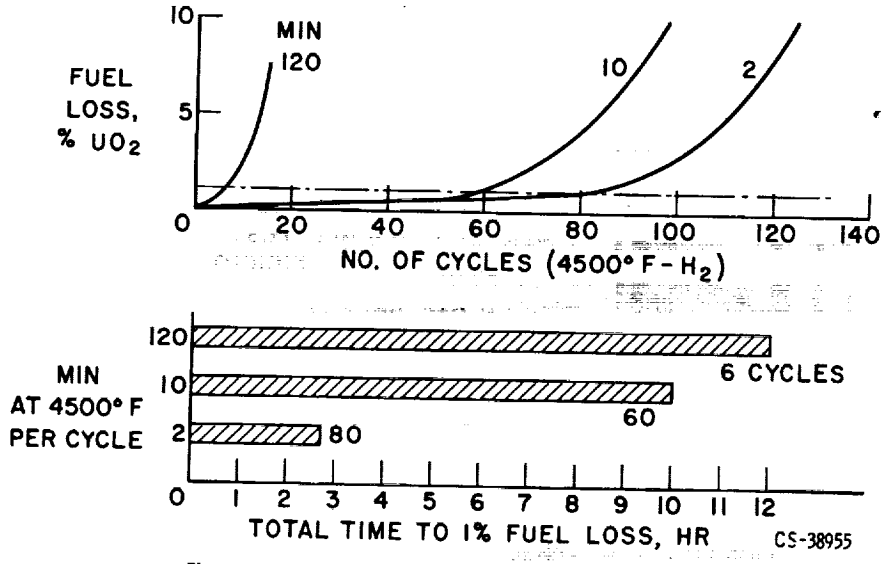

Figure VII-15. - Effect of time at temperature on tungsten - uranium dioxide composites stabilized with cerium oxide.

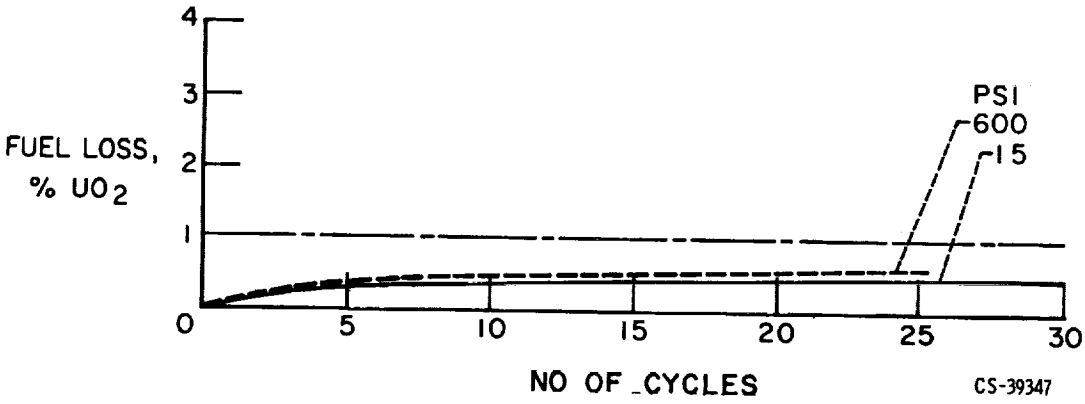

Figure VII-16. - Effect of hydrogen pressure on tungsten - uranium dioxide composites stabilized with cerium oxide. Cycle time, 10 minutes; temperature, 4500° F; pure hydrogen environment.

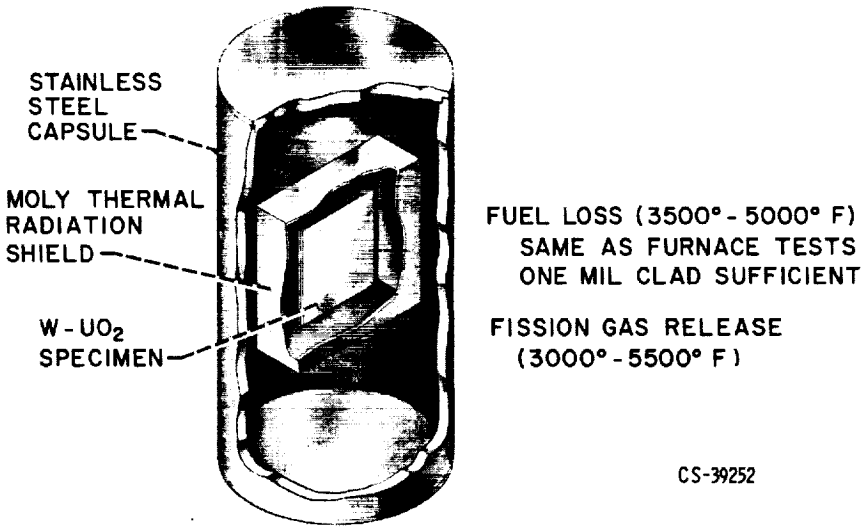

Figure VII-17. - In-pile capsule.

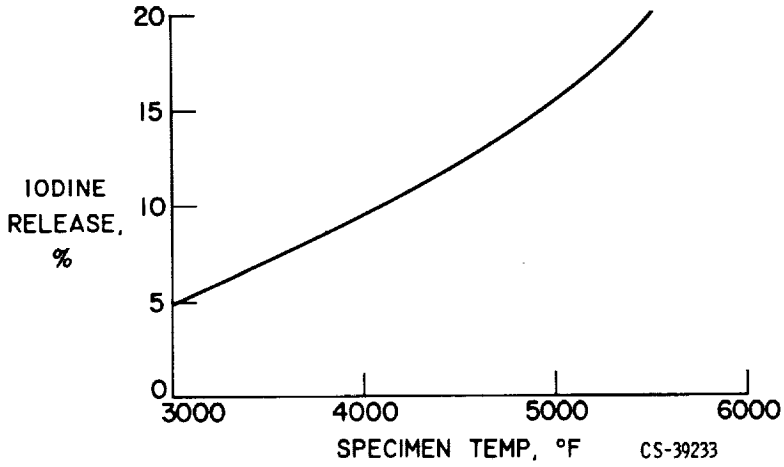

Figure VII-18. - Iodine release from tungsten - uranium dioxide composites.

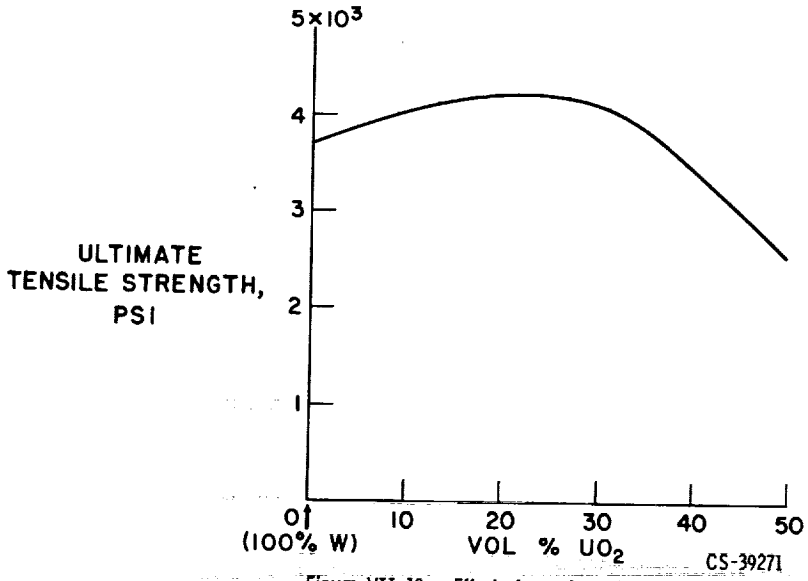

Figure VII-19. - Effect of uranium dioxide additions to the strength of tungsten - uranium dioxide composites at 4500° F.

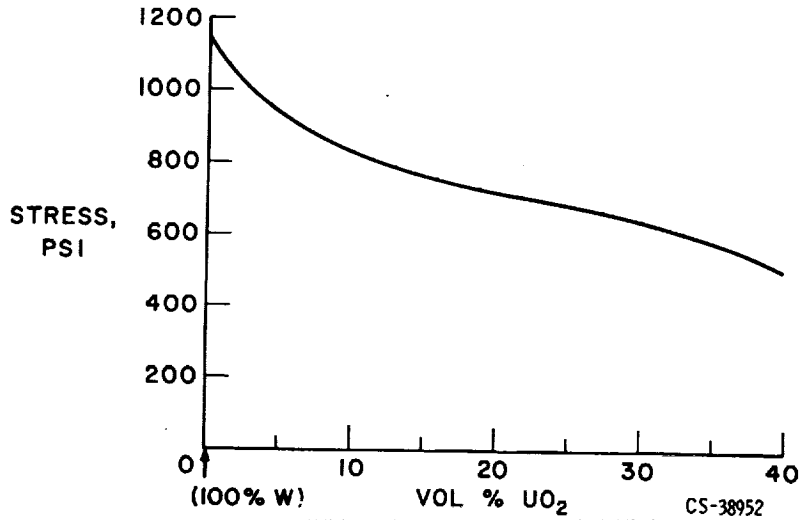

Figure VII-20. - Rupture stress for 10-hour life for tungsten and tungsten - uranium dioxide composites at 4500° F.

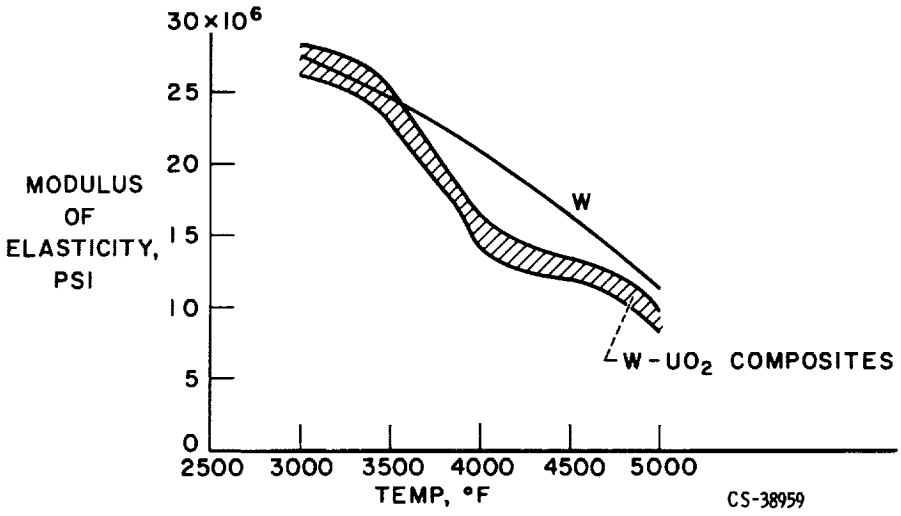

Figure VII-21. - Average Young's moduli as function of temperature for tungsten and tungsten - uranium dioxide composites.

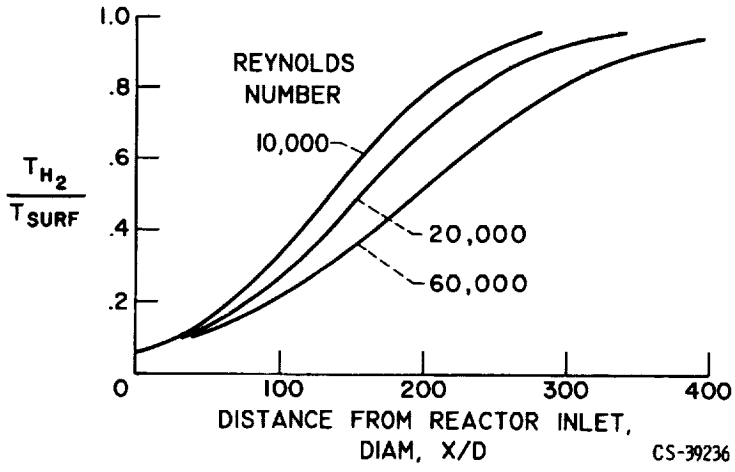

Figure VII-22. - Axial variation of propellant temperature. Surface temperature, constant.

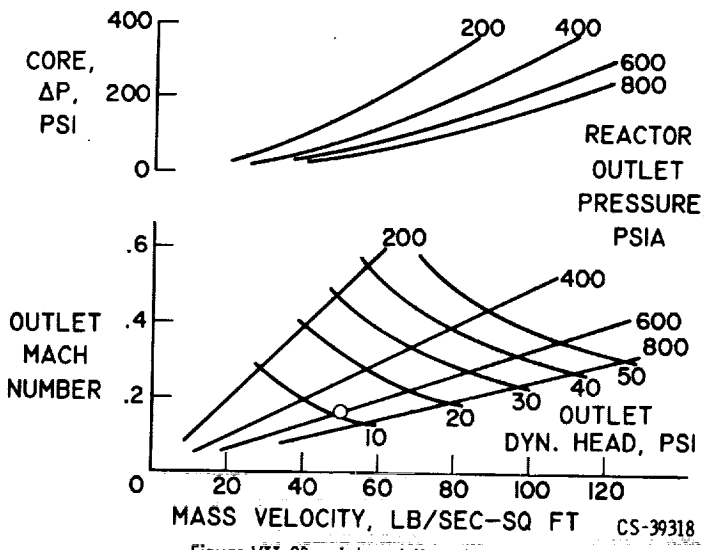

Figure VII-23. - Interrelation of operating parameters.

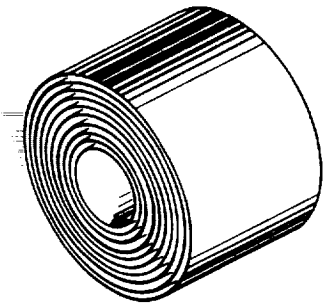

CS-39237

Figure VII-24. - Concentric cylinder configuration.

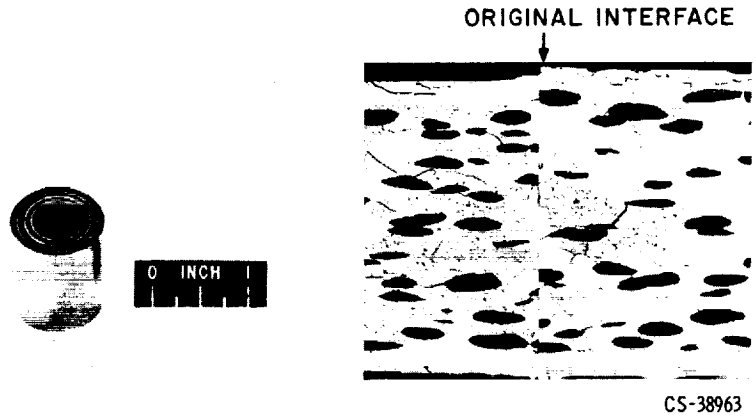

(a) Cylinders formed from tungsten - uranium dioxide plates.

(b) Joint obtained by gas pressure bonding.

Figure VII-25. - Forming and joining of tungsten - uranium dioxide plates.

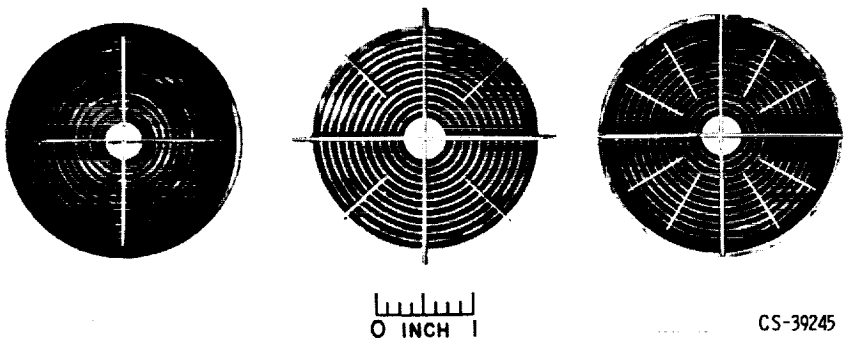

(a) 13 psi.

(b) 26 psi.

(c) 30 psi.

Figure VII-26. - Cold flow tests on lead antimony.

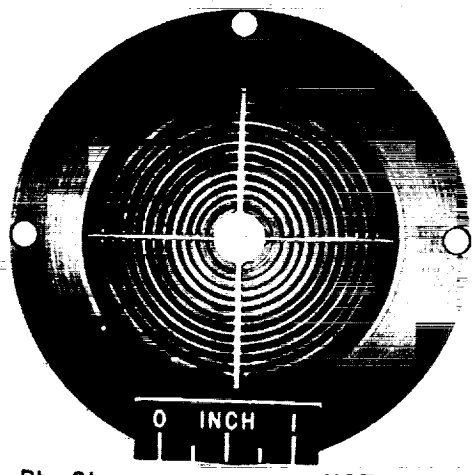

COLD Pb-Sb

$\frac{\rho V^2}{2g}$ = 12.6 PSI

HOT TUNGSTEN
4700° - 5100° F

$\frac{\rho V^2}{2g}$ = 12.0 PSI

C-65487
CS-39248

Figure VII-27. - Tungsten and lead-antimony comparison.

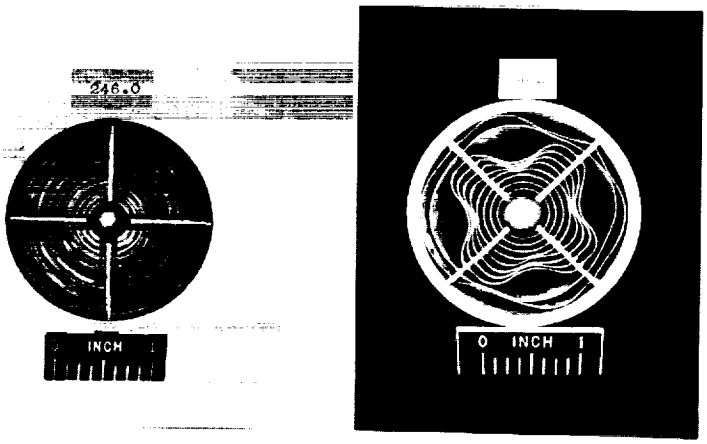

C-66-562

(a) Before test.

C-66-734

(b) After failure.

Figure VII-28. - Tests on lead-antimony cylinders; upstream views.

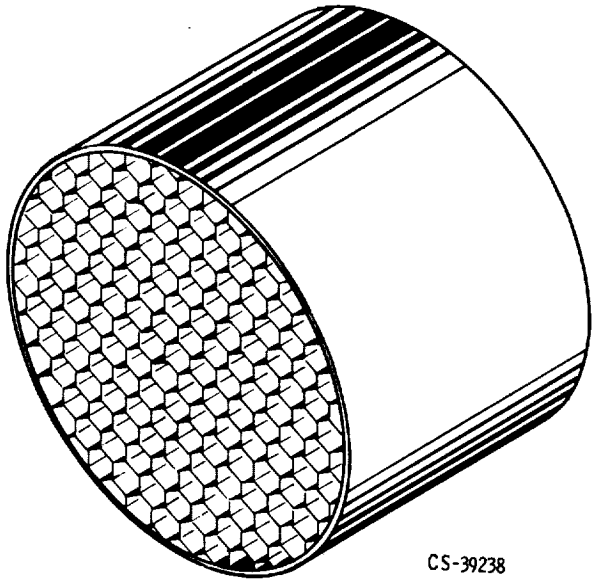

Figure VII-29. - Honeycomb configuration.

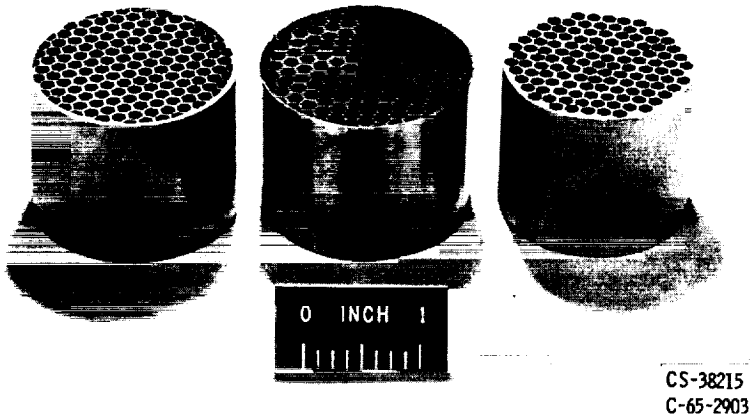

(a) Hot isostatic compaction. (b) Powder metallurgy forming and sintering. (c) Hot pneumatic impaction.

Figure VII-30. - Tungsten - uranium dioxide honeycomb structures fabricated by different processes.

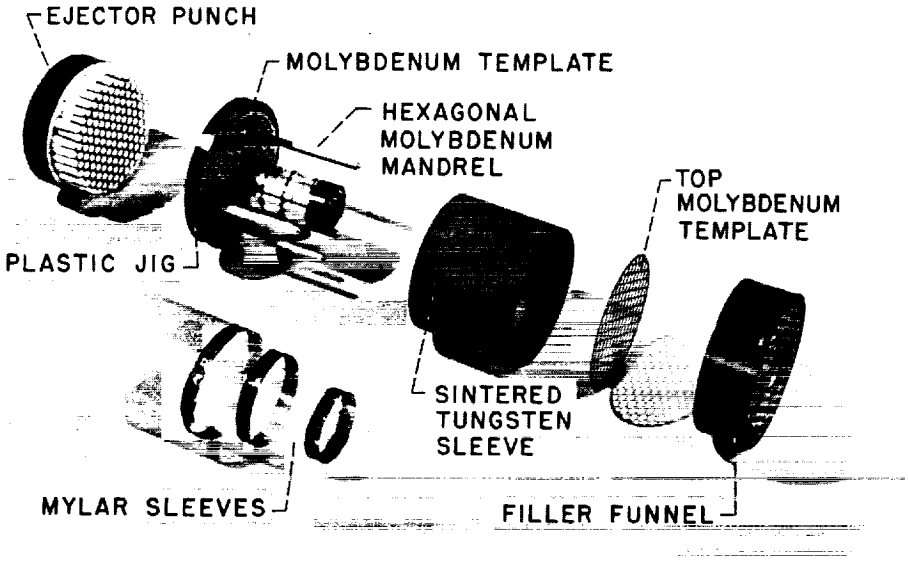

Figure VII-31. - Components for isostatic compaction of honeycombs.

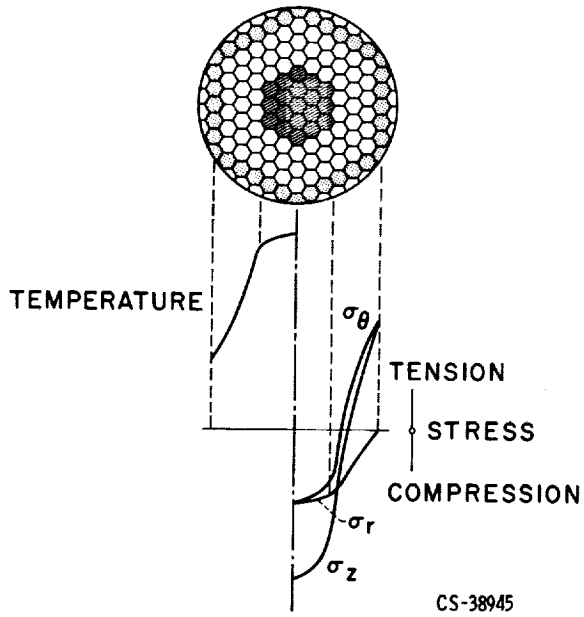

Figure VII-32. - Flow-induced thermal stresses.

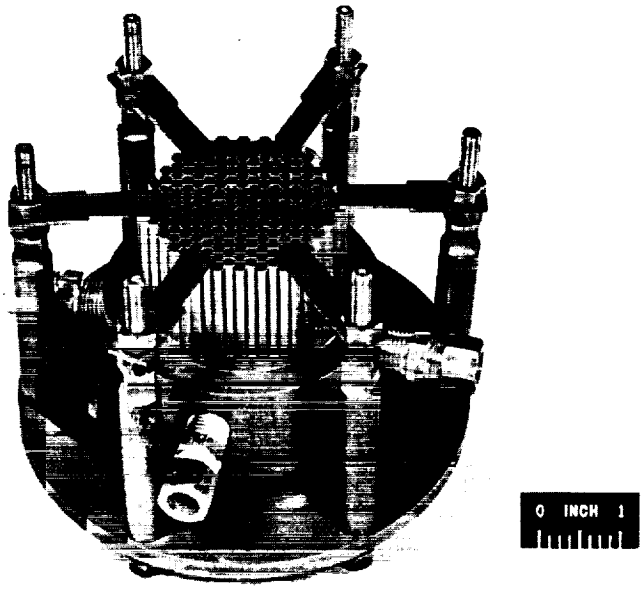

CS-39247
C-65-2502

Figure VII-33. - Thermal stress experiment.

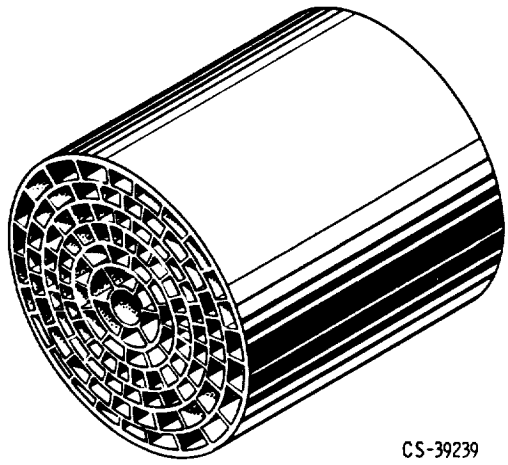

CS-39239

Figure VII-34. - Cylinder and ligament configuration.

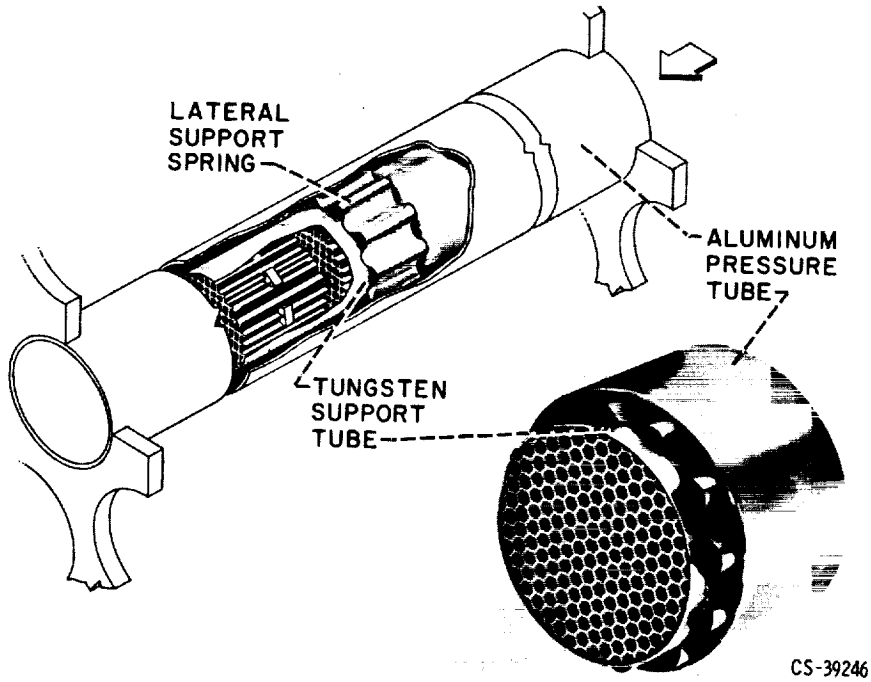

Figure VII-35. - Fuel element arrangement.

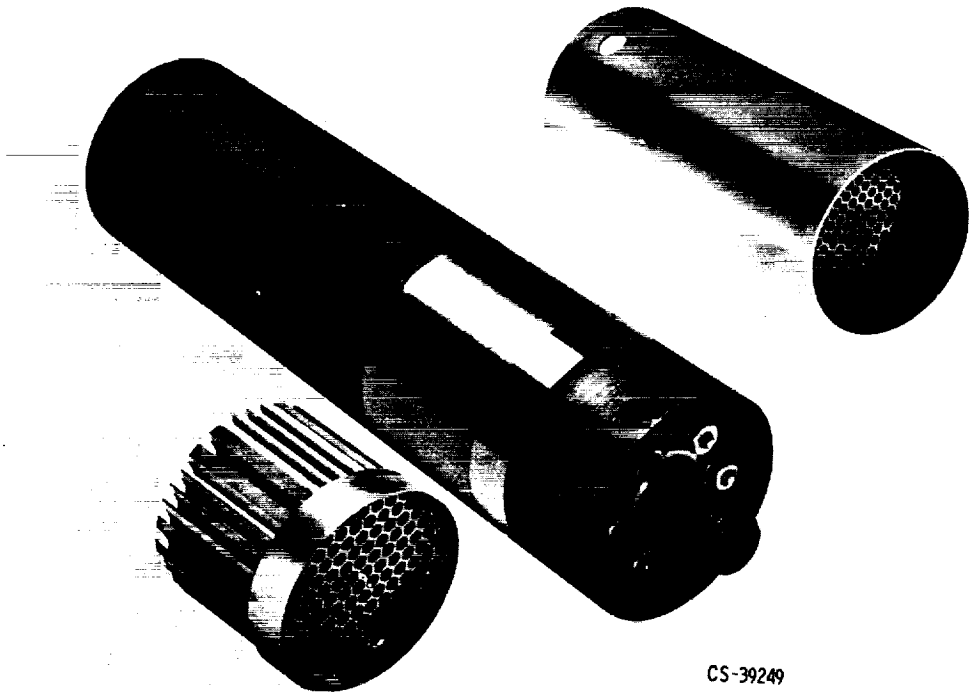

Figure VII-36. - Integral fuel element - support tube fabrication.

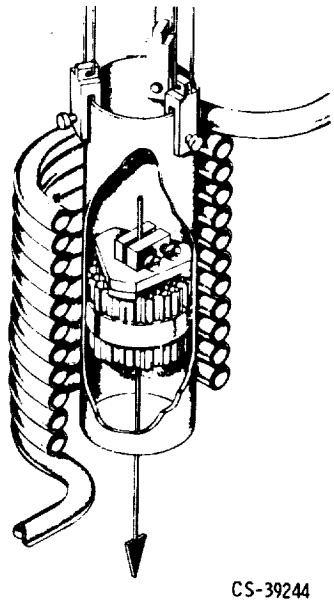

CS-39244

Figure VII-37. - Axial support test.

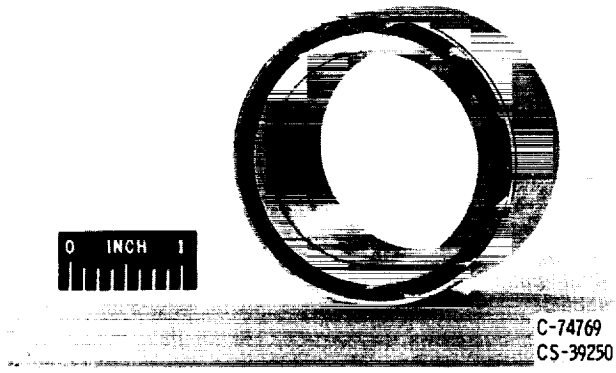

Figure VII-38. - Lateral support spring.

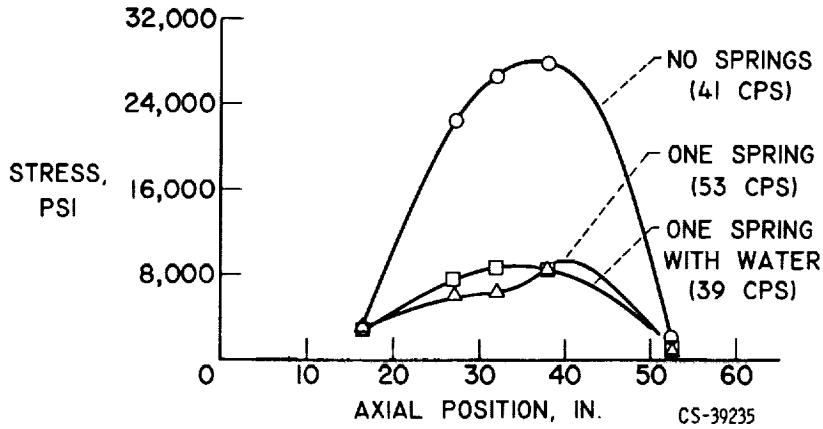

Figure VII-39. - Support tube bending stress. Forced vibration, 1 g.

X66-51414

VIII. FLUID SYSTEMS AND CONTROL

John V. Miller, Harry W. Davison, James R. Mihaloew,
Walter A. Paulson, and Guy H. Ribble, Jr.

Lewis Research Center

INTRODUCTION

The tungsten water-moderated reactor (TWMR) is actually composed of two major fluid systems, the hydrogen, or propulsion, loop and the water, or moderator, loop. These two flow systems, their components, characteristics, and interrelations are discussed herein.

The closed-loop flow path of the water (fig. VIII-1) is quite simple. The water leaves the pump, enters the reactor vessel, and passes through the core and the beryllium side reflector where it absorbs heat. The water then flows through the shell side of the heat exchanger where it gives up this energy and then back to the circulating pump to complete the cycle.

In this short 2- to 3-second trip around the loop, the water performs several functions and creates several problem areas. In the passage through the reactor, the water not only performs its main function as a nuclear moderator, but also acts as a structural coolant. This latter function is the principal reason why the temperature of the aluminum can be maintained at less than 300° F in such close proximity to the extremely hot fuel elements. The water flow rate and temperature must therefore be capable of adequately cooling the aluminum structure.

As the water flows through the heat exchanger, the energy absorbed by the water in flowing through the core region is transferred to the incoming hydrogen gas. The hydrogen enters the heat exchanger at -290° F, considerably below the freezing point of water. Unless the heat exchanger is properly designed, the water passing through it could freeze, which would stop the circulation of the water, result in a loss of coolant to the aluminum structure, and eventually lead to failure of the reactor.

The key to the design of the water system, therefore, is the balance between freezing in the heat exchanger on one hand and maintaining a low enough water temperature to assure cooling of the aluminum on the other.

Preceding page blank

The hydrogen, or propulsion, flow system is somewhat more complicated than the water loop. Two areas of concern in the propulsion loop, the design of the turbopumps that force the propellant through the system and the proper cooling of the nozzle, are discussed in some detail in papers II and III.

The flow path of the hydrogen in the TWMR concept is from the storage tank through the following components: the first and second stage pumps, the cooling tubes in the regeneratively cooled nozzle, the heat exchanger where the problem of freezing the water is again encountered, and then through the topping turbine. From there it enters the reactor core where most of the gas is heated to 4000° F and expanded through the propulsion nozzle.

About $2\frac{1}{2}$ percent of the hydrogen passes through four special fuel elements where the gas is heated to only 1400° F. This bleed gas drives the control solution turbopump, the moderator turbopump, and a hydrogen turbopump and is then discharged through an auxiliary nozzle.

In flowing through the core region, maximum heat transfer to the hydrogen is desirable within the limits of the fuel element operating temperature. Flow through parallel passages and variations from nominal conditions that create hot spots must be taken into account.

In addition to the independent behavior of the water and hydrogen flow loops, many components in the two systems are interrelated; for example, the hydrogen in the bleed system drives the water turbopump, and the water temperature affects core reactivity. The overall system then must also be examined to determine the character of these interrelations with regard to steady-state operation, startup, and control possibilities.

PROPELLANT FEED SYSTEM

The propellant pumping arrangement, the so-called feed system, must supply the pressure necessary to force the hydrogen through the fuel elements, propulsion nozzle, and other components in the system. The power for this can come either from the reactor or from a separate source. In the TWMR, only methods that used reactor power were studied.

One system studied was a topping system as shown in figure VIII-2. Hydrogen flows from the storage tank through the pump, the nozzle wall, the heat exchanger, a turbine that drives the pump, the reactor core, and out the propulsion nozzle. The topping system is simple and efficient because all the hydrogen passes through the nozzle to produce thrust. In this concept the topping turbine must be located downstream of the heat exchanger because it uses the energy picked up in cooling the nozzle walls and the water moderator to drive the pump. Although the energy in each pound of gas entering the

turbine is still low at -160° F, the turbine is capable of developing thousands of horsepower because of the large mass flow passing through it. In the topping system the turbine pressure drop must be added to the pump head. If there is enough energy available to drive the turbine, this simple feed system can be used.

Another classic method for pumping the propellant is the bleed system (fig. VIII-3), which is similar to the topping system except for the source of gas that drives the turbine. A small amount of hydrogen is bled from the main flow and heated in special fuel elements to about 1400° F. The bleed gas flows through the turbine that drives the hydrogen pump and is then discharged through an auxiliary nozzle. Since the gas is discharged at low temperature, its specific impulse is low, and the overall system specific impulse is reduced.

A comparison of the two systems is shown in table VIII-1 based on the same powerplant conditions of chamber pressure, temperatures, flow rate, pump efficiency, etc., that were used in the reference design. The bleed system has no upper chamber pressure limit. The topping system limit occurred around 700 pounds per square inch absolute for the engine considered. This is the point above which there is insufficient energy picked up in the nozzle and heat exchanger to provide the required pumping power. The bleed rate was 5.1 percent of the total hydrogen flow for the bleed system. The topping system has no bleed gas. The engine specific impulse values were calculated for a 40:1 area ratio propulsion nozzle discharging to vacuum with a nozzle efficiency of 98 percent. The bleed system specific impulse was 819 seconds, and that of the topping system was 839 seconds. The hydrogen pump discharge pressure was 945 pounds per square inch for the bleed system and 1490 pounds per square inch for the topping system. Higher pressures require heavier structures between the pump and turbine. In this concept, the nozzle would be the principal part affected. The bleed system requires 7200 hp and the topping system, 11 700 hp to drive the hydrogen pump. It should be pointed out that each system will also require about 1000 hp to drive the moderator and poison solution circulating pumps.

For cases in which a topping system cannot supply all the required pumping power, a combination of the two systems can be used to minimize the loss in thrust due to the bleed gas. This is done at the expense of some complexity, as shown in figure VIII-4. This combination is called a split feed system because the pump work is split between the topping turbine and the bleed turbine. As much work as possible is extracted from the topping turbine, which drives the second stage pump. The rest of the work is furnished by the bleed turbine, which drives the first stage pump.

The split feed system was used in the reference design in order to study its complexities and behavior. In view of the study-tool aspects of the design, the nozzle chamber pressure was chosen low enough to permit investigation of any combination of systems from all-bleed to all-topping systems. Since the 600 pound per square inch chamber

pressure selected would permit the use of an all-topping system, an arbitrary work split between the bleed and topping turbines was used. The resulting performance characteristics are a compromise between those of the all-bleed and all-topping systems given in table VIII-1. The split system gets around the chamber pressure limitation of the topping system and the high bleed rate of the bleed system.

There are, of course, the usual requirements of rotational speed, suction head, etc., for the turbomachinery used in this system. The design point operation of the turbopumps for the reference design is well within the present state of the art in these areas. These are grouped under the first item in the following list of general turbopump requirements:

(1) Rated conditions
(2) Nuclear environment
(3) Space environment
(4) Small size and light weight
(5) Long shutdown period between runs
(6) 10-Hour design life at rated conditions
(7) 25 Start-stop capability

The nuclear environment will dictate such items as materials of construction and method of fabrication. Items 3 and 4 are rather obvious requirements. The long shutdown period between runs will require low leakage shaft seals. The last two requirements of design life and restart capability should not present any difficulty.

These requirements for the system turbopumps are generally the same as those for the pumps of any nuclear rocket.

HEAT TRANSFER TO THE PROPELLANT

The heart of the system performance is the heat transfer in the reactor core. The performance objectives of a nuclear rocket are high specific impulse and small size. These depend, in turn, on high outlet gas temperature and efficient heat transfer from the fuel. Since gas temperature is primarily limited by fuel temperature, a high value of fuel temperature is desirable. Heat-transfer effectiveness depends on high temperature differences between the fuel element and the coolant. Therefore, the maximum specific impulse and smallest core would result if the maximum allowable operating temperature on the entire fuel element surface could be maintained.

Several factors influence the power capability of the reactor. The most important factors are as follows:

(1) Flow passage behavior
(2) Radial power distribution

(3) Axial power distribution

(4) Hot channel factors

First, all the flow passages in the reactor do not behave in exactly the same manner. Some tend to run hotter or cooler than the average. This makes it virtually impossible to attain a constant temperature everywhere. Figure VIII-5 shows a cross section of a typical fuel cell for the TWMR with the high-temperature fuel area, insulating gas gap, aluminum pressure tube, flow divider, and water regions. The function of this flow divider will be described later.

With the fuel operating at about 4500° F and with the aluminum restricted to about 300° F, a severe thermal gradient exists between the periphery of the high-temperature area and the aluminum. While most of the temperature drop is across the insulating gas gap, a gradient still exists in the outer fuel material. The flow passages in this peripheral region, therefore, do not behave exactly like a flow passage in the center of the fuel cell where no thermal gradient exists.

In order to minimize this problem, the fuel element is divided axially into 26 stages with an axial gap between each stage. This provides an opportunity for the flow among the passages to be mixed and to behave more uniformly since the pressure is balanced over each stage instead of over the entire length.

The analysis of this geometry is quite complicated. Two digital computer programs were used to predict behavior. Their use enabled the analysis of a variety of fuel element configurations that took into account variable radial and circumferential power distributions and variable conductivity.

The results of these calculations indicate that because of the finite geometry of the fuel cell, it is impossible to extract maximum power out of each and every passage. A uniform fuel element temperature may be approached but cannot be attained.

RADIAL POWER DISTRIBUTION

The radial power distribution across the reactor tends to produce nonuniform behavior between fuel elements; however, this irregular behavior can be compensated for by controlling the flow of propellant to each element.

Figure VIII-6 shows the gross radial power distribution of the TWMR. If the gas flow across the reactor were constant, obviously the gas temperature in the outer elements would not be as high as the temperature of the gas emerging from the center elements; however, by orificing the flow, the flow in each of the elements can be matched to obtain the same power-to-flow ratio. From the viewpoint of obtaining the same gas temperature from each element and operating the fuel material at its maximum temperature, this matching solves the problem of a radial power gradient.

The fact that there is a nonuniform radial power distribution does imply, however, an inefficiency of operation. The fuel elements near the outer edge of the reactor only produce 70 percent as much power as the center elements. For a given power level then, the reactor core is larger than would be required if the radial power distribution were uniform.

AXIAL-POWER DISTRIBUTION

In the axial direction, the effect of a nonuniform power distribution is more complex. If the power were uniform along the length of the core, for example, the temperature difference between the fuel element and the gas would nearly be constant. Under these circumstances, the maximum fuel temperature would occur only at the exit of the reactor, the point where the gas temperature is highest. This obviously would not result in good heat-transfer performance.

In nuclear reactors, the axial power naturally tends to be distributed according to some cosine function. Figure VIII-7 shows the fuel element and gas temperature variation associated with a cosine power distribution.

As in the case of uniform power, the maximum surface temperature occurs at one location only, and it would require a reactor length of about 37 inches to achieve a gas temperature of 4000° F. To obtain the more desirable condition of a uniform surface temperature along the entire length of the reactor, the shape of the power distribution must be altered. This alteration can be accomplished by tailoring the neutron power by zoning the fuel and absorber material and by using end reflectors (paper VI).

The problem is to determine what power distribution results in a uniform fuel element temperature and to tailor the neutronics as close to this distribution as possible.

One important factor that influences the optimization of the power distribution is the convective heat-transfer characteristics of hydrogen under the conditions found in a nuclear rocket reactor. Much experimental work has been done on gaseous heat transfer; however, with a nuclear rocket reactor a new problem has arisen because of the extremely high metal temperature and extremely low gas temperature that exist in the inlet region of the reactor.

For this sort of condition, the local heat-transfer coefficients are not accurately predicted by conventional heat-transfer correlations. Figure VIII-8 shows results of some experimental heat-transfer work performed at Lewis in which the hydrogen properties were evaluated at film conditions. The 20 to 30 percent uncertainty in convective heat transfer for conditions similar to those in the inlet region requires an extremely conservative approach to axial power optimization.

The experimental data were, therefore, reexamined to determine which parameters

were producing this scatter. From this investigation, a new correlation was evolved, which is shown in figure VIII-9. Obviously a considerable reduction in scatter was achieved with this correlation.

Bulk gas properties are used in this modified correlation and correction factors for surface-to-gas temperature ratio and for length-to-diameter ratio are included to obtain local heat-transfer coefficients.

When this modified correlation was used, an axial power distribution was established that would result in a constant surface temperature of 4500° F along the entire length of the fuel element. This power distribution is shown in figure VIII-10; the maximum allowable heat flux is approximately 10 Btu per second per square inch.

Note that the allowable power is not highest at the inlet as might be expected, but reaches a maximum a short distance from the inlet. This is due to the combined effect of an increasing heat-transfer coefficient and a decreasing temperature difference, the product of which determines allowable heat flux.

Figure VIII-11 shows the gas temperature variation along the reactor length for this power distribution. With a uniform surface temperature of 4500° F, the required length of the reactor to achieve an exit gas temperature of 4000° F would be about 25 inches, or a 33-percent decrease in length over the cosine distribution. Figure VIII-12 compares this desired distribution to the reference distribution, which was actually obtained by zoning the fuel and the absorber. The deviation shown between the two curves would require an increase in core length of $2\frac{1}{2}$ inches.

A better match to the desired power shape could probably have been obtained. The reference power distribution shown was calculated by using an inlet end reflector and only one region in which a mixture of natural and separated tungsten was substituted for the all-separated tungsten. Further complications to improve performance of this type of powerplant were not considered necessary. Furthermore, the desired curve, as ideally calculated, would have to be modified to account for uncertainties in the calculations.

CALCULATIONAL UNCERTAINTIES

One example of these uncertainties has already been seen in the scatter of data about the empirical heat-transfer correlation equation. Other unavoidable deviations from nominal design conditions exist and must be considered in evaluating the power capability of the reactor.

A few such uncertainties, in addition to the convective heat-transfer coefficient, are as follows:

(1) Spatial distribution of power in both the axial and radial directions

(2) Fuel loading

(3) Flow passage dimensions attributed to manufacturing tolerances

(4) Flow distribution

(5) Temperature sensing and reactor power adjustment

These uncertainties affect our ability to predict the maximum fuel element temperature during reactor operation. The concept of a "hot channel" or "hot spot" factor was used to account for these effects.

The hot-spot factor is a multiplier that must be applied to determine the possible effect of an uncertainty on the fuel temperature. It is essentially the ratio of the fuel element temperature including the uncertainty to the nominal fuel element temperature.

In the TWMR, the cumulative effect of all uncertainties is based upon a statistical combination of the increase in fuel temperature resulting from each uncertainty. This combined hot-channel factor establishes a probability for the occurrence of any given fuel element overtemperature. In this study an allowable overtemperature of 500° F was assumed. Once this maximum tolerable temperature has been established, the likelihood of reaching it can be determined as shown in figures VIII-13 and 14.

The design core length was established at 39 inches to allow for all the calculational uncertainties. At this length, the probability of exceeding the allowable overtemperature limit is 4×10^{-5}. Expressing this in another way, 1 fuel stage out of 25 000 will exceed the allowable hot-spot temperature of 5000° F. Since there are 26 stages per fuel element and 121 elements per reactor, this translates into 1 stage in 8 reactor cores experiencing excessive temperature.

As shown in figure VIII-13, the degree of risk can be increased or decreased by changing the core length. For example, a tenfold decrease in probability (1 stage in 80 cores) can be achieved by increasing the core length by about 3 inches.

Core outlet gas temperature can also be used to vary the probability of excessive overtemperature as shown in figure VIII-14. If the reference exit gas temperature is reduced by about 80° F, the same probability, 1 stage in 80 cores, can be obtained.

These two examples illustrate the sacrifice in performance resulting from uncertainties in one case in the form of increased core length and in the other in the form of decreased specific impulse.

WATER-MODERATOR SYSTEM

Except for the effect on the peripheral flow passages already discussed, the fuel element performance can be analyzed independent of the water system because only a small part of the total heat produced by the fuel element is transferred directly to the water. The problems associated with the water flow system have other effects on design and operation.

As already noted, the areas of concern in the water system are freezing in the heat exchanger and proper cooling of the aluminum. In the TWMR concept, an aluminum surface temperature of 275° F was used as a design point with 300° F as the allowable maximum. The operating water temperature, therefore, had to be greater than 32° F to prevent freezing, and less than 275° F to cool the aluminum.

Obviously a satisfactory design could be achieved if an unlimited water flow rate was used, but this would require excessive pumping power and much larger pumping equipment. Therefore, it becomes necessary to establish a reasonable combination of temperature and flow rate, which will provide adequate cooling of the aluminum and yet prevent freezing in the heat exchanger.

In order to determine this combination, the amount of heat transferred to the water in the core had to be known. There are several sources of this heat:

(1) Heat generated directly in the water by neutron and gamma radiation

(2) Heat generated in the aluminum by gamma and beta radiation and then transferred to the water

(3) Heat transferred from the hot fuel assembly by conduction and radiation through the aluminum pressure tube and into the water

(4) Heat generated in other components and transferred to the water; these components include the beryllium top and side reflectors, the water pump, and the heat exchanger

This total heat is not uniformly generated in the core. The radial distribution is shown in figure VIII-15. The ratio of the average heat load to the heat load at the center of the reactor is 74 percent.

To compensate for radial power distribution in the core, the gas flow was orificed to match the power distribution. Orificing the water flow in the same manner reduced the water flow requirement 26 percent.

Other ways exist in which the water cooling efficiency can be improved. One way this is accomplished is shown in figure VIII-16. This schematic shows the region surrounding a fuel assembly and the location of the inlet end reflector and pressure tube. A desirable water flow distribution is one in which a high-velocity stream exists adjacent to the pressure tubes and a slower moving region exists elsewhere in the core. The high-velocity stream provides good heat-transfer characteristics for the pressure tube, whereas the lower velocity stream, in noncritical regions of the core, reduces the pumping requirements. To achieve this flow pattern, an aluminum baffle tube was located concentrically about the pressure tube. Flow restrictions were located in the region between the concentric tubes and in the regions outside the baffles. The water is thus divided into two flow regions: a high velocity region of 12 feet per second inside the flow divider, or baffle, and a slower moving stream of 5 feet per second outside the divider.

Figure VIII-17 shows the water flow rate and temperature level requirements for

cooling the aluminum structure. The curves are based upon using flow dividers and being able to obtain the desired radial flow distribution; that is, the distribution that matches the heat load.

From the figure, it is obvious that if the flow were increased beyond 1150 pounds per second only a nominal increase in the allowable operating temperature would result. At the same time, flow rates below 750 pounds per second approach a very sensitive part of the curve where a small change in flow rate requires a large decrease in water temperature to maintain design aluminum temperature.

Also, at the lower flow rate and water temperatures, the water in the heat exchanger would be more subject to freezing. For best operation, therefore, the water flow rate should be somewhere between 750 and 1150 pounds per second depending on the operating temperature chosen.

Because of the complex nature of the flow paths within the reactor, the calculation of pressure losses and the orifice requirements necessary to obtain the proper flow distribution is quite uncertain. To check these uncertainties, a full-scale water flow test was performed to study the characteristics of the system (fig. VIII-18). In the flow test, provisions were made for readily changing the orifices at the entrance to the annular passages formed by the pressure tubes and the flow dividers (fig. VIII-16). The number of holes in the exit support plate could also be varied to control the flow in the low-velocity region.

After making a run with no orificing, orifices were installed based upon the estimated pressure losses and desired flow distribution of the system. Subsequent orifice changes were made on a trial-and-error basis by using the results of previous tests. The objective of each of these changes was to alter the flow in various regions of the core in an attempt to obtain the correct flow distribution. The total water flow rate for each test was changed to maintain at least the minimum required flow at every point in the core.

Figure VIII-19, which is a plot of flow as a function of reactor radius, shows the results of the first and last of these tests along with the desired distribution. Although the radial flow pattern is markedly improved between the first test with no orificing and the final test, it falls short of the desired distribution.

The area above the desired distribution represents overcooling of the structure due to an excess of flow in those regions. The first test, with no orificing, required more than twice the water flow rate desired. The final test required only 11 percent more flow than that of the desired distribution. This latter flow rate was used in the reference design. These tests indicate that in a complex flow system at least 10 to 15 percent excess flow must be allowed for to take into account maldistribution and calculational uncertainties.

WATER-HYDROGEN HEAT EXCHANGER

In flowing through the reactor, the water temperature rises about 50° F. After the water leaves the reactor, it flows through the heat exchanger, which serves as a cooler for the water and as a preheater for the incoming hydrogen gas. By properly sizing the heat exchanger, the water temperature is dropped 50° F and returns to the reactor.

Efficiency is not an important factor in the design of this heat exchanger. For example, the use of parallel flow, rather than counterflow, is less efficient. It increases the length of the heat exchanger by several inches; but more important, it provides an additional 30° to 40° F margin from freezing.

Figure VIII-20 shows the characteristic behavior of the TWMR heat exchanger. Calculated values of the overall heat-transfer coefficient as a function of the flow ratio of hydrogen-to-water at several water flow rates are given. As the hydrogen flow is increased at a constant water flow, the value of the coefficient moves along one of the lines shown toward the ice region; conversely, as the hydrogen flow is decreased at a constant water flow, the coefficient moves away from the ice region.

An icing condition is defined as one in which any local temperature of the heat-exchanger tubes drops below the freezing point of water. To the left of the line marked "ice", no such condition can occur. To the right of this line ice should begin to form.

A schematic representation of an equilibrium ice layer is shown in figure VIII-21. Ice usually begins to form at the exit of the heat exchanger, the point where the water temperature is lowest. As the ice thickness at this point increases, ice formation progresses along the tube until an equilibrium condition is reached. When the ice on two adjacent tubes reaches a thickness that is equal to one-half the tube clearance, complete blockage of the water flow passage is assumed. Once ice is predicted, the analysis takes into account its effect on heat transfer. The insulating effect of the ice causes the overall heat-transfer coefficient to remain virtually constant after the icing is reached despite the increase in film coefficient resulting from locally increased water velocity. Note that the design point for the TWMR is considerably to the left of the ice line. There is a 65° F margin from freezing at this point.

A portion of the reference design heat exchanger was tested at the Lewis Research Center to determine how well the heat-transfer characteristics could be predicted analytically. Figure VIII-22 shows some typical results of that test wherein the measured against the predicted overall heat-transfer coefficients have been plotted. Perfect agreement would fall on the solid curve. The open circles indicate no ice, while the solid circles indicate points where icing was predicted analytically. A ±10-percent error band is also shown.

No provision was made in the test to measure or even observe ice formation directly. The water pressure drop across the heat exchanger was measured. Increases in the ob-

served pressure drop would indicate the presence of ice; however, even this method of noting ice formation was not too successful, since the increase in pressure drop for predicted values of small ice thickness was too insignificant to detect. The predicted ice formation on the heat-exchanger tubes had to be quite thick before an appreciable increase in pressure drop could be detected.

The agreement between predicted and measured values of heat-transfer coefficient is excellent when no ice is predicted. When ice formation is predicted analytically, the measured values tend to be higher than the predicted value. Because of this additional uncertainty, the criterion established for the TWMR was that no icing was permitted under steady-state operation. This criterion was not extended to transient conditions since some icing was assumed to occur under what was considered the likely startup sequence (fig. VIII-23):

(1) With the water circulating at some low flow and with no hydrogen flow, the reactor is brought to a low power level.

(2) The water temperature is increased to near the operating point by radiant exchange between the fuel elements and pressure tube.

(3) At time zero, as shown in the figure, the flow of hydrogen is initiated.

As the cold hydrogen passes through the heat exchanger, it cools the water. Because of the negative water temperature coefficient, the reactor goes on a period driving up the power. During this time the hydrogen and water flow are increasing. As reactor power increases, more energy is deposited in the system, and the water temperature begins to increase. As design operating conditions are reached, the increased water temperature terminates the power increase.

The spectrum of conditions existing in the heat exchanger during this transient is quite large. Figure VIII-24 shows the heat-transfer characteristics during a typical startup, a 30-second startup with assumed defining temperatures as shown. The solid line is the overall heat-transfer coefficient of the heat exchanger, while the broken line defines the start of icing under the flow conditions which exist during the transient. Any time the actual heat-transfer coefficient falls above the icing line, ice formation is possible. The shaded area therefore represents the time during which icing of the heat exchanger can occur during this particular transient.

The problem of ice formation under transient conditions has been investigated at Lewis. The investigations have established the time required to form ice as a function of the heat-transfer characteristics of the system and the steady-state ice thickness which would result under the same conditions.

In the TWMR, the time required to form ice is of the order of 1 second, largely because of the use of small, thin-walled aluminum tubes in the heat exchanger.

Since the time constant for transient ice formation is short compared with the time in which icing conditions exist in this particular startup, a reasonable estimate of the ice

thickness can be made by using a pointwise steady-state analysis of the conditions existing during the transient. Such an analysis should also be conservative since the actual ice thickness lags the predicted ice thickness by this 1-second delay.

Figure VIII-25 shows the result of such a study. The maximum ice thickness predicted during this particular transient was 0.014 inch, much less than the 0.050 inch required to cause complete blockage of the water flow. No problems should result by permitting transient ice conditions of this magnitude.

Transient experiments on the 19-tube heat exchanger have been performed to verify the assumption that the heat exchanger can pass through an icing condition without damage during a startup similar to the one just described. No problems were encountered with ice blockage under conditions for which the predicted ice thickness was as high as 0.013 inch.

Another problem that must be faced in the heat exchanger is the sensitivity to changes in operating conditions. For example, suppose that the heating rates in the water and aluminum were somewhat different from those used to calculate the gamma heating in the core. The heat absorbed by the water in flowing through the reactor would therefore be different from that used to size the heat exchanger. Figure VIII-26 shows how the heat exchanger would behave under these conditions.

If the heat absorbed by the water in flowing through the reactor differs from the design value, the temperatures will adjust to compensate for this deviation and reach a new equilibrium condition. If more heat were absorbed, the water temperature would increase and tend to exceed the temperature necessary to keep the aluminum tubes below their 300° F limit. On the other hand, if the heat absorbed by the water were lower than the design value, freezing of the water in the heat exchanger would eventually result.

Once the heat exchanger is sized, the operating range is limited to this band, which in this case permits a variation in heat load of only 6 percent greater and 16 percent less than the value for which the heat exchanger was originally sized. From the standpoint of heat-exchanger sensitivity, being able to control the characteristics of the heat exchanger during operation would be desirable.

SYSTEM CONTROL STUDIES

A very effective means of controlling the heat-transfer characteristic of the heat exchanger is to install a hydrogen bypass around the heat exchanger. One of the previous figures (fig. VIII-20) showed the performance of the TWMR heat exchanger. As hydrogen flow was decreased the operating characteristics moved away from the icing region. Controlling the flow of cold hydrogen through the heat exchanger, can change its characteristic behavior.

The use of a bypass could therefore be used quite effectively to reduce the sensitivity of the heat exchanger to any deviation from nominal design conditions such as variation in the quantity of heat absorbed by the water.

The flexibility of the system is also improved considerably by a heat-exchanger bypass. Figure VIII-27 shows the steady-state operating envelope for the TWMR. Here, the reactor power is given as a function of total hydrogen flow rate with the design point shown at 100 percent power and flow. The system can operate at steady state anywhere within the shaded envelope.

This envelope was obtained by using analog and digital simulation of the entire system; the boundaries are physical limits that exist in various parts of the system.

The upper limits that define this envelope are the maximum pump speed limit on the first stage pump, the fuel element temperature limit, and below about 70 percent power and flow, the bleed gas temperature limit. This limit is reached when the temperature of the bleed gas exceeds the maximum assumed turbine materials limit. At a low flow rate, there is the pump stall limit. Below this limit, operation of the pumps is undesirable. Since there are two pumps in the system, this stall limit is at the lowest possible level when both pumps stall together. Under this condition, the pumps are said to be matched.

The lower boundaries of the operating envelope are the aluminum pressure tube temperature and the topping turbine power limit. In this region insufficient energy exists in the gas to drive the topping turbine.

In obtaining this operating envelope, a heat-exchanger bypass was used. If this bypass is not used, the lower boundary moves up to the boundary shown by the dotted line. This line represents heat-exchanger icing.

Obviously the heat-exchanger bypass dramatically increases the size of the system operating envelope. This increase in size is important because of the two basic operational requirements for the system.

First, the system must be capable of stable operation at the design point; and second, it must be capable of performing satisfactorily during startup and shutdown. These requirements denote that the system must go from low flow and power to the design point, operate for a period of time, and then return to the low power and flow condition.

While the transient limits may be somewhat more lax than the steady-state limits shown in this figure (fig. VIII-27), the size of the operating envelope indicates the ease with which the limits can be avoided during startup, operation, and shutdown. For example, in the description of the heat-exchanger problems, it was seen that a startup without a bypass would probably result in some heat-exchanger ice formation. Using the heat-exchanger bypass to eliminate this boundary, makes possible going from the startup condition to the design point without encountering heat-exchanger icing.

Figure VIII-28 shows the open-loop power-flow relation during a typical startup transient using the heat-exchanger bypass. Power and flow are shown as a function of time.

The transient starts from a motoring condition, that is, a condition where hydrogen flow is produced only by tank pressure. The hydrogen flow is then ramped to the 100-percent design point just as in the startup discussed previously. The bypass is also ramped to its 100-percent design value.

The total transient takes about 25 seconds. During the early part of the startup transient, the hydrogen flow increases more rapidly than the power; that is, the system responds quicker to a flow change. The area between the two curves represents overcooling of the fuel elements due to an excess of hydrogen flow. Conversely, during shutdown a fuel overtemperature could be expected since the power would tend to lag the flow. Therefore, care must be exercised during a shutdown sequence to insure a reduction in reactor power before flow is reduced to prevent fuel element overtemperature. This can be done by increasing the poison concentration or the heat-exchanger bypass before the hydrogen flow is decreased.

It appears then that the reference design is capable of starting up from a low power condition with only the hydrogen flow and the heat-exchanger bypass being controlled. A shutdown, however, may require an initial poison insertion.

The inherent stability of the reactor at the operating point was explained in paper VI; however, if an adjustment in power were required, two modes of control are available. The poison concentration in the tubes can be changed and the heat-exchanger bypass can be varied. In the latter case, the core water temperature responds to bypass variation, and the water temperature coefficient causes the core reactivity to vary.

Figures VIII-29 and 30 show some results of analog studies made to explore the basic characteristics of each of these control methods. Figure VIII-29 shows the response of the system to a step increase in poison concentration. Figure VIII-30 is the response to a step change in heat-exchanger bypass flow. In both cases, no other control devices were manipulated after the initial perturbation. This open-loop response is not typical of the response expected during normal reactor operation but is used in control studies to obtain information that is useful to determine the behavior, stability, and requirements of the control system.

If the two figures are examined carefully, the system response to the poison insertion is seen to be entirely different from that of the perturbation in heat-exchanger bypass flow. In the former, the initial reaction of the system to poison insertion is a sharp dip in reactor power. This power reduction at constant hydrogen flow causes a decrease in the fuel temperature, which has a negative temperature coefficient of reactivity.

The response of the fuel temperature change is practically instantaneous, and the reactor power is increased sharply to a value that is below the initial power level. This reduced power level causes the water temperature to start dropping slowly. Since the water temperature coefficient is also negative, this increases power until a new steady-state power level is reached.

During this relatively slow portion of the power recovery, the reactor could be held at any desired power level by stabilizing water temperature. For example, the hydrogen flow rate could be decreased; however, in this particular study no such action was taken, and the power returned to about 98 percent of the initial value. The fuel and water temperature at the new steady-state condition is slightly lower than the original level to compensate for the increased poison concentration.

Figure VIII-29 also shows that although the inherent tendency of the core to return to design conditions gives rise to initial oscillations these are very quickly damped out.

In contrast to this type of behavior, the characteristic of the system using the hydrogen bypass around the heat exchanger for control is slower and the tendency for the system to oscillate is eliminated because the primary effect of a step increase in bypass flow is a direct increase in water temperature that, in turn, affects the reactivity of the reactor. Because of the relatively large mass of water in the system and the transport time around the loop, this method of control is much slower than a corresponding insertion of poison directly into the core region.

With two such widely different power level controls available, the design of a control system to meet any specific control requirement would appear feasible.

In addition to the poison and bypass controls just discussed, the power can be changed by changing the total hydrogen flow. This control method makes use of the negative temperature coefficient of the fuel element. Figure VIII-31 shows the response of the system to an increase in hydrogen flow with poison and bypass held constant. Shown, as before, are power, exit gas temperature, and reactivity change as a function of time. The sharp response is similar to a change in poison concentration; however, in this case, the change in fuel plate temperature is caused by the increased hydrogen flow. The final power rise, as in the other cases, still depends on how fast the water temperature changes.

In generating the steady-state performance map (fig. VIII-27), the poison concentration was fixed, and only the total hydrogen flow rate and bypass were varied to obtain the complete operating envelope. Studies have shown that no other system parameters require control.

For example, during steady-state mapping, the bleed system flow was noted to be choked in the vicinity of the water pump turbine. This condition existed over the entire operating range. As a result, the relation between bleed flow and the flow required to cool the bleed tubes remained nearly constant. Therefore, no control was required.

The water flow rate is another parameter that does not need to be controlled. Studies have shown that by fixing the valves to obtain the desired water flow at the 100-percent power level, heat-exchanger icing can be minimized and loop response time reduced at any lower power level.

The work split between the two pumps does not require close control during normal operation either. During the first few seconds of a startup, the first stage pump tends to

carry the burden of the system load. The pumps are not matched under these conditions, and the stall limit on the operating map would become more restrictive than when the pumps are matched. Based on the results of the NERVA system (paper IV), however, this may not be a serious problem since the pumps can apparently pass through the stall region during startup.

In summary, the only controls required on the TWMR split feed system appear to be those on the poison, the heat-exchanger bypass, and the total hydrogen flow rate.

It would not appear that the control problems of the all-topping system would be much different from the split feed system. Basically, the same three control parameters would also be required for an all-topping cycle. The all-topping cycle would have the advantage of eliminating the bleed portion of the split feed system, and, although the control of the bleed flow is not critical, this would simplify the overall system. Therefore, if the fluid driving the topping turbine contains sufficient energy to provide all the power required by the system, including auxiliary pumps, the all-topping cycle would be preferred to the split feed system.

SYSTEM SIZE AND WEIGHT

In addition to the factors already noted, one measure of flight propulsion performance is the size and weight of the system. Table VIII-2 shows a weight breakdown of the reference 1500-megawatt system. The weight of all shielding that might be required has been omitted. The nozzle weight shown is for a 40:1 cooled nozzle. Engine thrust structures, gimbals, and thrust vector system are not included in this weight breakdown.

The choice of the 1500-megawatt power level for the reference design was somewhat arbitrary. As already discussed (paper VI), a range of reactor sizes with the same general configuration was investigated. Using the same system operating limits, chamber pressure, fuel loading, etc., as were established for the reference design permits varying the power of the reactor by increasing or decreasing the diameter of the core while keeping the length the same. The size of other system components must also change to accommodate the new flow rates.

The fine geometry fuel elements eliminate the allowable dynamic head limit of 12.5 pounds per square inch used in the reference design. Therefore, the power output of a given reactor core size can be increased by increasing the flow and improving the heat transfer. The limiting condition for this upgraded system would be the magnitude of the pressure drop associated with the higher flow rate. A core pressure drop of 250 pounds per square inch is felt to be a reasonable value at this time.

Figure VIII-32 shows thrust-weight ratios for various systems up to about 10 000 megawatts. The lower curve is for a system with the reference 12.6 pounds per square

inch dynamic head limit. The design point is shown at 1500 megawatts. The upper curve is for a case in which a reactor core pressure drop of 250 pounds per square inch was imposed. The resulting power output of each fuel element for this case is approximately $1\frac{1}{2}$ times that of the lower curve.

The reactivity limit for U^{235} fuel is reached for small size reactors. Using U^{233} instead of U^{235} below this level allows the limiting power to be reduced until the reactivity limit of the U^{233} is finally reached. This is the smallest feasible size for reactors using the reference parameters. The thrust-weight ratio varies from about 5 to 8.5 (lb/lb) for the cases shown.

Figure VIII-33 shows the pressure vessel diameter as a function of reactor power level for these two cases. Again, the results for the 12.5 pound per square inch dynamic head case and the 250 pound per square inch reactor core pressure drop case are shown, along with the reactivity limits for U^{235} and U^{233} fuel. The pressure vessel diameter varies from 31 to 109 inches for the power range shown.

It should be emphasized that all the systems represented by figures VIII-32 and 33 were obtained by using the same parameters as in the reference design. These parameters are not necessarily the optimum combination for all reactor sizes and power levels. For example, by changing such things as the chamber pressure, the fuel element size, the fuel loading, or the percent of enriched tungsten, many other curves could be generated similar to those shown in these two figures.

The TWMR, therefore, is not limited to the range of sizes shown herein, but depending on specific mission requirements, could be optimized at many other sizes and power levels.

SUMMARY

Although some of the problems associated with the tungsten water-moderated reactor (TWMR) appear formidable at first glance, testing and analysis have shown that they can generally be solved and that the system can be designed to accommodate the problem areas. For example, using a hydrogen bypass around the heat exchanger virtually eliminated the serious problems of icing during startup and sensitivity to changes in operating conditions.

The TWMR has three independent and quite different methods of control: the poison control system, the heat-exchanger bypass, and the total hydrogen flow rate. Depending on a specific control requirement, these can be used individually or in combination to obtain the desired system response. Analog simulation has demonstrated that the system can be started and shut down and that it can be controlled at the operating point.

The reference design is representative of a family of systems that have the same gen-

eral characteristics. Reactors within the power range of from about 400 to over 10 000 megawatts can be achieved by merely changing the diameter of the core and modifying the size of the auxiliary components. Slightly lower powers, down to about 250 megawatts, can also be achieved by using U^{233} instead of U^{235} as a fuel. Higher power levels can be obtained for a given size reactor by using fine geometry fuel elements to increase the allowable dynamic head.

From a system and control viewpoint, the TWMR appears feasible over a wide range of reactor sizes.

TABLE VIII-1. - SYSTEM COMPARISON

[Chamber pressure, 600 psia; flow rate, 92.7 lb/sec.]

	Bleed	Topping
Upper chamber pressure limit, psia	None	≈700
Bleed rate, percent	5.1	0
Engine specific impulse, (lb)(sec)/lb	819	839
Hydrogen pump discharge pressure, psia	945	1490
Hydrogen pump horsepower	7200	11 700

TABLE VIII-2. - WEIGHT OF TUNGSTEN WATER-MODERATED REACTOR SYSTEM

Component	Weight, lb
Reactor components (no shield):	
Uranium dioxide fuel	200
Tungsten	3000
Water moderator	1840
Reflectors	1330
Structure and controls	2640
Total weight of reactor components	9010
Nonreactor components:	
Nozzle (40:1)	1280
Pumps	900
Piping	1600
Fluids	950
Total weight of nonreactor components	4730
Total weight of system	13 740

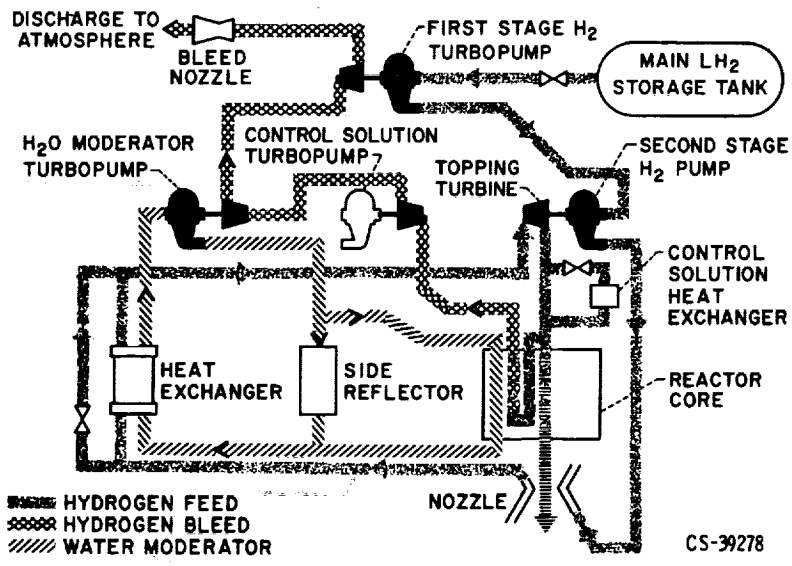

Figure VIII-1. - Overall system schematic.

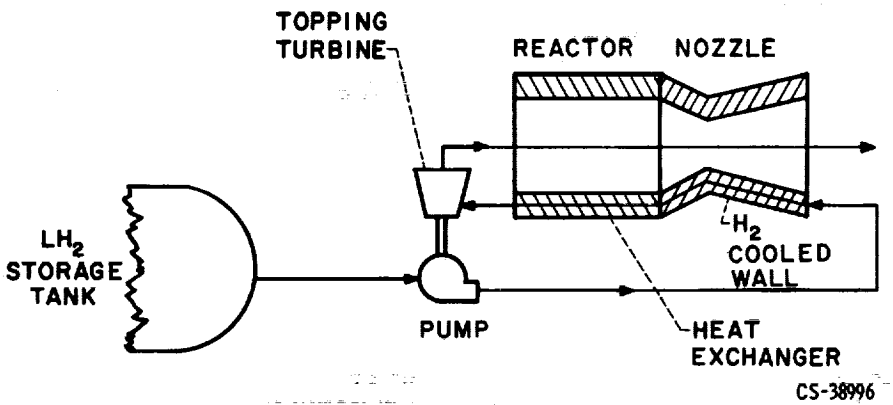

Figure VIII-2. - Topping system.

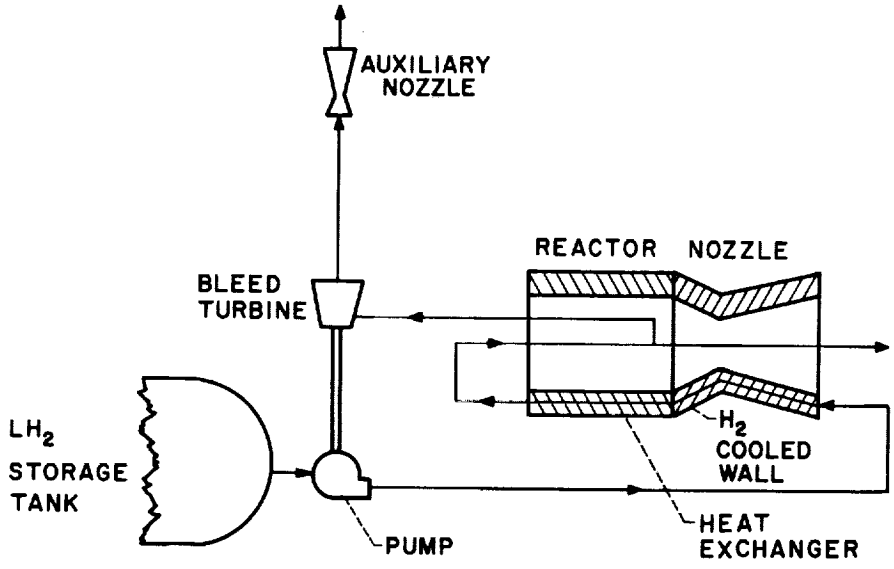

Figure VIII-3. - Bleed system.

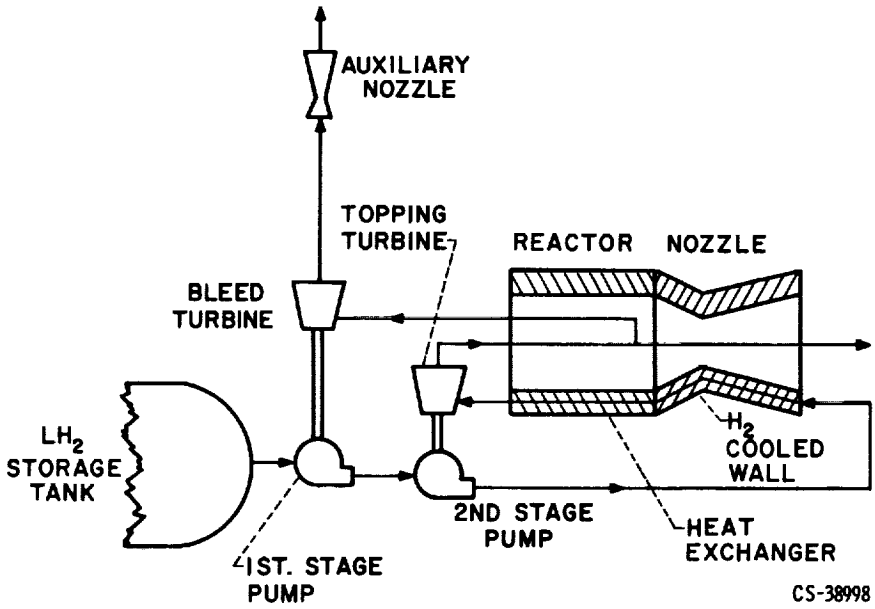

Figure VIII-4. - Split feed system.

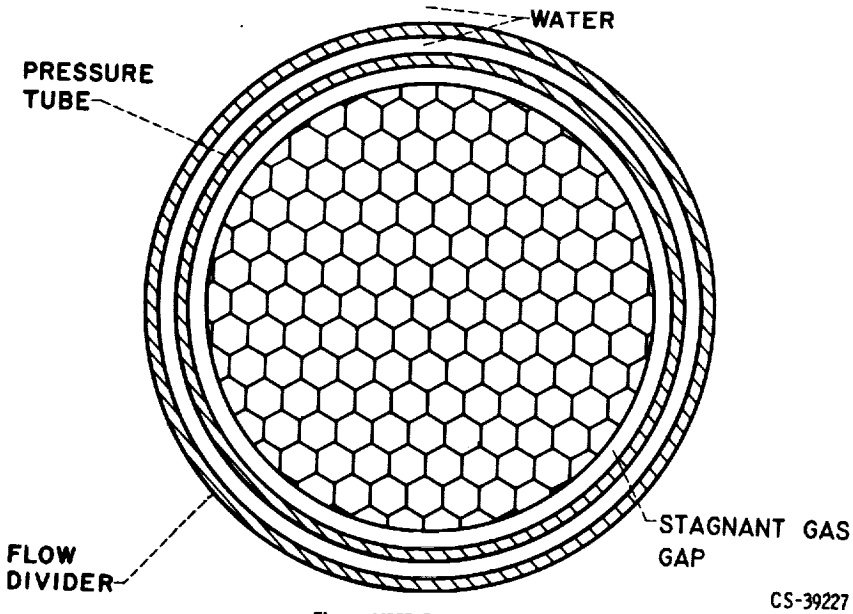

Figure VIII-5. - Fuel cell.

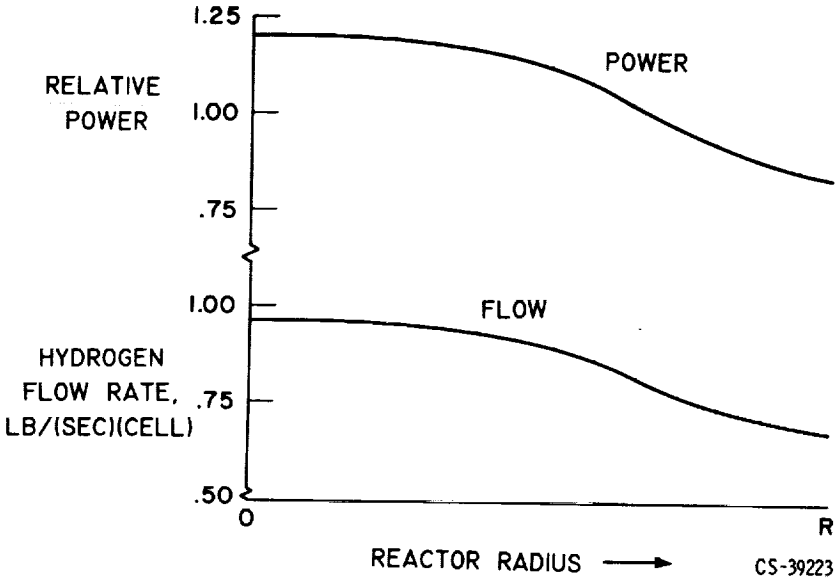

Figure VIII-6. - Radial power and flow distribution. Total flow, 92.7 pounds per second.

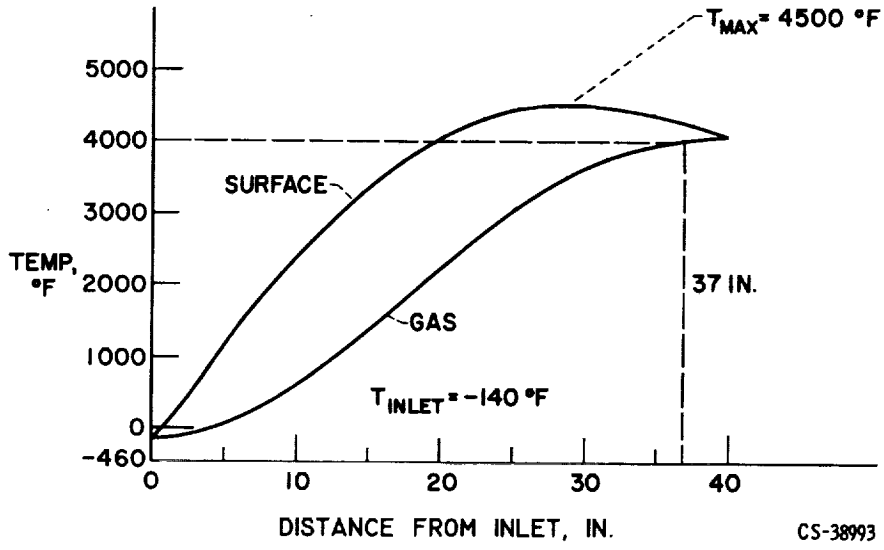

Figure VIII-7. - Axial-temperature variation with cosine power distribution.

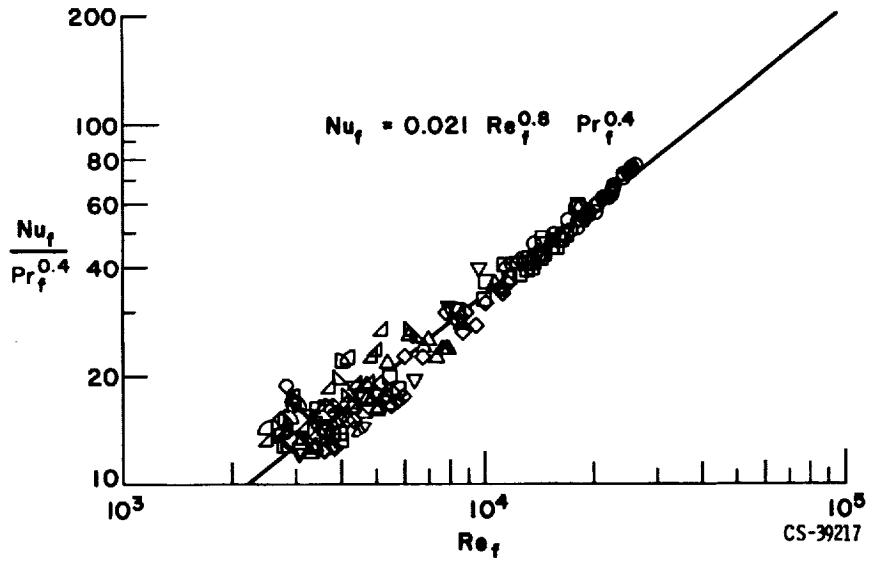

Figure VIII-8. - Film correlation of local heat-transfer coefficients for hydrogen.

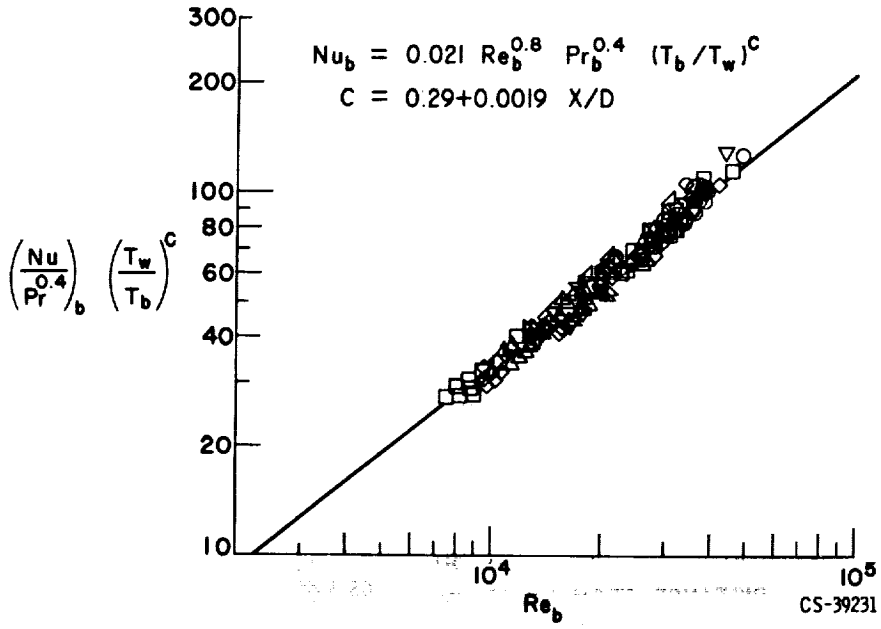

Figure VIII-9. - Modified correlation of local heat-transfer coefficients for hydrogen.

This figure UNCLASSIFIED

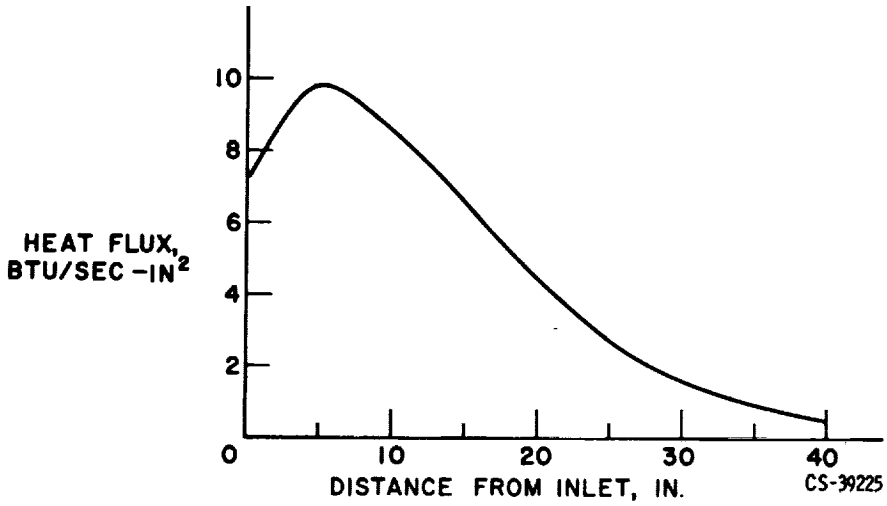

Figure VIII-10. - Desired axial-power distribution for constant surface temperature. T_s = 4500° F; T_{inlet} = -140° F.

This figure CONFIDENTIAL

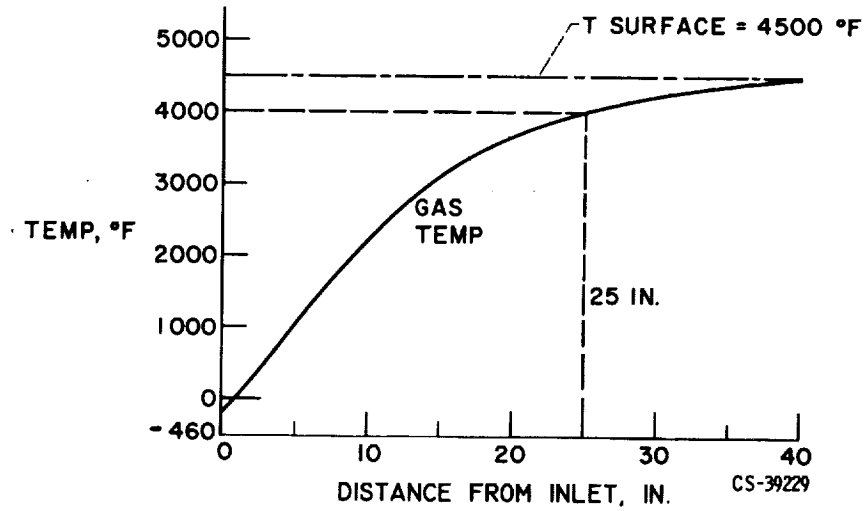

Figure VIII-11. - Axial gas temperature variation for constant surface temperature.

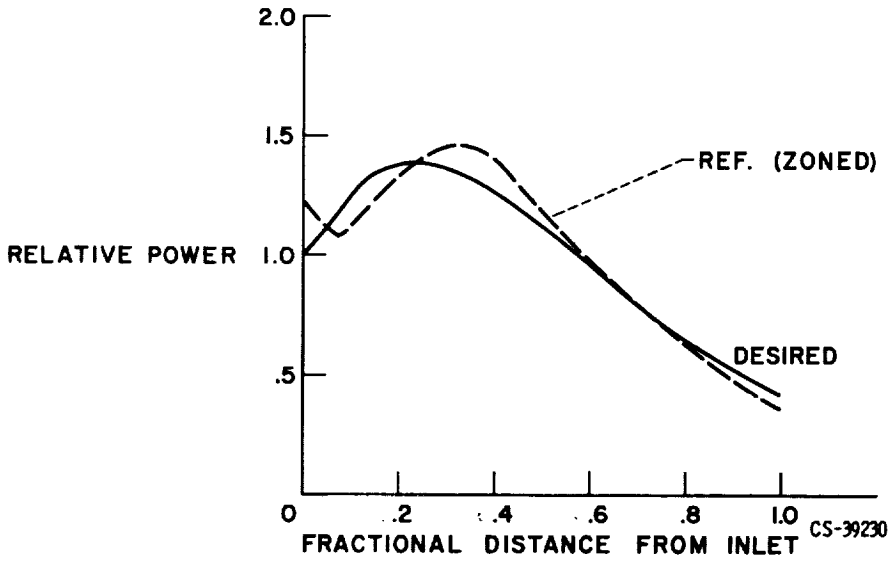

Figure VIII-12. - Comparison between desired and reference power distribution.

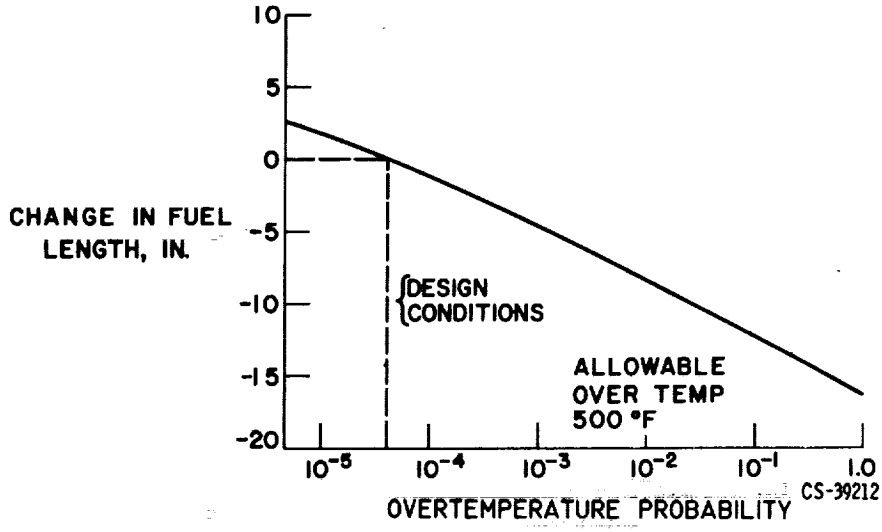

Figure VIII-13. - Effect of fuel overtemperature probability on fuel length. Nominal conditions: exit gas temperature, 4000° F; reactor length, 39 inches; reactor power, 1500 megawatts; fuel temperature, 4500° F. Allowable overtemperature, 500° F.

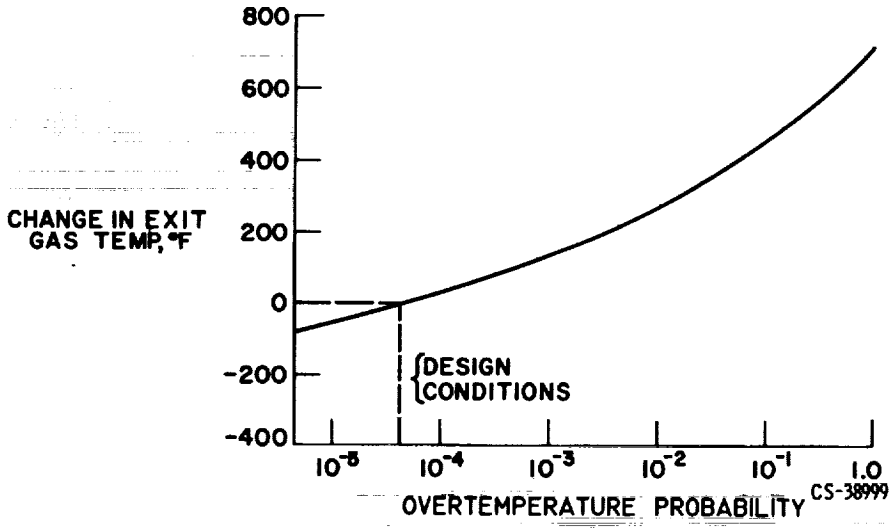

Figure VIII-14. - Effect of fuel overtemperature probability on exit gas temperature. Nominal conditions: exit gas temperature, 4000° F; reactor length, 39 inches; reactor power, 1500 megawatts; fuel temperature, 4500° F. Allowable overtemperature, 500° F.

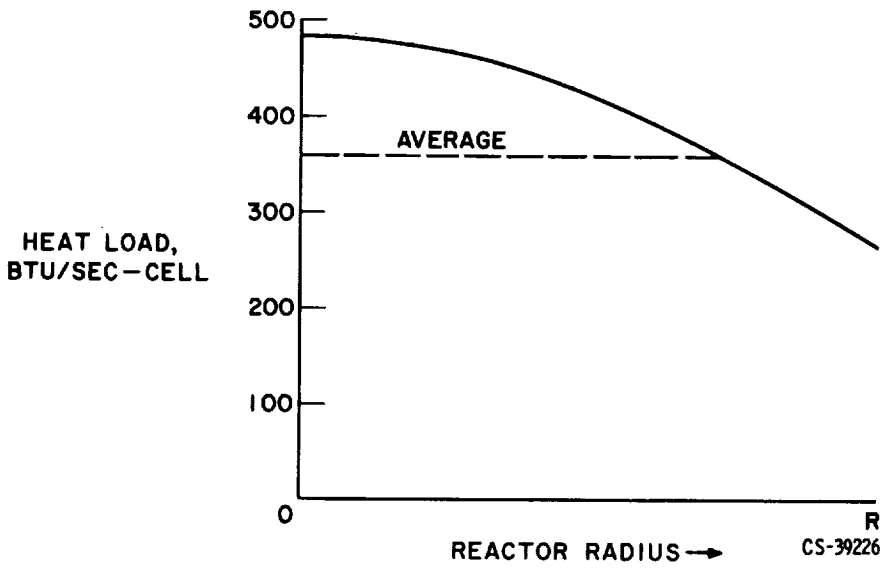

Figure VIII-15. - Distribution of heat load in water. Average is 74 percent of maximum.

This figure CONFIDENTIAL

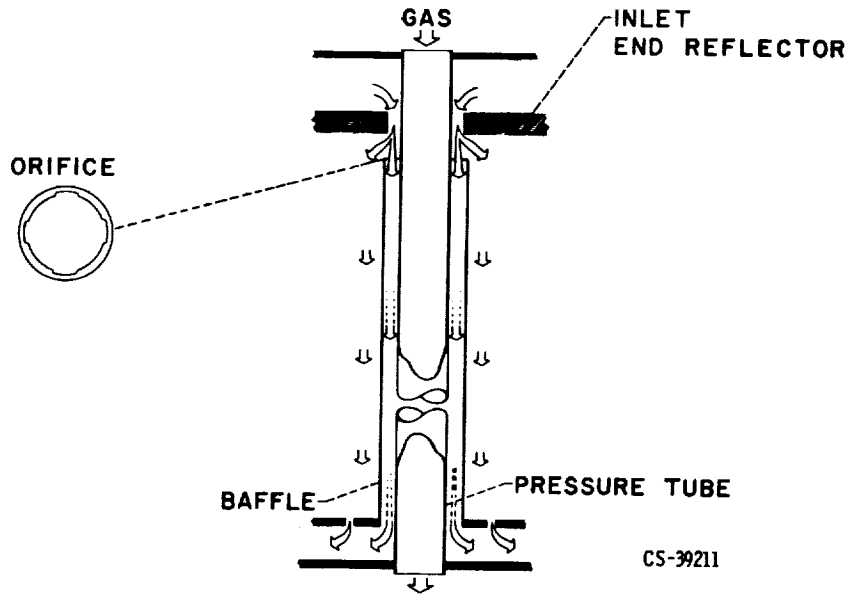

Figure VIII-16. - Water flow passages.

This figure UNCLASSIFIED

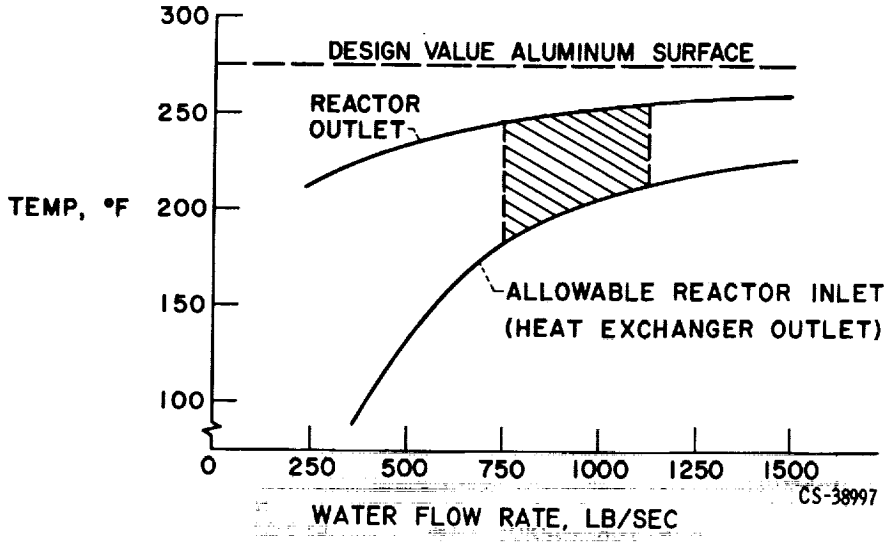

Figure VIII-17. - Cooling requirement of aluminum structure.

This figure UNCLASSIFIED

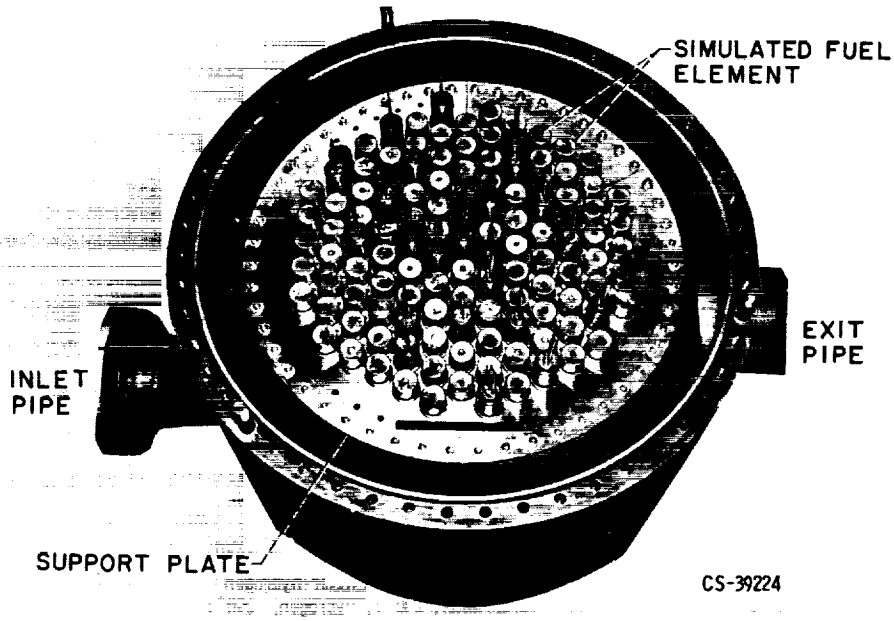

Figure VIII-18. - Tungsten water-moderated reactor water flow test.

This figure CONFIDENTIAL

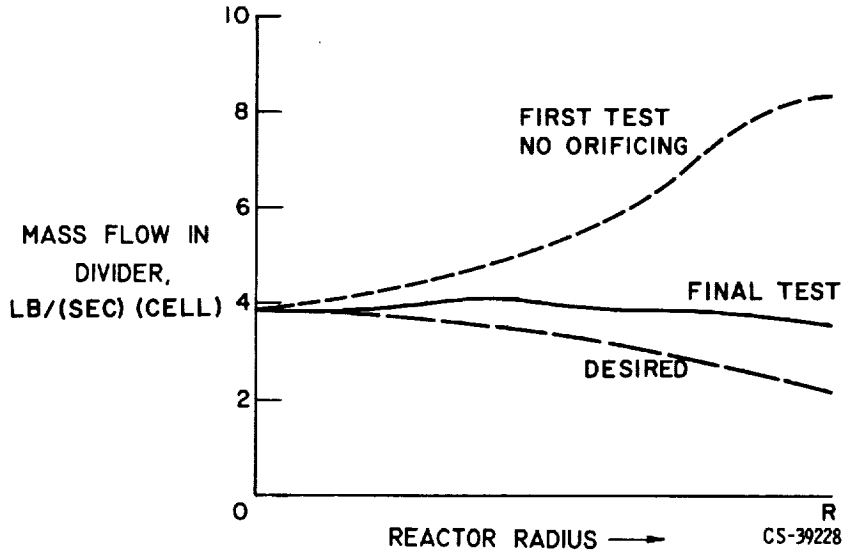

Figure VIII-19. - Results of water flow test.

This figure CONFIDENTIAL

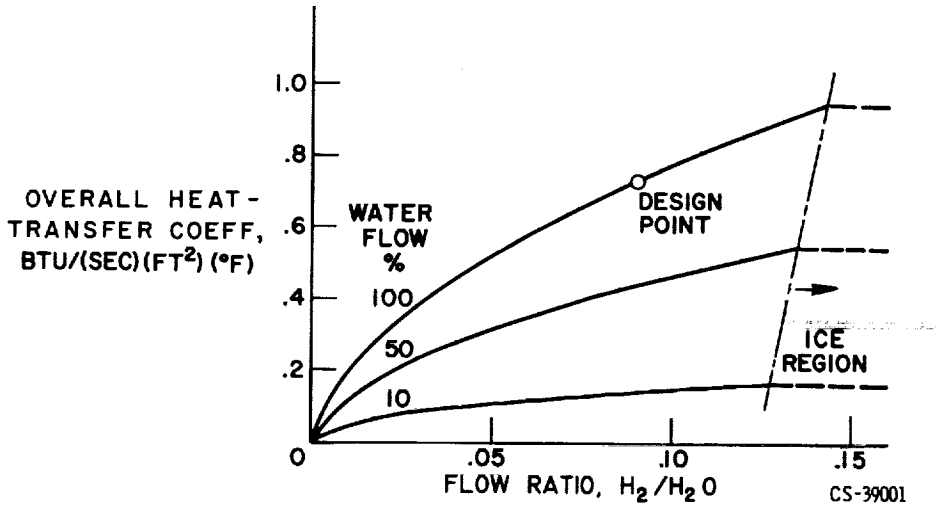

Figure VIII-20. - Overall heat-transfer coefficient of water-hydrogen heat exchanger. Inlet temperature: water, 240° F; hydrogen, -290° F.

This figure UNCLASSIFIED

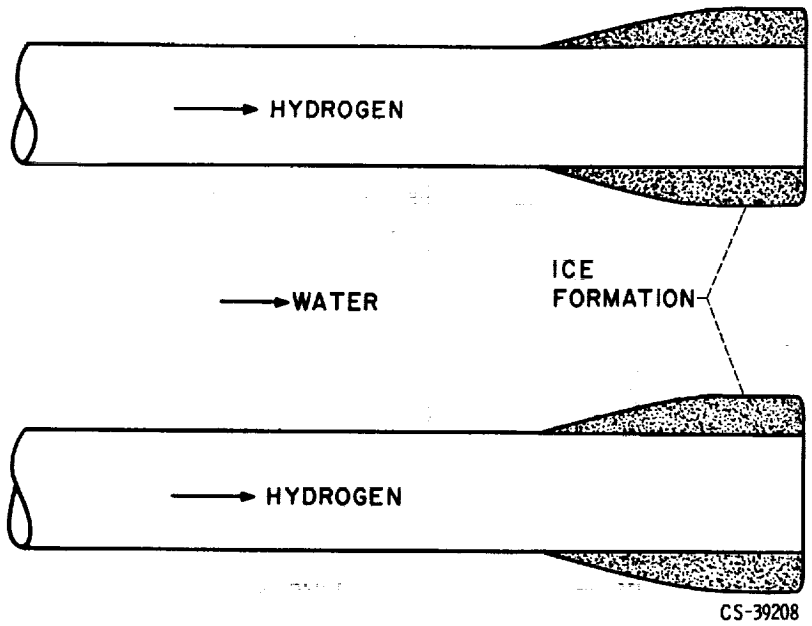

Figure VIII-21. - Ice formation in heat exchanger.

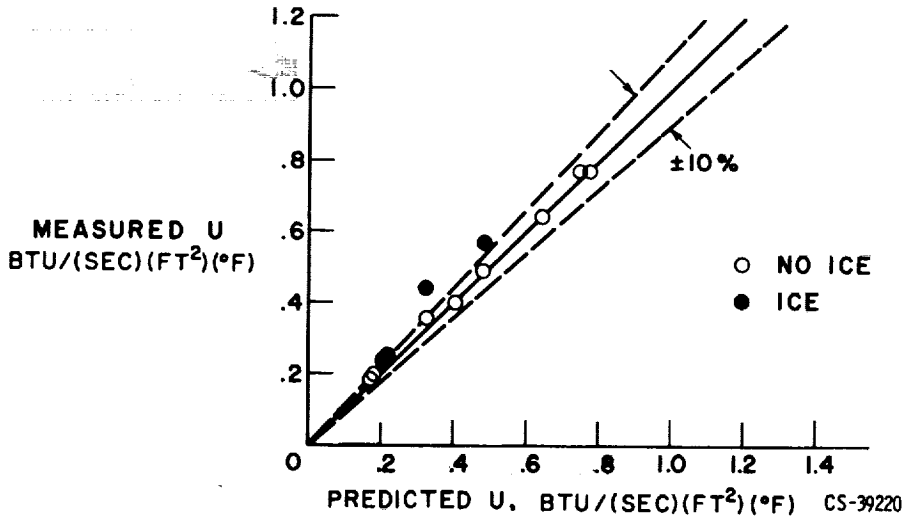

Figure VIII-22. - Steady-state heat exchanger tests. Overall heat-transfer coefficient, U.

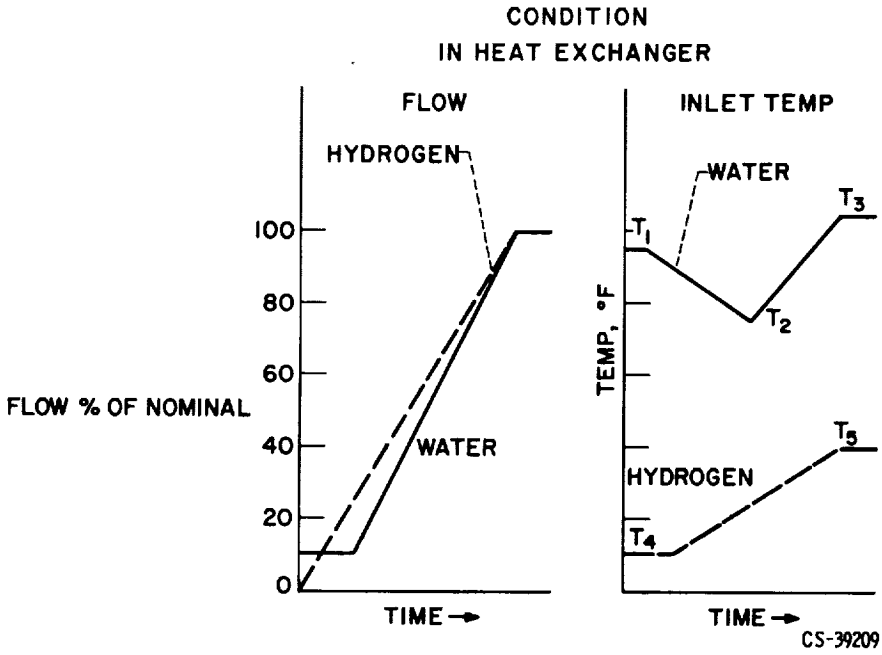

Figure VIII-23. - Generalized startup transient.

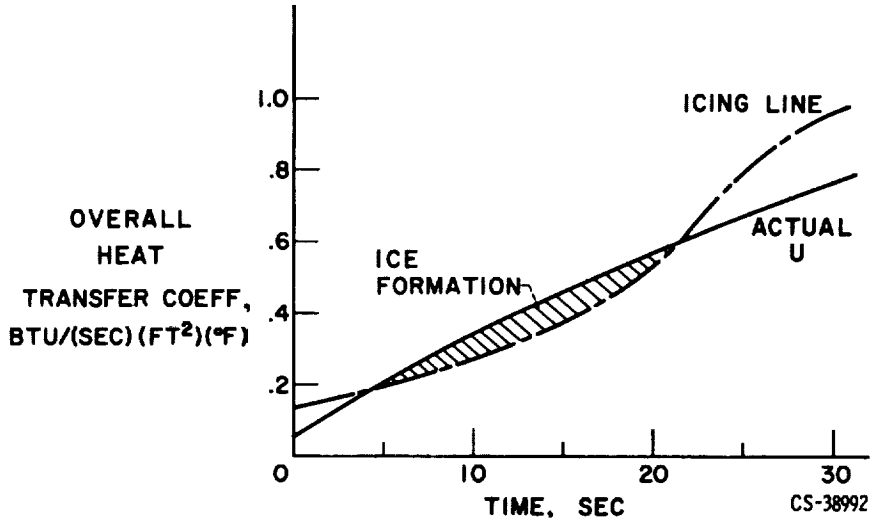

Figure VIII-24. - Variation in heat exchanger heat transfer during typical startup. T_1 = 220° F; T_2 = 190° F; T_3 = 240° F; T_4 = -410° F; T_5 = -280° F. Overall heat-transfer coefficient, U.

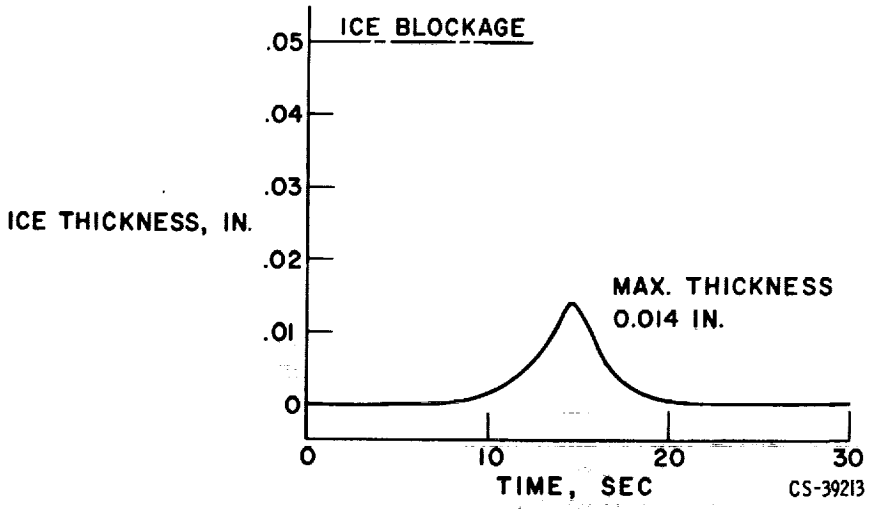

Figure VIII-25. - Ice thickness variation during 30-second startup pointwise steady-state analysis.

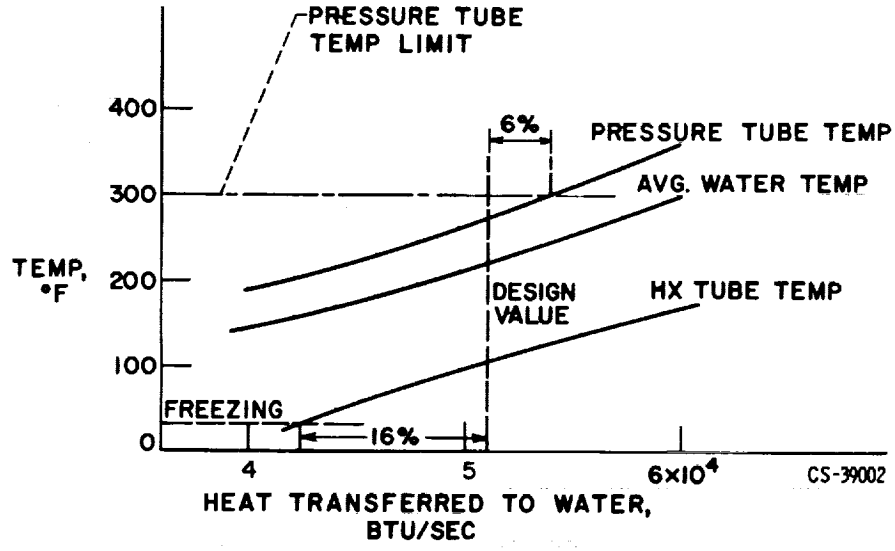

Figure VIII-26. - Effect of heat-transfer rate on heat exchanger performance.

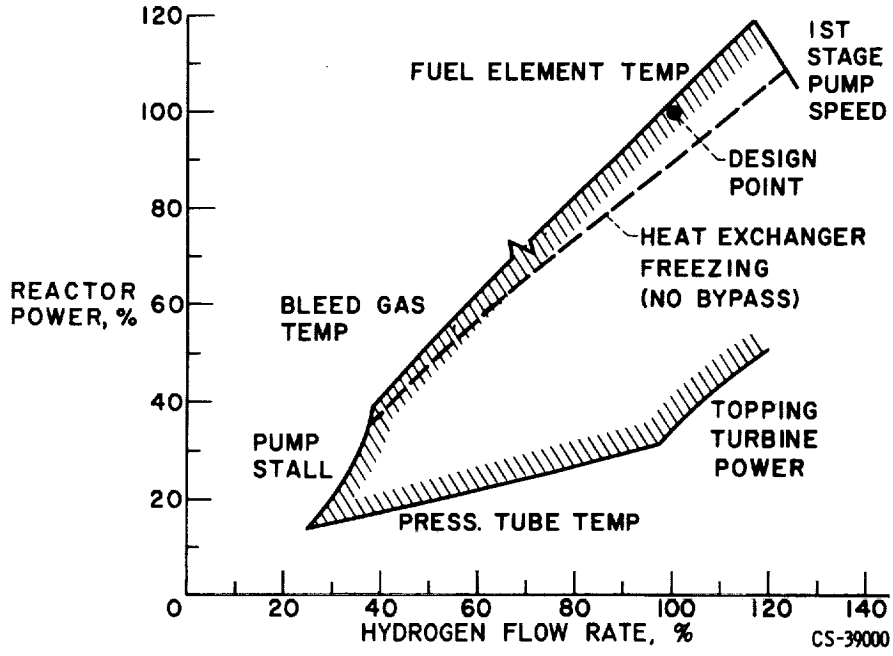

Figure VIII-27. - Steady-state operating region.

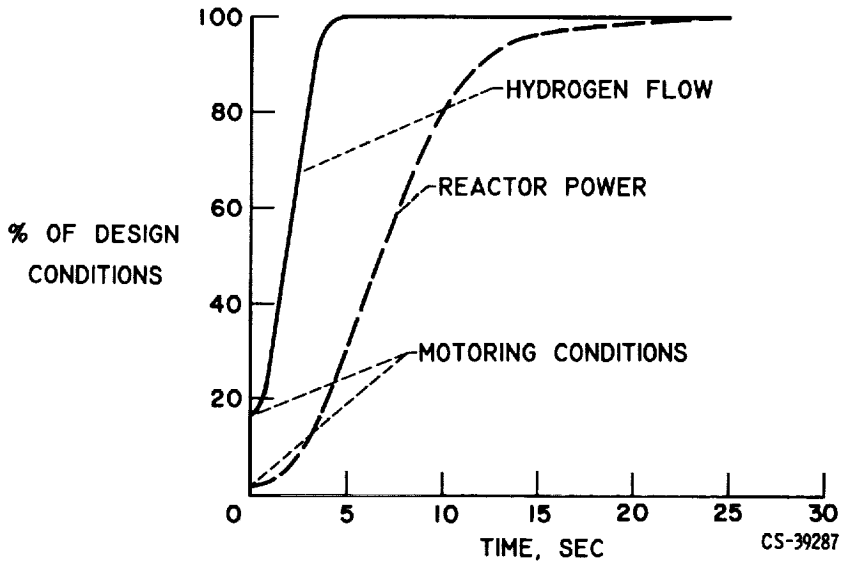

Figure VIII-28. - Open-loop startup transient.

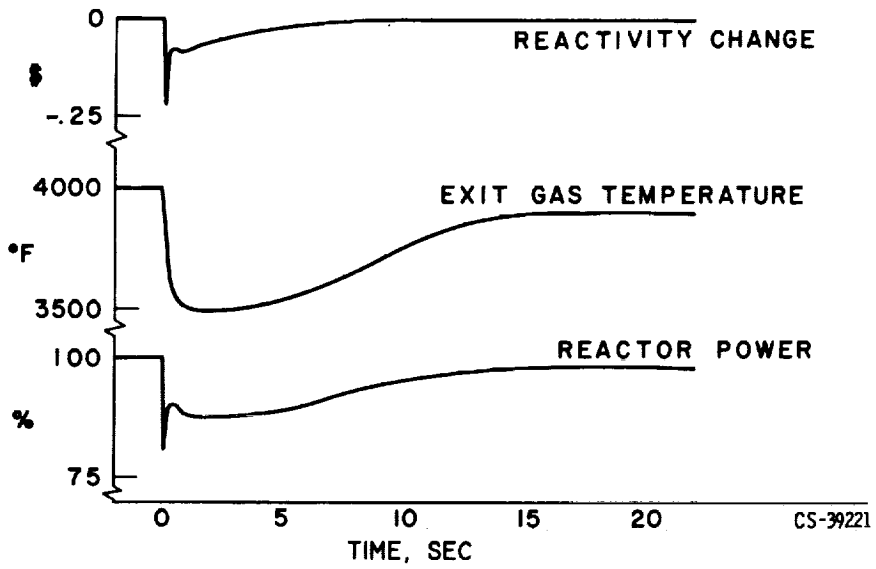

Figure VIII-29. - Open-loop response to step increase in poison concentration.

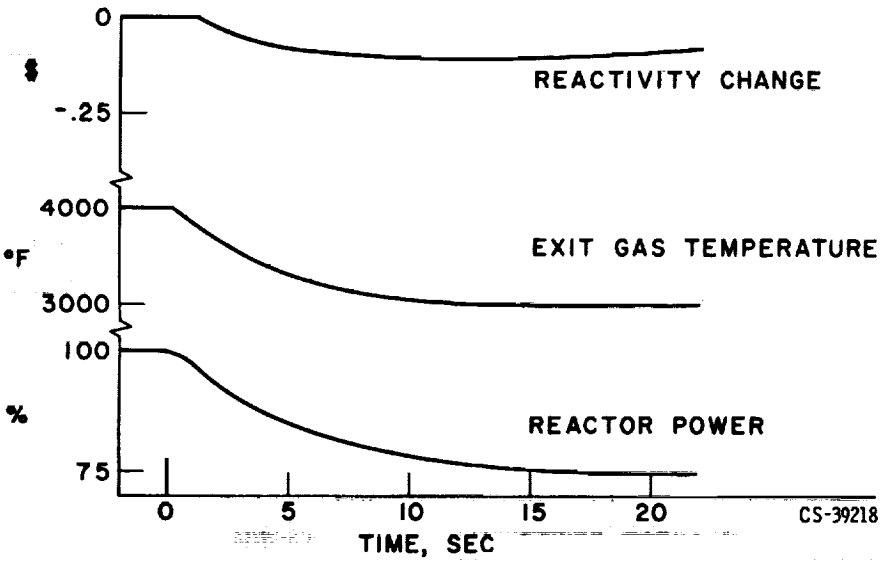

Figure VIII-30. - Open-loop response to step increase in heat exchanger bypass flow.

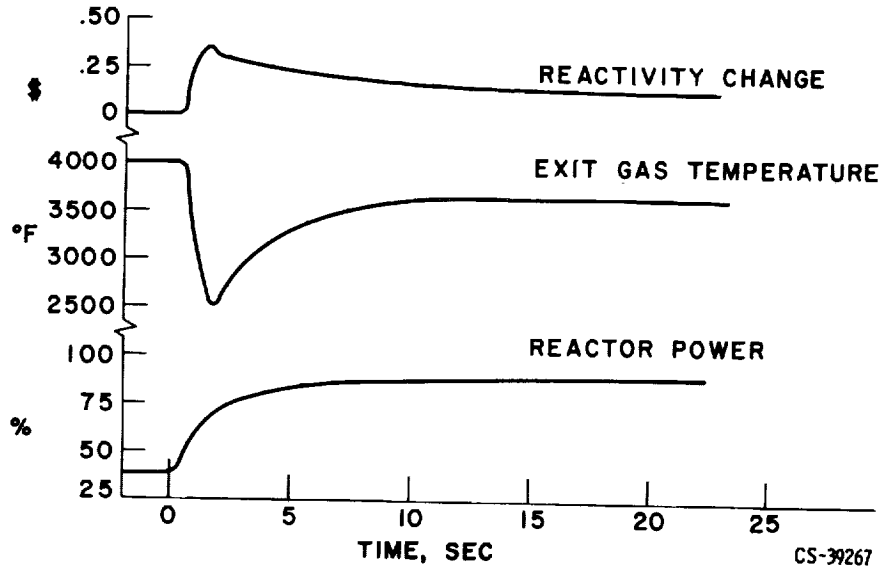

Figure VIII-31. - Open-loop response to step increase in hydrogen flow rate.

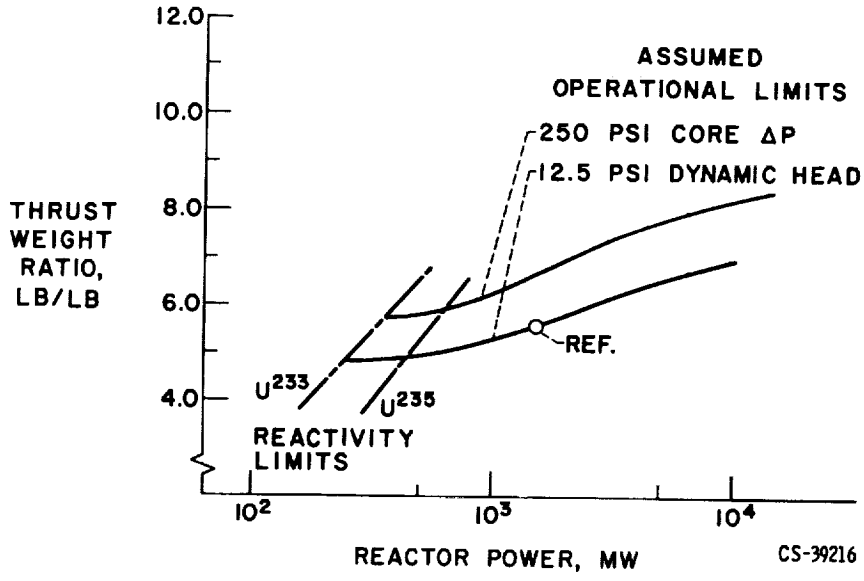

Figure VIII-32. - Effect of power level and operational limits on thrust-weight ratios.

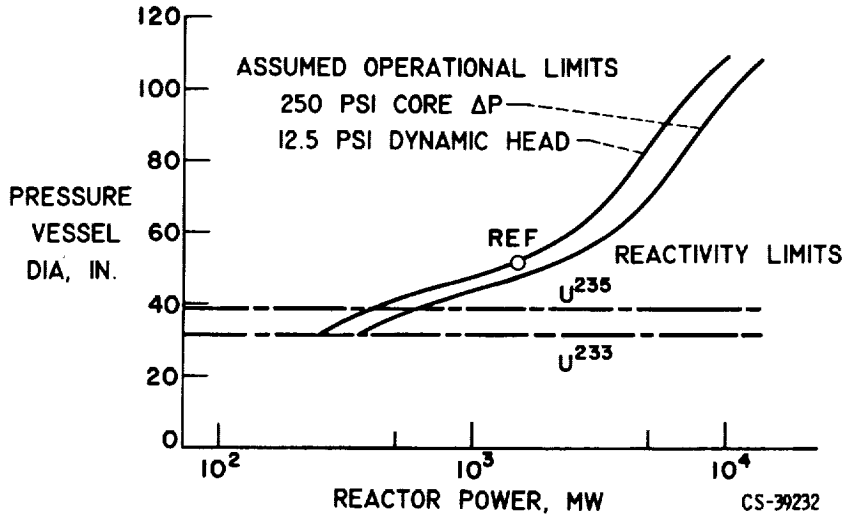

Figure VIII-33. - Effect of power level and operational limits on pressure vessel diameter.

BIBLIOGRAPHY

TUNGSTEN WATER-MODERATED NUCLEAR ROCKET

(Papers V to VIII)

NASA REPORTS

Conceptual Rocket Reactor Studies - General

Hyland, Robert E.: Reactor-Weight Study of Beryllium Oxide, Beryllium, Lithium^{-7} Hydride, and Water as Moderators with Tungsten 184 Structural Material and Uranium Dioxide Fuel. NASA TN D-1407, 1962.

Hyland, Robert E.; Sams, Eldon W.; and Rom, Frank E.: Comparison of Fast, Moderated-Heterogeneous, and Moderated-Homogeneous High-Temperature Reactors for Nuclear-Rocket Propulsion. NASA TM X-871, 1964.

Lietzke, Armin F.: Water-Moderated Tungsten Nuclear Rocket Reactor Concept. NASA TM X-1044, 1965.

Rom, Frank E.: Fast and Moderated Low-Power, Lightweight Reactors for Nuclear Rocket Propulsion. Paper presented at the Second Lecture Series on Nuclear and Electrical Rocket Propulsion, AGARD, Brussels, Sept. 28-Oct. 3, 1964. (Also available as NASA TM X-52047, 1964.)

Rom, Frank E.: Applications of Low-Power Nuclear Rockets. Paper presented at the Second Lecture Series on Nuclear and Electrical Rocket Propulsion, AGARD, Brussels, Sept. 28-Oct. 3, 1964. (Also available as NASA TM X-52048, 1964.)

Rom, Frank E.; and Petry, Mary Lee: Technology and Application of Lightweight Low-Power Nuclear Rockets - Selected Bibliography. Paper presented at the Second Lecture Series on Nuclear and Electrical Rocket Propulsion, AGARD, Brussels, Sept. 28-Oct. 3, 1964. (Also available as NASA TM X-52047.)

Heat Transfer

Miller, John V.; and Taylor, Maynard F.: Improved Method of Predicting Surface Temperatures in Hydrogen-Cooled Nuclear Rocket Reactor at High Surface- to Bulk-Temperature Ratios. NASA TN D-2594, 1965.

Siegel, Byron L.; Maag, William L.; Slaby, Jack G.; and Mattson, William F.: Heat-Transfer and Pressure Drop Correlations for Hydrogen and Nitrogen Flowing Through Tungsten Wire Mesh at Temperatures to 5200° R. NASA TN D-2924, 1965.

Slaby, Jack G.; Maag, William L.; and Siegel, Byron L.: Laminar and Turbulent Hydrogen Heat-Transfer and Friction Coefficients over Parallel Plates at 5000° R. NASA TN D-2435, 1964.

Taylor, Maynard F.: Experimental Local Heat-Transfer and Average Friction Data for Hydrogen and Helium Flowing in a Tube at Surface Temperatures up to 5600° R. NASA TN D-2280, 1964.

Taylor, Maynard F.: Experimental Local Heat-Transfer Data for Precooled Hydrogen and Helium at Surface Temperatures up to 5300° R. NASA TN D-2595, 1965.

Material Properties

Buzzard, Robert J.; and Gill, Frank L.: High-Temperature Mechanical Properties of a Tungsten - Uranium Dioxide Composite. NASA TM X-1018, 1964.

Garfinkle, Marvin: Effect of Additives on Thermal Stability of Tungsten - Uranium Dioxide Composites. NASA TM X-1118, 1965.

Gedwill, Michael A.; Sikora, Paul F.; and Caves, Robert M.: Fuel-Retention Properties of Tungsten - Uranium Dioxide Composites. NASA TM X-1059, Feb. 1965.

Grisaffe, Salvatore J.; and Caves, Robert M.: Fuel-Retention Improvement at High Temperatures in Tungsten - Uranium Dioxide Dispersion Fuel Elements by Plasma Spraying. NASA TM X-1028, 1964.

Miller, John V.: Predicting Thermal Conductivity of Tungsten - Uranium Dioxide Dispersions. NASA TM X-1145, 1965.

Raffo, Peter L.; Klopp, William D.; and Witzke, Walter R.: Mechanical Properties of Arc-Melted and Electron-Beam-Melted Tungsten-Base Alloys. NASA TN D-2561, 1965.

Material Fabrication

Blankenship, Charles P.; and Gyorgak, Charles A.: Preliminary Investigation of Extruding Composite Tungsten - Uranium Dioxide Tubing. NASA TM X-1072, 1965.

Watson, Gordon K.: Fabrication of Thin Tungsten - Uranium Dioxide Composite Plates. NASA TM X-1073, 1965.

Neutronics

Fieno, Daniel; Gunn, Eugene; Barber, Clayton; Fox, Thomas; Alger, Donald; and Mueller, Robert: Criticality Effects of Centrally Located Tubes and Rods of Aluminum, Iron, and Tungsten in a Homogeneous Reactor. NASA TN D-1322, 1962.

Semler, Thor T.: Neutron Self-Shielding Factors for Multiple-Body Concentric Cylindrical Configurations. NASA TN D-1587, 1964.

Shook, Donald F.: Two-Phase Hydrogen Density Measurements by Neutron Attenuation. Paper presented at the 11th Annual Nuclear Science Symposium, IEEE, Philadelphia, Oct. 28-30, 1964.

Engine Dynamics

Whitney, Warren J.: Analysis of Turbopump Feed Systems for Hydrogen-Nuclear Rockets. NASA TN D-2712, 1965.

CONTRACTOR REPORTS

Material Properties

Bowersock, R. V.; and Last, G. A.: Submicron Dispersion of UO_2 in Tungsten. Rep. No. BNWL-65 (NASA CR-54318), Battelle Pacific Northwest Labs., Aug. 1965.

Langer, S.; Baldwin, N. L.; and Burris, F. O., Jr.: Determination of Effects of Metal Oxide Additives on the Solubility of Uranium in UO_2. Rep. No. GA-6664 (NASA CR-54745), General Dynamics Corp., Aug. 1965.

Langer, S.; Baldwin, N. L.; and Burris, F. O., Jr.: Determination of Effects of Metal Oxide Additives on the Solubility of Uranium in UO_2. Rep. No. GA-6848 (NASA CR-54898), General Dynamics Corp., Nov. 1965.

Precht, W.; and Sundquist, L.: Investigation of Fuel Loss from Tungsten - Uranium Dioxide Bodies. Rep. No. MND-3178 (NASA CR-54329), Martin Co., Nuclear Div., Nov. 1964.

Taylor, R. E.: Thermal Properties of Tungsten - Uranium Dioxide Mixtures. Rep. No. AI 64-153 (NASA CR-54141), Atomics International, Sept. 1964.

Weber, C. W.; and Kwasnoski, T.: Determination of Impurities in Tungsten - Uranium Dioxide Mixtures. Rep. No. K-1621 (NASA CR-54275), Carbide and Carbon Chemicals Corp., Feb. 1965.

Zocher, R. W.: High Temperature Measurements of Young's Moduli for Tungsten and Tungsten - Uranium Dioxide Composites. Union Carbide Corp. (NASA CR-54847), Dec. 1965.

Material Fabrication

Abraham, L.; Katz, N. H.; and Supan, E. C.: Development of a Magneforming Process for the Fabrication of Thin-Wall Tungsten Cylinders. Rep. No. AI-65-12 (NASA CR-54316), Atomics International, Jan. 1965.

Allison, G. S.: Extrusion of Tungsten - UO_2 Honeycomb Structures. Battelle Pacific Northwest Labs. (NASA CR-54317), July 1965.

Anon: Ceramics Research and Development Operation. Quarterly Rep. HW-76304A (Oct.-Dec. 1963), HW-81600A (Jan.-Mar. 1964), HW-81601A (Apr.-June 1964), General Electric Hanford Atomic Products Operation, 1964.

Anon: Cermet Research and Development Activities. Rep. No. HW-84611 (NASA CR-54229), General Electric Hanford Atomic Products Operation, Apr. 1965.

Anon: Cermet Research and Development Activities. Quarterly Report on Tungsten - Uranium Dioxide. Rep. No. BNWL-39 (NASA CR-54304), Battelle Pacific Northwest Labs., Feb. 1965.

Anon: Tungsten - Uranium Dioxide Cermet Research and Development Activities. Rep. No. BNWL-110 (NASA CR-54409, Jan.-Mar. 1965), Apr. 1965; (NASA CR-54721, Apr.-June 1965), July 1965; (NASA CR-54851, July-Sept. 1965), Battelle Pacific Northwest Labs., Jan. 1966.

Cochran, W. L.; Knight, R. G.; and Stanley, F. S.: Final Report for FY 1965 on Tungsten - Uranium Dioxide Materials for NASA. Part I: Preparation of High Purity Uranium Oxide Powders. Part II: Cladding and Joining of Tungsten Cermets by Plasma Spraying. Part III: Tungsten Coating of Uranium Dioxide Particles. Rep. No. K-1647 (NASA CR-54482), Carbide and Carbon Chemicals Corp., Oct. 1965.

Douglas, A. David: Joining of Tungsten - Uranium Dioxide Composites by Vapor Deposition. Rep. No. SYL-6334-F, Sylvania Elec. Prods., Dec. 15, 1964.

Foley, E. M.; Wagner, R. L.; and White, D. E.: Fabrication of Tungsten - Uranium Dioxide Honeycomb Structures. Rep. No. K-1648 (NASA CR-54483), Carbide and Carbon Chemicals Corp., Nov. 1965.

Goetsch, G. R.; Cover, P. W.; Gripshover, P. J.; and Wilson, W. J.: Fabrication of Tungsten - UO_2 Hexagonal-Celled Fuel-Element Configurations. Battelle Memorial Inst. (NASA CR-54796), Oct. 1965.

Hoppe, A. W.; and Lamartine, J. T.: Tungsten Cladding of Tungsten - Uranium Dioxide (W-UO_2) Composites by Deposition from Tungsten Hexafluoride (WF_6). Rep. No. WANL-PR(Z)-003 (NASA CR-54835), Westinghouse Astronuclear Corp., Jan. 1966.

Japka, J. E.; and Gordon, E.: Joining of Tungsten - Uranium Dioxide Composites by Gas Tungsten-Arc and Electron Beam Brazing. Rep. No. UNC-5120 (NASA CR-54294), United Nuclear Corp., May 1965.

Johnson, D. D.; Leak, V. G.; and Pettman, R. E.: Research and Development on Tungsten, Uranium Dioxide, Fuel-Element Configuration. Minnesota Mining and Manufacturing Nuclear Prods. (NASA CR-54218), Aug. 1964.

Johnson, D. D.; and Pettman, R. E.: Fabrication of Tungsten - UO_2 Composites by a Powder Metallurgy Process. Rep. No. MMM-8094 (NASA CR-54342), Minnesota Mining and Manufacturing Nuclear Prods., Feb. 1965.

Johnson, D. D.; and Pettman, R. E.: Fabrication of Tungsten - UO_2 Composites by a Powder Metallurgy Process. Rep. No. MMM-8932 (NASA CR-54766), Minnesota Mining and Manufacturing Nuclear Prods., July 1965.

Johnson, D. D.; Pettman, R. E.; and Jackson, D. E.: Fabrication of Tungsten - UO_2 Composites by a Powder Metallurgy Process. Rep. No. MMM-8439 (NASA CR-54424), Minnesota Mining and Manufacturing Nuclear Prods., May 1965.

MacInnis, M. B.; and Schulze, H. O.: Tungsten Cladding of Tungsten - Uranium Dioxide Composites by Chloride Vapor Deposition. Rep. No. Syl 6335-FR1 (NASA CR-54728), Sylvania Elec. Prods., 1965.

Peterson, J. H.; Meiners, K. E.; and Gripshover, P. J.: Joining of Tungsten - UO_2 Components by Diffusion Bonding. Battelle Memorial Inst. (NASA CR-54791), Oct. 1965.

Weinberg, A. F.; and Lindgren, J. R.: Joining of Tungsten - Uranium Dioxide Composites. Phase I. Rep. No. GA-5858 (NASA CR-54253), General Dynamics Corp., Dec. 1964.

Archibald, G. R.; Jacoby, M. A.; and Pincock, G. D.: Control Absorber and Fuel Element Mockup Experiment for the Tungsten, Water-Moderated Nuclear Rocket Reactor. Rep. No. GEMP-350 (NASA CR-54335), General Electric Co., Flight Propulsion Lab., March 1965.

Carpenter, S. G.; Otter, J. M.; Paschall, R. K.; and Royden, H. N.: Tungsten Resonance Integrals and Doppler Coefficients. Rep. No. AI-65-225 (NASA CR-54769), Atomics International, Oct. 1965.

Celnik, J.; and Spielberg, D.: Gamma Spectral Data for Shielding and Heating Calculations. Rep. No. UNC-5140 (NASA CR-54794), United Nuclear Corp., Nov. 1965.

Cohen, S. C.; Joanou, G. D.; Moore, R. A.; and Peak, J. C.: Neutronic Simulation of the Tungsten - Water-Moderated Nuclear Rocket Reactor. Rep. No. GA-6141 (NASA CR-54293), General Dynamics Corp., Feb. 1965.

Friesenhahn, S. J.; Haddad, E.; Fröhner, F. H.; and Lopez, W. M.: The Energy Dependence of the Neutron Capture Cross Section of the Tungsten Isotopes from .01 to 10 EV. Rep. No. GA-6832 (NASA CR-54860), General Dynamics Corp., 1965.

Friesenhahn, S. J.; Haddad, E.; Fröhner, F. H.; and Lopez, W. M.: The Neutron Capture Cross Section of the Tungsten Isotopes from 0.01 to 10 Electron Volts. Rep. No. GA-6882, General Dynamics Corp., Jan. 20, 1966.

Joanou, G. D.; and Drake, M. K.: Neutron Cross Sections for U^{235}. Rep. No. GA-5944 (NASA CR-54263), General Dynamics Corp., Dec. 1964.

Joanou, G. D.; and Stevens, C. A.: Neutron Cross Sections for Aluminum. Rep. No. GA-5884 (NASA CR-54260), General Dynamics Corp., Nov. 1964.

Joanou, G. D.; and Stevens, C. A.: Neutron Cross Sections for Beryllium. Rep. No. GA-5905 (NASA CR-54262), General Dynamics Corp., Nov. 1964.

Joanou, G. D.; and Stevens, C. A.: Neutron Cross Sections for Tungsten Isotopes. Rep. No. GA-5885 (NASA CR-54261), General Dynamics Corp., Nov. 1964.

Joanou, G. D.; and Stevens, C. A.: Neutron Cross Sections for U^{238}. Rep. No. GA-6087 (NASA CR-54290), General Dynamics Corp., Apr. 1965.

Lofthouse, J. H.; Masson, L. S.; Pincock, G. D.; and Sims, F. L.: Data Results from NASA Fuel Cartridge Experiment in 630A Critical Experiment Reactor. Rep. No. TM-63-7-701, General Electric, National Reactor Testing Site, July 19, 1963.

Peak, J. C.; Cohen, S. C.; Merrill, M. H.; and Lovallo, J. M.: Criticality Calculations for the Three-Inch Pitch As-Built Core. Rep. No. GA-6484 (NASA CR-54431), General Dynamics Corp., June 1965.

Peak, J. C.; and Lovallo, J. M.: Precritical Calculations for the 2.9 in. Pitch, TWMR Critical Assembly. Rep. No. GA-6633 (NASA CR-54644), General Dynamics Corp., Aug. 1965.

Peak, J. C.; and Lovallo, J. M.: Precritical Calculations for the 3.0 in. Pitch, Beryllium Reflected, TWMR Critical Assembly. Rep. No. GA-6807 (NASA CR-54786), General Dynamics Corp., Nov. 1965.

Pincock, G. D.; and Jacoby, M. A.: Data Results from NASA Fuel Cartridge Experiment in 630A Critical Experiment Reactor. Rep. No. GEMP-262, General Electric, Advanced Tech. Services, Dec. 23, 1963.

Pincock, G. D.; and Jacoby, M. A.: A Tungsten Water-Moderated Nuclear Rocket Reactor Critical Experiment with 37 Fuel Elements. General Electric Atomic Products Div. (NASA CR-54453), July 1965.

Spielberg, D.: Recommended Monte-Carlo Program for Computing Radiation Heating in a Tungsten Water-Moderated Reactor (TWMR). Rep. No. UNC-5105 (NASA CR-54202), United Nuclear Corp., Dec. 1964.

Valerino, Michael F.; Harding, Robert S.; and Bevilacquo, F.: Reactivity Control of a Water-Moderated Tungsten Rocket Reactor, Vol. I - Evaluations of Control Concepts. Rep. No. GNEC-334, Vol. I, General Nuclear Corp., Mar. 31, 1964.

Valerino, Michael F.; Harding, Robert S.; and Bevilacquo, F.: Reactivity Control of a Water-Moderated Tungsten Rocket Reactor, Vol. II - Heat Exchanger - Reactor System Kinetic Characteristics in the 20% to Full Power Range. Rep. No. GNEC-334, Vol. II, General Nuclear Corp., July 10, 1964.

Engine Dynamics

Marcy, R.; Cannon, W.; and Bulgier, L.: Feed System Analysis - Tungsten Water-Moderated Reactor. Rep. No. R-6338 (NASA CR-54438), Rocketdyne Div., North American Aviation, Oct. 1965.

Marcy, R.: Cannon, W.; Bulgier, L.; and Harper, B.: Feed System Analysis - Tungsten Water-Moderated Reactor. Rep. No. R-6124 (NASA CR-54270), Rocketdyne Div., North American Aviation, March 1965.

Wasserman, A. A.; Maguire, A. F.; Gurski, P. S.; and Stock, A. H.: Tungsten Reactor Dynamics Analysis Project Phase I, Summary Report. Rep. No. WANL-PR(W)-005 (NASA CR-54212), Westinghouse Astronuclear Corp., Nov. 1964.

Chemistry

Griess, J. C.; Jenks, G. H.; Eissenberg, K. M.; and Bohlmann, E. G.: An Evaluation of the Chemical Problems Associated with the Aqueous Systems in the Tungsten - Water-Moderated Reactor. Rep. No. ORNL-TM-913 (NASA CR-54198), Oak Ridge National Labs., Aug. 1964.

Jenks, G. H.; Bohlmann, E. G.; and Griess, J. C.: An Evaluation of the Chemical Problems Associated with the Aqueous Systems in the Tungsten - Water-Moderated Reactor - Addenda 1 and 2. Rep. No. ORNL-TM-978 (NASA CR-54214), Oak Ridge National Labs., March 1965.

Jenks, G. H.; Savage, H. C.; and Bohlmann, E. G.: NASA Tungsten Reactor Radiation Chemistry Studies Phase I, Experiment Design. Rep. No. ORNL-TM-1403 (NASA CR-54887), Oak Ridge National Labs., March 1966.

Reactor Control

Eanes, W. F.: Design of Laboratory Tests. Task II - Feasibility of a Chemical Poison Loop System. Rep. No. WCAP-2803 (NASA CR-54420), Westinghouse Elec. Corp., June 1965.

Eanes, W. F.: Summary Report - Analysis of Reference System. Task I - Feasibility of a Chemical Poison Loop System. Rep. No. WCAP-2690 (NASA CR-54291), Westinghouse Elec. Corp., Feb. 1965.